2021

Neutron Cross Section Measurement In The Protodune-Sp Experiment

David Orlando Rivera
University of Pennsylvania

Recommended Citation

Rivera, David Orlando, "Neutron Cross Section Measurement In The Protodune-Sp Experiment" (2021). *Publicly Accessible Penn Dissertations*. 4676.
https://repository.upenn.edu/edissertations/4676

Neutron Cross Section Measurement In The Protodune-Sp Experiment

Abstract

Understanding the detector response to neutrons will be critical for performing neutrino oscillation analyses in the next-generation Deep Underground Neutrino Experiment (DUNE). The DUNE physics program is centered around measuring the neutrino flavor composition as a function of their energy both at the near and the far detector. Neutrinos in the DUNE beam will have energies ranging between 100 MeV and 10 GeV, which is significant, because individual neutrino energies will not be known beforehand and will have to be reconstructed. Neutrino interactions in DUNE will produce leptons and hadrons – including protons, pions, and neutrons. Neutrons can transport energy away from their origin and sometimes go undetected. In addition to the primary neutrons produced by the neutrino, subsequent interactions of the charged hadrons can result in secondary neutrons. Neutrons are a source of missing energy and will bias the neutrino energy measurement. Currently, there is also a 20% energy scale uncertainty and a 40% uncertainty on the energy resolution for neutrons in DUNE, which must be addressed. ProtoDUNE Single-Phase (ProtoDUNE-SP) is a 770-ton prototype for the DUNE far detector and was designed to both validate the technology that will be employed in DUNE and to measure cross sections for the charged hadrons (pions, protons, and kaons) at the relevant energies for DUNE. The ProtoDUNE-SP experiment, therefore, is in a unique position to characterize the secondary neutron component for DUNE. This is achieved by searching for candidate neutron interactions in ProtoDUNE-SP events and using these to facilitate a measurement of the neutron inelastic cross section as well as an estimate of the neutron energy and number. The cross section measurement presented here is based on neutrons produced in 1 GeV, π^+ events captured in 2018 by ProtoDUNE-SP in accordance with the production and cross section models in theGEANT4 simulation toolkit, version 4.10.6p1. The best-fit neutron inelastic cross section, in the kinetic energy range of 114 to 314 MeV, is $1.24(+0.10)(-0.08)$ (stat. $\oplus$ syst.) barns.

Degree Type

Dissertation

Degree Name

Doctor of Philosophy (PhD)

Graduate Group

Physics & Astronomy

First Advisor

Joshua R. Klein

Keywords

cross section, DUNE, LArTPC, Long Baseline, neutrinos, neutrons

Subject Categories

Elementary Particles and Fields and String Theory

NEUTRON CROSS SECTION MEASUREMENT IN THE PROTODUNE-SP EXPERIMENT

David Orlando Rivera Jr.

A DISSERTATION

in

Physics and Astronomy

Presented to the Faculties of the University of Pennsylvania

in

Partial Fulfillment of the Requirements for the

Degree of Doctor of Philosophy

2021

Supervisor of Dissertation

____
Joshua R. Klein, Edmund J. and Louise W. Kahn Term Professor of Physics and Astronomy

Graduate Group Chairperson

____
Ravi K. Sheth, Professor of Physics and Astronomy

Dissertation Committee

James Aguirre, Associate Professor of Physics and Astronomy

I. Joseph Kroll, Professor of Physics and Astronomy

Christopher M. Mauger, Associate Professor of Physics and Astronomy

Mark Trodden, Fay R. and Eugene Langberg Professor of Physics and Astronomy and Department Chair

NEUTRON CROSS SECTION MEASUREMENT IN THE PROTODUNE-SP
EXPERIMENT

In memory of Marjorie Diane Corcoran and Luis Alejandro Ramirez Delgado – may you rest in peace. Dedicated to my family.

ACKNOWLEDGMENT

This work is supported by the University of Pennsylvania, the DOE Office of HEP (DE-FG02-95ER40893), the Fermi National Accelerator Laboratory, and the University Research Association.

I would like to thank my advisors over the years: Marj Corcoran[†][*], Aseet Mukherjee[‡], Mitch Newcomer[§], Rick Van Berg[§], Godwin Meyers[§], Bill Badgett[‡], Michelle Stancari[‡], Gennadiy Lukhanin[‡] , Tingjun Yang[‡], Hans Wenzel[‡], and Josh Klein[§]– I owe a lot of great learning opportunites to you. A huge thanks to the professors in the Department of Physics and Astronomy at the University of Pennsylvania who both challenged us and took their role in our education seriously. I would also like to thank post docs and fellow graduate students with whom I have collaborated over the years and from who I also learned a lot.

I am especially grateful to friends and family who have provided their unwavering support. To my sister, Erika Rivera, who has always served as an exceptional role model for as long as I have the capability of remembering.

Un agradecimiento especial para mis padres Lorena y David Rivera quienes se sacrificaron para poder proveer una mejor vida para mi hermana Erika y para mi en este país. Me gustaria tambien reconocer y agradecer a mis familiares en El Salvador quienes han tenido que superar muchas dificultades pero que siempre nos mantienen en sus pensamientos y oraciones.

[†] Deceased

[*] Rice University

[‡] Fermi National Accelerator Laboratory

[§] University of Pennsylvania

ABSTRACT

NEUTRON CROSS SECTION MEASUREMENT IN THE PROTODUNE-SP EXPERIMENT

David Orlando Rivera Jr.

Joshua R. Klein

Understanding the detector response to neutrons will be critical for performing neutrino oscillation analyses in the next-generation Deep Underground Neutrino Experiment (DUNE). The DUNE physics program is centered around measuring the neutrino flavor composition as a function of their energy both at the near and the far detector. Neutrinos in the DUNE beam will have energies ranging between 100 MeV and 10 GeV, which is significant, because individual neutrino energies will not be known beforehand and will have to be reconstructed. Neutrino interactions in DUNE will produce leptons and hadrons – including protons, pions, and neutrons. Neutrons can transport energy away from their origin and sometimes go undetected. In addition to the primary neutrons produced by the neutrino, subsequent interactions of the charged hadrons can result in secondary neutrons. Neutrons are a source of missing energy and will bias the neutrino energy measurement. Currently, there is also a 20% energy scale uncertainty and a 40% uncertainty on the energy resolution for neutrons in DUNE, which must be addressed. ProtoDUNE Single-Phase (ProtoDUNE-SP) is a 770-ton prototype for the DUNE far detector and was designed to both validate the technology that will be employed in DUNE and to measure cross sections for the charged hadrons (pions, protons, and kaons) at the relevant energies for DUNE. The ProtoDUNE-SP experiment, therefore, is in a unique position to characterize the secondary neutron component for DUNE. This is achieved by searching for candidate neutron interactions in ProtoDUNE-SP events and using these to facilitate a measurement of the neutron inelastic cross section as well as an estimate of the neutron energy and number. The cross section measurement presented here is based on neutrons produced in 1 GeV, π^+ events captured in

2018 by ProtoDUNE-SP in accordance with the production and cross section models in the GEANT4 simulation toolkit, version 4.10.6p1. The best-fit neutron inelastic cross section, in the kinetic energy range of 114 to 314 MeV, is $1.24^{+0.10}_{-0.08}$ (stat. $\oplus$ syst.) barns.

TABLE OF CONTENTS

LIST OF TABLES

LIST OF FIGURES

PREFACE

0.1. Introduction

Over the last few decades, several neutrino experiments have been designed and built to measure the physical parameters that govern neutrino flavor oscillations – the mixing angles (θ), the mass splittings (Δm^2), and the Charge-Parity (CP) violating phase δ_{CP}.

Consider a two-neutrino (ν_α, ν_β) oscillation model, it will be shown in CHAPTER 1 that the probability for a neutrino produced as a flavor eigenstate ν_α, with energy E (in GeV), to be detected as a ν_β flavor eigenstate, after propagating to a detector L kilometers away from its origin is:

$$P_{\nu_\alpha \to \nu_\beta}(L, E) = sin^2(2\theta) sin^2\Big(1.27 \Delta m^2 \frac{L}{E}\Big), \tag{1}$$

where θ and Δm^2 (in eV^2) are the oscillation parameters to be determined empirically, and where L is referred to as the *baseline.*

A handful of these experiments fall into the category of long-baseline (L ~ hundreds of kilometers) oscillation experiments, which rely on intense neutrino beams generated at accelerator complexes. Among these experiments are Tokai to Kamioka (T2K) (Abe et al., 2020) in Japan, and two U.S.-based experiments, namely, the Main Injector Neutrino Oscillations Search experiment (MINOS) (Adamson et al., 2013) and the NuMI Off-axis ν_e Appearance experiment (NOvA)(Acero et al., 2021), where NuMI refers to the Neutrinos at the Main Injector beamline located at the Fermi National Accelerator Laboratory (Fermilab). In addition to facilitating the study of long baseline oscillations, accelerator-based neutrino experiments have the flexibility (through the choice of L/E) to enable searches for evidence of additional, non-interacting (sterile), neutrino flavors with oscillation parameters favorable for flavor transitions at short baselines (hundreds of meters). The Liquid Scintillator Neutrino Detector (LSND) (White and Collaboration, 1999) at Los Alamos and MiniBooNE (Aguilar-Arevalo et al., 2018) belong to the short-baseline subcategory of accelerator-based neutrino experiments.

Oscillation experiments must be designed with the complication in mind that neutrinos rarely interact. One way to make a neutrino oscillation experiment feasible is to select a dense target or to increase the intensity of the neutrino beam. Experiments discussed in this dissertation rely on a recently developed technology, Liquid Argon Time Projection Chambers (LArTPCs), which were first proposed in the late 70s. LArTPCs present a relatively dense target for neutrino experiments (1.4 g/cm^3). Argon is also abundant and relatively cheap, and it can be condensed into liquid form through the use of liquid Nitrogen, which is commonplace. LArTPCs can be densely instrumented to provide good vertex reconstruction (mm scale). For reference, a minimum ionizing particle (MIP) is likely to deposit 1.8 MeV/cm.

The experiments that will be explored in more detail, include the Deep Underground Neutrino Experiment (DUNE) – a next-generation long baseline neutrino oscillation experiment, two DUNE prototypes, and the Short Baseline Near Detector (SBND) based at Fermilab. Of these experiments, only the DUNE prototypes, i.e. the 35-ton and ProtoDUNE-SP, have been in operation – SBND is under construction, and DUNE is projected to turn on in 2028.

0.2. Motivation

A source of uncertainty that must be addressed for any neutrino oscillation experiment, in order to make an accurate measurement, is the flavor and energy profile of the neutrino beam itself. Typically this is mitigated through an experiment design that includes a near detector, which can sample the flux and composition of the neutrino beam at the origin, where the transition probability is negligible, purely by construction.

One can appreciate, from equation 1, that a measurement of the transition probability depends on the energy of the neutrinos. For experiments that are *On-Axis*, i.e. where the far detector is centered within the neutrino beam, the beam can have a sizable spread in energy*, thus neither the flavor nor the energy of the incident neutrinos is known *a-priori*. These two, very important properties of the incident neutrinos must be determined from the data produced by the interactions themselves, i.e. the flavor and the energy must be reconstructed. The flavor can be determined, more easily, depending on the topology of the interaction, however, the energy can have a sizable uncertainty.

Something that is clear is that having poor energy resolution will result in significant smearing of the oscillation parameters. A poor resolution can be the result of several factors, but among the biggest concerns are missing energy and a poorly known or understood detector response. One of the dominant sources of missing energy are neutrons, whose detection in a LArTPC is further complicated by the large uncertainties on neutron interactions in liquid argon. Thus understanding neutron interactions in LAr and constraining uncertainties on these is critical to the neutrino oscillation program planned for these detectors. Figure 1 below, shows the impact of missing energy and poor energy resolution on a DUNE-style long baseline experiment.

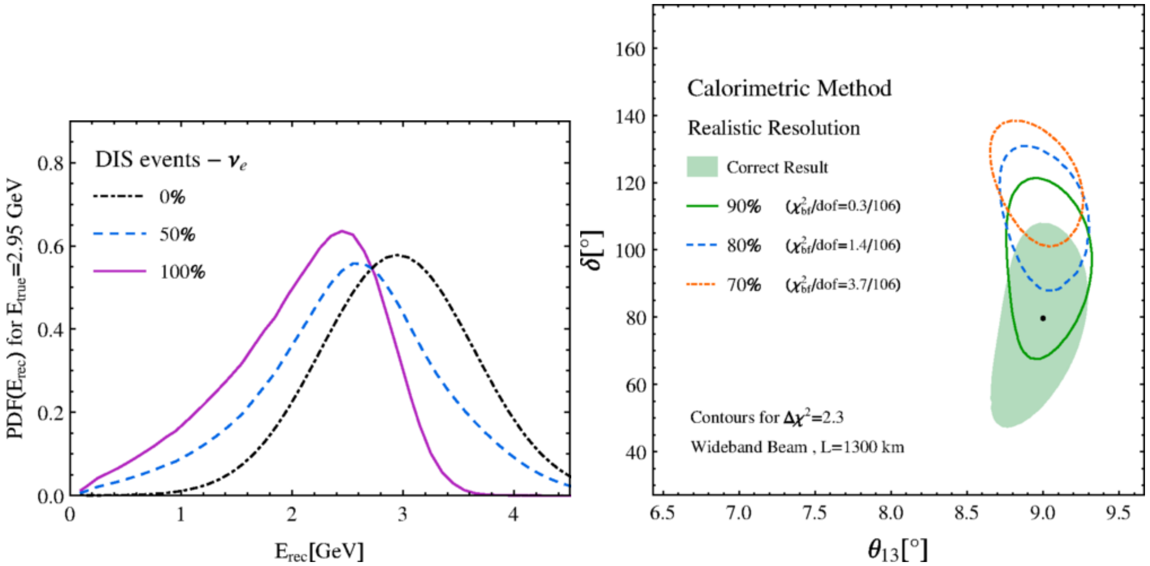

Figure 1: Left: ν_e reconstructed energy with 0%, 50%, and 100% missing energy resulting in an increasing bias for the peak energy. **Right**: δ_{CP} vs. θ_{13} parameter space with full and partial account for missing energy. Reprinted figures with permission from (Ankowski et al., 2015) Copyright (2021) by the American Physical Society.

---

*The beam is said to be wideband.

The effects of ignoring the neutron depositions in performing reconstruction on neutrino events for DUNE are a loss in resolution of 10% – from a best case scenario of 6% up to 16%.

LArTPCs are great for imaging charged particle interactions and have a short radiation length (14 cm) which also makes them ideal target for electromagnetic showers; however they are not great for stopping neutrons. Neutrons can be problematic for LArTPCs, because they:

- can travel meters without producing significant visible energy
- can escape the detector without interacting – missing energy
- can penetrate detectors and be mistaken with internally generated neutrons
- are copiously produced in nuclear de-excitation and evaporative processes
- release 6.6 MeV worth of gamma rays upon being captured and present a threat for low energy physics

The hadronic energy resolution for LArTPCs largely affects the ability to reconstruct and associate energy deposits from neutrons to their production vertices. Neutrons produce visible energy *indirectly* – through collisions that directly eject charged particles or that result in gamma ray emission. These gammas can undergo electromagnetic processes that result in ionization and the resulting visible energy is, at least, twice removed from the neutron origin. In addition to elastic and inelastic collisions, neutrons can be captured on Argon. Typically they approach thermal equilibrium through a series of collisions with the LAr through inelastic collision with liquid argon, which result in low energy de-excitation gammas. These gammas can displace the energy further and can produce ionization through Compton scattering, photoelectric ejection, and pair production.

The goal of the author in this dissertation is to address some of the nuisances posed by neutrons for LArTPC-based neutrino experiments, such as DUNE, by using test-beam data collected by the ProtoDUNE-SP experiment in 2018. Although the test-beam only included charged hadrons and leptons, the author relies on the prevalence of neutrons in the final states of primary pion interactions in LAr to serve as a source of neutrons for this study to facilitate a cross section measurement. The interactions of interest for this analysis are neutron inelastic collisions, because they are, arguably, easier to identify when they are energetic enough to result in proton tracks.

0.3. Organization

This document is organized as follows: the first chapter, CHAPTER 1, is a review of some of the relevant neutrino physics and includes a brief review of the Standard Model, as well as some of the history surrounding neutrinos that has led to the field of experimental neutrino physics. This is followed by a description of the LArTPC technology (CHAPTER 2) as it applies to the LArTPC-based experiments mentioned in this foreword. The third chapter, CHAPTER 3, covers triggering in LArTPC experiments, and it includes some of the work by the author on the SBND trigger and on the DUNE software trigger.

The study presented here relies on LArSoft, introduced in CHAPTER 5, which uses the GEANT4 toolkit to simulate particle interactions in the ProtoDUNE-SP detector. GEANT4 is very flexible – the physical interactions between particles and the detector can be controlled and both the models that determine the final states as well as the cross sections for these processes can be be independently chosen. More details can be found in CHAPTER 4 and 5.

CHAPTER 4 will re-emphasize the importance and impact of understanding the detector response to neutrons and will mention relevant measurement in other experiments. The remaining chapters focus on the cross section analysis and the work by the author in order to be able to measure the neutron cross section in ProtoDUNE-SP, using 1GeV, π^+ events as the effective source of neutrons. Although the neutron trajectory cannot be known, the neutron displacement from the primary pion vertex is used as a proxy to the neutron cross section.

CHAPTER 6 includes a secondary result, which was obtained in order to cover the largest source of systematic uncertainty in the analysis, namely, the position reconstruction. It will be mentioned that a detector such a ProtoDUNE-SP, which is on Earth's surface, must cope with the accumulation of positive ions in the bulk of the detector, which ultimately *distorts* the field experienced by the ionization electrons – this is known as the Space Charge Effect (SCE). The ProtoDUNE-SP collaboration, along with other surface LArTPC experiments, address SCE via corrections and calibrations. A study of the impact of the position reconstruction, and the residual SCE, on a measurement of the interaction length for gamma rays from π^0 decays, is performed in order to gauge the magnitude of this systematic on the neutron cross section. CHAPTER 7 presents the results of the analysis and includes additional studies and suggestions to improve the understanding of neutrons in liquid argon, looking towards DUNE.

The appendices contain additional work by the author on triggering. On a final note, various acronyms are used throughout this document and are defined once, on their first appearance, however the reader can also find them in APPENDIX E.

CHAPTER 1 : INTRODUCTION

Since Wolfgang Pauli proposed their existence in 1930, the particles that we now know as neutrinos were perplexing to the particle physics community, who believed at the time that a complete nuclear model only required electrons, protons, and photons[1]. Pauli postulated the existence of this additional, neutral particle as a way to reconcile the observations in beta decays of an energy spectrum for electrons[2] with fundamental conservation laws, for it is not possible to conserve energy, momentum, and spin in a decay where the recoiling nucleus and the electron do not equally share the energy. It should be noted that gamma rays were ruled out as the source of missing energy long before Pauli proposed his neutron. It was known at the time that photons are spin 1 particles, furthermore, their absence from these decays could also be confirmed by surrounding the beta decay source with materials of short radiation length that would present obvious signatures from gamma rays.

Shortly after, in 1932, J. Chadwick deduced the existence of particles with zero electric charge and mass close to that of protons (Chadwick, 1932) , which he called neutrons. It became clear that Chadwick's neutrons were distinct from the neutral particle postulated by Pauli, which had to be light compared to the proton in order to leave the atomic mass of the beta decay isotopes relatively unchanged following beta ray emission.

Enrico Fermi reconciled the two neutral particles with his model for beta decay, in which, a neutron decays into a proton, an electron, and Pauli's neutrino. The direct detection of neutrinos did not occur for two decades following Fermi's theory. In 1956 Cowan and Reines were the first to report a direct detection (Cowan et al., 1956-07), establishing neutrinos as elementary particles and opening up the field of neutrino detection experiments.

---

[1] This was following Compton's experiment in 1923 which demonstrated conservation of energy and momentum in individual scattering interactions between light and electrons, which itself, was controversial, but that supported the wave-particle duality of photons as advocated by Einstein.

[2] James Chadwick noted and studied the properties of beta decays in 1914.

1.1. The Standard Model of Particle Physics

Before moving on to the topic of neutrino physics, a short review of the Standard Model (SM) is presented here for context. A basic understanding of particle physics will be assumed in the current section and many claims/results will be outlined without proof in the interest of brevity.

The SM of particle physics is a theory summarizing the known particles, forces, and the equations governing their interactions. In general, it is a Quantum Field theory in which the fields are the fundamental objects and the particles are viewed as the quanta of the fields. The forces include the Electromagnetic, Weak, and Strong – each is described in connection with the fundamental particles that mediate them (known as vector bosons): photons, $\mathrm{W}^{\pm}$ and Z^0, and gluons, respectively. Each force is also characterized by a coupling strength that is relevant when performing calculations of quantities such as decay rates and cross sections, and is, in part, what makes the SM a useful theory. A fourth fundamental force, Gravity, is in a category of its own, and for the purposes of studying elementary particles it is negligible compared to the other three and currently absent from a verified SM theory.

The Electromagnetic (EM) force is mediated by the massless photon and couples to all charged SM particles, with coupling strength α (~1/137 with a small energy scale dependence). Electromagnetism was the first theory, of what is now the SM, to be quantized and has been widely studied under the name of Quantum Electrodynamics (QED). The Weak force is responsible for radioactive decays but encompasses all interactions that couple to the neutral Z (Z^0) and charged W (W^- and W^+) bosons with coupling strength α_W. The Strong force is mediated by massless gluons and is characterized by the coupling strength α_S, which has a relatively large energy scale dependence.

A defining property of all SM particles is known as intrinsic spin, which dictates how these particles interact with various fields, how they occupy quantum states in ensembles of identical particles, and how they can (potentially) combine into composite particles. All

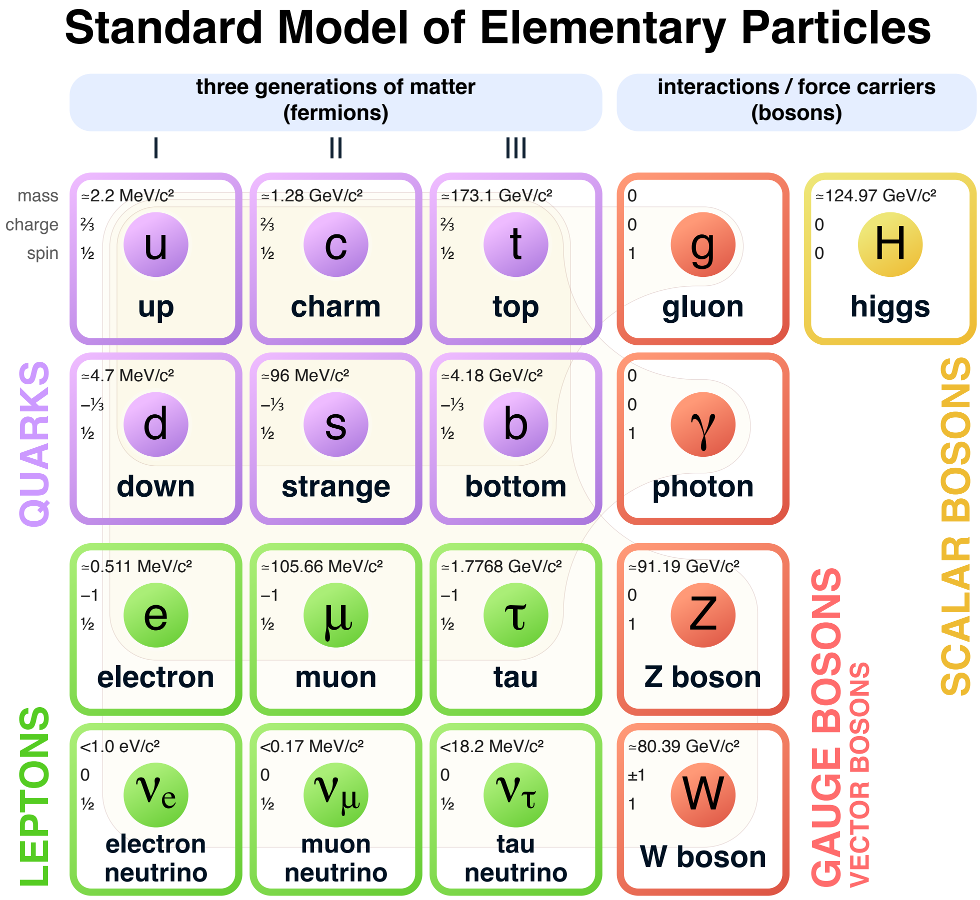

Figure 2: Depiction of the Standard Model of Elementary Particles. An equivalent table exists for the anti-particles. Original figure from public domain.

particles that propagate in 3D Euclidean space have either spin 1/2 (fermions) or integer spin (bosons). The particles that mediate the aforementioned forces have been established as gauge (vector) bosons and are all spin-1 particles while the known fermions are subdivided into Quarks and Leptons as shown in fig. 2. Fermions obey Fermi-Dirac statistics and are subject to the Pauli exclusion principle, while the bosons have integer spin (zero spin in the case of the Higgs Boson) and adhere to Bose-Einstein statistics.

Quarks are the constituents of all hadronic matter and are the only fermions that experience the fundamental Strong force. They have fractional positive and negative electromagnetic charge and are organized into three generations – each generation with one up-type (Q=$+\frac{2}{3}$e) and one down-type quark (Q=$-\frac{1}{3}$e) for a total of six quarks and six anti-quarks. In addition to electromagnetic charge, quarks carry a quantum number known as color charge, dictating how they interact via the exchange of gluons. Two important features of the strong force are:

1. color confinement, which requires that *free* hadronic states exist in “colorless” combinations of quarks (i.e. color singlets) and
2. asymptotic freedom – referring to the fact that the strength of the Strong force, characterized by α_s, weakens as the energy scale increases (and the distance scale decreases).

These two properties are naturally born out of, what are known as, non-Abelian gauge theories, which result from a non-commutative property of the generators of the corresponding symmetry group. Another important result that is manifest in a non-Abelian gauge theory is that the fields, even in the absence of fermions, carry a charge and therefore have non-trivial interactions. In contrast to this, QED is an Abelian gauge theory, described through a unitary phase transformation where the generator is a constant and naturally commutes. As a result, the QED photon carries no electromagnetic charge and has no self-couplings. The Strong force, like the EM force, is mediated by massless vector bosons i.e. gluons. Gluons are electrically neutral but do carry color charge, and unlike the photon of the EM field, gluons couple to themselves resulting in a highly nontrivial quantum field theory known as Quantum Chromodynamics (QCD).

The Leptons are not known to arrange into composite particles[1] but exist in three known pairs – charged leptons and their neutral, partner neutrinos. Neutrinos are the only SM particles that interact solely via the Weak force making them relatively hard to detect. They are also the only SM particles that can be either Dirac or Majorana fermions, where Majorana fermions are their own anti-particles. The properties of neutrinos will be discussed in more detail in the remainder of this chapter.

The Higgs Boson is the final, and most recently confirmed particle of the SM and is in a category of its own due to its zero spin, which makes it a *scalar* particle. It can be understood as a quantum excitation of the scalar Higgs field, which spontaneously obtains a non-zero Vacuum Expectation Value (VEV) resulting in the Electroweak (EW) Symmetry Breaking.This same symmetry breaking is responsible for introducing mass terms to the SM Lagrangian for the weak vector bosons whose masses are related via the following equation:

$$m_W = m_Z \cos\theta_W \quad , \tag{1.1}$$

where θ_W is known as the weak, or Weinberg, angle and is a measurable parameter of the SM. The predictive power of the SM is regarded as a huge success for the theory. Interactions with the Higgs field result in another defining property of fermions i.e. mass; this will be further discussed in section 1.1.3. Another important consequence of the spontaneous symmetry breaking resulting from the non-zero VEV of the Higgs field is the re-shuffling of the degrees of freedom in the EW theory such that the massless (Goldstone) bosons of the unified EW force become associated with the conserved currents of the theory. The

---

[1] An exception to this exists in condensed matter and results in superconductivity through formation of Cooper pairs (e^-e^-). The electrons form "composite-bosons" in the presence of a lattice of positive ions; however, these are very weakly bound states and "occupy" space much larger (nm) than baryons (fm) for example.

relatively large mass of these bosons (~90 GeV) is what restricts the range of the Weak force.

Particles of the SM are described through the use of various quantum numbers, some of which correspond to direct observables (e.g. charge) and some that are not observable (isospin) but dictate if and how they interact.

An additional property dictating the interactions of the SM particles is known as the chirality and has two states: left and right. Chirality indicates the sign of the projection of the intrinsic spin of a particle (m_s) in the direction of motion and therefore takes on values of $\pm m_s \hbar$.

The SM is typically presented as a Lagrangian density ($\mathscr{L}$) written with manifestly covariant terms in order to make apparent the global and local symmetries in the underlying physics [1]. The Action ($S = \int L dt = \int (\int d^3x \mathscr{L}) dt$) is a conserved quantity and the Lagrangian can be used to derive the equation of motion via the Euler-Lagrange equation. This notion arises in classical physics – through variational calculus; however, it remains useful in Quantum Field Theory via the principle of least action.

The SM is also what is referred to as a gauge theory, and as such, it can be expressed as a Lagrangian invariant under a symmetry group G_{SM}, where $G_{SM} = SU(3)_C \times SU(2)_L \times U(1)_Y$. The Symmetry group is associated with complete sets of generators that can be used to map out the interactions and transformations of the fields. G_{SM} is explicitly factorized into three parts – this highlights that each factor is associated with different quantum numbers that pertain to specific interactions and therefore the factors commute, resulting in the different coupling strengths for each gauge group factor. The SU(N), i.e. the N-dimensional Special Unitary groups, are characterized by $N^2 - 1$, independent unitary matrices with dimensions N-by-N and have determinant equal to 1. In $SU(3)_C$ these correspond to the (eight) Gellman matrices which are analogous to the Pauli σ matrices

---

[1] This is in contrast with the Hamiltonian equivalent, which is not manifestly covariant but whose results are equally invariant

of $SU(2)$. U(1) refers to the unitary 1-D phase rotations which are characterized by a single parameter α and which famously surfaces in the theory of Quantum Electrodynamics (QED).

$SU(3)_C$ is the symmetry group that encompasses the Strong force and has eight associated generators corresponding to eight gluon fields. The $SU(2)_L \times U(1)_Y$ subgroup corresponds to the unbroken Electroweak force, which has 3 + 1 associated boson fields $(\{\tilde{A}_1, \tilde{A}_2, \tilde{A}_3\}, B_0)$. Following the introduction of a Higgs field with a non-zero VEV into the SM Lagrangian, the EW $SU(2)_L \times U(1)_Y$ group is spontaneously broken down to $U(1)_Q$ which is the gauge group corresponding to QED.

A simplified version of the SM Lagrangian, excluding corrections such as the so-called Fadeev-Popov ghost terms used cancel unphysical degrees of freedoms (e.g. unphysical gluon fields), (below) illustrates its covariant nature and makes it possible to recognize gauge invariance.

$$\mathscr{L} = -\frac{1}{2}\mathrm{tr}[F_{\mu\nu}F^{\mu\nu}] + i\overline{\Psi}_L \not{D}\Psi_L + \mathrm{tr}\Big[(D_\mu\Phi)^\dagger(D^\mu\Phi)\Big] \tag{1.2}$$

$$+ \mu^2\Phi^\dagger\Phi - \frac{1}{2}\lambda(\Phi^\dagger\Phi)^2 + \Big(\frac{1}{2}\Psi_L^T Ch\Phi\Psi_L + h.o.c.\Big) \tag{1.3}$$

Ψ_L in eq. 1.3 represents the left-handed fermion fields and $\overline{\Psi}_L$ represents the so-called adjoint of these fields, both of which are related through eq. 1.4.

$$\overline{\Psi} = \Psi^\dagger\gamma^0 \quad \text{, where } \gamma^0 = \begin{pmatrix} 0 & 1 \\ 1 & 0 \end{pmatrix} \tag{1.4}$$

D_μ is the covariant derivative, which is carefully chosen to preserve local gauge invariance, and $F_{\mu\nu}$ is the field-strength tensor (analogous to the energy-momentum tensor in Electromagnetism), which is directly related to D_μ through the following commutation relation:

$$F_{\mu\nu} = -\frac{1}{g}[D_\mu, D_\nu] \quad ; \mu, \nu = 0, 1, 2, 3 \tag{1.5}$$

where D_μ has the general form: $(\partial_\mu \mathbb{1} + gA_\mu)$ and A_μ is a matrix that includes the interactions between the fermion and gauge boson fields of the theory. Φ represents the Higgs field. The right-handed fermion fields enter through the final term where Ψ_L^T is a transposed vector containing all left-handed fermions and where C is the charge conjugation operator that yields the anti-particles.

1.1.1. Neutrinos

Neutrinos are the only neutral fermions, which makes them intractable via charge, and they appear to only exist in one chirality, immediately breaking the parity operation. They are the only fermions that only interact weakly, making them hard to detect.

The lack of a right-handed neutrino and a left-handed anti-neutrino was an early assumption of the SM and is consistent with photon helicity measurements in weak decays, e.g. see the Goldhaber experiment (Goldhaber et al., 1958).

Experimentally, neutrinos have been confirmed to have mass, and although the masses are small compared to those of other SM particles, one can perform a Lorentz boost to a reference frame where the chirality of left-handed neutrinos is reversed. It is possible that the right-handed neutrinos exist, but because they do not interact weakly they would be considered sterile and have to enter the SM as an extension.

1.1.2. Weak Interaction

The Weak interaction is peculiar in that only left-handed fermion fields transform non-trivially under the weak isospin (I) symmetry group, also known as $SU(2)_L$. $SU(2)_L$ has three associated generators that behave analogously to the angular momentum generators and satisfy the commutation relation: $[I_i, I_j] = i\epsilon_{ijk}I_k$, $(i, j, k = 1, 2, 3)$, and $U(1)_Y$ is the 1-D unitary group mentioned previously, which is associated with the weak hypercharge quantum number. In the chiral (weak isospin basis) the left-handed fermion fields form doublets while the right handed fermions are represented as singlets under this group.

$$\begin{pmatrix} \nu_{eL} \\ e_L \end{pmatrix}, e_R, \begin{pmatrix} u_L \\ d_L \end{pmatrix}, u_R, d_R \tag{1.6}$$

All right-handed fermions have zero weak isospin; it then follows from the Gellman-Nishijima relationship 1.7 that Hypercharge (Y) for the neutral leptons (neutrinos) must also be zero.

$$Q = I_3 + \frac{Y}{2} \tag{1.7}$$

Fermions in the SM Lagrangian are expressed in the chiral basis as Dirac spinors, and naturally arise as solutions to the Dirac equation. Looking only at the Electroweak portion of the SM Lagrangian for the first generation quarks (u and d) and the electron, we have the following:

$$\begin{aligned}
\mathscr{L}_{EW} = {} & i\overline{L_L}\not{D}L_L + i\overline{Q_L}\not{D}Q_L + \sum_{f=e,u,d} i\overline{f_R}\not{D}f_R && (1.8)\\
& - \frac{1}{4}\underline{\mathrm{A}}_{\mu\nu}\underline{\mathrm{A}}^{\mu\nu} - \frac{1}{4}B_{\mu\nu}B^{\mu\nu} && (1.9)\\
& + (D_\mu\Phi)^\dagger(D^\mu\Phi) - \mu^2\Phi^\dagger\Phi - \frac{1}{2}\lambda(\Phi^\dagger\Phi)^2 && (1.10)\\
& - y^e(\overline{L_L}\Phi e_R + \overline{e_R}\Phi^\dagger L_L) && (1.11)\\
& - y^d(\overline{Q_L}\Phi d_R + \overline{d_R}\Phi^\dagger Q_L) - y^u(\overline{Q_L}\widetilde{\Phi}u_R + \overline{u_R}\widetilde{\Phi}^\dagger Q_L) \quad , && (1.12)
\end{aligned}$$

where

$$\underline{\mathrm{A}}^{\mu\nu} = (A_1^{\mu\nu}, A_2^{\mu\nu}, A_3^{\mu\nu}). \tag{1.13}$$

The first line includes the fermion fields, the second line includes the kinetic and self-interaction terms of the boson fields of the unbroken EW force, the third line includes terms from the Higgs field Φ which then breaks the $SU(2)_L \times U(1)_Y$ group symmetry, and the fourth and fifth lines are fermion mass terms from Yukawa couplings between the first generation fermions and the Higgs field.

1.1.3. Fermion masses

In the current EW theory, fermions also obtain their mass through interactions with the Higgs field(s) Giunti and Kim. The Higgs field must have two components which form a weak-isospin doublet. One field is a neutral complex-scalar field, which yields the vacuum expectation value, and the other is a charged complex-field.

For example we can write:

$$\Phi = \begin{pmatrix} \phi^+ \\ \phi^0 \end{pmatrix} \tag{1.14}$$

This forms a weak isospin doublet similar in form to those in section 1.1.2 and is coupled to fermions via Yukawa interactions which yield (Lorentz invariant) mass terms that mix the left- and right-handed fermion fields:

$$\bar{f}f = \bar{f}_L f_R + \bar{f}_R f_L \quad . \tag{1.15}$$

Note that mass terms of the form $m_x x_L \bar{x}_R$ are prohibited because they do not respect the weak isospin symmetry since they transform differently (as a doublet and singlet, respectively) and cannot therefore be Lorentz invariant (chirality is not Lorentz invariant for particles with mass).

The absence of the chiral counterparts to neutrinos and anti-neutrinos renders neutrinos

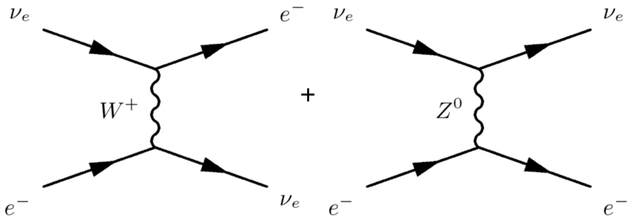

Figure 3: Elastic scattering interactions for electron neutrinos.**Left:** Feynman diagram for the Charged Current interaction, **Right:** Feynman diagram for the Neutral Current interaction.

massless under this mechanism.

The lowest order neutrino interactions can be grouped into those involving the exchange of the charged Bosons $\mathrm{W}^{\pm}$ i.e. Charged Current interactions (CC) and those that involve the exchange of the Z^0 boson, Neutral Current (NC) interactions. The neutrino interactions can be further broken up into groups depending on what the initial and final products are. For example, interactions which preserve the initial states are considered elastic scattering. The Feynman diagrams for the elastic scattering of electron-type neutrinos are depicted in figure 3. Note that muon and tau neutrinos can also scatter elastically off of an electron via the NC interaction. The muon and the tau are not stable, therefore, the author will focus on the interactions which are of relevance to terrestrial experiments.

The CC interactions can also occur between different flavor families if the interaction preserves lepton number.

$$\nu_\mu + e^- \to \mu^- + \nu_e \tag{1.16}$$

$$\nu_\tau + e^- \to \tau^- + \nu_e \tag{1.17}$$

1.2. History

Pauli initially proposed the existence of neutrinos to account for observations of a continuous energy spectra in beta and inverse beta decays indicative of a multi-body problem. The apparent interactions were:

$$(Z, A) \quad \rightarrow \quad (Z + 1, A) + e^- \tag{1.18}$$

$$(Z', A') \quad \rightarrow \quad (Z - 1, A') + e^+ \tag{1.19}$$

However, the study of the energy and momenta of beta rays revealed a distribution for both of these measurements. It was also noted that the atomic recoil was not always in the direction opposite to that of the beta particle. The simple two-body decays in equations 1.18 and 1.19 would yield monoenergetic beta rays, hence they were inconsistent with these observations.

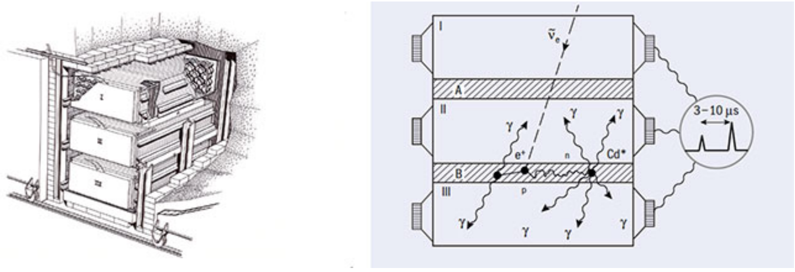

Figure 4: Cowan et al anti-neutrino detector assembly at the Savannah River Plant. Figure from CERN-Courier (Sutton, 2016).

Cowan and Reines originally conducted their experiment in 1953 at the Hanford nuclear site in Washington State but then relocated to the Savannah River Plant in South Carolina in 1955 where they repeated the experiment with various upgrades and with better shielding from cosmic rays. The experimental setup consisted of two tanks filled with an aqueous cadmium chloride solution, sandwiched between three tanks filled with a hydrogenous scintillator solution. The scintillator tanks were instrumented with 110 Photomultiplier Tubes (PMTs) while the cadmium-doped tanks were less voluminous and served the role of targets for the byproducts of the anti-neutrino interactions. Figure 4 depicts the setup at Savannah River.

Reactor anti-neutrinos can be directly detected if they undergo an inverse beta decay (IBD): $\bar{\nu}_e$ + p → n + e^+. Positrons from IBD reactions in the target, promptly slowed down and annihilated producing two back-to-back, 0.5 MeV gammas that could then interact and be detected in the scintillator tanks. The IBD neutron was moderated in the detector and captured by Cadmium whose nuclear de-excitation results in 9 MeV worth of gammas. The neutron moderation and eventual capture results in delayed signals relative to the prompt positron annihilation – in the order of microseconds and ultimately depending on the Cadmium concentration – the identification of these two delayed sets of signals, along with an energy requirement, guided the event selection for the experiment.

1.2.1. Solar Neutrinos

Interest in the fusion reactions of the Sun led to the design and construction of the Homestake Solar Neutrino Experiment (Cleveland et al., 1998-03) at the Homestake mine in Lead, South Dakota. This experiment was designed to use the inverse beta decay reaction on Chlorine-37 to measure the solar neutrino flux in order to test a nuclear model of the sun. Upon running for a few years, the results indicated that the solar neutrino flux was roughly 1/3 of the predicted rate – this became known as the Solar Neutrino Problem.

The detector consisted of a large tank containing 615 metric tons of tetrachloroethylene (C_2Cl_4) sitting 1478 meters underground and serving as a radiochemical target for neutrino interactions. Each molecule of C_2Cl_4 contains approximately one atom of the desired ${}^{37}_{17}Cl$ isotope that interacts with neutrinos to produce Argon-37 via the following reaction:

$$ {}^{37}_{17}Cl + \nu_e \rightarrow^{37}_{18} Ar + e^- . \tag{1.20}$$

Note that this has an energy threshold of 0.814 MeV, making the Homestake Experiment sensitive to ν_e with energy above this threshold. The radioactive Argon isotope was allowed to accumulate in the tank for weeks, and the flux of electron neutrinos was inferred from the content (Cleveland et al., 1998-03). The measured flux by the Homestake Experiment which ran from 1970 to 1994 was $(30.1 \pm 2.7)\%$ of the theoretical rate. This discrepancy between the solar model and the measured rate of electron neutrinos arriving to Earth is known as the Solar Neutrino Problem (SNP). In the years that followed, experiments were designed to shed light on the perceived issue. A model for neutrino oscillations had been proposed in 1958 by Bruno Pontecorvo (Pontecorvo, 1958) , thus it was to be determined whether the inconsistency was the result of an incorrect Standard Solar Model (SSM), improper measurements, both, or if neutrinos themselves were not massless under a mechanism not covered by the Standard Model (SM) of particle physics.

1.2.2. Water Cherenkov Experiments

The next generation of neutrino experiments utilized water detectors in conjunction with PMTs in order to detect neutrino interactions via Cherenkov radiation.

Water Cherenkov experiments are sensitive to elastic scattering (ES) interactions between neutrinos and atomic electrons. The first of these experiments was Kamiokande, which was originally designed to study nucleon decay but was later modified to study the flux of Boron-8 solar neutrinos by dividing the detector volume into an inner detector and an outer veto region. Kamiokande's solar flux measurement, under the no-oscillation hypothesis, differed from the expected flux by a factor of two with a 2σ significance. Super–Kamiokande, a much larger water detector, was later built to include close to 1000 PMTs and was more naturally suited to lower detection thresholds.

The Sudbury Neutrino Observatory (SNO) in Ontario, Canada was designed to study solar neutrinos and was built 2092 meters underground, in an active mine, to provide shielding from cosmic rays. The SNO detector is equipped with more than 9000, 20 cm PMTs surrounding an acrylic vessel, which was filled with ultra-pure heavy water (D_2O) making it suitable to study Boron-8 solar neutrinos through Neutral Current and elastic scattering interactions with deuterium. Sufficiently energetic neutrinos can dissociate deuterium, which has a 2.2 MeV binding energy, through an NC interaction, resulting in a free proton and neutron. The free neutron can be detected through its capture on deuterium to produce tritium, releasing additional energy in the form of gammas rays.

Both SNO (Ahmad et al., 2001) and Super–Kamiokande (Kajita et al., 2016) were able to prove the phenomenon of neutrino flavor oscillations, and in doing so they solved the Solar Neutrino Problem and the Atmospheric Neutrino Anomaly, respectively. Table 1 presents a timeline with a handful of events that mark the history of neutrinos in the 20th century.

Table 1 Timeline

1930	Pauli proposes the existence of a neutral particle which is also emitted during beta decay to explain why electrons from Nitrogen and Lithium 6 beta decays had a momenta in a continuum.
1950	Pontecorvo proposes an extension to the SM for massive neutrinos
1956	Direct detection of electron anti-neutrinos achieved by Cowan et. al (Cowan et al., 1956-07)
1962	Muon neutrinos discovered by Lederman et. al
Late 1960's	Homestake Experiment and the Solar Neutrino Problem
1970-1994	Homestake Experiment continues to take data
1987	SN 1987A events detected
1998	Super–Kamiokande Experiment and SNO (2002) confirm neutrino oscillations
2000	Direct detection of the tau neutrino

During the last 30 years of the 20^{th} century, neutrino detectors discovered and confirmed additional properties such as neutrino oscillations.

Experiments such as SNO and other water Cherenkov experiments utilize neutrino-nucleon scattering to identify particles. The main interactions that fall under this category are:

$$\nu_\alpha + N(A,Z) \rightarrow l_\alpha + X \tag{1.21}$$

$$\nu_\alpha + N(A,Z) \rightarrow \nu_\alpha + X \tag{1.22}$$

$$\nu_\alpha + N(A,Z) \rightarrow \nu_\alpha + N(A,Z) \tag{1.23}$$

where X denotes the final state hadrons which depend on the neutrino energy as well as the number of protons and neutrons. For example, SNO used heavy water to produce thus the final state hadrons are simple for solar neutrinos which have energies typically in the MeV range.

1.2.3. Neutrino oscillations

Bruno Pontecorvo was the first person to express neutrino wavefunctions as linear combinations of two mass eigenstates (ν_1, ν_2), where at least one of the two had to have nonzero mass, but more importantly, where the two masses are non-degenerate $(m_1 \neq m_2)$. Only one neutrino was known to exist at the time that he wrote this model. The main implication was that neutrinos participate in weak interactions, such as beta decays, only some portion of the time and were *sterile*, i.e. non-interacting, the rest of the time (except via the gravitational force if the electron neutrino were to have mass). The idea became known as coherent oscillation because as will be shown, this type of oscillation can occur in vacuum due to interference. Upon the discovery of muon neutrinos by Leon Lederman et. al (Danby et al., 1962) Pontecorvo wrote the model for oscillations between ν_e and ν_μ (Pontecorvo, 1968).

Two-Neutrino oscillations

Following tradition, I will now discuss the famous model for two-neutrino oscillations in vacuum. Let ν_α and ν_β denote the two flavor eigenstates and let ν_1 and ν_2 denote the two mass eigenstates with corresponding masses m_1 and m_2. Note that the flavor eigenstates are required to be Lorentz invariant in the SM, such that there is no ambiguity in what flavor different observers "see". It then follows that:

$$\begin{pmatrix} \nu_\alpha \\ \nu_\beta \end{pmatrix} = \begin{pmatrix} \cos\theta & \sin\theta \\ -\sin\theta & \cos\theta \end{pmatrix} \begin{pmatrix} \nu_1 \\ \nu_2 \end{pmatrix} \tag{1.24}$$

where θ is the so-called mixing angle. This parametrization enforces the orthogonality of mass eigenstates, namely:

$$\langle \nu_i | \nu_j \rangle = \delta_{ij} \tag{1.25}$$

The wavefunctions can be expressed as:

$$|\nu_\alpha\rangle = \sum_k U_{\alpha k} |\nu_\alpha\rangle$$

where $U_{\alpha k}$ is the corresponding entry of the matrix in equation 1.24. Taking the free neutrino states to be plane waves, we immediately know the time evolution as dictated by the Schrödinger Equation:

$$|\nu_k(t)\rangle = e^{-iE_k t/\hbar} |\nu_k\rangle \tag{1.26}$$

Where E_k is used to denote the energy associated with the k mass eigenstate arising from the energy of the originally produced flavor eigenstate $|\nu_\alpha\rangle$. Expressing $|\nu_\alpha\rangle$ and $|\nu_\beta\rangle$ in terms of the mass eigenstates and applying the time evolution operator we arrive at an expression for the wavefunction of the neutrino at time t:

$$|\nu(t)\rangle = A(t)|\nu_\alpha\rangle + B(t)|\nu_\beta\rangle \tag{1.27}$$

where:

$$A(t) = e^{-iE_it/\hbar}\cos^2\theta + e^{-iE_jt/\hbar}\sin^2\theta \tag{1.28}$$

$$B(t) = \sin\theta\cos\theta e^{-i(E_i-E_j)t/\hbar} \tag{1.29}$$

Therefore, the probabilities that a neutrino, created in the flavor eigenstate $|\nu_\alpha\rangle$, will oscillate into a ν_β at a time t is:

$$P_{\nu_\alpha\to\nu_\beta} = |\langle\nu_\beta|\nu(t)\rangle|^2 = \sin^2(2\theta)\sin^2\left(\frac{(E_j-E_i)}{2\hbar}t\right) \tag{1.30}$$

Similarly, the probability that the neutrino will remain in the $|\nu_\alpha\rangle$ state is given by:

$$P_{\nu_\alpha\to\nu_\alpha} = |\langle\nu_\alpha|\nu(t)\rangle|^2 = 1-\sin^2(2\theta)\sin^2\left(\frac{(E_j-E_i)}{2\hbar}t\right) \tag{1.31}$$

which must necessarily be equal to $1 - P_{\nu_\alpha\to\nu_\beta}$ by conservation of probability in this two-neutrino model. The probability in equation 1.31 is often called the **survival probability**.

We can make some approximations to get a qualitative idea of what this model implies for oscillation experiments. Neutrino flavor is detected via inverse lepton decays such as those given in 1.21. The threshold energies for these interactions render all neutrinos highly relativistic. The expression for the relativistic energy is given by:

$$E = \sqrt{p^2+m^2} = p\big(1+\frac{m^2}{2p^2}+...\big) \tag{1.32}$$

Taking the difference in momenta due to the differences between the masses of ν_1 and ν_2

to be negligible, the energy difference in equations 1.30 and 1.31 then becomes:

$$E_i - E_j = p_i + \frac{m_i^2}{2p_i} - p_j - \frac{m_j^2}{2p_j} + ... \approx \frac{(m_i^2 - m_j^2)}{2p} \tag{1.33}$$

assuming that $m_i > m_j$; however, this is arbitrary choice. Furthermore if we approximate pc with E and take (ct) to be the distance traveled by the relativistic neutrinos denoted as L, the time-dependent $\sin^2$ term becomes:

$$\sin^2\left(\frac{m_i^2 - m_j^2}{4E}L\right) = \sin^2\left(\frac{\Delta m_{ij}^2 L}{4E}\right)$$

It becomes relevant now to point out that if we take the argument of $\sin^2$ to be very large, this term oscillates rapidly in time thus yielding a time average transition probability. If we take the same argument to be very small the transition amplitude goes to zero as does the sensitivity to any oscillation measurements. All limits are essential to understanding neutrino oscillations; however, the parameters which are available for tuning and the sources of neutrinos up for detection determine what can be measured with high sensitivity for each experiment. The main sources of neutrinos are reactors, accelerators, the sun, and cosmic rays originating outside our solar system which collide with Earth's atmosphere and produce particles that then decay into neutrinos. The bulk of neutrino experiments fall into three main categories: Nuclear, Observatory, and Accelerator based experiments.

Three-Neutrino Oscillations

The three, Standard Model (SM) neutrinos ν_e, ν_μ, and ν_τ can be understood as linear combinations of three mass eigenstates ν_1, ν_2, and ν_3 with corresponding masses m_1, m_2, and m_3 which are not, themselves, eigenstates of the SM Hamiltonian. The propagation of neutrinos in time causes interference terms to arise which lead to oscillations between the flavors produced and the flavors detected. Various experiments have measured the neutrino oscillation amplitudes, which are encapsulated by the Pontecorvo-Maki-Nakagawa-Sakata (PMNS) matrix. An expression relating the flavor and mass eigenstates is shown below:

$$\begin{pmatrix} \nu_e \\ \nu_\mu \\ \nu_\tau \end{pmatrix} = \underbrace{\begin{pmatrix} U_{e1} & U_{e2} & U_{e3} \\ U_{\mu 1} & U_{\mu 2} & U_{\mu 3} \\ U_{\tau 1} & U_{\tau 2} & U_{\tau 3} \end{pmatrix}}_{U_{\text{PMNS}}} \begin{pmatrix} \nu_1 \\ \nu_2 \\ \nu_3 \end{pmatrix} \tag{1.34}$$

where U$_{PMNS}$ is often factorized into three, two-neutrino oscillation matrices as shown below:

$$U_{\text{PMNS}} = \underbrace{\begin{pmatrix} 1 & 0 & 0 \\ 0 & c_{23} & s_{23} \\ 0 & -s_{23} & c_{23} \end{pmatrix}}_{\text{I}} \underbrace{\begin{pmatrix} c_{13} & 0 & e^{-i\delta_{\text{CP}}} s_{13} \\ 0 & 1 & 0 \\ -e^{i\delta_{\text{CP}}} s_{13} & 0 & c_{13} \end{pmatrix}}_{\text{II}} \underbrace{\begin{pmatrix} c_{12} & s_{12} & 0 \\ -s_{12} & c_{12} & 0 \\ 0 & 0 & 1 \end{pmatrix}}_{\text{III}} \tag{1.35}$$

where c_{ij} and s_{ij} are short-hand notation for $cos\theta_{ij}$ and $sin\theta_{ij}$ and where θ_{ij} are physical constants known as the neutrino mixing angles.

Neutrino experiments utilize various sources and targets to measure both the oscillation amplitudes and the frequencies, which are proportional to the mass squared differences ($\Delta m^2_{ij} = m^2_i - m^2_j$). In a two-neutrino oscillation model, the probability that a neutrino will transition from flavor ν_α to ν_β is given by:

$$P_{\nu_\alpha \to \nu_\beta}(L, E) = sin^2(2\theta) sin^2\Big(\frac{\Delta m^2 L}{4E}\Big) \tag{1.36}$$

Currently, the three mixing angles, and the two independent mass squared differences between the three masses have been measured. δ_{CP}, and the sign of Δm^2_{31} have yet to be determined and are among the goals of future neutrino experiments. Currently we only know the sign for one of the mass squared differences; the sign of Δm^2_{31} will determine the full mass ordering, i.e., whether $m_1 < m_2 < m_3$ following the Normal Hierarchy (NH) or $m_3 < m_1 < m_2$ following the Inverted Hierarchy (IH). δ_{CP}, the CP-violating phase, may help explain why matter, and not equal parts matter and anti-matter, makes up the visible universe.

A more common expression of the disappearance probability is given by Equation 1.37, below.

$$P_{\nu_\alpha \rightarrow \nu_\beta}(L, E) = sin^2(2\theta) sin^2\Big(1.27 \Delta m^2 \frac{L}{E}\Big), \tag{1.37}$$

where L is in km, E is in GeV, and Δm^2 is in eV^2.

1.2.4. Matter Effects

The presence of matter introduces an additional potential (A_{CC}) to the Hamiltonian and therefore affects the time evolution of the neutrino wavefunction. This term arises from Charged Current (CC) and Neutral Current (NC) interactions between neutrinos and electrons and nucleons, respectively; however, only electron neutrinos interact via charged currents and only NC interactions with neutrons contribute, but they contribute equally to all flavors (Giunti and Kim, 2007). The additional CC terms resulting from this potential can be absorbed into an effective mixing angle θ_{eff} and an effective $\Delta m^2_{\mathrm{eff}}$. The following equation presents the relationship between the effective mixing angle and the vacuum oscillation angles:

$$tan2\theta_{\mathrm{eff}} = \frac{tan2\theta}{1 - \frac{A_{CC}}{\Delta m^2 cos2\theta}} \tag{1.38}$$

where $A_{CC} = 2\sqrt{2} E_\nu G_F N_e$ and where E_ν is the neutrino energy, G_F is the Fermi Constant, and N_e is the electron density.

Wolfenstein and Mikheev and Smirnov independently showed that a resonance condition exists for neutrino oscillations in matter there that can induce complete (90°) flavor transitions; this is known as the MSW effect. Neutrino oscillations meet the resonance condition in matter when A_{CC} approaches $\Delta m^2 cos2\theta$ for $\Delta m^2 cos2\theta > 0$.

It can be shown (see (Nunokawa et al., 2007) for example) that the transition probability for the three-neutrino mixing model in matter is:

$$\begin{aligned} P(\nu_\mu \to \nu_e) &= \sin^2\theta_{23}\sin^2 2\theta_{13}\frac{\sin^2(\Delta_{31}-aL)}{(\Delta_{31}-aL)^2}\Delta_{31}^2 \\ &+ \sin 2\theta_{23}\sin 2\theta_{13}\sin 2\theta_{12}\frac{\sin(\Delta_{31}-aL)}{(\Delta_{31}-aL)}\Delta_{31}\frac{\sin(aL)}{(aL)}\Delta_{21}\cos(\Delta_{31}+\delta_{\mathrm{CP}}) \\ &+ \cos^2\theta_{23}\sin^2 2\theta_{12}\frac{\sin^2(aL)}{(aL)^2}\Delta_{21}^2, \end{aligned} \tag{1.39}$$

where $\Delta_{ij} = \Delta m^2_{ij} L/4E_\nu$, $a = G_F N_e/\sqrt{2}$, L is the baseline in km, and E_ν is the neutrino energy in GeV.

1.3. Number of neutrinos

Among the successes of experimental particle physics is providing evidence for the existence of three different active (light) neutrinos (Zyla). This result comes from the EW theory which tells us that width of the Z^0 peak is given by:

$$\Gamma_Z^{tot} = \Gamma(Z \to hadrons) + 3\Gamma(Z \to l^+l^-) + N_\nu \Gamma(Z \to \nu_l \bar{\nu}_l) \tag{1.40}$$

Using the PDG values for the Z width, (2.4952 ± 0.0023) GeV, the average decay rate to the three charged leptons (e, μ, τ) $\Gamma(Z \to l^+l^-) = (3.3658 \pm 0.0023)\%$ we obtain the following result:

$$N_\nu = \frac{(0.4989 \pm 0.0021)}{\Gamma(Z \to \nu_l \bar{\nu}_l)} = (3.0052 \pm 0.1634) \tag{1.41}$$

where $Z \to \nu_l \bar{\nu}_l$ has been taken to be the entire invisible decay width (0.166 ± 0.009) GeV. Thus we see that the theory is consistent with three light neutrinos. Additional neutrino flavors would have to be very massive or at least have a mass of $m_\nu > m_Z/2$. Figure 1.3 depicts a fit of the neutrino numbers to the Z^0 boson resonance.

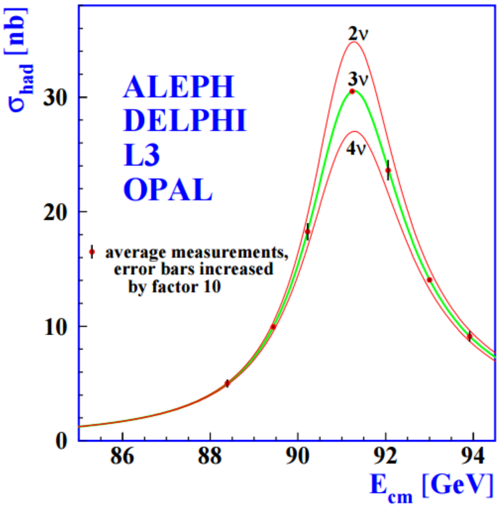

Figure 5: LEP cross sections for Z to hadron decays assuming two, three, and four light (active) neutrinos.Collaboration et al. (2005-09)

1.4. Sterile neutrinos

The idea of additional neutrinos that do not interact via the Weak force i.e. “sterile neutrinos” is motivated, in part, by anomalies observed in both reactor and accelerator neutrino experiments at short baselines. The highest statistics from accelerator anomalies come from the Liquid Scintillator Neutrino Detector (LSND) and the MiniBooNE experiments, which have L/E values of order ~1 km/GeV. Short baseline oscillations could be modeled by introducing at least one additional mass splitting. More detail on the theory can be found in (Carena et al., 2017).

One key signature for short baseline oscillations would be the appearance of $\nu_e(\bar{\nu}_e)$ beyond the contamination level in a $\nu_\mu(\bar{\nu}_\mu)$ beam. For an L/E of 1km/GeV an excess of this sort would have to be the result of a relatively large Δm^2 compared to Δm^2_{32} and Δm^2_{21} which are of order $\sim 3 \times 10^{-3}\mathrm{eV}^2$ and $\sim 10^{-4}\mathrm{eV}^2$, respectively (Mocioiu and Shrock, 2001). From equation 1.36 we can deduce that if the LSND and MiniBooNE detectors are situated at the first maximum for their energies, i.e. if the argument of the sin^2 term $\approx \pi/2$, then Δm^2 is of order ~1 eV^2.

In the

$$\begin{pmatrix} \nu_e \\ \nu_\mu \\ \nu_\tau \\ \nu_s \end{pmatrix} = \begin{pmatrix} U_{e1} & U_{e2} & U_{e3} & U_{e4} \\ U_{\mu 1} & U_{\mu 2} & U_{\mu 3} & U_{\mu 4} \\ U_{\tau 1} & U_{\tau 2} & U_{\tau 3} & U_{\tau 4} \\ U_{s1} & U_{s2} & U_{s3} & U_{s4} \end{pmatrix} \begin{pmatrix} \nu_1 \\ \nu_2 \\ \nu_3 \\ \nu_4 \end{pmatrix} \tag{1.42}$$

$$P_{\nu_\alpha \to \nu_\beta} = \delta_{\alpha\beta} - 4|U_{\alpha 4}|^2(\delta_{\alpha\beta} - |U_{\alpha 4}|^2) \sin^2\left(\frac{\Delta m^2 L}{4E}\right) \tag{1.43}$$

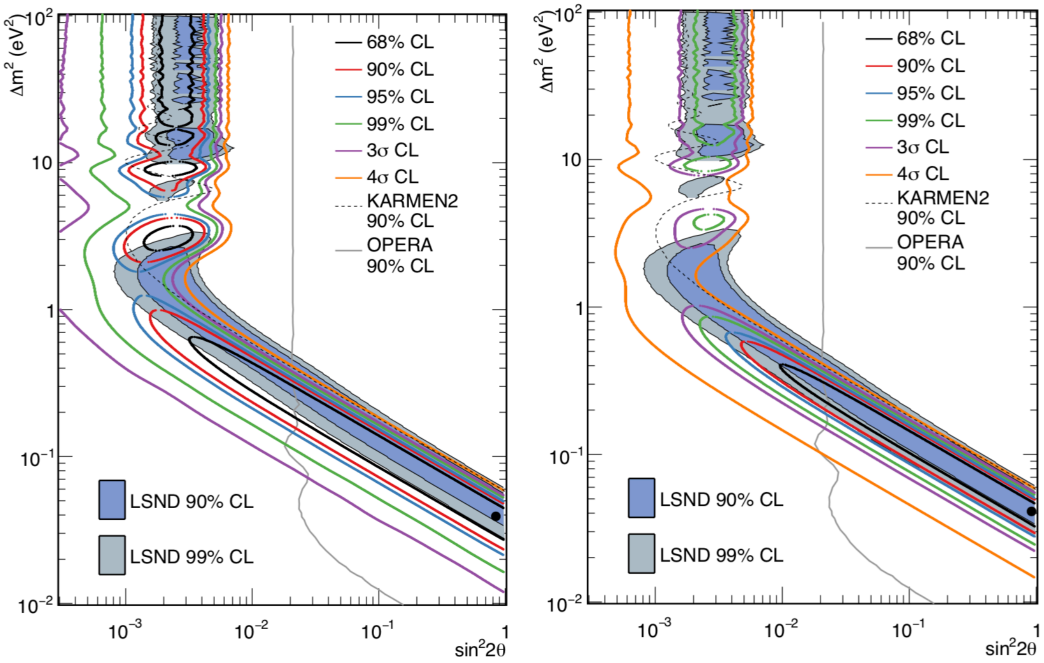

Figure 6: Left: MiniBooNE exclusion curves for neutrino mode and **Right:** combined neutrino and anti-neutrino mode. Figures from ref. (Aguilar-Arevalo et al., 2018).

The MiniBooNE collaboration updated its limits and best fits for sterile neutrino oscillations in 2018, found here Aguilar-Arevalo et al. (2018). The best fit values as claimed in the paper are $(\Delta m^2, sin^2 2\theta) = (0.041 eV^2, 0.958)$.

CHAPTER 2 : LIQUID ARGON TPC-BASED DETECTORS

The Time Projection Chamber (TPC) was invented by David Nygren at the Lawrence Berkeley National Lab (LBNL) in 1974 (Marx and Nygren, 1978). The basic principle behind a TPC is that charged particles passing through the target material produce ionization tracks. The incident particle need not be charged, however, in order to produce visible energy the interactions between the incident particles and the target volume must result in ionization. One way to collect/read out the charge from the interactions is to establish an electric field ($\mathbf{E_{drift}}$) across the target to drift the electrons and ions towards opposite ends of the drift at a constant velocity given a uniform field. The electric field defines the *active* volume (AV) of the detector, and the Coulomb force ($\mathbf{F} = \mathrm{q}\mathbf{E_{drift}}$) acts on the electron-ion pairs. A constant drift velocity is achieved through the balance of the Coulomb force with the collisions along the direction of motion. Under these assumptions, time and distance in the axis of the field, are directly proportional.

The original proponent for the use of liquid Argon as the medium for at TPC was Carlo Rubbia (Rubbia, 1977). His proposal in 1977, was motivated in part by properties of argon as a noble element, the availability of argon, and its density. Interactions between charged particles with the LAr medium generally result in both ionization and scintillation. At the onset of the ionization, electrons are likely to recombine with nearby positive Argon ions, which also results in scintillation light. Fifteen years later, in 1992, the ICARUS collaboration published a Nuclear Instruments and Methods paper demonstrating the first working 3-ton LArTPC (Bettini et al., 1992).

Liquid Argon is ideal for this type of detector because Argon has no electron affinity and can be safely placed in a relatively large electric field[1]. An electric field is established in the AV by applying a potential difference between the cathode and the anode. The cathode is typically held at a high voltage (HV) while the anode, which is where the ionization electrons are collected, is typically grounded. Electrons are collected by sense wires that comprise the

---

[1] Typical drift fields for a LArTPC are in the order of a few hundred volts-per-centimeter.

anode. In order to do 3D-reconstruction, at least one additional sense wire plane is required. The layers of sense wires closest to the drift region do not collect electrons but detect their passage through induction currents produced on wires in these planes. The wire pitch, both in the drift direction and in the 2D-plane perpendicular to the drift direction, are said to voxellize the AV. Any induced signals in the outer sense wire planes have net-zero area as depicted by the V wire plane waveforms in Figure 7.

The liquid argon time projection chamber (LArTPC) technology takes advantage of the optical properties of argon as well as the fact that ionization tracks are preserved with reasonably achievable purity. Liquid argon is transparent to its own scintillation light. Light and charge are anti-correlated and make it possible to do particle identification and measure energy more accurately if both the charge and light are read out efficiently.

Some of the LArTPC-based experiments to date include: ICARUS, ArgoNeuT (Anderson et al., 2012), LArIAT (Acciarri et al., 2020), Darkside-50 (Rossi et al., 2016), 35-ton (Adams et al., 2018-06), MicroBooNE (Acciarri et al., 2017b), and ProtoDUNE-SP (Abi et al., 2017).

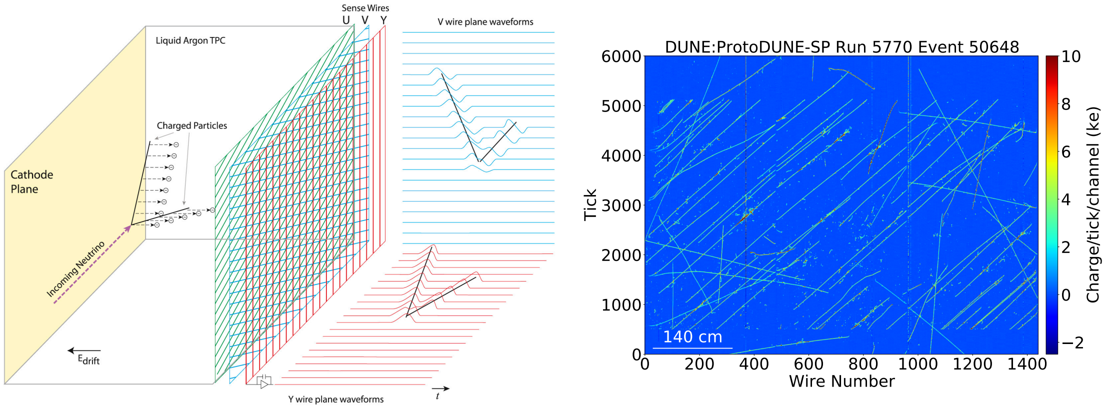

Figure 7: Left: LArTPC functional diagram. Figure from ref. (Cavanna et al., 2018-11). **Right**: Event display from ProtoDUNE-SP showing a high multiplicity cosmic ray shower. Figure from (Abi et al., 2020a).

An operable LArTPC must preserve as much of the initially deposited charge as possible. There are losses which are intrinsic to the technology, e.g. recombination and diffusion, and some which are related to contaminants and impurities present in the detector. The concentration of electronegative elements and isotopes directly impacts the signal-to-noise ratio and must therefore be as low as possible. Under the assumption that contaminants are homogeneously distributed in the active volume of the detector, there are trade-offs between field strength, drift distance, and the allowable levels of contamination. Large drift distances result in larger diffusion, recombination, and other effects that reduce or smear the energy deposits spatially. A higher magnitude electric field can be used to compensate for a longer drift distance. The electron mobility (μ) increases linearly ($\mathbf{v} = \mu\mathbf{E}$) up to *roughly* 200 V/cm. The electric field is established by an HV supply. It is also increasingly difficult to maintain a stable HV; breakdowns occur with higher propensity due to charge buildup as well as any “sharp” features in detector materials.

Experiments such as ProtoDUNE-SP, discussed in section 2.5, include a recirculation system, which has filtering stages in order to prevent contamination of the detector volume. In ProtoDUNE-SP, approximately 1/3 of the ionization charge recombines, however this has a dependence on the particle species responsible for the ionization[1].

2.1. Ionization production and detection

LArTPC-based experiments depend on charge measurements to estimate energy.

---

[1] Generally, heavier particles e.g. α particles result in higher fractional recombination losses for a given kinetic energy.

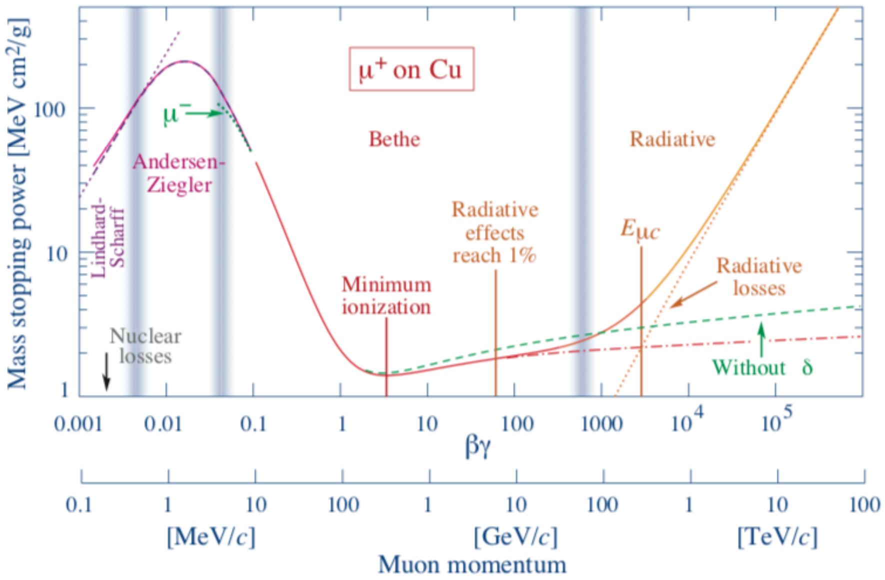

Figure 8: Stopping power for a μ^+ in Copper. This demonstrates the regions of interest as a function of $\beta\gamma$. Figure from the Particle Data Group ref. (PDG).

The mean energy loss, $\langle dE/dx \rangle$, for a particle in matter is described by the Bethe-Bloch formula:

$$-\left\langle \frac{dE}{dx} \right\rangle = \frac{Dq^2 N_e}{\beta^2}\left[ln\left(\frac{2m_e c^2\beta^2\gamma^2}{I}\right) - \beta^2\right] \quad , \tag{2.1}$$

where I is the mean ionization energy potential of the atoms averaged over all electrons, β = v/c, $\gamma = 1/\sqrt{1-\beta^2}$, N_e is the electron density for the material, m_e is the electron mass, q is the particle charge, and

$$D = \frac{4\pi\alpha^2\hbar^2}{m_e} = 5.1 \times 10^{-25}\text{MeV cm}^2 \quad . \tag{2.2}$$

This is an approximation and does not take into account additional mechanisms for energy loss, including Bremstrahlung and delta ray production, both of which cause the energy loss to increase with increasing energy. LAr experiments, like ProtoDUNE-SP, instead use the Landau-Vavilov formula 2.3 for the most probable energy loss of a particle because it accurately predicts the energy loss in LAr. A comprehensive review of the passage of particles through matter and the formulas mentioned here can be found in the Particle Data Group (PDG). Formula 2.3 below, includes corrections and reports the Most Probable Value (MPV) as a function of thickness and the relativistic β and γ factors along with other constants for the material and incident particle. This is far more accurate because energy loss is not normally distributed for thick targets, but rather, it conforms to a Landau distribution with some smearing by the resolution of the detector (see figure 9 for an example from ProtoDUNE-SP).

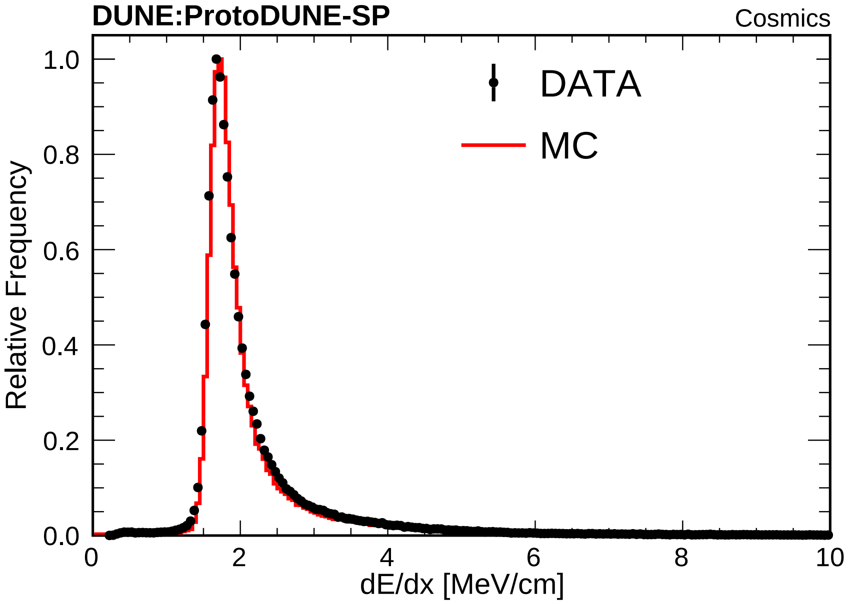

Figure 9: dE/dx distribution comparison between data and Monte Carlo. Original figure from the ProtoDUNE-SP performance paper (Abi et al., 2020a).

$$-\left\langle \frac{dE}{dx} \right\rangle_{MPV} = \xi \left[ln\left(\frac{2m_e c^2 \beta^2 \gamma^2}{I} \right) + ln\left(\frac{\xi}{I} \right) + j - \beta^2 - \delta(\beta\gamma) \right] \quad , \tag{2.3}$$

where

$$\xi = \frac{K}{2} \langle \frac{Z}{A} \rangle q^2 \frac{x}{\beta^2} \quad , \tag{2.4}$$

and j = 0.200. $\delta(\beta\gamma)$ is a density effect correction for ionization energy losses specific to the material, K=0.307 MeV·cm^2, Z is the proton number (Z_{Ar} = 18), A is the atomic mass (39.948 for LAr), and x is the detector thickness in units of g/cm^2 (ρ·x).

Sternheimer et al. provide a parametrization for the density correction, which is a function of various parameters particular to the material. The prescription within (Sternheimer, 1981) is provided in equation 2.5 below.

$$\delta(\beta\gamma) = \begin{cases} 2(ln10)y - \overline{C}, & y \geq y_1 \\ 2(ln10)y - \overline{C} + a(y_1 - x)^k, & y_0 \leq y \leq y_1 \\ 0, & y \leq y_0 \end{cases} \tag{2.5}$$

where y = $log_{10}(\beta\gamma)$, y_0 = 0.2, y_1 = 3.00, $\overline{C} = -5.2146$, a = 0.19559, and k = 3 for LAr (Group).

It is useful to outline the properties of liquid argon as they pertain to Minimum Ionizing Particles (MIPs); the typical MIP is a cosmic muon. Table 2 contains several parameters relevant to the ionization of LAr.

Table 2: Liquid Argon properties (BNL) at 87 K.

Property	Value	Unit
Normal boiling point	87.303	K
Density	1.3973	gm/cm^3
Ionization energy	23.6	eV
Radiation length	14	cm
MIP -$\langle dE/dx \rangle$	2.1	MeV/cm
MIP -dE/dx Most Probable Value	1.8	MeV/cm

A useful quantity to define, for particles that stop in the medium, is the residual range, which is the remaining distance that the particle will travel until it stops as is propagates. The dE/dx vs. residual range is used in various LAr experiments to do particle identification.

Figure 10 below is a comparison of the dE/dx vs. residual range curves for protons and muons, by the author, using NIST tables and equations 2.3 and 2.5.

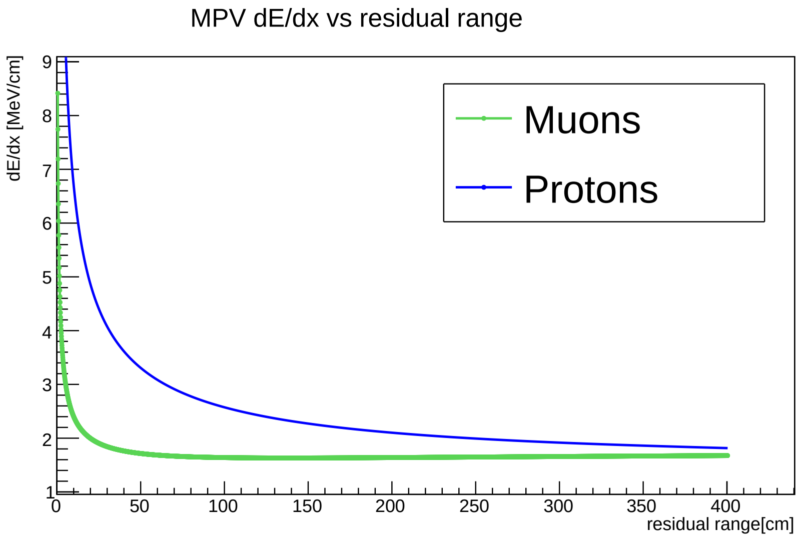

Figure 10: Example curves of most probable dE/dx vs. residual range for muons and protons in LAr.

2.2. Optical photon production and detection

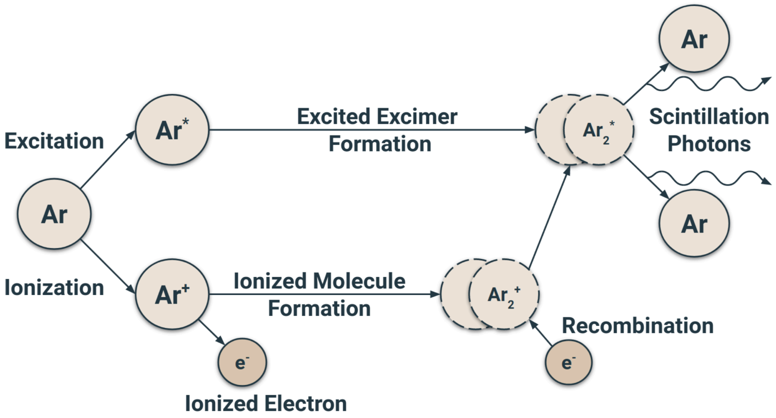

Figure 11: Production of prompt and delayed scintillation light in LAr. Original figure from the DUNE TDR: Volume IV (Abi et al., 2020b).

LAr emits scintillation light through two transitions – one which is prompt (singlet) and one which is delayed (triplet). The peak wavelength of the scintillation light is the same for both components, 128 nm; however the prompt component has an associated time constant, $\tau_{\text{singlet}} = 6$ ns while the late light has a time constant $\tau_{triplet} \approx 1.6\mu$s.

In addition to scintillation light, Cherenkov light is also produced for particles with $\beta > 1/n = 1/1.38 = 0.725$, where n is the refractive index. Table 3 contains several parameters relevant to the scintillation of LAr.

Table 3: Liquid Argon scintillation properties (BNL).

Property	Value	Unit
Peak scintillation wavelength	128	nm
Prompt decay time constant	6	ns
Late decay time constant	1590	ns
Dielectric constant	1.506	-
Index of refraction	1.38	-
Scintillation yield	~20,000	photons/MeV

128 nm light falls into the category of Vacuum Ultra-Violet (VUV) light. Although photosensors for VUV light exist, a common method for increasing the efficiency for the detection of VUV photons is to utilize a wavelength shifter film or material to convert them to visible light and to use more conventional photosensors. Blue-sensitive PMTs and Silicon Photo-Multipliers (SiPMs) are common and have been used for decades in water Cherenkov and scintillation experiments and have relatively high efficiency (Kuźniak and Szelc, 2020).

The photodetectors for a LArTPC must be able to withstand and operate safely at cryogenic temperatures. There are PMTs designed to function at these low temperatures, however, they are often used in conjunction with tetraphenyl-butadiene (TPB), which can be chemically deposited onto the PMT glass, or onto a material transparent to the emitted light that can sit in front of the photodetector.

TPB absorbs VUV photons and has a re-emission spectrum peaked at 430 nm with a 2 ns time constant. The re-emission is isotropic, therefore a coating directly on the surface of the photosensor tends to be the most beneficial. A technical and thorough review of wavelength shifters for LAr experiments can be found in (Kuźniak and Szelc, 2020).

A more recent photosensor, know as an ARAPUCA (Motta et al., 2018), was developed for potential use with current and next generation LAr experiments and have demonstrated great results (Totani and Cavanna, 2020). ARAPUCAS make use of a dichroic filter, which allows VUV light to be wavelength-shifted into a gap in the device; upon entering, the photons undergo total internal reflection until they strike a photo-sensor.

2.3. Deep Underground Neutrino Experiment (DUNE)

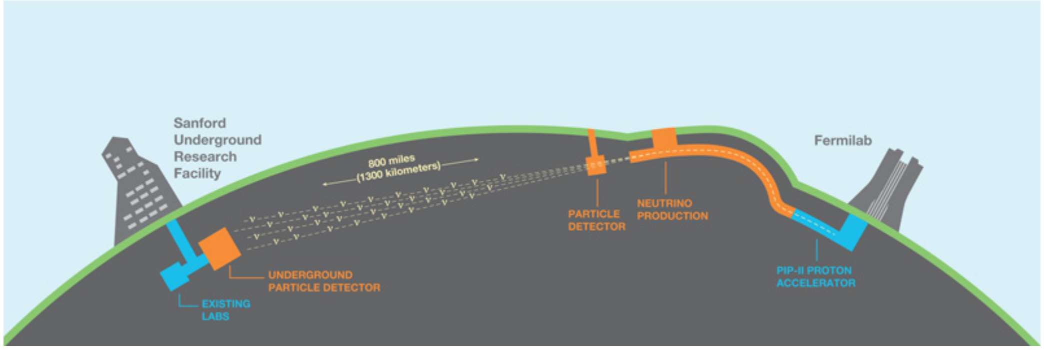

Figure 12: Cartoon depicting the DUNE experiment – both near and far detectors.

The Deep Underground Neutrino Experiment (DUNE) is a next-generation long-baseline oscillation experiment that will search for differences in the oscillation spectrum of $\nu_\mu \to \nu_e$ and $\bar{\nu}_\mu \to \bar{\nu}_e$. Its two main physics goals are determining the neutrino Mass Hierarchy (MH) and measuring the Charge-Parity violating phase (δ_{CP}) in the neutrino sector(Acciarri et al., 2015b) of the Standard Model.

The DUNE beam will be produced by dumping protons with tunable energy between 60 and 120 GeV onto a multi-layered graphite target to produce large numbers of positive and negative pions and kaons that will decay in flight(Acciarri et al., 2015b) into, mostly, muon neutrinos in the case of π^+, K^+ and into muon anti-neutrinos for π^-, K^-. The resulting neutrino beam will be very nearly on-axis and thus wide-band in energy allowing for better coverage of the phase-space than previous long-baseline experiments. The unoscillated beam content will be sampled by the near detector (Abud et al., 2021) at Fermilab and will be critical for interpreting the neutrino rates at the far detector 1300 km away.

DUNE will have sensitivity to the MH through the matter effect between the near and far detectors. It is known that θ_{13} is small (so $cos2\theta > 0$) thus by eq. 1.38 if the MH is normal, i.e., if the sign of $\Delta m^2_{31} (= m^2_3 - m^2_1)$ is positive then the spectrum for ν_e for which $A_{CC} > 0$, has the possibility of undergoing a resonance. If the hierarchy is inverted, i.e., if the sign of Δm^2_{31} is negative, then the spectrum for $\bar{\nu}_e$ for which $A_{CC} < 0$, will be affected by the matter effect. These two possibilities can be appreciated in equations 2.6 below.

$$\begin{aligned} \nu_e : tan2\theta_{eff} &= \frac{tan2\theta_{13}}{1 - \frac{(ACC>0)}{(\Delta m^2_{31}>0)(cos(2\theta_{13})>0)}} \text{ and} \\ \bar{\nu}_e : tan2\theta_{eff} &= \frac{tan2\theta_{13}}{1 - \frac{(ACC<0)}{(\Delta m^2_{31}<0)(cos(2\theta_{13})>0)}} \end{aligned} \tag{2.6}$$

DUNE will be sensitive to δ_{CP} via the transition probability in eq. 1.39. The following figure shows the transition probability for various values of δ_{CP} in both neutrino and anti-neutrino mode:

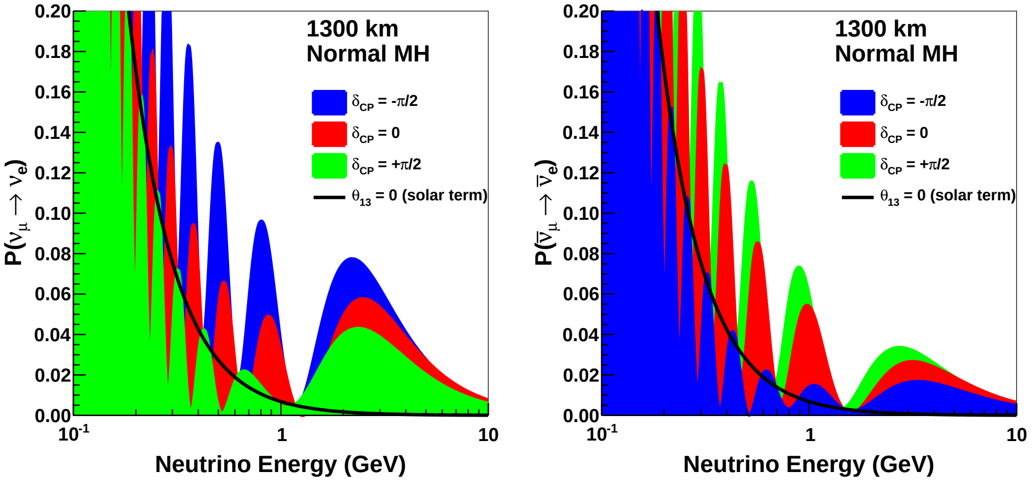

Figure 13: Left: ν_e appearance. **Right:** $\bar{\nu}_e$ appearance. Original figures taken from the DUNE Conceptual Design Report(Acciarri et al., 2015b).

2.3.1. DUNE Far Detector (FD)

The DUNE FD is being built 1,300 km away from the Near Detector and 30 km underground – at the Sanford Underground Research Facility (SURF).

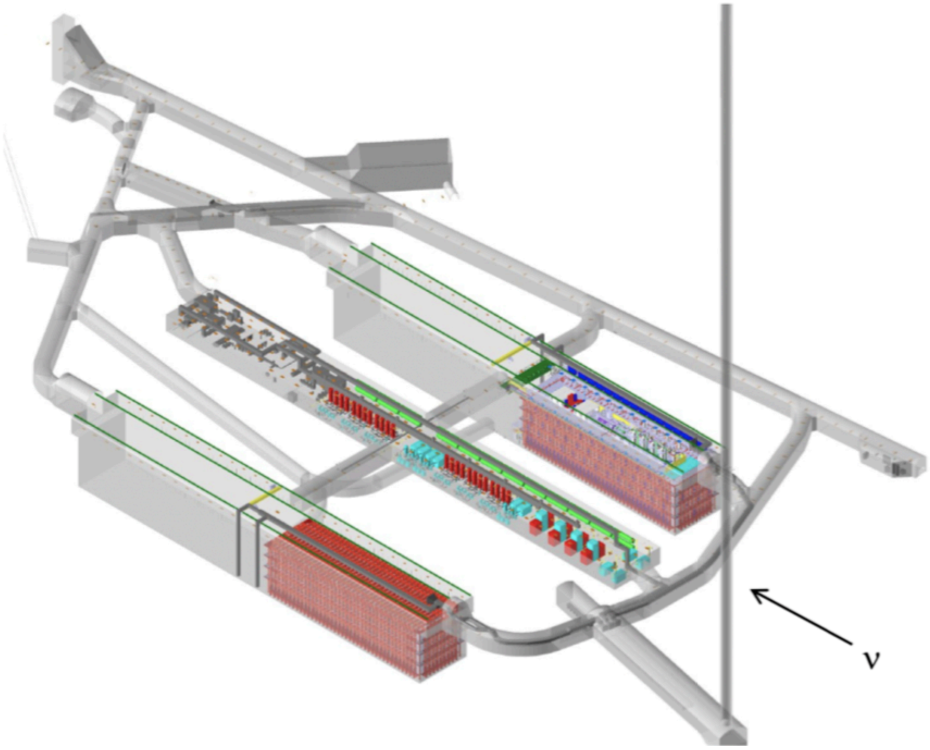

Figure 14: DUNE FD diagram depicting the caverns for the four 10 kt modules in the nominal design. Original figure from (Abi et al., 2020b).

Nominally, the DUNE FD will consist of four modules with 10 kilotons of active LAr, each. The DUNE sensitivity predictions assume 3.5 years in neutrino and 3.5 years in anti-neutrino mode with 300 kt·MW·yrs(Acciarri et al., 2015b). DUNE, as a whole however, is being designed to operate for 30 years.

To guarantee this level of longevity for DUNE, a couple of smaller scale prototypes have been designed and used to test and commission important components of the DUNE design, e.g., the wire planes. The first of these prototypes were the 35-ton (see chapter 3 for more information) and ProtoDUNE-SP, which is currently the largest LArTPC, by volume, to be built and will be referenced heavily throughout this document.

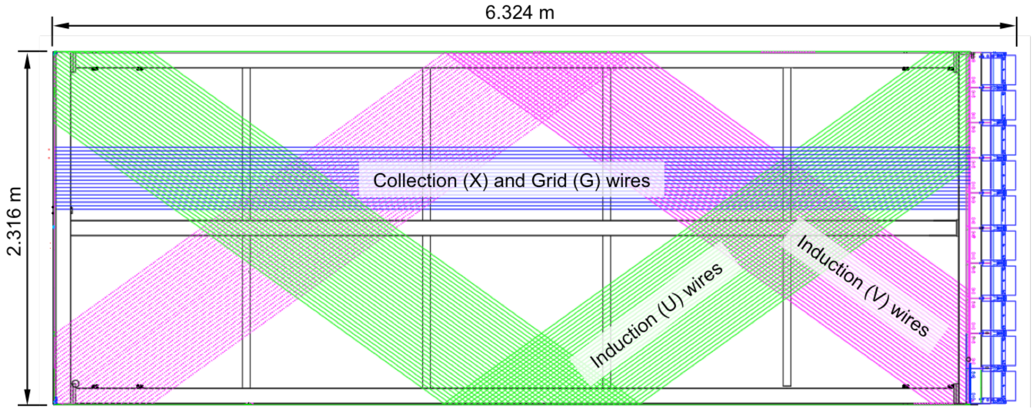

Figure 15: Anode Plane Assemblies (APAs) constitute the basic readout unit for the DUNE-type detectors. Oriented to the right for convenience only. Figure from ref. (Abi et al., 2020a).

The topology of the Anode planes for DUNE-style detectors is shown in figure 15, n.b., only a subset of each wire plane is shown in the diagram. Each APA has four wire planes – in order from closest to furthest from the drift region: grid (G), first induction (U), second induction (V), and collection (X). Collection plane wires often go by different names (W, X, Y, or Z) , however, the induction planes are always U and V, and the grid, if present, is denoted by label G. The wire pitch is 5 mm for each plane and the gap between planes is 4.75 mm. As indicated by the diagram, induction plane wires wrap around the APA, while there are two sets of grid and collection wires, one on each side of the APAs. Grid wires serve to shield charge from the U plane wires until they pass the grid plane. This results in bipolar waveforms for the two induction wires and unipolar signals for the collection plane. Wire wrapping was proposed as a way to reduce the number of readout channels required for the Single-Phase designs for the far detector.

The Single-Phase DUNE FD design is for a cryostat that is 14 meters tall, however, each APA is only 6 meters tall due to noise requirements. Thus, two APAs will span the height of the DUNE FD modules, with the bottom rows of APAs hanging upside-down in order disturb the active volume as little as possible.

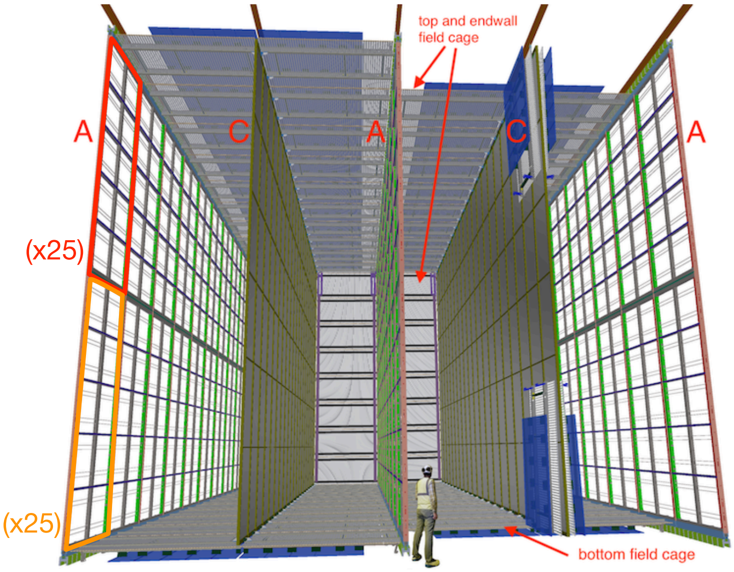

Figure 16: 10 kt DUNE Single-Phase module with three rows of APAs, labeled A, and two cathodes (C). Each row contains 50 APAs, in 25 columns of two APAs – one hanging from the top of the cryostat (boxed red) and the second hanging upside-down (boxed in orange) from the top APA. Original figure from (Abi et al., 2020b).

Photodetectors are mounted on the APAs as well – in between the two collection wire-planes – as shown in Figure 17.

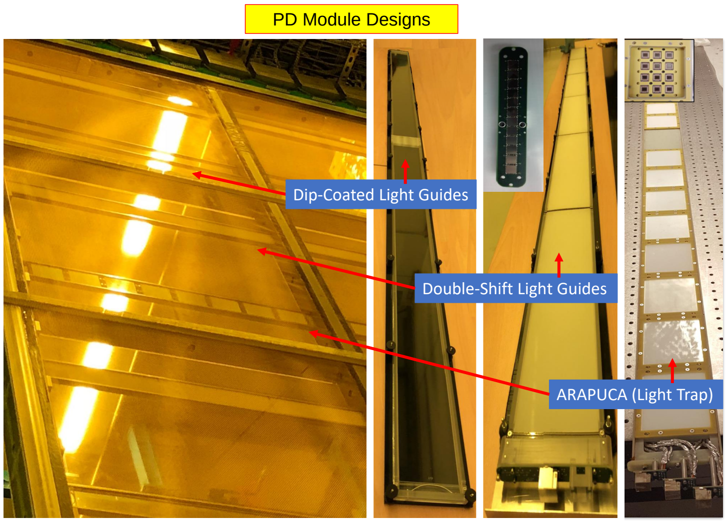

Figure 17: DUNE-style light detection system. Original figure from the ProtoDUNE-SP performance paper (Abi et al., 2020a).

Table 4: Specifications for Single-Phase DUNE FD modules. Table values partially from (Abi et al., 2020b).

Property	G-plane	U-plane	V-plane	Z-plane
№ wires/APA	960	800	800	960
Grid wire pitch [mm]	4.79	4.67	4.67	4.79
Wire orientation [°] w.r.t. vertical	0	-35.7	35.7	0
Voltage w.r.t ground [V]	-665	-370	0	820
Wire length [m]	6	6	6	6

Property	Value
Single-Phase TPC dimensions	12 m(x)×14 m(y)×58.2 m(z)
№ APA / 10 kt module	150
№ wires / APA	2560
№ wires / 10 kt module	384,000
Sampling rate	2 MHz
ADC	12-bit

The data budget for DUNE is 30 PB/year, more specifically, this is the limit for data written to tape. The breakdown of the data budget for DUNE can be found in Table 7.1 of the DUNE TDR: Volume 4 (Abi et al., 2020b). Readout for DUNE is designed to be continuous, thus we have a stream of more than 6 Terrabytes-per-second (384,000 × 2×10^6 samples/second × 2 bytes/sample).

2.3.2. Electronics

The analog signals in the experiment arise from the collection of charge or through the induction of charge, in the case of the U and V planes. The wires are sensitive to drifting ionization depositions – these can be represented as sources of current (i=dq/dt). The wires are best described as capacitors [1] in reference to the APA frame and to their neighboring wires. For both channel types (induction and collection), the signals are amplified, shaped, and digitized in the liquid argon using custom Application Specific Integrated Circuits (ASICs). Figure 18 depicts the wire-readout, system design for single-phase, DUNE-type detectors as it was implemented in ProtoDUNE-SP.

---

[1] The wire capacitance is in the order of 100 pF for six meter sense wires, alone.

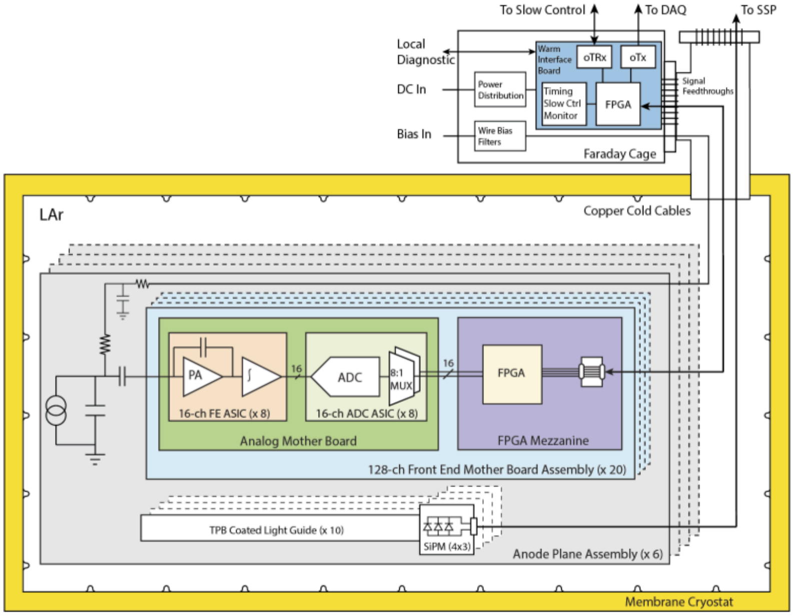

Figure 18: ProtoDUNE-SP electronics. Original figure from the ProtoDUNE-SP Technical Design Report (Abi et al., 2017).

The decision to invest in R&D for these chips was guided by noise requirements and an effort to reduce the cable mass needed to read out the 384,000 channels per 10 kt module. The noise for LArTPCs is often reported in the form of an Equivalent Noise Charge (ENC), which is in units of electrons. The noise requirements for DUNE require less than 1000 e^- ENC per channel to achieve a signal-to-noise ratio of 10 for MIPs (~10,000 e^- not taking into account diffusion and recombination losses).

The leading contribution to the ENC for the sense wires is the series, white noise, which is due to the thermal fluctuations in the Copper-Beryllium wires themselves – this contribution is directly proportional to the sense wire capacitance. Clearly if the wire signals are routed directly from the APAs to feed-throughs at the top of the crysotats, this would increase both the wire length and parasitic capacitances for each channel. Naturally this means that the cables for the upside-down APAs (see Figure 16) would be significantly longer (30 m) and would spoil DUNE's low energy physics program through white noise alone.

The three-chip solution for DUNE-style wire readout consists of a Front End (FE) chip, a cold ADC, and a data chip known as COLDATA – all interconnected on the Front End Mother Boards (FEMBs), which are mounted via connectors directly onto the top of the APAs (20 per APA – 10 on each side of the APAs). The FEMBs are depicted as blue boxes on the rightmost part of the APA in Figure 15.

The FE ASIC includes a charge sensitive amplifier with configurable gain and a 4th-order semi-Gaussian [1] shaper with configurable shaping time. Each FE chip has 16 input and 16 output channels that are routed to the ADC ASICs which digitize the shaped FE signals at 2 MHz with a 342 μV resolution (12-bits and 1.4 V dynamic range). The COLDATA chip is designed to configure the FE and ADC ASICs, run calibrations for each channel, and read out and package the ADC data, which is transferred to the Warm Interface Boards (WIBs) via a small bundle of data cables (one bundle per FEMB). The WIBs plug in to crates, which are bolted onto flanges protruding through the top of the cryostat. The WIBs synchronize and package the data for consumption by the downstream Data Acquisition (DAQ) electronics.

---

[1] A fourth-order semi-Gaussian shaper is simply an RC-CR^4 analog circuit, i.e., a differentiation stage followed by four integrators.

2.4. Short Baseline Neutrino Program at Fermilab

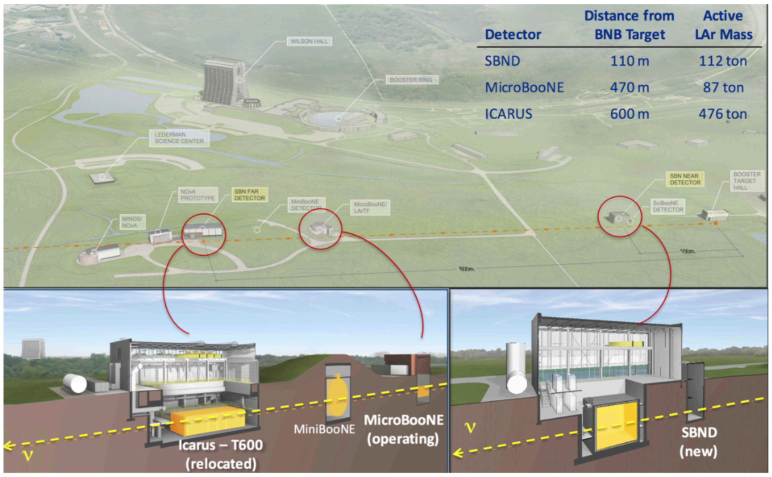

Detector	Distance from BNB Target	Active LAr Mass
SBND	110 m	112 ton
MicroBooNE	470 m	87 ton
ICARUS	600 m	476 ton

Figure 19: Detector and beam configuration for the SBN program at Fermilab. Figure from (Bass, 2017).

The Short Baseline Neutrino (SBN) program at Fermilab consists of three detectors: SBND (the near detector), MicroBooNE, and ICARUS T600 (the far detector) all of which are Liquid Argon Time Projection Chambers. SBND will sit 110m from the beam source and will sample the unoscillated ν_μ beam. A joint analysis between the three detectors will look for ν_e appearance and ν_μ disappearance in order to determine whether missing/emerging neutrinos are a result of oscillations to and from additional "sterile" flavors.

A more thorough description of the Short-Baseline Program at Fermilab can be found in a 2019 Annual Review of Nuclear and Particle Science (Machado et al., 2019).

The ICARUS T600 experiment has been operational since January 2021 and has completed initial commissioning of the individual subsystems. SBND has incurred various delays, however, at the time of this document, SBND is expected to turn on in early 2022.

2.4.1. Short Baseline Near Detector (SBND)

SBND will serve as the near detector for the SBN program and will constrain the systematic uncertainties for the oscillation search by sampling the unoscillated flux of neutrinos 110 m from the beryllium target. SBND will enable a sensitive test of the light sterile neutrino hypothesis, aiming either at an unambiguous discovery or a 5σ exclusion of the area of 3+1 oscillation parameter space allowed by the LSND and MiniBooNE anomalies.

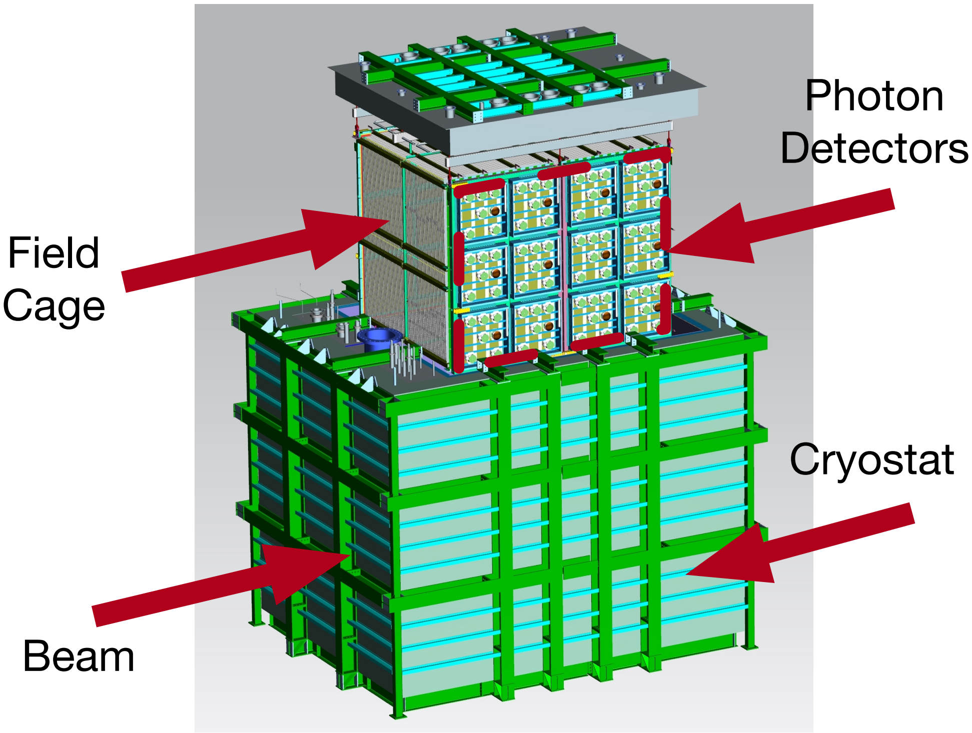

Figure 20: SBND – exploded view. Original figure from the SBND homepage. Modified by the author to outline the beam and detector components.

The near detector will have:

- 112 tons of active LAr divided into two, 2 m drift regions
- 500 V/cm nominal drift field
- 11,264 channels of charge readout

- Supplementary Cosmic Ray Tagger (**CRT**)
- Complementary Photon Detection System (**PDS**) - 120 PMTs + 192 ARAPUCAS

The physics program for SBND also includes measurements of neutrino-argon cross sections, facilitated by the high statistics of the experiment.

2.4.2. Booster Neutrino Beam (BNB)

SBN will have access to ν_μ and $\bar{\nu}_\mu$ beams. The (anti)neutrino beam is derived primarily from pions produced in 8 GeV proton collisions with a beryllium target. A magnetic horn downstream from the target focuses the positively or negatively charged products of the collisions on target. Depending on the polarity of the horn current, the $\pi^\pm$ subsequently undergo weak decays which are predominantly of the form:

$$\pi^\pm \rightarrow \mu^\pm + \overset{(-)}{\nu}_\mu, \tag{2.7}$$

with some contamination from pion decays to $e^\pm + \overset{(-)}{\nu}_e$. Muon absorbers are situated after the decay pipe in order to prevent charged particles reaching the detector. The resulting composition of the BNB is expected to be ~90% ν_μ in neutrino mode, and ~80% $\bar{\nu}_\mu$ in anti-neutrino mode. The peak ν_μ energy will be 700 MeV and a total exposure of 6.6×10^{20} P.O.T. is expected over three years.

2.4.3. Cosmic Ray Tagger (CRT)

The SBND CRT will provide nearly 4π coverage and will aid in tagging most cosmic rays entering the detector. SBND will rely on the PDS in order to identify neutrino interactions, and it would benefit from precision tagging of cosmic rays in order to rule them out as having neutrino origin.

Figure 21 below depicts a fraction of the CRT, and demonstrates the individual bars in which one would expect to see hits.

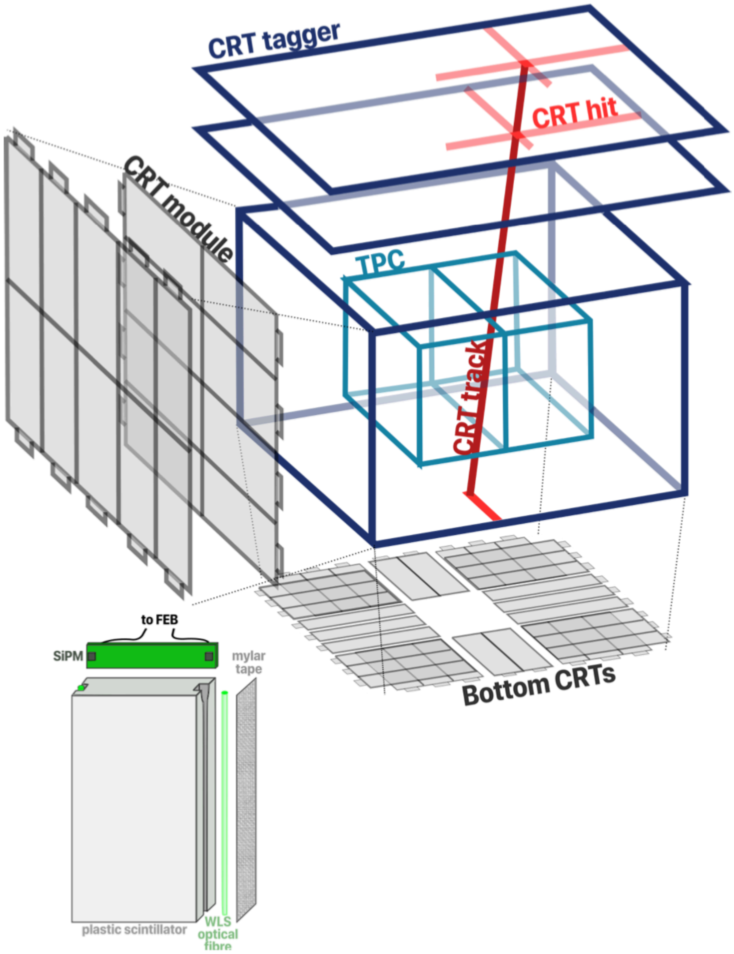

Figure 21: Usage and structure of the CRT. Original figure from T. Brooks

The full CRT is comprised of seven planes, each with an x and a y layer, with one plane on each of the four sides, one plane at the bottom, and two planes at the top. The planes are comprised of several plastic scintillator strips providing a segmented readout that will be used for cosmic ray tagging. The two top layers will serve as a cosmic ray telescope, i.e., they will constrain the direction of cosmic rays passing through them.

In addition to tagging particles of cosmogenic origin, the CRT will also intercept beam-related, background particles, and although these may correlate to the beam structure they may differ in time-of-flight. The CRT is sensitive to beam-related neutrons and gammas, which can interact with the scintillator strips. This has been demonstrated with the BNB at the Near Detector hall, during the commissioning of one of the CRT planes.

2.4.4. Photon Detection System

The SBND PDS consists of PMTs and ARAPUCAs. All photodetectors will be mounted in boxes, for structural support, and these will be mounted onto the APAs, behind the wire planes. Additionally, SBND will test the use of TPB-coated-foils mounted onto the reflective cathode. The additional TPB at the cathode will serve to homogenize the detector response across the entire drift. Without the foils, scintillation light produced near the reflective cathode undergoes more Rayleigh scattering, resulting in a decaying light yield as a function of distance from the photodetectors.

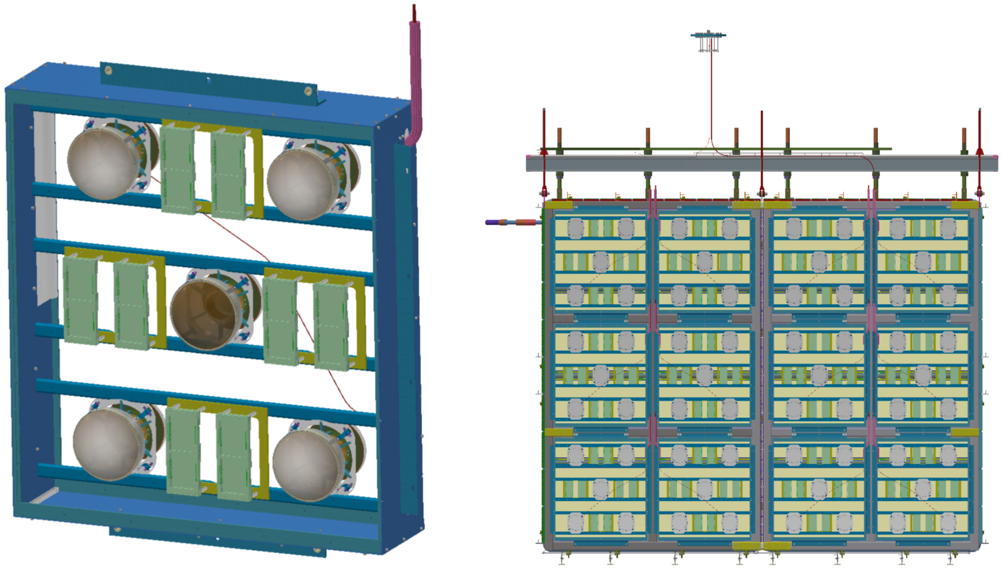

Figure 22: Left: PDS box for SBND containing four coated PMTs, one uncoated PMT (center) and eight ARAPUCA modules. **Right:** PDS boxes mounted onto the APAs.

The 120 PMTs are Hamamatsu R5912, which are 8 inches in diameter, and have all been tested and commissioned inside the CAPTAIN-Mills detector located in Los Alamos. For 96 out of the 120 total PMTs the glass was sandblasted and coated with TPB – this was in an effort to avoid TPB flaking, observed in coating tests. The remaining 24 PMTs are uncoated and are sensitive to Cherenkov light as well as wavelength-shifted light, particularly reflected light from the cathode. The 192 ARAPUCAs for SBND are also mounted onto the PDS boxes and will provide additional coverage with high efficiency.

2.5. The ProtoDUNE Single-Phase Detector

ProtoDUNE-SP is one of two prototype detectors located at the CERN Neutrino Platform and sitting downstream of a new beamline designed to help validate the two detector technologies – the other detector being ProtoDUNE Dual-Phase[1].

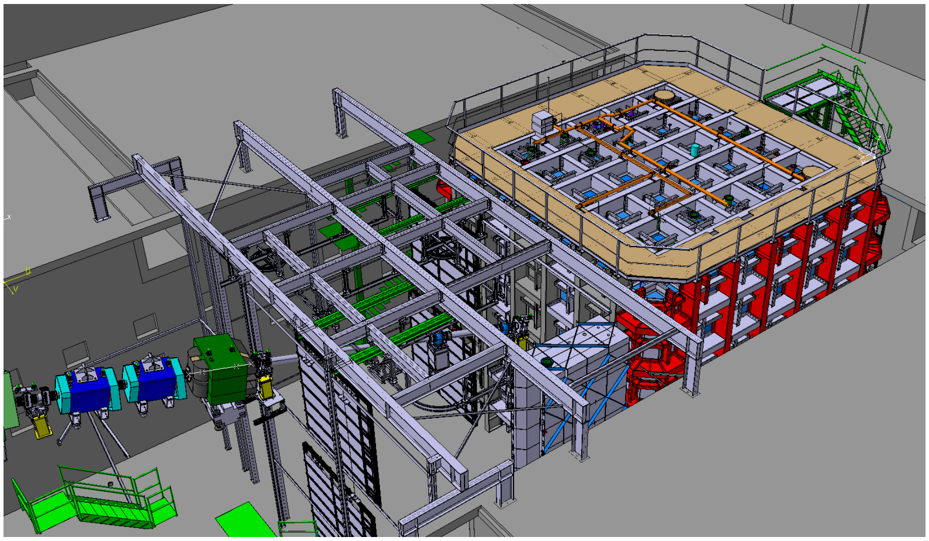

Figure 23: 3D model of the ProtoDUNE-SP beamline and detector. Figure from (Abi et al., 2020a).

Following the air contamination of the DUNE 35-ton prototype in March of 2016, the focus of the DUNE collaboration shifted fully towards the ProtoDUNEs. In order to acquire beam data, ProtoDUNE-SP had to be assembled and commissioned in anticipation of the 2018 LHC Long Shutdown 2 (LS2) (Wik) in December.

---

[1] The dual-phase technology consists of a vertical drift established across a liquid and a gas region inside a membrane cryostat. ProtoDUNE-DP will not be discussed in the remainder of this work.

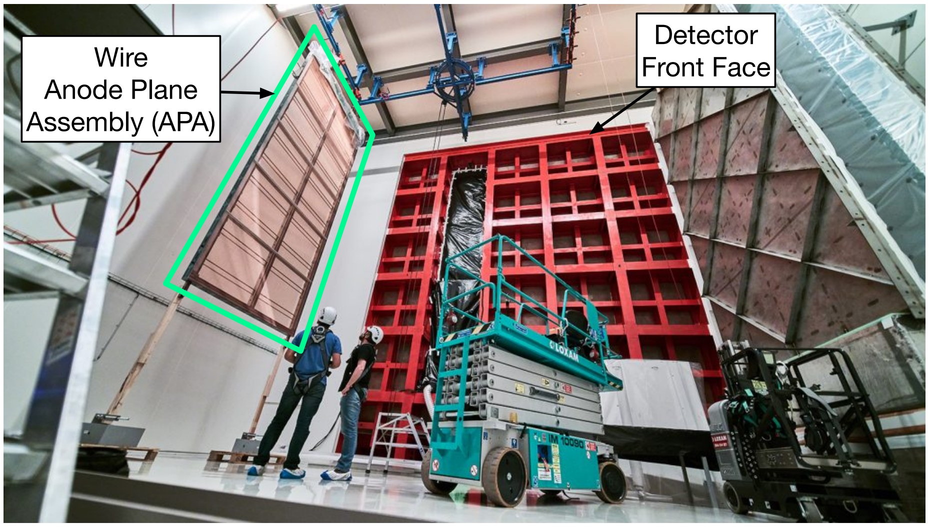

Figure 24: Full-size, DUNE-style APA being loaded into the ProtoDUNE-SP cryostat. Photo credit: CERN

In addition to serving as a test-ground for full-scale DUNE components and a demonstrator of the Single-Phase design, ProtoDUNE-SP has physics goals, namely:

- Measurement of cross sections for charged particles: e^+, π^+, K^+, and protons in LAr
- Study the ability to do energy reconstruction with both light and charge

2.5.1. The ProtoDUNE Beam

The ProtoDUNE-SP beam is produced in a tertiary branch of the H4 beamline located at the EHN1 CERN facility. The primary source of protons is the Super Proton Synchrotron (SPS) accelerator. SPS protons are extracted and directed towards a primary beryllium target (T2) producing low momentum hadrons (80 GeV/c). The secondary hadrons are charge-selected and redirected towards the secondary target to further scale down the momenta into the range of interest for DUNE, i.e. 0.1 GeV/c - 10 GeV/c. More information on the design and performance of the ProtoDUNE-SP H4 beamline can be found in Booth et al. (2019-06).

The beam design includes magnets with configurable magnet current to do charge and momentum selection. ProtoDUNE-SP took beam data for seven magnet current configurations corresponding to : 0.3 GeV/c, 0.5 GeV/c, 1.0 GeV/c, 2.0 GeV/c, 3.0 GeV/c, 6 GeV/c, and 7 GeV/c momenta. Due to the tight schedule for acquiring beam data, only positively-charged beam particles were selected due to their higher yield in the proton collisions on the primary target and the subsequent collisions on the secondary targets.

Each spill lasts 4.8 seconds and is de-bunched in an effort to deliver single particles to the detector; ideal for particle identification with the beam instrumentation. The beamline is directed towards a beam window centered 30 cm to the right of the cathode plane, and 422 cm from the bottom of the cryostat. The ProtoDUNE-SP coordinate system is oriented such that z is the downstream direction, y is the vertical direction, and x is the drift direction. The beam points 10 degrees towards the Anode ($\hat{\mathbf{x}}$) and 11 degrees down from the horizontal (-$\hat{\mathbf{y}}$). The origin in this coordinate system is located at the base of the cryostat – at the cathode location and at the front face of the active volume. The beam-half of the cryostat corresponds to -360 cm< x < 0 – this will also be referred to as **beam-right**; conversely, the region 0 < x < 360 cm, is **beam-left**.

Concrete blocks were placed around the beamline to provide shielding from byproducts of the secondary target collisions for the downstream detectors (Single and Dual-Phase). Nevertheless, a beam-related flux of muons was detected, predominantly in the beam-left region of the detector – this is referred to as the muon halo.

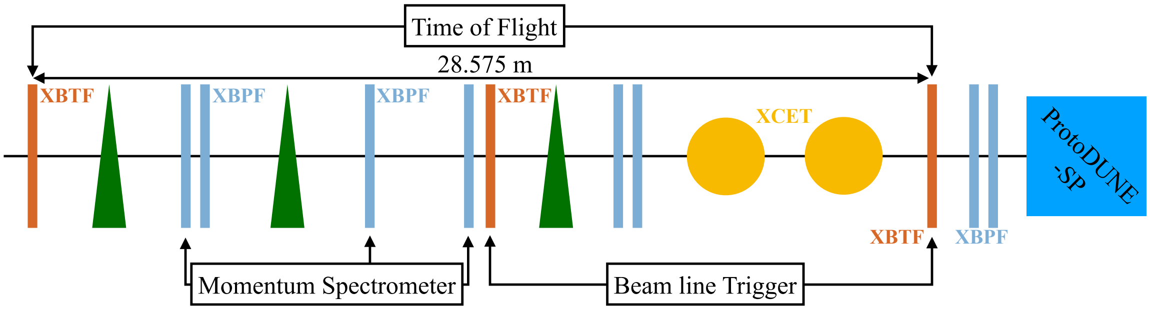

Figure 25: ProtoDUNE-SP beamline instrumentation. Figure from (Abi et al., 2020a).

More details on the ProtoDUNE-SP performance can be found in the performance paper (Abi et al., 2020a). The author was involved in the final phase of commissioning – as ProtoDUNE-SP was being filled with LAr.

2.5.2. CRT

The ProtoDUNE-SP CRT was procured from Double-Chooz and re-purposed to provide coverage in the beam direction of the detector. As mentioned previously, a beam-related muon halo intersected the TPC, and having the CRT was useful for studying and tagging this halo. The upstream CRT was suspended in front of the TPC in two half-planes with a $\hat{z}$-offset of 7 meters, to allow the beamline to get close to front face of the detector. The downstream CRT sits roughly 10 meters from the front face. Following LS2, the CRT was used to identify and tag muons crossing the up and downstream faces of the TPC.

2.5.3. PDS

The ProtoDUNE-SP PDS consists of 60 light bar modules mounted on the APAs as shown in Figure 17. With the exception of the two modules containing ARAPUCAs, all light bars are dip-coated with TPB. Light that scatters onto the edges of the bars, enters waveguides running along both sides and is directed towards an array of SiPMs on one side of the bars.

2.5.4. TPC

By design, ProtoDUNE-SP is large enough to house six, full-size APAs – three on each of the two sides facing the center cathode (depicted in Figure 26). The TPC dimensions represent only a small fraction of a DUNE 10 kt module (6%), namely 1/2 in width, 1/2 in height, and 6/25 in length.

The membrane cryostat was welded inside a steel support structure with internal layers of insulation (see Figure 27). The six APAs hang vertically from the top of the cryostat but remain electrically insulated from the grounded inner wall, which serves as a Faraday

Cage [1].

The electric field is established by a series of field-cage bars that segment the four walls that are perpendicular to the APAs and the central cathode. Each bar is separated from its adjacent bars by resistors that gradually step down the high voltage, as they approach the anode planes.

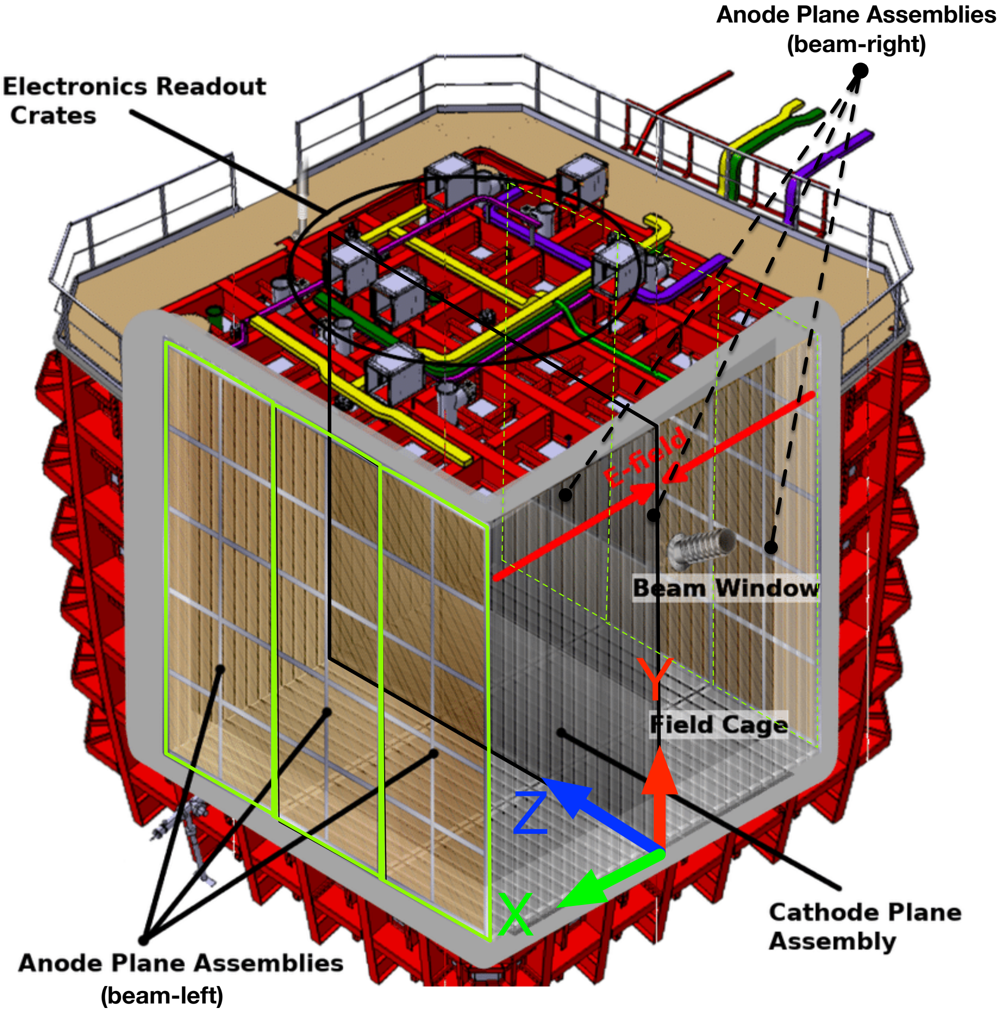

Figure 26: ProtoDUNE-SP model showcasing the beam entry point, the cathode, and the three APAs on each wall facing the cathode. Original figure from (Abi et al., 2017); modified by the author to depict the coordinate system and to outline the three APAs on either side of the CPA.

---

[1] This was essential for noise reduction – each APA is grounded at a single point – at the feed-throughs (through the return lines for the power lines for the Cold Electronics).

2.5.5. Future tests

A second phase for ProtoDUNE-SP will enable a final round of tests of updated components for DUNE. The test beam will, again, deliver charged particles to the detector for additional measurements[1]. ProtoDUNE-SP-II will serve as a test-bed for new electronics, the laser calibration system, and additional structural tests – including the support structure needed to hang a (single) APA upside-down[2], corresponding to half of the DUNE FD APAs.

Figure 27: ProtoDUNE-SP membrane cryostat. Photo credit: CERN.

---

[1] Negative charged particles will likely be sampled.

[2] That is, with the top of the APAs, onto which the electronics are mounted, positioned right above the cryostat floor instead of hanging from the cryostat ceiling.

CHAPTER 3 : TRIGGERING IN LAR EXPERIMENTS

One of the guiding principles for triggering in the LArTPC-based experiments under consideration by the author is that drift times are slow (~ms), compared to the time-of-flight or time of interaction of the particles across the detector (~ns).

One can decide whether the physics of interest occurred in the detector by utilizing information from prompt subdetector systems such as a CRT or a PDS ahead of the time the charge readout occurs.

ProtoDUNE-SP benefits from being in a charged-particle test-beam that is instrumented with inline detectors and profile monitors that can inform the trigger decision. This is to be contrasted with an experiment like SBND that will sit in a neutrino beamline and must, therefore, rely more loosely on the beam signals – in that case: an early warning (EW) signal issued in anticipation of Protons-on-Target (POT).

Beam events are not the only events of interest in surface LArTPC experiments. Cosmic ray events, particularly those which cross the detector are ideal for performing detector calibrations because they are easy to identify and can help understand non-uniformities in the detector. This will be addressed in section 5.4

3.1. The Penn Trigger Board

The 35-ton was an early DUNE prototype that was constructed to validate the membrane cryostat technology as well as to test some of the preliminary versions of the cold electronics designed for DUNE. This prototype is located at Fermilab and was operated as a detector in early 2016 for a period of six weeks. The data acquisition for the 35-ton was driven by scintillator paddles, arranged around of the concrete structure, housing the cryostat, to intercept cosmic rays.

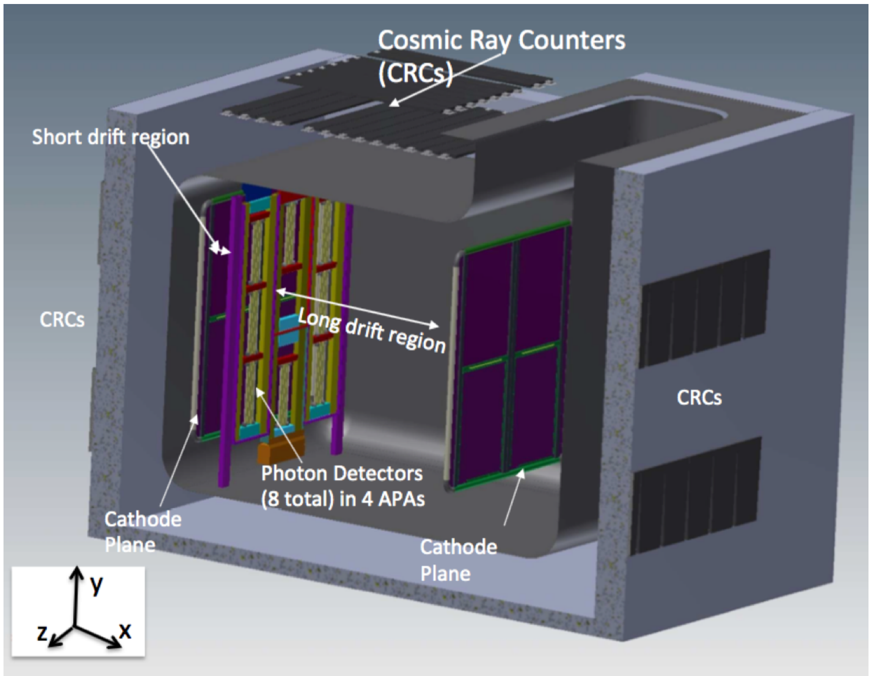

Figure 28: The 35-ton prototype design, with two cathode planes on opposite sides of the membrane cryostat. Figure from (Adams et al., 2018-06).

The University of Pennsylvania designed a Printed Circuit Board (PCB) that can: process discriminated signals from these paddles, form coincidences between them, as well as generate records of the triggers issued.

It was the author's responsibility to stuff and debug the Penn Trigger Boards (PTB) and aid in their commissioning at the 35-ton, from late 2015 to early 2016. Following the experiences in the 35-ton, the PTB was proposed, and chosen, for use in next generation LAr experiments: ProtoDUNE-SP and SBND. However, in order to accommodate the specific needs for these two experiments, the PTB input processing circuits were replaced while preserving the conceptual design of the board.

3.1.1. Conceptual design

The design phase of the PTB preceded the author's involvement and was the work of the instrumentation group at Penn as well as that of J. Klein and his postdoc N. Barros.

The main idea behind the PTB is to facilitate the triggering of experiments that are instrumented with systems that can provide digital logical signals conforming to various logic standards such as Transistor-Transistor Logic (TTL), in timescales that are prompt compared to the readout of the detector. These signals will be referred to as **trigger primitives** because they precede and inform the trigger generation, that is, they are necessary, but not necessarily sufficient to lead to a trigger.

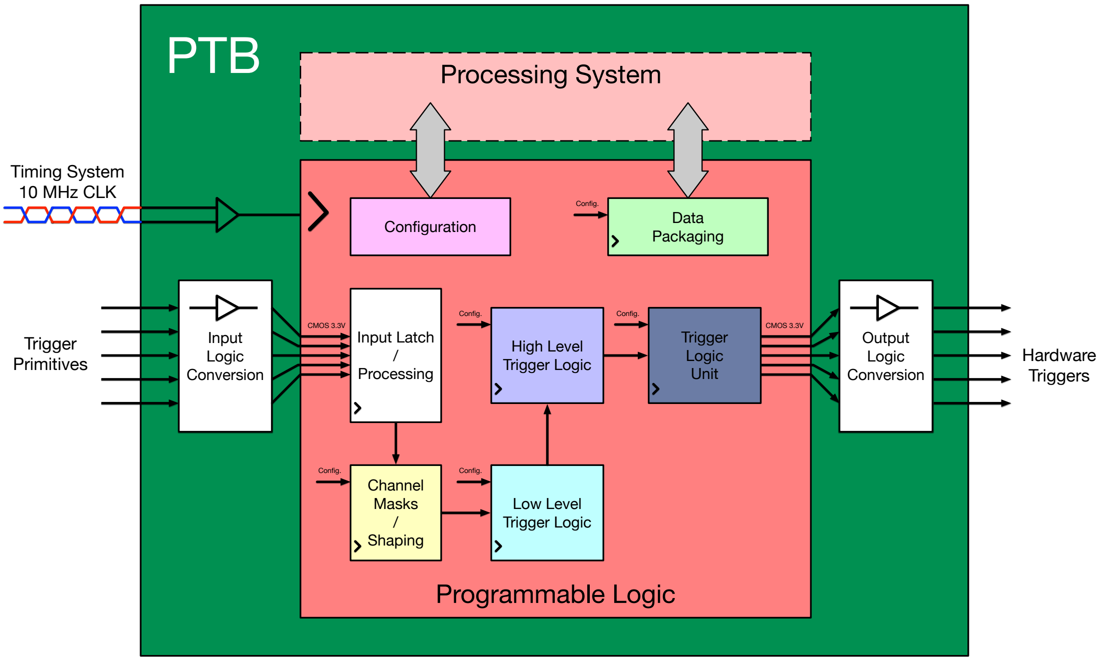

Figure 29: PTB conceptual design.

As shown in figure 29, the PTB first converts all input trigger primitives into logic signals of a single flavor, namely Complementary Metal-Oxide-Semiconductor (CMOS) 3.3 V, before routing it into the MicroZed™. The MicroZed™ is a commercial, printed circuit board containing a Zynq®-7Z020 System-On-a-Chip (SoC), which provides the flexibility of a Programmable Logic (PL) core, essentially an FPGA, as well as a Processing System (PS) with direct access to the PL.

All trigger logic is implemented in the form of firmware (FW) that runs on the PL fabric, and the software that communicates with the DAQ is in the form of a service that runs on an Ubuntu Operating System (OS) installed on the PS side of the Zynq®-7Z020.

The PTB FW utilizes synchronous logic, i.e., clocked-logic, in processing trigger primitives and issuing outputs. All information originating from the trigger logic is accompanied by a timestamp and packaged into 128-bit words that are then offloaded to the DAQ and stored as part of the overall event record.

The PTB trigger logic was designed to be configurable at run time and to be self-documenting, meaning that it provides unique IDs for the types of trigger conditions met in conjunction with the status of all inputs that led to the trigger decision. In this way, we ensure that trigger decisions can be decoded and reconstructed from the PTB data.

Despite its exclusive use in LArTPC-based experiments so far, the PTB is an extremely flexible board due to its access to both firmware and software that can be configured to process generic detector-related signals and can execute instructions transferred via a data link.

3.2. The Central Trigger Board

This section will provide a more detailed look into the second generation version of the PTB, i.e., the Central Trigger Board (CTB) as it was named for ProtoDUNE-SP, and the PTB Mark II (PTBMk2/PTB) as it known in SBND. For simplicity and to avoid confusion the board will be referred to as the CTB.

3.2.1. The CTB hardware

The CTB is a printed circuit board designed by J. Sensenig at Penn with guidance from N. Barros, R. Van Berg, J. Klein, G. Meyers, and the author. It accepts a total of 100 inputs comprised of the following logic standards:

- Nuclear Instrumentation Modules (NIM) - ProtoDUNE-SP and SBND
- Transistor-Transistor Logic (TTL) - ProtoDUNE-SP and SBND

- Low Voltage Differential Signals (LVDS) - SBND only
- Emitter-Coupled Logic (ECL) - SBND only
- Optical - ProtoDUNE-SP only

The inputs vary between the two experiments, and in order to accommodate the inputs from both within the limits of the MicroZed™[1], there are jumper resistors specific to each experiment that need to be populated on the board. These jumper resistor, along with the sub-circuits needed to convert input and output logic to/from LVCMOS 3.3V, define the “flavor” of the PTB (either ProtoDUNE-SP or SBND).

The author was responsible for stuffing, testing, and making modifications to the boards for SBND, and to a more limited extent, ProtoDUNE-SP.

---

[1] The MicroZed™ has 115 pins accessible in the PL – these can be designated as either inputs or outputs.

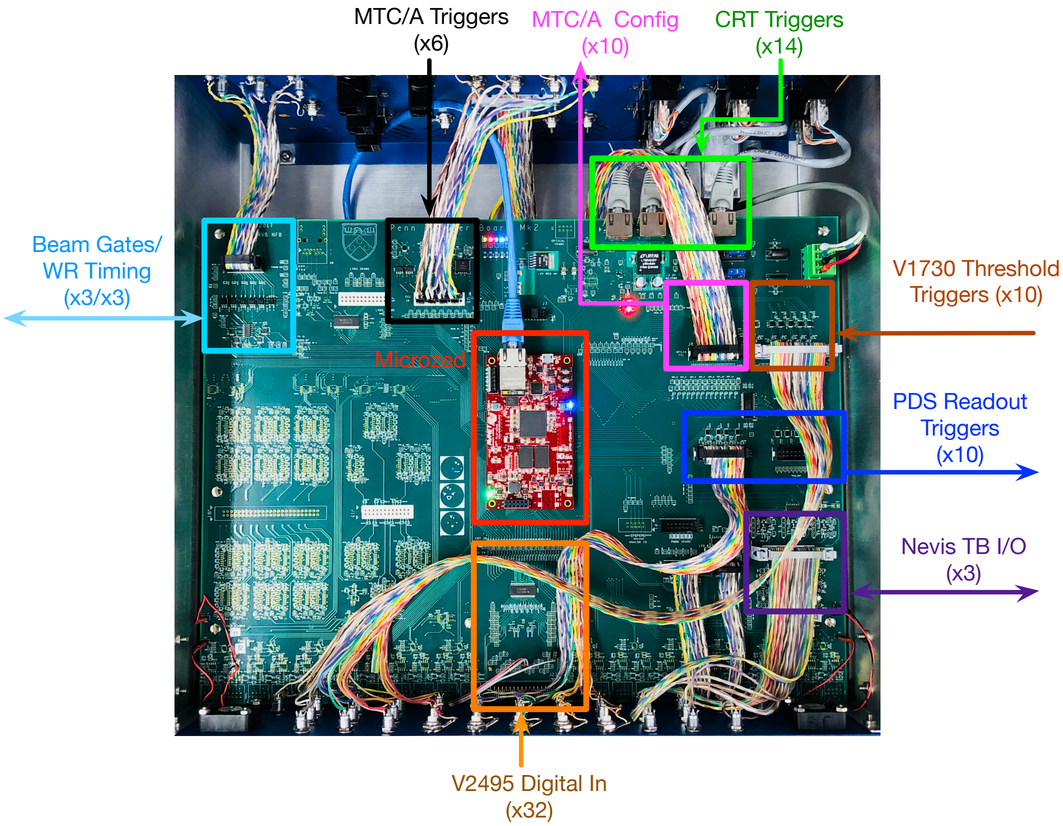

Figure 30: The PTB inputs and outputs in SBND enable it to make trigger decisions based on information from the several subsystems and to drive the readout of the PDS.

3.2.2. The CTB firmware

The user-written FW for the CTB is in Very Large Scale Integration (VLSI) Hardware Description Language or VHDL. It is comprised of various block designs, some custom-written and some available as configurable Intellectual Properties (IPs) from Xilinx, the company that owns a variety of PL devices and the tools necessary to program them.

The majority of the FW and system designs for the Zynq®-7Z020 onboard the CTB's MicroZed™ was fathered by N. Barros particularly for the 35-ton and ProtoDUNE-SP designs. The author contributed mainly to the FW for the SBND flavor of the PTB, which adopted/built on existing infrastructure in the CTB FW design.

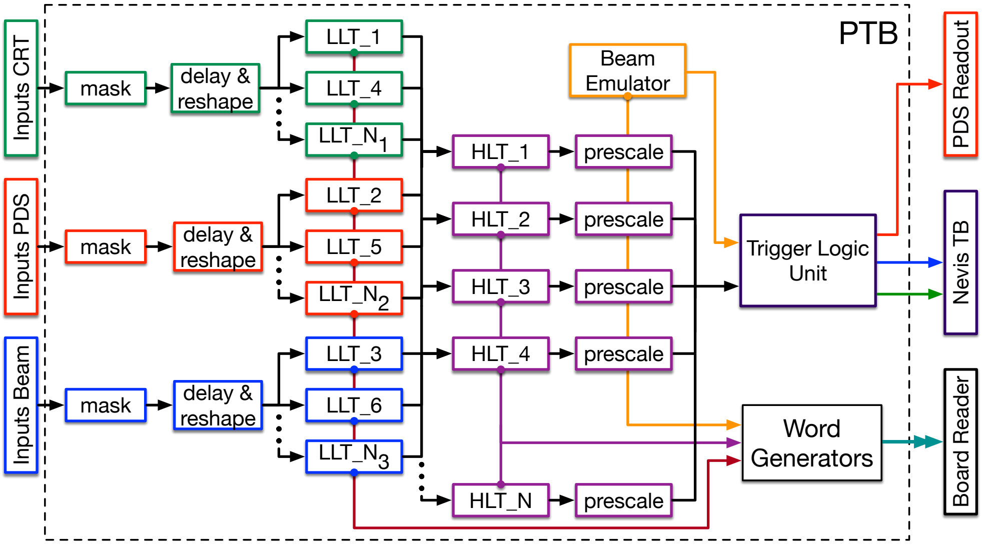

Figure 31: PTB top-level FW design for SBND.

The firmware for the CTB is organized as shown in Figures 31, 32. The main categories of IP cores are:

- Configuration
- Timing
- Low-Level Triggers (LLTs)
- High-Level Triggers (HLTs)
- Word Generators
- Data Packaging
- Data Transfer

The Configuration IP handles two important components of the firmware, one is the Finite State Machine (FSM) which communicates (bi-directionally) with the CTB software to execute the core functions such as **Start Run** and **Stop Run**. The configuration IP (labeled in figure 32) also handles reading and writing to the field of registers which correspond to various configurable parameters utilized by other IPs, hence the large fanout from the configuration block to many other IPs.

The Timing IPs include the 64-bit timestamp generator and allow for syncing via the 1PPS. More specifically, at the arrival of the 1PPS signals.

The Low-Level Triggers (LLTs) are derived from the input trigger primitives of a single subsystem while the high-Level Triggers (HLTs) incorporate the trigger outputs from one or multiple LLTs.

In general there are three types of words, LLT-based words, HLT-based words, and timestamp words. The Word Generator IPs construct the 128-bit words containing the word type, a 27-bit timestamp, and the payload which relates the type of trigger to the BoardReader software (discussed in section 3.2.3).

Is also accompanied by an End-of-Run word containing statistics i.e. the number of each type of trigger word that was sent during the run.

If additional words are needed they can easily be added to the firmware and the overlay class. For example, in the 35-ton, there are calibration words that indicate when an LED inside the cryostat was flashed.

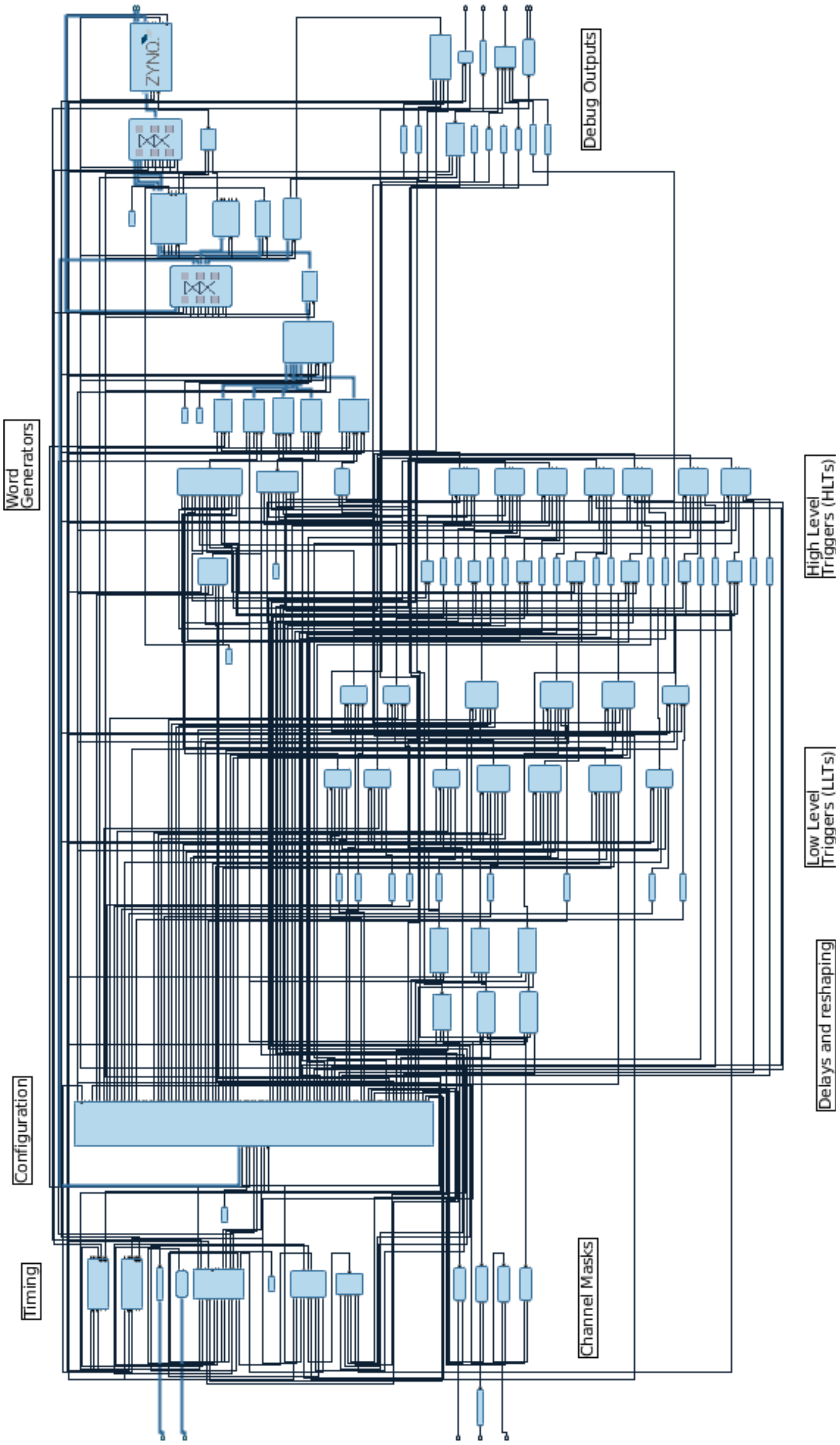

Figure 32: Firmware block design for the PTB in SBND.

The Data Packaging IPs include a *serializer* which concatenates the outputs of all Word Generator IPs into a single stream and a *bundler*, which keeps track of the number of words being generated in order to package them in groups of N words (configurable) and appends a header with a sequence ID.

The trigger words and timestamps are read out through the use of Scatter-Gather Direct Memory Access (DMA), which moves the bundles of N words into Random Access Memory (RAM) where it is accessible to the user applications. Roughly 50% of the FPGA resources are utilized by the use of Scatter-Gather, thus, it is not a negligible impact. Nevertheless, the firmware occupancy of the current design is roughly 85% and has proven to be highly efficient, maintaining stable throughput at trigger rates of 1 MHz. This rate is much, much higher than necessary for LArTPC experiments which cannot be triggered at rates higher than a few 10's of Hz[1]. The readout of the PDS electronics, i.e. the CAEN V1730 boards, for SBND will be driven by the PTB at higher *instantaneous* rates but will, at most, need to be triggered at a rate of 1.2 kHz, which is the maximum rate that the CAEN boards can be read out if each trigger captures 1 μs of PMT data.

3.2.3. The CTB software

CTB software encompasses code including kernel modules, drivers, and user applications. The CTB design incorporates kernel modules and DMA drivers available as a github project called PothosZynq, which is based on a larger data-flow framework called Pothosware (Blum) both of which are made available by their author J. Blum and are subject to v1.0 of the Boost Software License.

The details of how the PothosZynq DMA works is beyond the scope of this document. The motivation for utilizing DMA as opposed to other methods for reading and transmitting data to the downstream DAQ is that this reduces the load on the CPU. It does so at the cost of resources in the PL fabric.

---

[1] Recall that LArTPC drifts are in the order of milliseconds.

The CTB receives its configuration through communication with the DAQ in the form of JSON fragments transmitted as Transmission Control Protocol (TCP) packets. A host server runs on the PTB that accepts connections from clients. The client can be established locally in standalone mode, or remotely on a client machine. The user application was written by N. Barros for use with the CTB, where it runs as a service listening for a host connection. Once the connection is established the host can issue commands in order to control and configure the board.

The CTB data acquisition was designed to interface with the DAQ software developed by Fermilab, known as *artdaq* (Biery et al., 2017). The DAQ process that interacts with the PTB is known as a BoardReader, which inherits from an artdaq class called FragmentGenerator. This class has fundamental functions such as GetNext(), which has to be defined for the specific hardware being read out. In the artdaq scheme, several BoardReaders interact with the EventBuilder which is in charge of distributing requests for data and gathering the fragments corresponding to each specific event based on a sequence ID or on a timestamp.

The CTB BoardReader was written by M. Roda for ProtoDUNE-SP and was adapted and imported into SBND and is maintained by the author. In the grand scheme of data acquisition for both ProtoDUNE-SP and SBND, the CTB operates in a mode (pull mode) in which it provides a window of data, of configurable length, defined relative to the timestamp contained within the EventBuilder requests.

3.3. Triggering in ProtoDUNE-SP

The beam physics program for ProtoDUNE-SP began in October 2018, following the commissioning phase of the detector in late September. During this period, ProtoDUNE-SP used the Central Trigger Board to drive the readout of the detector.

As previously mentioned, the CTB was designed at Penn, building on the experience with the 35-ton DUNE prototype at Fermilab. The trigger logic for ProtoDUNE-SP was developed by N. Barros and J. Sensenig, and it was the author's job to aid in commissioning at

CERN. A significant difference between the two DUNE prototypes is the added complexity from having a charged-particle test-beam. The CTB receives seven inputs from the Beam Instrumentation (BI) subsystem, these include:

- 1 spill early warning signal,
- 1 beam gate,
- 3 XY scintillator plane signals, and
- 2 Cherenkov counters.

The beam trigger required a coincidence between the two downstream XY scintillator planes – referred to as *profilers* in the ProtoDUNE-SP TDR (Abi et al., 2017) – during the beam gate window. The author constructed the beam gate window using a beam early warning and the end of extraction signals provided by the Beam Instrumentation group and derived from the accelerator complex signals. This was a accomplished externally from the CTB, using a CAEN Dual Timer and logic converters.

During the 2018 beam campaign, Cherenkov counters were sometimes included in the beam trigger decision to yield events with reduced/increased positron content in order to yield events better suited for studies of positrons or hadrons. This is achieved by tuning the Cherenkov counter thresholds such that only positrons exceed the β threshold for the two counters. The majority of runs did not explicitly veto triggers with/without positrons, however, because the CTB data stream could be used to sort the beam candidates based on the status of the Cherenkov counters, offline. In total, 4 M events were accumulated using the test-beam – these include e^+, π^+, K^+, and p.

In addition to the Beam Instrumentation signals, the CTB is able to trigger on the 32 CRT modules, 24 trigger outputs from the PDS, or a combination of these. The CRT trigger primitives were used extensively after the CERN long shutdown, to capture crossing muons.

3.3.1. The SBND trigger

The author is solely responsible for creating a working firmware design for the SBND trigger based on the experience and firmware written for ProtoDUNE-SP. The SBND trigger system utilizes coincidences between the Booster Neutrino Beam (BNB) and detected scintillation and Cherenkov light to identify neutrino interactions. It is also responsible for issuing cosmic and random triggers for efficiency and background studies to aid in calibrating the detector. The trigger system is comprised of three custom-built modules: Columbia's Nevis Trigger Board (TB), and two contributions from the University of Pennsylvania, namely, the Penn Trigger Board (PTB), and the Analog Master Trigger Cards (MTC/As), of which, there are two.

The role of the PTB is to receive trigger primitives, apply trigger logic, send trigger signals to the PDS electronics and the Nevis TB, and send a timestamped record of the input and output signals to the DAQ. These trigger primitives are, essentially, how the different subsystems communicate to the PTB what they see. In the current scheme there is a total of 33 trigger primitives: 10 from the CAEN digitizers in the PDS, 3 from each MTC/A (6 total), 14 from the CRT, and 3 early warning signals from the accelerator complex in order to generate the experimental triggers. Each (non)beam trigger is forwarded directly to the Nevis TB, which oversees readout of the wires in the LArTPC and issues the global trigger to other subsystems. In this scheme, the PTB also generates a timestamped record of the input trigger primitives and the trigger outputs in the time-window of interest around any trigger issued to the Nevis TB and sends this data record to the DAQ system over Gigabit Ethernet to be integrated into the overall event record.

Table 5: PTB trigger primitives in SBND.

Source	Number of inputs	Description
Beam Inst.	3	Beam early warning signals
MTC/As	6	LO, MED, and HI threshold triggers per MTC/A
CAEN	10	10 board-level majority triggers
CRT	14	Seven X and seven Y CRT planes

One of the beam early warning signals is reserved for the BNB, one for the NuMI beamline, and one for off-target (potential Dark Matter searches). SBND will be very off-axis in relation to the NuMI baseline and therefore it is unlikely that SBND will receive a significant flux in comparison to both MicroBooNE and ICARUS.

The ten signals from the CAEN digitizers going directly to the PTB provide a logic HIGH when a desired number of pairs of channels have crossed (configurable) waveform thresholds. Two of the ten CAEN V1730s, will be used to read out a subset of the ARAPUCAs in SBND. At the moment, only the eight boards that correspond to the PMTs are configured to participate in the trigger. If SBND decides to include them, the additional input, majority-level primitives can be masked back into the LLT definitions.

Figure 33 below, is an example of a beam ν_μ induced trigger based on the board-level trigger primitives from the CAEN V1730s digitizing the PMTs on the beam-side. In this example the PTB trigger is configured to require that at least three of the four majority trigger primitives to be asserted in *coincidence* with the beam gate to produce a beam trigger for the experiment.

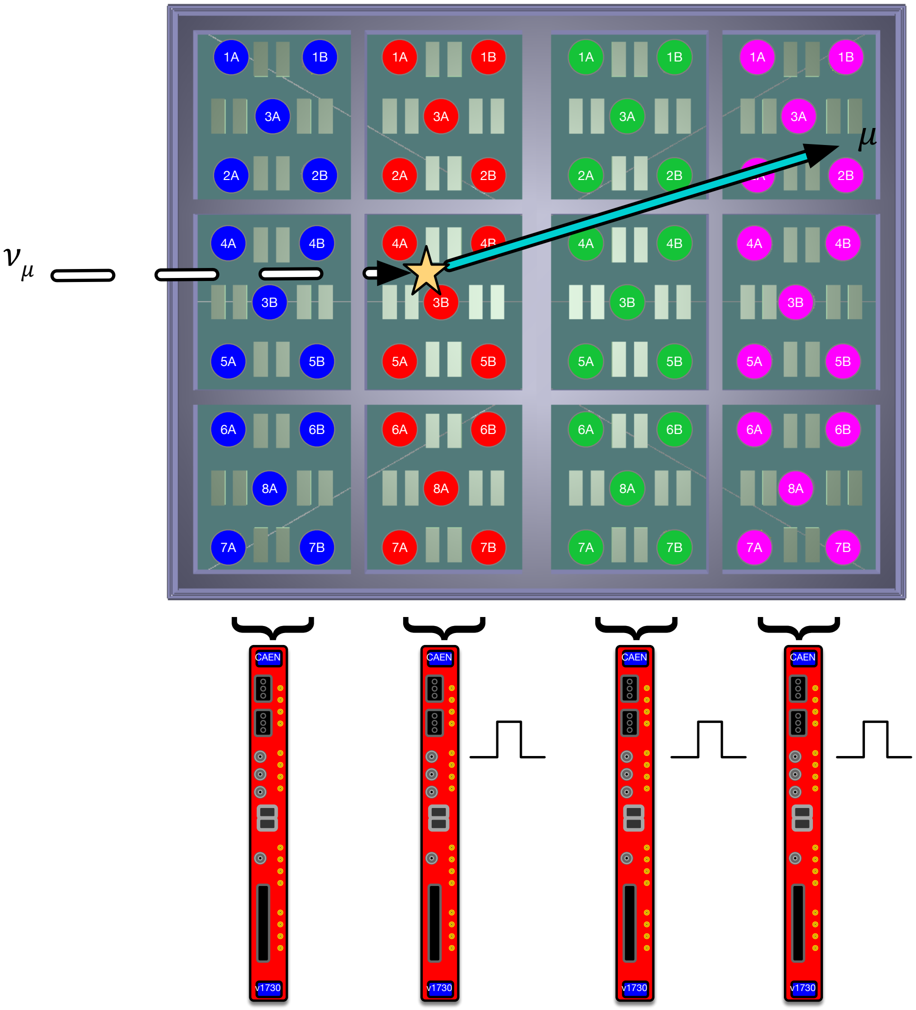

Figure 33: Figure depicting the beam-side photodetectors in the SBND detector – viewed from the perspective of an observer facing the PDS electronics mounted behind the beam-right APA plane. Each solid circle (blue, red, green, and violet) represents a PMT facing the drift volume. The ν_μ-CC event occurs within the active volume, which is into the plane of the page.

The MTC/A is a PCB designed by J. Klein in 1996 to perform a similar function in the SNO experiment. The MTC/As accept a separate set of ten signals (labeled Σ/Mon on the boards themselves) from the CAENs, which are proportional to the number of pairs of Photo Multiplier Tubes (PMTs) that have crossed threshold and they perform an analog sum of these multiplicities. The sum is then compared to three individually programmed thresholds (LO, MED, and HI) on each MTC/A in order to produce 20 ns logic pulses when the input sums exceed one or more of these thresholds. Figure 34 depicts the underlying function of the MTC/As and how it relates to the PTB.

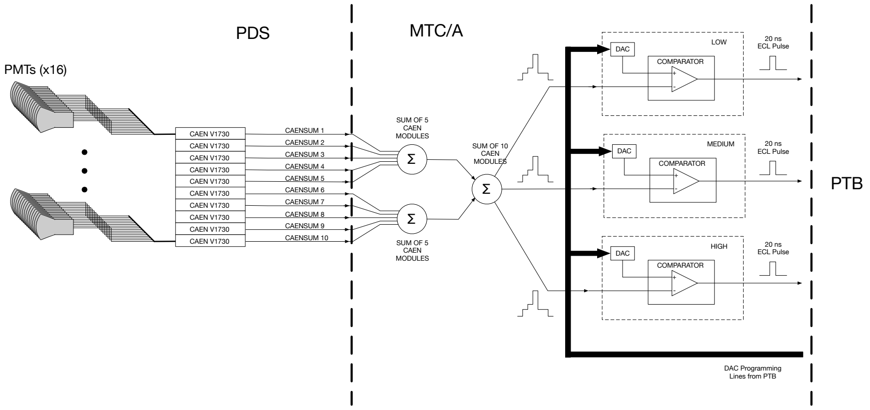

Figure 34: MTC/A trigger primitive generation.

This allows us to form triggers based on hit multiplicities of pairs, rather than boards. This is desirable for events that produce light that is distributed across many pairs but with fewer pairs per CAEN module e.g. Supernovae. There is a limited amount of time to trigger the readout of the CAEN modules before buffers fill up, therefore understanding and minimizing the latency of the trigger path is critical.

The PTB input primitive bandwidth in SBND will include random pulses at rates of 100's of kHz (mainly from ^{39}Ar decays and cosmic rays) as well as very rare events with high multiplicity in the PDS system (e.g., charged current quasi-elastic neutrino scattering). One of the main goals for the commissioning efforts of the trigger board and MTC/As is to demonstrate that the full signal bandwidth can be processed to create the global triggers for the experiment.

3.3.2. Triggering system

The MTC/As, PTB, and the Nevis Trigger Board are all part of the triggering system as depicted in figure 35. The PTB is central to the DAQ system – it receives trigger primitives from all subsystems and utilizes that information to make trigger decisions. This is facilitated by the various inputs and outputs (I/O) on the board and the onboard FPGA.

The PTB trigger decisions are forwarded to the Nevis TB, which will ultimately decide to veto or issue a global trigger to the TPC electronics in order to capture the wire information.

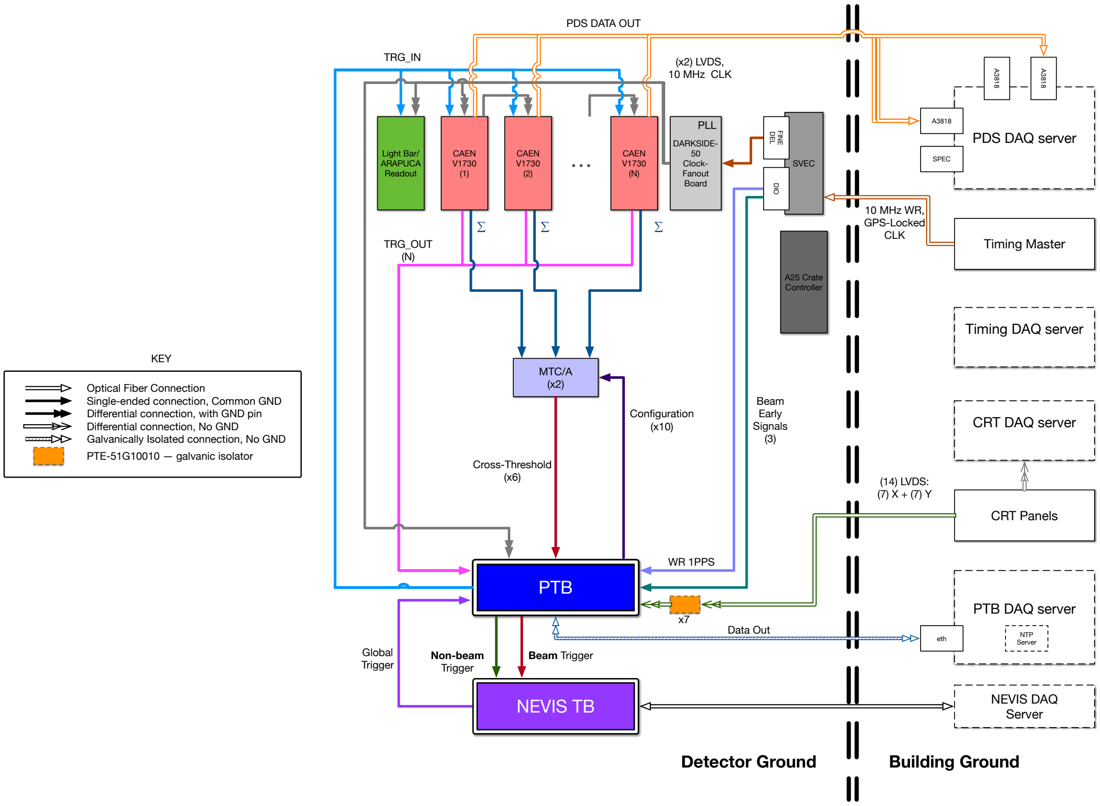

Figure 35: Triggering scheme.

The PTB sends/receives signals across the two grounds, detector and building, therefore special care is to be taken at the interface between PTB and CRT, and PTB and the DAQ. The PTB receives signals carrying a ground reference ONLY from other hardware that is on the detector ground. The signals from the CRT, which is on building ground, are galvanically isolated and terminated via a dedicated circuit designed by the author.

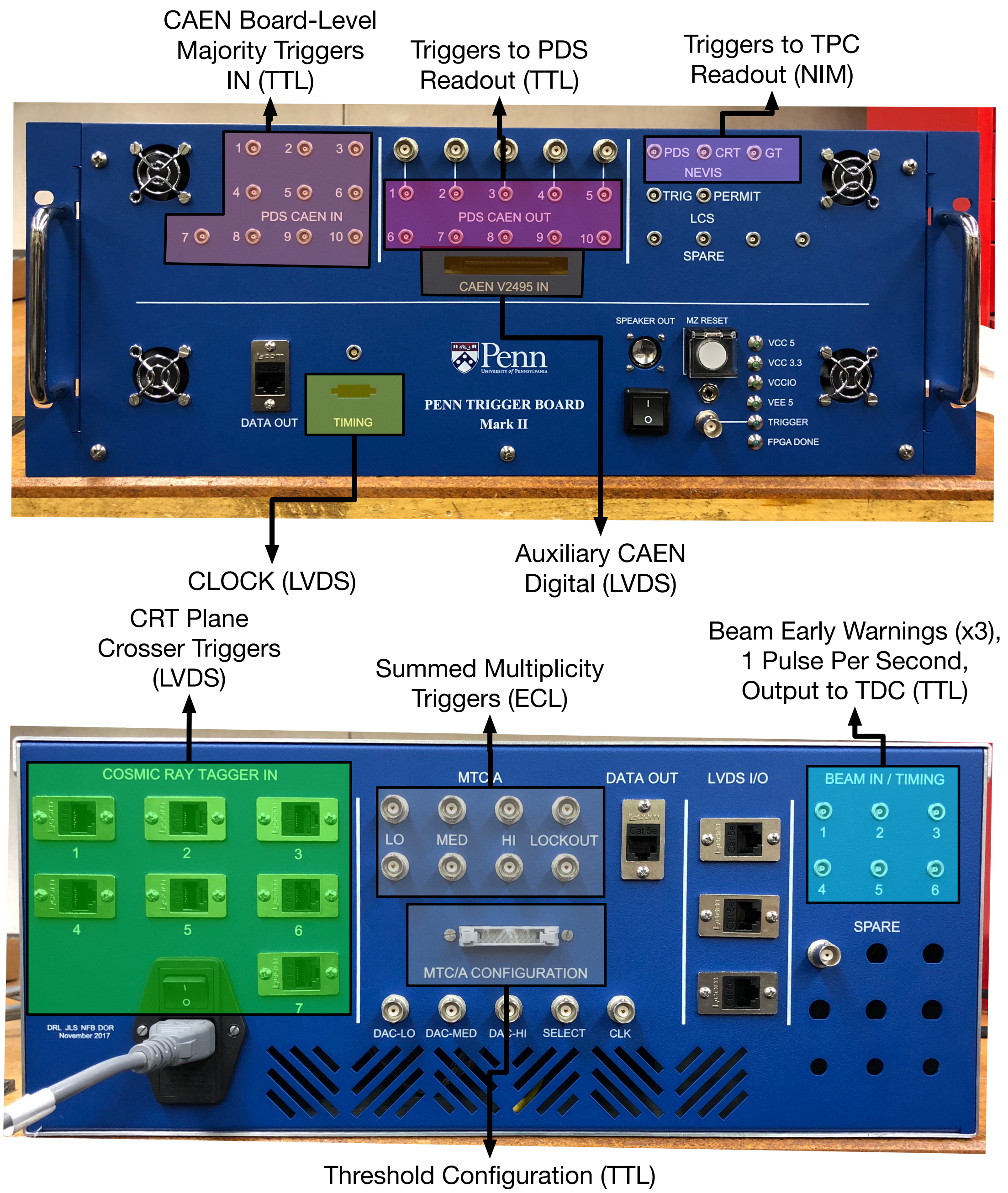

Figure 36: Top: The front panel of the Penn Trigger Board for SBND. **Bottom**: The back panel of the PTB.

The PTB can trigger on the following:

- pseudo-random triggers (internally or externally generated)

- through-going cosmic ray candidates
- stopping muon candidates
- dirt muons[1]
- PDS-based triggers (a combination of CAEN and MTC/A)
- minimum-bias triggers (trigger based on the beam early warning, alone)

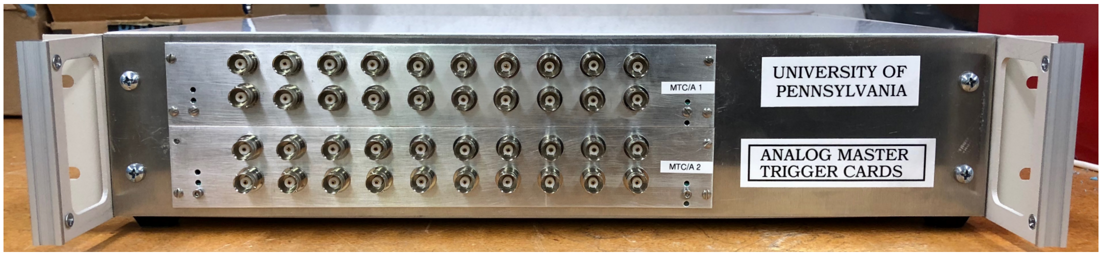

Figure 37: The front panel for the MTC/A chassis. The chassis contains two MTC/As, each with 20 analog inputs.

3.3.3. Trigger calculation

All BNB extractions *potentially* contain neutrino events; the PTB will issue Beam triggers to the PDS electronics in order to digitize ~24 μs around all spills. Each BNB spill delivered to SBND is 1.6 μs long. The Early Warning will arrive with a lead time (t_{lead}) ahead of the neutrinos to the SBN Near detector. Upon arriving at the PTB, the Early Warning Signal will initiate a counter, and subsequently open a 1.6 μs (configurable) beam acceptance gate. t_{lead} must be measured to align the beam acceptance gate with the spill. This is discussed in more detail in Appendix A.

For 1.32×10^{8} spills expected, this is equivalent to ~211 seconds of "in-spill" time over the three years required for the SBN program to acquire sufficient statistics for its measurements. For this level of exposure, the near detector (SBND), expects to capture a total of 7,251,948 neutrino events, including CC and NC interactions by both ν_μ and ν_e. The

---

[1] Muons produced by ν_μ interactions in the dirt or concrete prior to entering the ND hall. These muons will be tagged by the CRT panels covering the front face of the cryostat.

breakdown of this number can be found in table X (page II-55) of the SBN proposal (Acciarri et al., 2015a). The rate of neutrino interactions ($r_{\nu-interaction}$) per spill is given by eq. 3.1.

$$r_{\nu-interaction} = \frac{\text{№interactions}}{\text{№spills}} = \frac{7,251,948}{1.32 \times 10^{8}} = 0.055 \text{ interactions/spill}, \tag{3.1}$$

or approximately **1 neutrino interaction every 18 spills**.

In real-time, this will be modulated by the spill rate delivered to the BNB. Assuming that for each event, we write three full-drifts to disk, this is equivalent to : 7,251,948 interactions $\times 3 \times 1.28$ ms, or 27,848 s of readout. For the nominal BNB spill rate of 5 Hz, this equals: 5Hz $\times$ 0.055 or 0.275Hz of neutrino interactions in SBND.

Some of the remaining (5Hz - 0.275Hz) bandwidth for the experiment will be used to acquire minimum-bias triggers to evaluate the triggering efficiency for the beam trigger. SBND will also collect cosmic-ray-based triggers to be used for calibration, as well as beam triggers to study the triggering efficiency for other physics triggers.

Figure 38: PTB at the Near Detector Building.

3.3.4. Software triggering in DUNE

The static data rate, per 10 kt DUNE module, is 6 Terrabytes-per-second as calculated in section 2.3.1. This is for the charge readout alone, there will also be a significant contribution from the DUNE PDS, with the specific data throughput depending on the digitization rate for the ARAPUCAs. Some of the rates for physics and background are depicted on the rate vs. visible energy cartoon in Figure 39.

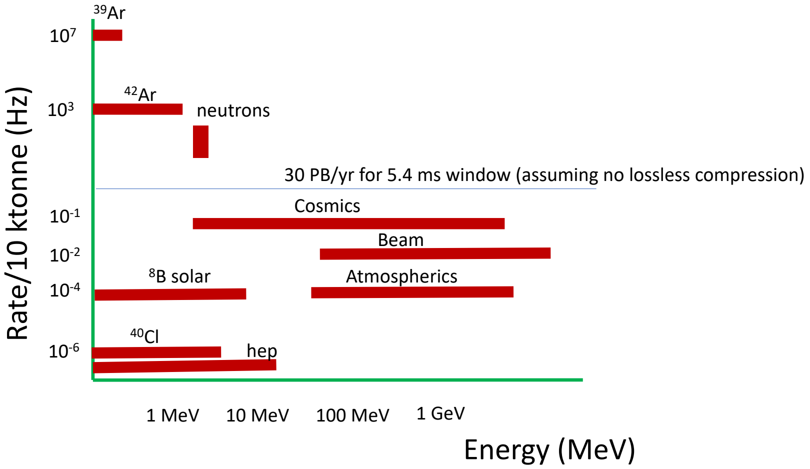

Figure 39: Physics rate cartoon for DUNE. Original figure by J. Klein.

The dominant source of signals for DUNE are radiologicals, which include ^{39}Ar, ^{42}Ar, and neutrons from concrete. ^{39}Ar is a beta decay isotope with an endpoint of 565 keV, and is naturally present in LAr at ~1 Bq/L, which is equivalent to 10 MHz per 10 kt module.

In DUNE, the neutrino event rate will be sub-Hz, and because the detector modules will be underground with a 1.5 km rock overburden to reduce the cosmic ray rate, online self-triggering is feasible and perhaps a more natural option than a hardware trigger. To demonstrate that we can meet basic trigger requirements for DUNE, D. Last, a fellow graduate student, and the author came up with software triggering algorithms that allow for high efficiency triggering on the primary and auxiliary DUNE physics program (Abi et al., 2020c) – this includes beam and atmospheric neutrino interactions as well as nucleon decays, all the while, rejecting radiological backgrounds such as ^{39}Ar.

The resulting efficiency of our triggering algorithms have served as a baseline for the software trigger in DUNE, which is discussed in the DUNE Technical Design Report (Abi et al., 2020b). To expand on the physics reach for DUNE, we would like to be able to trigger on low energy physics, such as solar neutrinos, while staying within our data budget of 30 PB / year / 10 kt module.

The general sequence for processing the data to generate trigger candidates is as follows:

Hit Finding → Clustering → Trigger Candidate Finding

The Hit Finder operates on raw waveforms from simulated, or real, data and returns a channel-ordered series of hits for the entire drift. For simplicity, only the collection wires considered[1]. The hits are produced anytime the raw waveforms cross the desired threshold.

For collection signals, the hit objects contain the following variables of interest:

- **time**: Start tick, End tick, Peak time, RMS peak time,
- **amplitude**: Peak amplitude, Summed charge

where the Start and End Ticks correspond to the time at which the waveform crossed a pre-defined threshold in the positive and negative direction, respectively. Prior to processing hits, these are sorted into time bins corresponding to candidate generation windows (50μs).

The total charge ($\Sigma_{TPC-ADC}$) captured in a single TPC for each APA (whichever had more is used), is considered as the primary parameter on which to issue a trigger candidate. The decision for issuing a candidate is further parametrized into a basis composed of the spread in z (Adjacency/Cluster Size), Time Over Threshold (TOT), wire total charge ($\Sigma_{wire-ADC}$), and the approximate 2D length ($\mathcal{L}$) (this is discussed in Section 3.5.1).

The Time-Over-Threshold (TOT) is simply the time difference between the End and Start ticks of a hit, and the maximum per candidate generation window is utilized to make the decision. The maximum Summed ADC (SADC) of a single hit is similarly the defined Wire Summed ADC (WADC) parameter used in the decision.

---

[1] Collection signals, alone, cannot distinguish between ionization events observed along the vertical direction; this would require induction wire information. Induction wires were neglected to avoid incurring additional latency from the disambiguation of the induction hits – i.e., determining which side of the APA observed the charge – recall that the induction wires wrap around the DUNE-style APAs.

The effective method utilized to cluster hits is referred to as “Adjacency”, and it requires counting the number of adjacent collection wires for which a hit was found in a pre-defined candidate window (Δt), where the candidate window is a fraction of the full 3 ms drift (see Figure 40). As with the other variables above, the maximum in the window is taken to be the parameter on which the candidate decision is made.

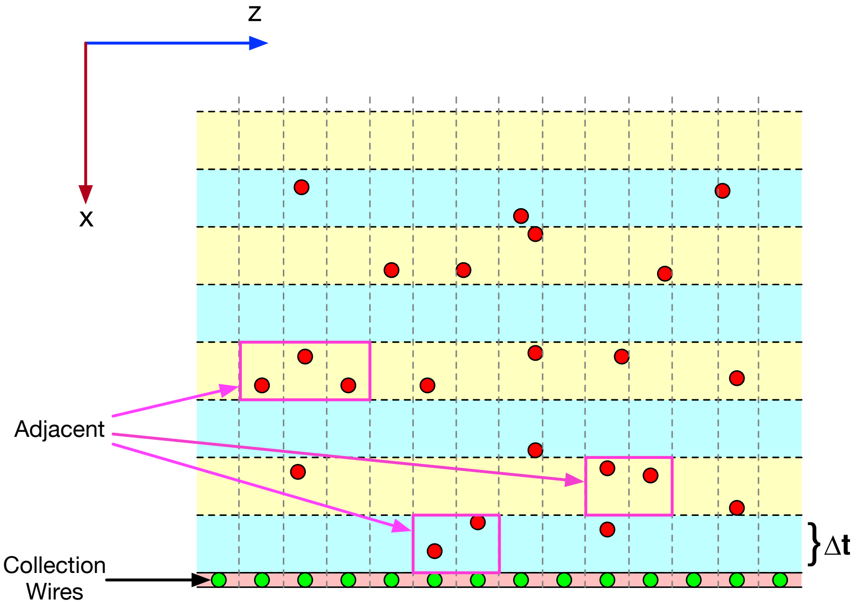

Figure 40: The Adjacency algorithm relies on finding clusters of hits occurring in adjacent wires, within a candidate generation window Δt. In this example the maximum wire adjacency is three. The figure is an x-z projection of the drift volume. The green circles represent the cross section of the collection wires.

DUNE's main physics program requires the trigger to be practically 100% efficient above 100 MeV of visible energy. Furthermore, the rate of fake triggers should not exceed the rate of cosmic events in the detector, as to limit the data processing rates to acceptable levels. The current structure of the DUNE triggering system is such that primitives are processed at the APA-level to generate trigger candidates. These candidates are then processed by a module-level trigger and if the trigger is asserted, the data for the entire module is written out for a two-drift-sized window centered around the time the trigger was issued.

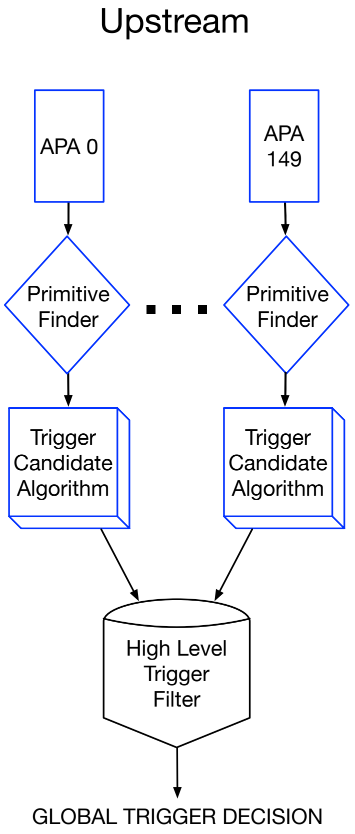

Supernova events are triggered via a different schema that will rely on a large (≈10 s) data buffer. The focus of these trigger algorithms is mainly to ensure DUNE's capability to trigger on Beam and Atmospheric events. The algorithms are generic with the goal that they apply to other interesting physics for DUNE, e.g., solar neutrinos and cosmics.

The guiding assumption for the studies discussed here is that, for every trigger candidate generated, a module-level trigger will be issued. This means (based on an estimated cosmic event rate of 1000/day) that the maximum acceptable rate of fake triggers from radiological backgrounds (as this will dominate the overall trigger rate) is as follows:

$$\frac{1000}{\text{day} * \text{module}} \cdot \frac{1\text{module}}{150\text{APA}} \cdot \frac{1\text{day}}{24\text{hr} * 3600\text{sec/hr}} \approx 77\mu\text{Hz/APA}$$

Therefore the goal for the triggering studies were to limit the rate to 7.7μHz/APA as to potentially be stable against variations in radiological and random-noise rates. This is a conservative approach, and it is foreseen that a fraction of the active volume may be read out and be stored on tape, as opposed to an entire 10 kt module's worth of data, all depending on the type of trigger activity[1].

Argon-39 is expected to be the primary radiological contribution, by rate (>100 Hz/collection wire). The accidental trigger rate (Γ_{acc}) as a function of the maximum wire adjacency (n_{adj}) is given by Equation 3.2.

$$\Gamma_{acc}(n_{adj}, r, n_w, \Delta t) = [3(n_w + 1 - n_{adj}) + n_w] \cdot r(r\Delta t)^{n_{adj}-1}, \tag{3.2}$$

where n_{adj} is the number of *maximum* adjacent wires (as shown in Figure 40), n_w is the total number of collection wires in the detector, r is the rate at which the radiological generates hits for a given wire, and Δt is the candidate generation window.

Equation 3.2 was derived by the author in Appendix C and validated with a Toy Monte Carlo simulation. It was determined that ^{39}Ar pileup is well-mitigated by breaking up a drift into 50μsec windows and requiring a maximum adjacency of 5 or more, at which the rate will drop to less than 30 mHz (also shown in Appendix C.4). Therefore, 50 μs was taken to be the candidate generation window for these algorithms.

3.4.1. Geometry for trigger studies

All samples generated and studied here utilize the 1x2x6 geometry, shown and described in Figure 41, in accordance with Monte Carlo Challenge (MCC) simulations. This geometry represents a subset of the central portion of the full 10kt module geometry, i.e., the row of APAs is surrounded on both sides by a full 3.6 meter drift.

---

[1] High energy triggers from beam candidates would result in a full detector readout, as would a supernova trigger, however low energy, isolated, triggers would requires a smaller readout.

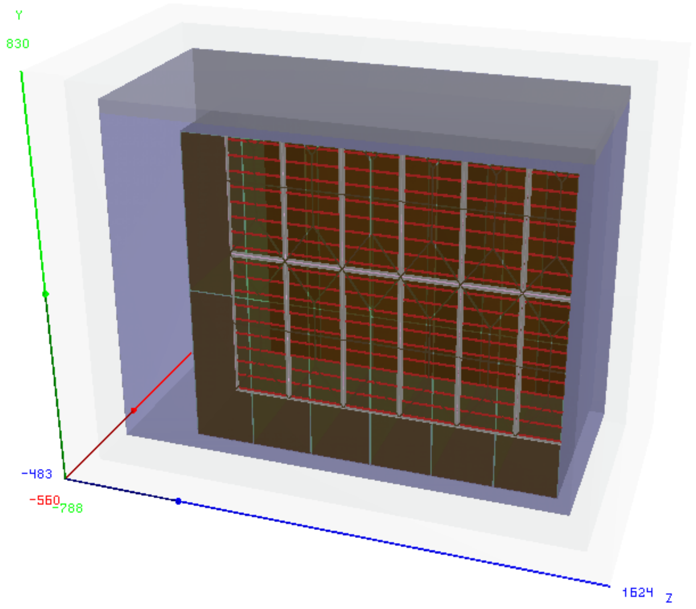

Figure 41: 1x2x6 DUNE geometry corresponding to a single row of two vertically-stacked APAs that is 6 APAs deep and centered between two CPAs.

3.4.2. Trigger thresholds from radiologicals

Table 6: Simulated Backgrounds

Background	Source/Nuclide	Content (Bq/cc)
CPA	^{40}K	2.72E-3
^{39}Ar	^{39}Ar	1.41E-3
^{85}Kr	^{85}Kr	1.60E-4
APA	^{60}Co	8.20E-5
^{222}Rn	^{222}Rn	5.58E-5
Neutron	Concrete	3.04E-5
^{210}Po	^{222}Rn	5.00E-6
^{42}Ar	^{42}Ar	1.28E-07

To determine “keep-all” thresholds which properly limit the rate near to the desired value, it is necessary to have 0 triggers in roughly 1,000,000 events in the 12 APA, 1x2x6 Geometry.

The below results were obtained by simulating 1,028,000 events with the background rates outlined in Table 6.

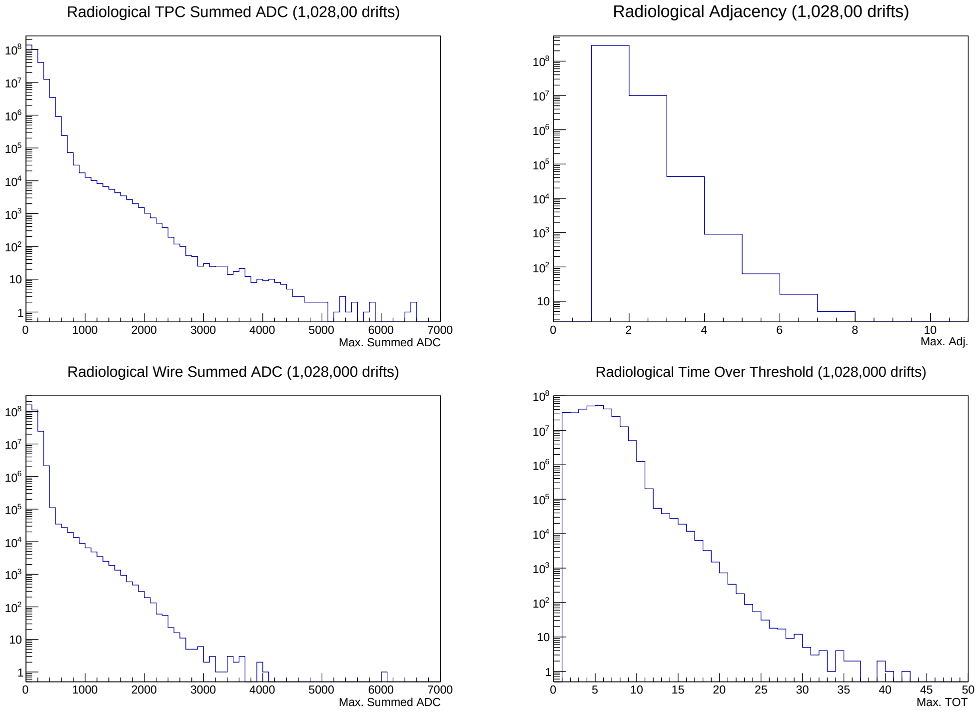

Figure 42: Radiological distributions for trigger candidate generation variables.

From these plots, it was determined that the following four thresholds would sufficiently limit the rate:

- Summed ADC $\geq$ 7000 counts
- Adjacency/Cluster Size $\geq$ 8
- Wire Summed ADC $\geq$ 6500 counts
- Time Over threshold $\geq$ 45 ticks

3.4.3. Efficiency

The definition of efficiency was defined, *a priori*, for events whose primary interaction vertex is contained within the active volume of the detector. An active volume cut on the vertex position was applied to exclude vertices extending outside of:

- $\mid x \mid > 360.0$ cm
- $\mid y \mid > 600.0$ cm
- 0 cm $< z <$ 1390.0 cm

in the 1x2x6 geometry shown in figure 41.

Beam MCC

The following shows the trigger efficiency as a function of energy for the MCC10 sample of beam events.

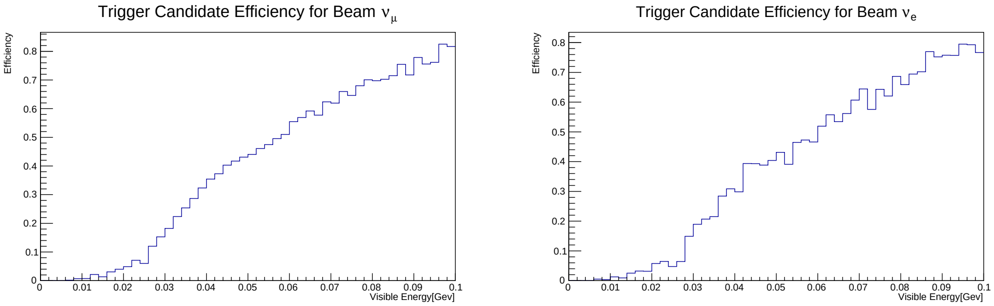

Figure 43: Left: Efficiency as a function of visible energy for un-oscillated Beam events from MCC10. Therefore, this sample is primarily ν_μ. **Right**: Differential efficiency for Beam events oscillated to ν_e from MCC10.

As can be seen from the above, the differential efficiency, i.e. the efficiency as a function of visible energy, is quite low due to the measured visible energy not necessarily being contained in the detector. Figure **??** shows the integral efficiency for the Adjacency algorithm to trigger on any given beam event.

A useful quantity when evaluating the triggering efficiency for physics that have a distribution in energy is the integral efficiency (ϵ_I), given by Equation 3.3, below.

$$\epsilon_I(E_{vis}) = \frac{\int_{E_{vis}}^{\infty} n_{trig}(E)dE}{\int_{E_{vis}}^{\infty} n_{evt}(E)dE}, \tag{3.3}$$

where $n_{trig}(E)$ is the differential trigger efficiency curve and $n_{evt}(E)$ is the number density for the physics of interest as a function of the energy. This would account for the fact that ν_μ-CC interactions in DUNE are unlikely to produce little visible energy.

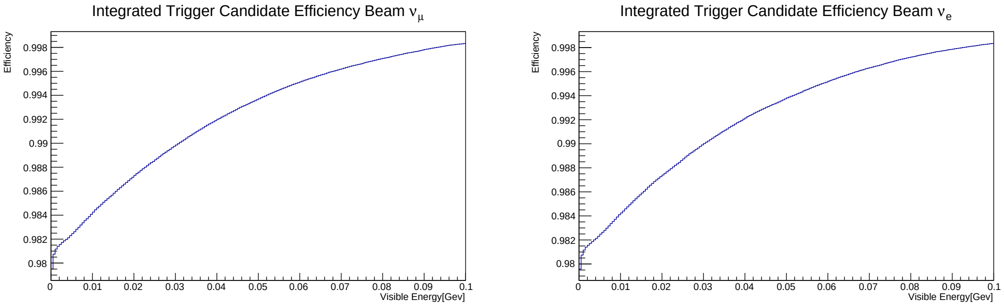

Figure 44: Integral efficiency for issuing a trigger candidate at or above the given visible energy for un-oscillated Beam events from MCC10 for the sample contain primarily of ν_μ (**Left**) and primarily ν_e (**Right**). Note that the vertical axes are zero-suppressed and begin near 0.98.

Atmospherics MCC

As shown in Figure 39, there will be a flux of atmospheric with an energy spectrum similar to that of the DUNE beam, but at a rate two orders of magnitude lower. Atmospheric neutrinos pose additional physics, therefore, DUNE has added them to their physics program.

The following figure shows the trigger efficiency as a function of visible energy for a simulated sample of atmospheric events. This particular sample uses the so-called Bartol Flux model of atmospheric neutrinos. The integral efficiency is included for the same reason as above and the efficiency axis is also zero-suppressed here.

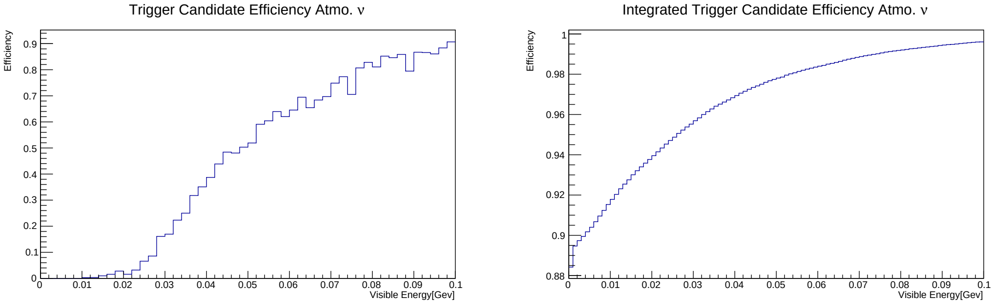

Figure 45: Differential (**Left**) and integral (**Right**) efficiency for simulated atmospheric events with Maximum Bartol Flux.

As with the beam neutrinos, the trigger efficiency is favorable for atmospheric neutrinos using the same triggering algorithm.

3.4.4. Algorithm benchmarks

To ensure that the algorithms meet the timing constraints imposed by the limited buffer capabilities under normal streaming conditions for TPC data, the process for generating the trigger candidates, after being passed hit objects from an event, was timed. Table 7 below, summarizes the average processing time for the various samples when executing the triggering algorithm on a single core process.

Table 7: Benchmark results for the Adjacency algorithm.

Sample	№ of Evt.	№ of APA	№ of APA Windows	APA Data Time	Processing Time
Beam	945,500	12	11,346,000	424.72 min	592.97 s
Atmospherics	99,800	12	1,197,000	44.83 m	16.26 s
Radiologicals	103,000	1	103,000	3.85 m	15.35 s

Given that the radiological activity will be a constant sink of the allotted processing time, we can take the reduction factor, F, for the candidate finding algorithms in the radiological sample as a baseline. This reduction factor is the ratio of APA Data Time to Processing Time i.e. F = 15.03 for the Adjacency-based algorithm.

3.5. Single-particle trigger efficiency

The triggering efficiency for physics which is of interest for DUNE can be studied in a more general way, by determining the efficiency for triggering on the various final state particles. This is especially important for understanding how well we can do at low energy physics. We expect that electrons and gammas are among the most common final state particles hence we start with those.

Sample Details:

- 1-100 MeV Kinetic Energy
- 100k events
- isotropic
- generated at the center of the drift volume corresponding to a single APA

A 1-100 MeV, isotropic, electron sample without radiological backgrounds was generated to demonstrate the trigger efficiency for events resulting in daughter electrons at the low energy range. The following results stand as a measure of the algorithms' handling of energy deposits from electrons, which inherently makes them a measure of the algorithms' handling of compact energy deposits.

The gamma sample, like the electron sample, was generated with KE ranging between 1 and 100 MeV. The efficiency curve is very similar as one would expect.

Muons are a special case because as MIPs they can cross the entire detector; however at low energies they readily decay and the Michel electrons can deposit significant energy thus making it more difficult to quantify the efficiency of triggering on them at low visible energy. A similar sample of μ^+ were produced with kinetic energy ϵ [1,100] MeV but with the decay physics disabled in GEANT4 such that these muons deposited their kinetic energy before coming to a stop in the fiducial volume.

We conclude that the 50% efficiency threshold for muons, corresponds to roughly 18 MeV.

A sample of protons was generated for completeness, given that we are unlikely to need to trigger on low energy, single protons. We expect very short, but high dQ/dx tracks and thus our best handles on protons are the summed ADC metrics (TADC, WADC).

Note that the charged pions are very similar to muons both in mass and dE/dX, thus we expect that the efficiency curve should be similar as well.

Even at 100 MeV one can see that the efficiency is still asymptotically approaching 100%, thus it is more desirable to investigate multi-dimensional cuts to improve this efficiency.

Figure 46 below overlays the four particle types under consideration.

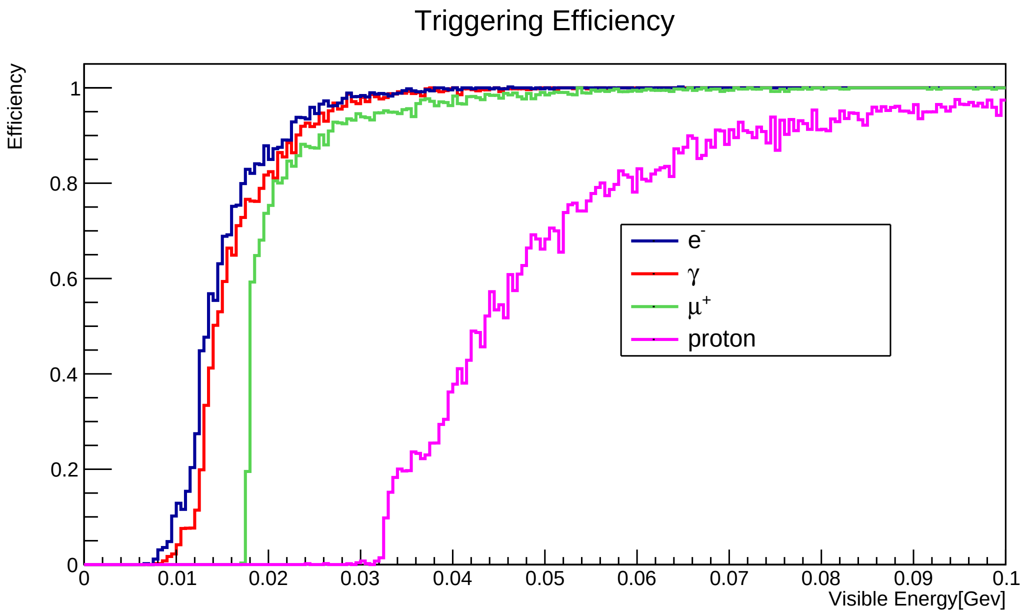

Figure 46: Single-particle trigger efficiency as a function of visible energy.

Solar neutrinos

The ν_e (CC) interaction on Argon-40:

$$^{40}Ar + \nu_e \rightarrow {}^{40}K^* + e^- \tag{3.4}$$

has a 4.4 MeV threshold in ^{40}Ar. The neutral current interactions are not considered here. ^{40}K, itself has a very long lifetime, however the interaction in Equation 3.4 can leave it in an excited state (denoted by the *) which can de-excite promptly via gamma emission. For Boron-8 energies, a burst of gammas, can look very similar to neutron captures, depending on how energy is distributed among the electron and these gammas. In order for DUNE to have a chance at studying Boron-8 solar neutrinos, it will be important to trigger on *these* gammas while rejecting backgrounds from neutron captures, which are topologically similar and have a relatively large uncertainty (see Figure 39 in expected rate, underground – at SURF. The effective neutron capture rate will depend on the sources of materials used for the concrete, the steel, and anything else located within the caverns. Currently, the rates are loosely expected to be between 1 and 100 Hz.

An additional problem is the low efficiency for triggering on low energy gammas, as shown in Figure 46 – the 50% efficiency visible energy threshold with the Keep-All cuts is ∼13 MeV.

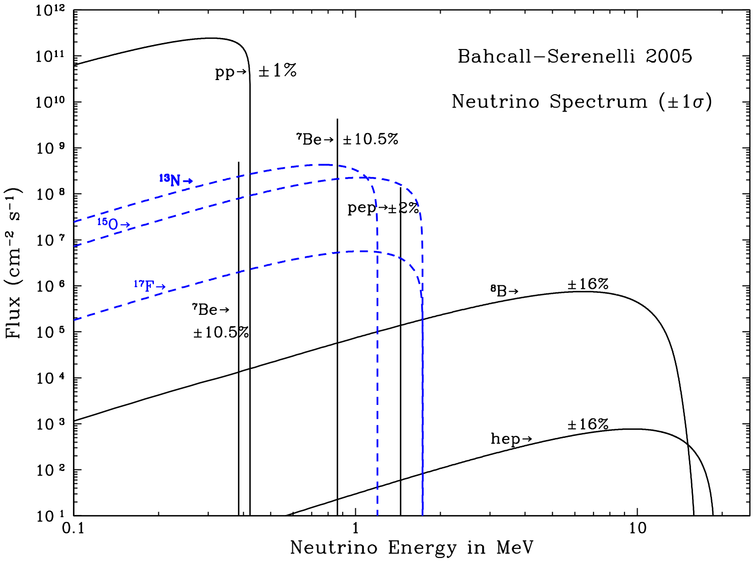

Figure 47: Solar neutrino flux as a function of energy (Bahcall et al., 1996).

The total expected number of solar neutrino interactions per day is ∼120; however, this includes low-energy Elastic Scattering (ES) interactions and includes *pp* neutrinos which are below threshold. The rate of (CC) interactions in the SNO experiment, for example, was in the order of ~3000 per year for 1kt of heavy water (Klein, 2019).

3.5.1. Low energy triggering

To address the low efficiency for low energy gammas for the Candidate finding algorithms, an additional cut was introduced by the author, to approximate the 2-D span of a candidate. The approximate 2D track length (eqn. 3.5) is calculated in wire and time space using the wire pitch of 5 mm and the nominal drift velocity in a LArTPC with a 500 V/cm drift field (1.603 mm/μs).

$$\mathcal{L} = \sqrt{(adj_{max} * 5mm)^2 + (TOT_{max} \times v_{drift})^2} \tag{3.5}$$

Note: this quantity is calculated from the maximum quantities of the APA and not per cluster. Admittedly this discriminates less on backgrounds which are more numerous than signals in DUNE than a cluster-centric approach.

The current schema for issuing a trigger candidate is to only issue a candidate if at least one of the five parameters crosses a predetermined threshold.

$$\begin{aligned} \text{trigger} = \Big(& max(\Sigma_{TPC-ADC}) >= 7000 \quad || \quad max(\Sigma_{wire-ADC}) >= 6500 \\ & || \quad max(Adjacency >= 8 \quad || \quad max(TOT) >= 45) \quad || \quad \mathcal{L} > 20.9 \Big) \end{aligned} \tag{3.6}$$

The specific thresholds for the various candidate quantities were obtained by considering the trigger rates from radiological-only samples. The maximum TOT, TPC-ADC, Wire-ADC, and Adjacency thresholds were set to reject majority of backgrounds and yielded a 20.6 mHz background rate on a large radiological sample. The efficiency for low energy physics such as solar neutrinos was similarly low with these harsher cuts.

A study comparing neutrons and 5 MeV electrons was used to optimize the $\mathcal{L}$-cut for solar neutrinos while rejecting low energy gammas from potential neutron captures. The $\mathcal{L}$-cut was maximized at a value of 24.4 mm, where the signal-to-noise ratio (ratio of triggers for 5 MeV electrons vs. thermal neutrons) was approximately 10-to-1 (31.67% / 3.19%).

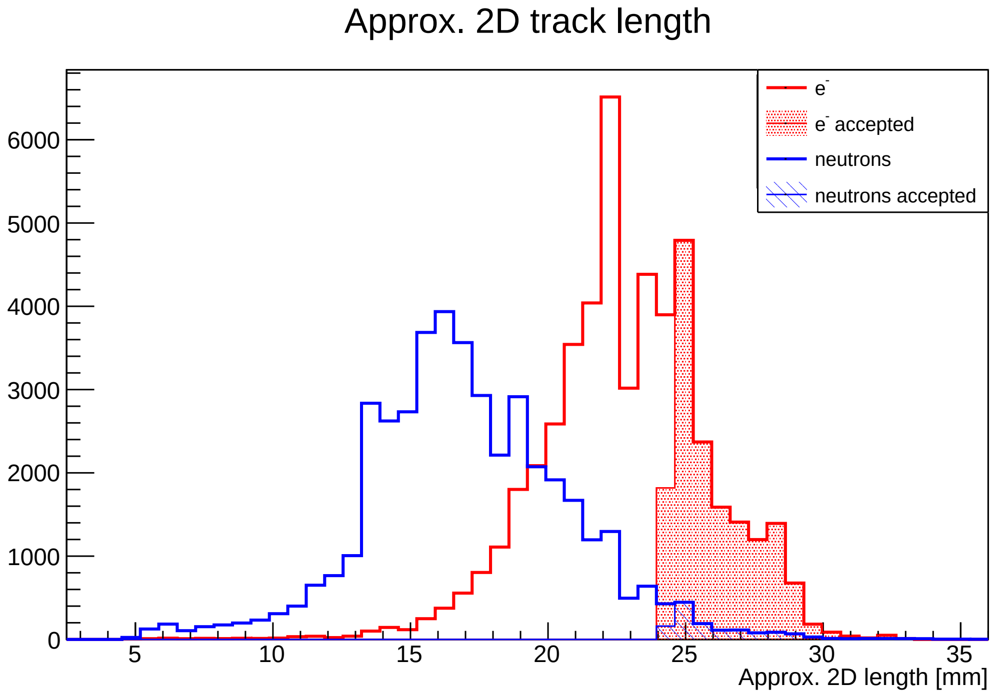

Figure 48: Comparison of $\mathcal{L}$ for 5 MeV electrons (red) and thermal neutrons (blue).

3.5.2. Solar neutrino trigger efficiency

The author simulated solar neutrinos within LArSoft, the liquid argon simulation toolkit (discussed in CHAPTER 5), and applied the triggering algorithm described above, including the approximate 2D-length cut optimized for 5 MeV electrons. The solar neutrino energy spectra from Bahcall et al. (Bahcall et al., 1996) were utilized for both Boron-8 (^{8}B) and *hep* neutrinos for these simulations. To this date, *hep* solar neutrinos have not been directly detected, making it very attractive for DUNE. The selection efficiency for Boron-8 and *he* solar neutrinos are shown in figures 49, 50, below.

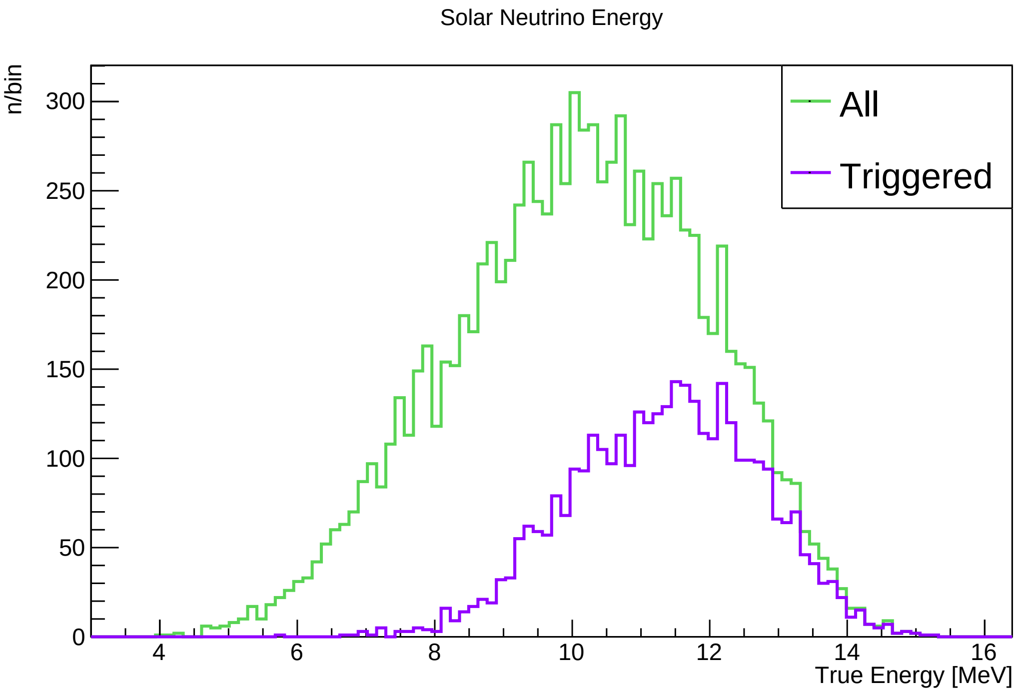

Figure 49: Triggered true Boron-8 solar neutrino energies for $\mathcal{L}$-cut of 24.4 mm. The selection efficiency for this sample is 35.3%.

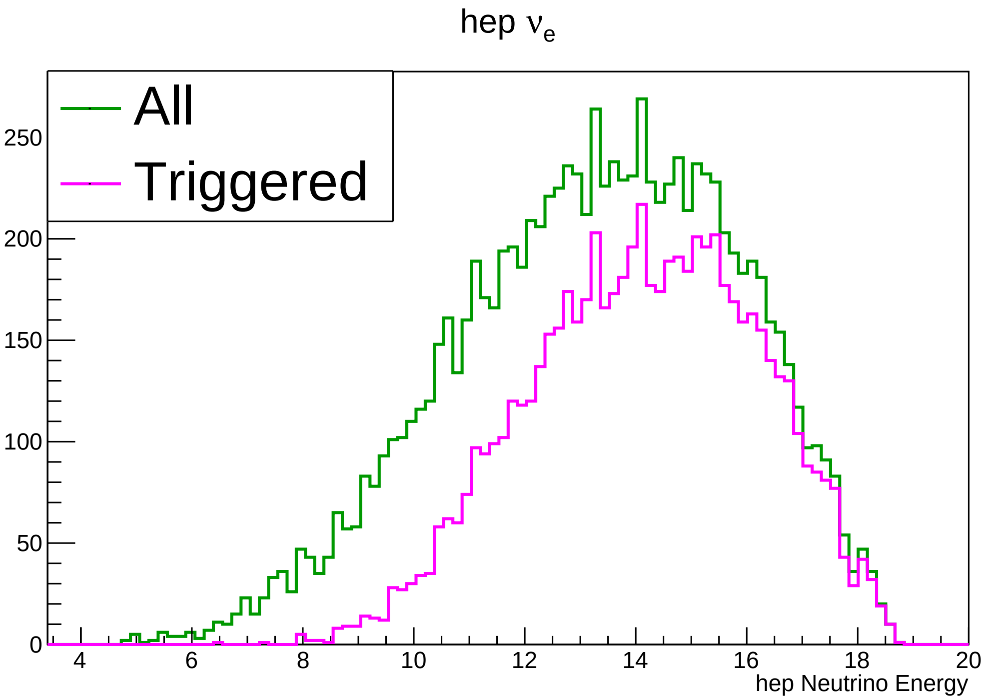

Figure 50: Triggered true solar *hep* neutrino energies for $\mathcal{L}$-cut of 24.4 mm. The selection efficiency for this sample is 67.9%.

The approximate 2D-length trigger condition was found to be beneficial for the selection of low energy physics such as solar ν-CC.

For a neutron-driven background shown in Figure 51, a rate of 100 Hz of neutron captures is assumed, thus, if the neutron rate at the Far Detector is lower, the cut on $\mathcal{L}$ can be reduced. The threshold for $\mathcal{L}$ was selected based on the tolerance for background trigger rates (shown in figure 51).

For low energy candidates, there is no need to write an entire 10 kt module's worth of data to disk – instead, a single APA's worth of data can be written, making a background trigger rate of 10 Hz/10 kt module, tolerable. In this case, the $\mathcal{L} > 20.9$ mm results in a 10Hz background trigger rate.

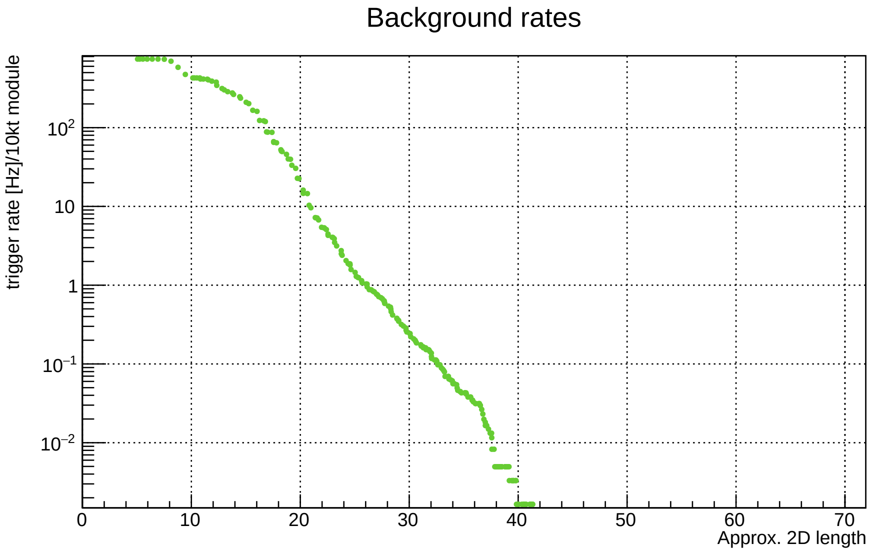

Figure 51: Background trigger rates.

The differential efficiency curves for Boron-8 and *hep* solar neutrinos with the trigger definition in 3.6 and a $\mathcal{L}$-cut of 20.9 mm, are shown below.

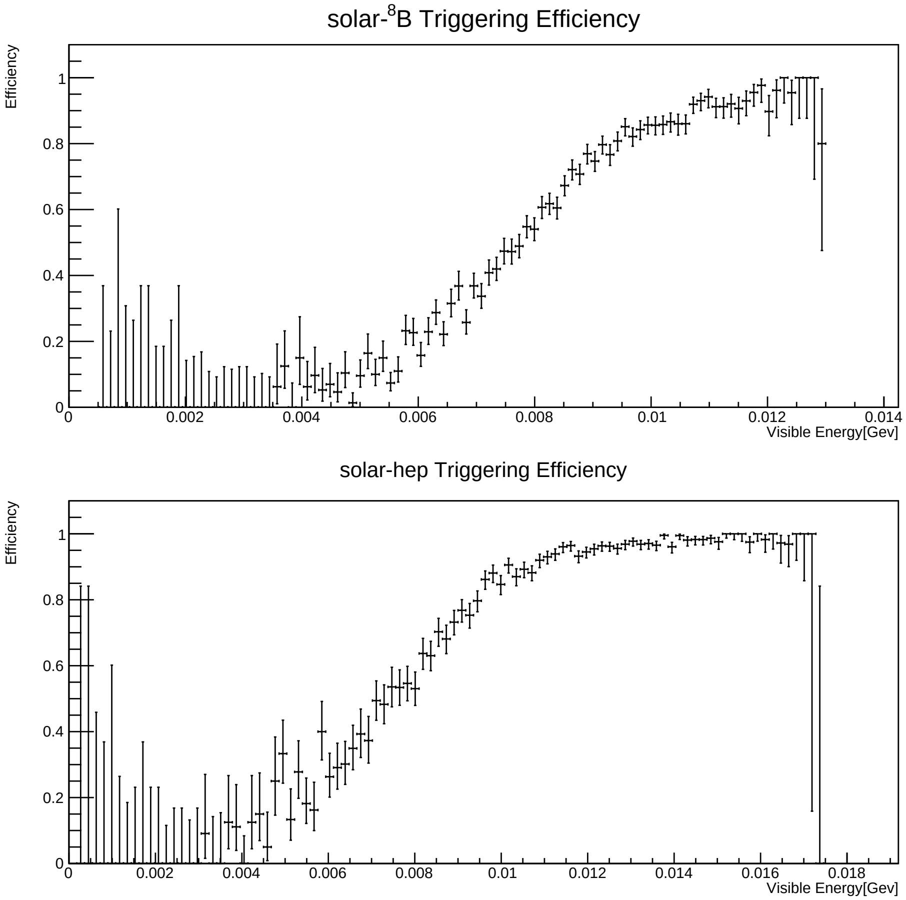

Figure 52: Solar neutrino differential triggering efficiency.

This would be a more ideal solar neutrino trigger, however, the neutron capture rate in the Far Detector cavern will, most likely, determine how low a threshold DUNE can afford.

CHAPTER 4 : NEUTRON INTERACTIONS IN LAR

The DUNE, neutrino energy spectrum is wideband (100 MeV - 10 GeV), which is significant, because the oscillation probabilities are energy-dependent (Equation 1.39). The neutrino energy will not be known *a priori* and must therefore be reconstructed from the data.

The choice of liquid Argon as a target is advantageous for many reasons, including prompt scintillation light for t_0 tagging; however, it is not great for neutron containment. Neutrons can transport energy away from the vertex and can sometimes exit the active volume undetected. Undetected neutrons can be problematic because they lead to inaccurate reconstruction – both in energy and event topology. Additionally, they displace energy from the interaction vertex and can deposit this elsewhere, sometimes making it difficult to discern from backgrounds.If these neutrons are properly accounted for, the hadronic energy resolution will be degraded[1].

The ability to make an accurate measurement, in a long-baseline experiment such as DUNE, is limited by the energy uncertainty on these neutrinos. Neglecting the neutron energies could result in a large smearing of the neutrino energy, as shown in (Friedland and Li, 2018), which would undoubtedly smear the measured oscillation parameters, as shown in Figure 1. Additionally, the hadrons from primary neutrino interactions can, themselves, eject neutrons from the argon atoms resulting in multi-component smearing of *their* energies as illustrated in Figure 53.

---

[1] If bad enough, one may have to resort to placing stringent visible energy threshold or interaction topology cuts to compensate for the uncertainty of the hadronic component.

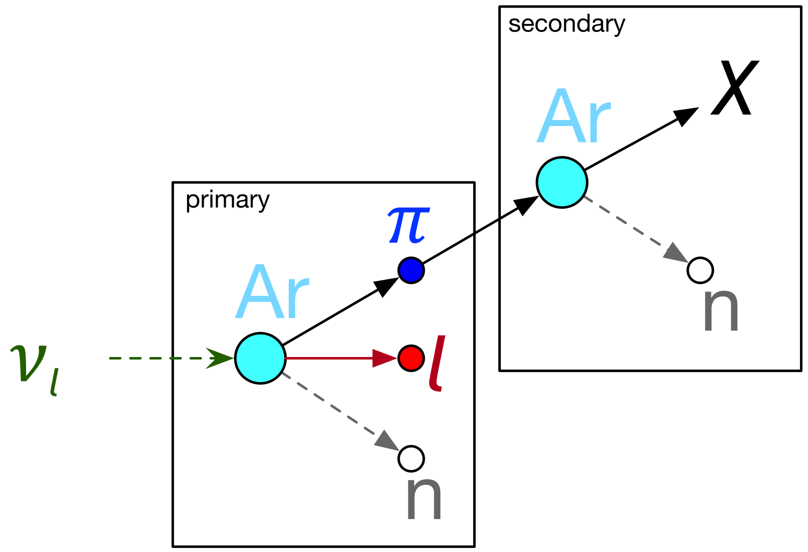

Figure 53: Example neutrino interaction showcasing the primary and secondary hadronic components.

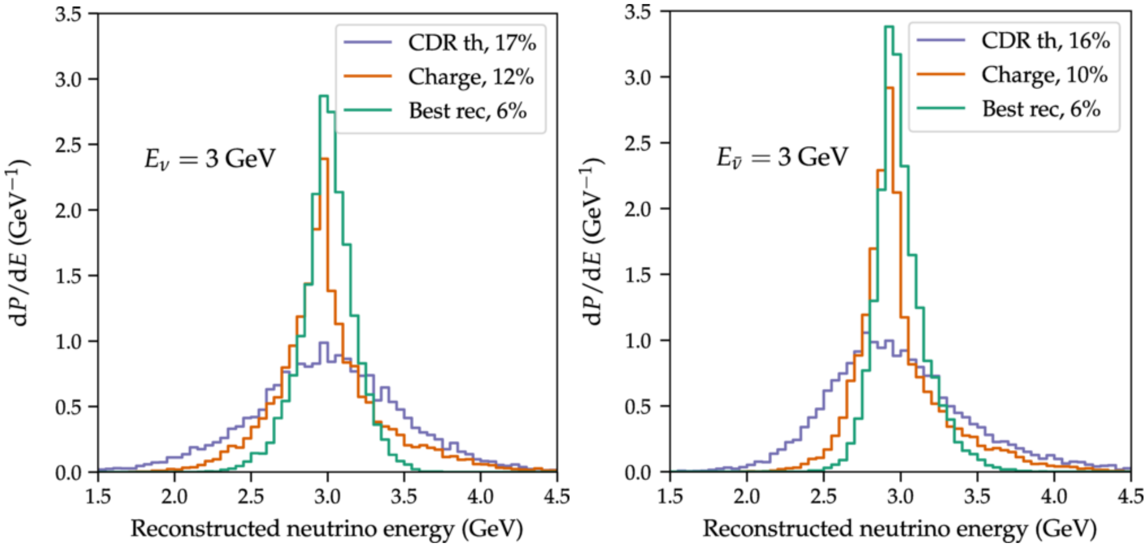

Figure 54: Reconstructed neutrino (**Left**) and anti-neutrinos (**Right**) energies with (green) inclusion of low energy EM activity from neutrons, no inclusion – charge only (orange), and with reconstruction from the original DUNE Conceptual Design Report (magenta). Figures from (Friedland and Li, 2018).

Second (and higher) order component(s) of neutrons come from the interaction of primary-component hadrons in the liquid argon to produce/eject neutrons. These two sources can be confused and can also lead to inaccurate event topology The hadronic energy resolution can be improved by understanding the detector response to neutrons.

Another long-baseline neutrino oscillation experiment, NOvA, reports a ±14% hadronic energy scale uncertainty – the largest in their reconstruction (Adamson et al., 2016), which, if nothing else, confirms that that this is a real concern for neutrino oscillation experiments.

To pin down the energy uncertainty in the hadronic component of neutrino interactions the detector response for each species of charged particle produced in the primary neutrino interaction should be studied. ProtoDUNE-SP Abi et al. (2017) is well-suited for this study because the charged particle test-beam was designed to do charge and momentum selection and was instrumented to provide additional handles on particle ID, as described in Section 3.3.

4.0.1. Neutrino interactions

Neutrino interactions are diverse and for DUNE energies, there will be contributions from: Quasi-Elastic scattering (QE), Resonance production (RES), and Deep Inelastic Scattering (DIS). The cross sections for these processes, per nucleon in the target material, are shown in Figure 55 below.

Resonance production refers to the process by higher mass excited states of the nucleons (n/p) can be produced. These so-called resonance states decay quickly via the strong force into nucleons and mesons. An example is the resonance Δ^+ (1.232 GeV/c^2) production, which decays to π^+ n or π^0 p, with a mean lifetime of order 10^{-24} s. Note that the (anti)neutrino cross section peaks at around 2 GeV, and will common at DUNE energies.

DIS dominates in the higher energy regime, where the neutrino wavelength is short enough to to probe the quark structure of the nucleons, hence the name Deep Inelastic Scattering. Naturally, at higher energies, DIS interactions can result in hadronic showers.

There are a variety of interactions that can contribute to final state neutrons in (anti)neutrino interactions. This includes neutrons from resonance production (left), and $\bar{\nu}$ CC Quasi-

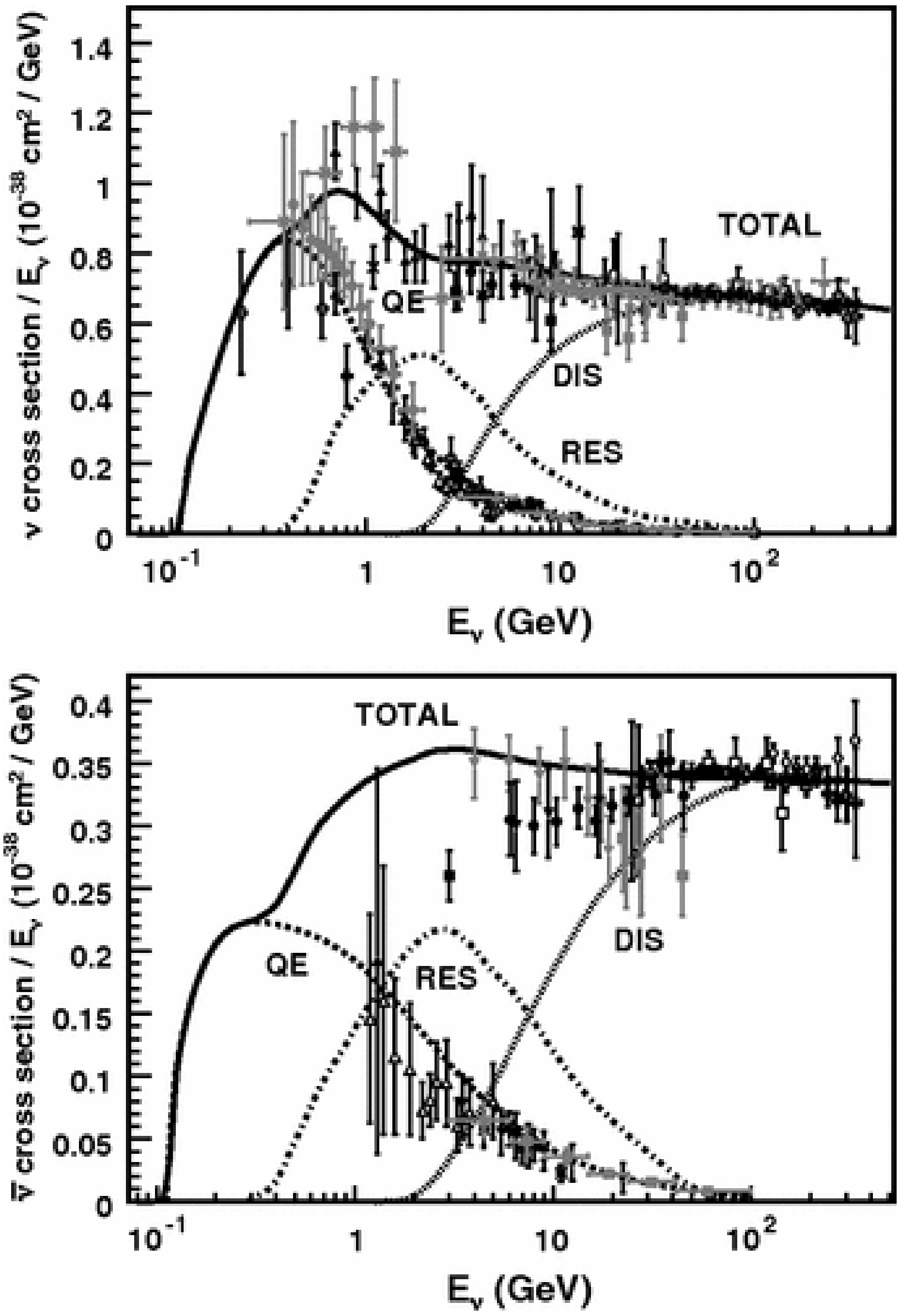

Figure 55: Neutrino cross sections per nucleon in the energy range of 100 MeV-500 GeV. Reprinted figures with permission from (Formaggio and Zeller, 2012) Copyright (2021) by the American Physical Society.

Elastic scattering (right). Figure 56, below, is a zoom of the interactions. At DUNE energies, resonance production will be prominent. Δ baryon production, for example, will result in neutron and pions in the neutrino final states.

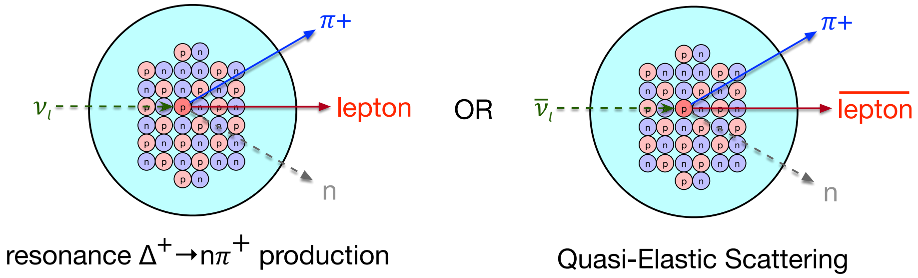

Figure 56: Left: neutrino resonance Δ^+ production. **Right**: anti-neutrino quasi-elastic CC scattering.

Failing to tag and associate the neutrons to the reaction the reaction in Figure 56 (Left), could result in a neutrino resonance production event to appear like a quasi-elastic, 1π interaction instead.

4.1. Neutron simulations

The liquid argon simulation software, LArSoft, was used for all studies reported in this dissertation and will be described in more detail in CHAPTER 5.

For now, it is necessary to mention that LArSoft adopts the use of GEANT4 (Agostinelli et al., 2003) as the simulation engine for particle propagation in LArTPCs. The version of GEANT4 used for these studies is v4.10.6 patch 1.

4.1.1. GEANT4 physics lists

Some terminology must be defined in order to be as clear a possible about how the GEANT4 simulation feeds into the analysis presented here. A physics list defines the set of "physics" processes that are simulated – examples of these include: Hadronic, EM, Decay, and Optical. The physics list must *register* each type of physics that will be included.

Each physics, in turn, is responsible for defining several key components, such as the particles, their properties and their available interactions. There are several wrapper classes that make it easy for different physics lists to override the same generic functions with their specific implementations (e.g., the G4NeutronInelasticProcess class).

The physics define the particles, the processes, and the cross sections sampled for the simulation. There are several physics lists that are maintained and updated by the GEANT4 collaboration (e.g. QGSP_BERT), but one can choose to build a physics list using the different models and cross section tables available in GEANT4. For historical reasons, the physics list is based on **QGSP_BERT**. QGSP_BERT includes hadronic, standard EM, decay, stopping, and ion physics definitions For clarity, the author will use the hadronic physics for neutrons as an example. The processes defined for the hadronic (and any other) physics fall into the categories of *AtRest*, *AlongStep*, or *PostStep*. The available process include the Elastic, Inelastic, Capture, and Fission **processes**[1]. Each process must also define a cross section table , which used during particle propagation, by the Monte Carlo method, to determine if and when a particular interaction occurs. The physics must also define a model that describes how the particle-medium system changes when the process occurs. Each model must be accompanied by an energy range where it is applicable for each particle, as well.

Elastic scattering is modeled by the CHiral Invariant Phase Space (CHIPS) model, while for inelastic scattering, there is no single model. Instead, a combination of overlapping models, as shown in Figure 57, is defined and used. The overlapping regions must still preserve probability, therefore the overlap is represented as complementary probability distribution functions of energy.

---

[1] Additional processes will be defined by the additional physics registered by the list e.g., neutron decay is defined within the Decay physics.

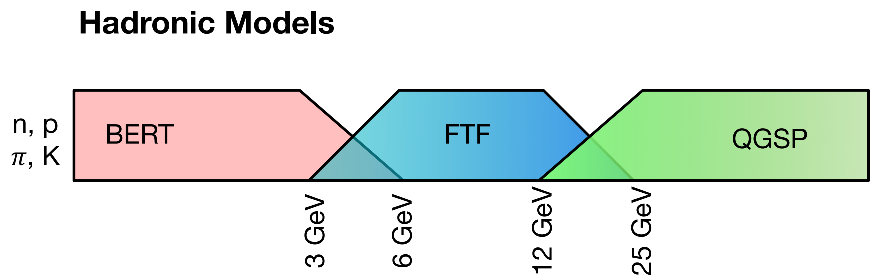

Figure 57: QGSP_BERT hadron-inelastic models.

The set of hadronic interactions for neutrons, along with the corresponding information for the interactions is defined in Table 8, below.

Table 8: Neutron Hadronic Processes.

Object	Name	Energy Range
Process	hadElastic	
Model	hElasticCHIPS	19.5 MeV → 100 TeV
Model	NeutronHPElastic	0 eV → 20 MeV
Cross sections	NeutronHPElasticXS	0 eV → 20 MeV
Cross sections	G4NeutronElasticXS	0 eV → 100 TeV
Process	neutronInelastic	
Model	QGSP	12 GeV → 100 TeV
Model	FTFP	9.5 GeV → 25 GeV
Model	BertiniCascade	19.9 MeV → 9.9 GeV
Model	NeutronHPInelastic	0 eV → 20 MeV
Cross sections	NeutronHPInelasticXS	0 eV → 20 MeV
Cross sections	BarashenkovGlauberGribov	0 eV → 100 TeV
Process	nCapture	
Model	NeutronHPCapture	0 eV → 20 MeV
Model	nRadCapture	19.9 MeV → 100 TeV
Cross sections	NeutronHPCaptureXS	0 eV → 20 MeV
Cross sections	G4NeutronCaptureXS	0 eV → 100 TeV
Cross sections	NeutronHPCaptureXS	0 eV → 20 MeV
Cross sections	G4NeutronCaptureXS	0 eV → 100 TeV
Process	nFission	
Model	NeutronHPFission	0 eV → 20 MeV
Model	G4LFission	19.9 MeV → 2.88022e+295 J
Cross sections	NeutronHPFissionXS	0 eV → 20 MeV
Cross sections	GheishaFissionXS	0 eV → 100 TeV

For the study detailed here (p = 1GeV/c), pions and the resulting particles will have energies below the 3GeV range and thus the Bertini Cascade is the most relevant model for the hadron-inelastic interactions of interest.

4.1.2. The Bertini Cascade

The Bertini Cascade model applies to inelastic collisions of neutrons, proton, pions, and kaons and is a model of how these interact with a target nucleus. The nucleus is treated as a Fermi gas of nucleons with a shell-like structure whose size depends on the atom – Argon is considered a medium sized nucleus and has three "shells". As the projectile is transported through the gas, it has a chance reflecting off the shell boundaries or being transmitted, and if its energy is not sufficient to overcome the potential barriers posed by the shells, the projectile may be trapped within the nucleus. The details of how this intra-nuclear cascade model is implemented in GEANT4 can be found in reference (Wright et al., 2015).

The nature of the interactions is determined by the projectile momentum (p). The wavelength for a massive particle, i.e. the de Broglie wavelength, is given by:

$$\lambda_{dB} = \frac{h}{p}, \tag{4.1}$$

where h is Planck's constant (4.136×10^{-15} eV$\cdot$ s).

A projectile particle with a long λ_{dB}, interacts with the Fermi gas, as a whole. If the momentum is large enough, then λ_{dB} is short compared to the inter-nucleon spacing, and the projectile can interact with individual nucleons in the current shell. Energetic collisions can result in secondary production of particles and holes within the nuclear medium. The secondaries from the primary bullet particle are propagated until they are either trapped, they generate additional (tertiary) cascader particles, or they exit the outer shell – this proceeds until the cascade (if any) is brought to completion. The absorbed particles can result in excited nuclear states, and if these particles are not stable they are decayed.

Compound particles such as αs can be formed for the outputs of the cascade or the final de-excitation stages of the nucleus. The nucleus is finally returned to a ground state through the emission of particles (e.g. neutrons), nuclear fragments, gamma rays, or a combination of these.

Within the Bertini Cascade model, outgoing neutrons are copiously produced in pion interactions with LAr via :

- elastic collisions
- inelastic collisions
- unstable particle decays
- intra-nuclear cascade processes
- evaporative processes
- nuclear de-excitation

An example, intra-nuclear cascade interaction is shown in Figure 58.

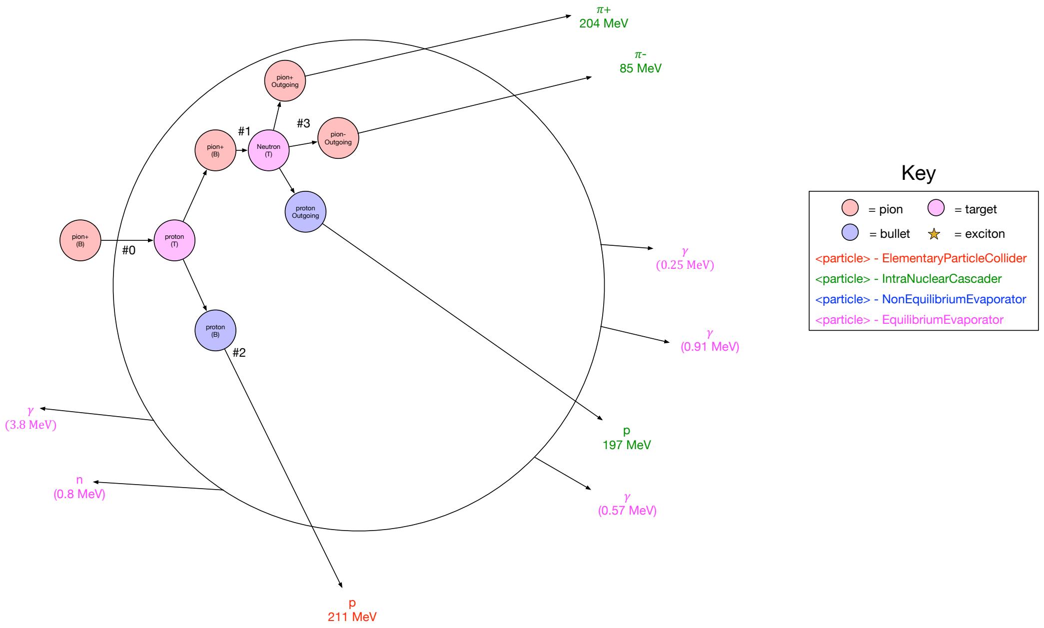

Figure 58: Bertini Cascade example interaction for a 1 GeV/c π^+ simulated ProtoDUNE-SP event. The event depicts a pion that ejects a 211 MeV proton, and then cascades into a 197 MeV proton, a π^+, and π^-. The remnant nucleus then de-excites via four evaporative gammas and a neutron.

4.1.3. GEANT4 neutron cross section tables

The cross section table defined for the neutron inelastic process in the physics list utilized for this analysis is the default for the QGSP_BERT_HP reference physics list in GEANT4, i.e., the Barashenkov-Glauber-Gribov model, which applies between 20 MeV and 100 TeV. Below 20 MeV, the G4NeutronHP model utilizes the G4ENDL 4.6 cross section tables, however, this analysis is effectively limited to neutrons with KE>30 MeV – through the track reconstruction (section 7.3).

The Barashenkov parametrization (Equation 4.2) for the neutron cross section with nuclei is used between 20 MeV and 91 GeV, and the Glauber-Gribov parametrization above this range.

$$\sigma_{\text{inelastic}}(T,A) = 44 \cdot A^{0.69}\{1 + 3.9\times10^{-2}\cdot A^{-2/3}[\bar{\sigma}(T)-33] - 9\times10^{-4}\cdot A^{-1/3}[\bar{\sigma}(T)-33]^2\}\text{mb}, \quad (4.2)$$

where A is the atomic number and $\bar{\sigma}$ is a function of the kinetic energy (T) which is close to the N-N or π-N cross section (see (Barashenkov et al., 1969) for more details).

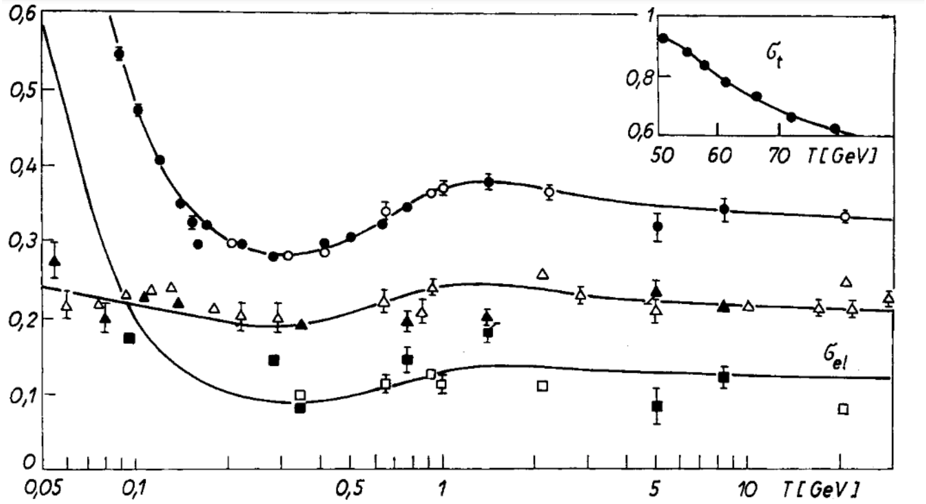

Fig. 4. Cross sections for interaction of nucleons with C^{12}. (in units 10^{-24} cm^2).
The signs ○, ▽, □ denote the experimental cross sections σ_t, σ_{in}, σ_{el} for protons, the shaded signs are the corresponding experimental cross sections for neutrons.
The curves are plotted by the optical model for the parameters which are in best agreement with the available experimental data

Figure 59: Barashenkov fit to Carbon-12 data for both protons and neutrons (solid points). Original figure from (Barashenkov et al., 1969).

The focus of the analysis will be on neutrons produced by the interactions of 1 GeV π^+, therefore, it will suffice to look at the cross section and interaction lengths for neutrons up to 1 GeV. The parametrized, neutron cross section sampled by GEANT4 is shown in Figure 60, below.

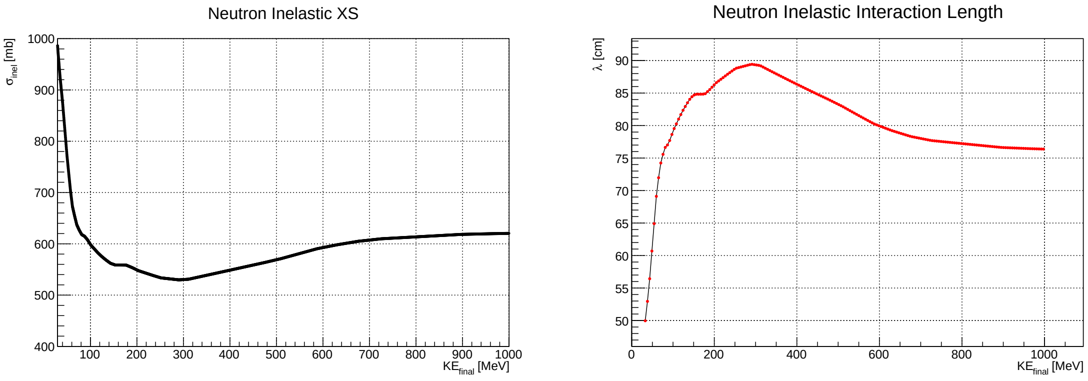

Figure 60: Left: The neutron inelastic cross section from GEANT4 in the range of 30 MeV-1 GeV. **Right**: The corresponding neutron interaction length for the range of 30 MeV-1 GeV.

4.2. Neutron detection in LAr

Neutron interactions in liquid argon are diverse, therefore, it is often helpful to categorize them by energy. For the energies of interest in this analysis the following energy ranges are the *natural* kinetic energy ranges for the analysis in this dissertation:

1. **Low** : < 20 MeV
2. **Medium** : 20 MeV $<$ KE $<$ 80 MeV
3. **High** : > 80 MeV

Neutrons indirectly produce charge and light via scattering and captures. In the low energy range, neutrons lose energy, and eventually reach thermal equilibrium through elastic and inelastic collisions with argon atoms that result in the emission of de-excitation gammas. Neutrons thermalize on a timescale of 100 μs and promptly capture. Capture/de-excitation gammas can undergo electromagnetic processes such as pair-production (e^+e^-) and Compton scattering of electrons, which then produce low energy clusters of ionization charge. In these cases we have interactions of the form (n$\rightarrow \gamma \rightarrow$ e$^{\pm}$). Low energy elastic/inelastic scattering can also result in the ejection of nucleons (n, p). Protons lose energy more quickly than electrons, therefore they often produce short stubs of ionization.

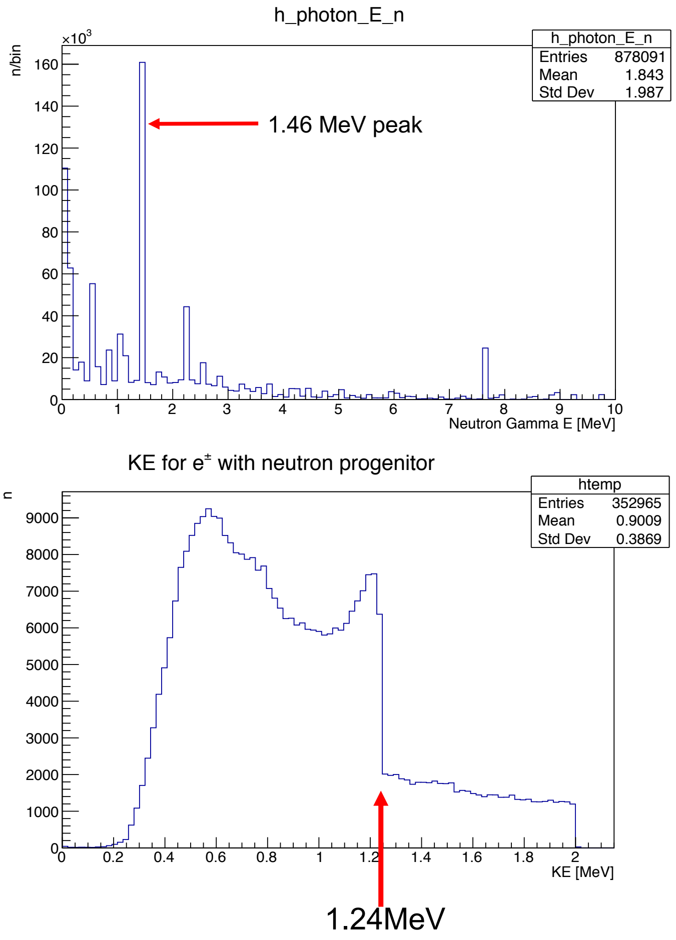

Figure 61: Top: Low energy gammas from neutrons. **Bottom:** KE for e$^\pm$ from EM processes of neutron-generated gammas. A 1.24 MeV Compton edge can be observed and is largely due to Compton scattering of the 1.46 MeV line, above.

At the high energy range, neutron inelastic scattering leads to ejection of protons or other charged particles which are energetic enough to produce tracks.

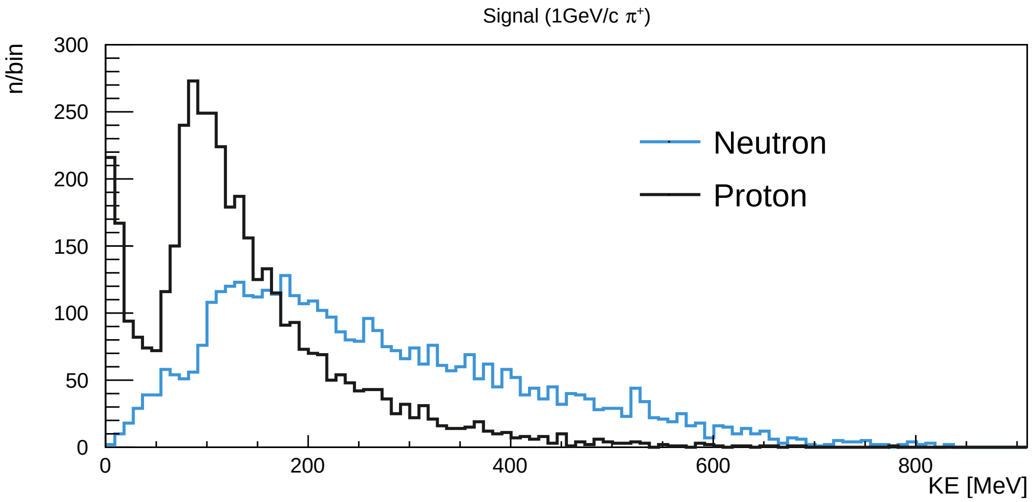

Figure 62: KE spectra for neutrons and their proton "descendants", produced through neutron inelastic scattering.

In the medium energy range, both de-excitation gammas and proton tracks are present. A simulated ProtoDUNE-SP, 1 GeV, π^+ event containing neutrons from all three ranges is depicted in Figure 63.

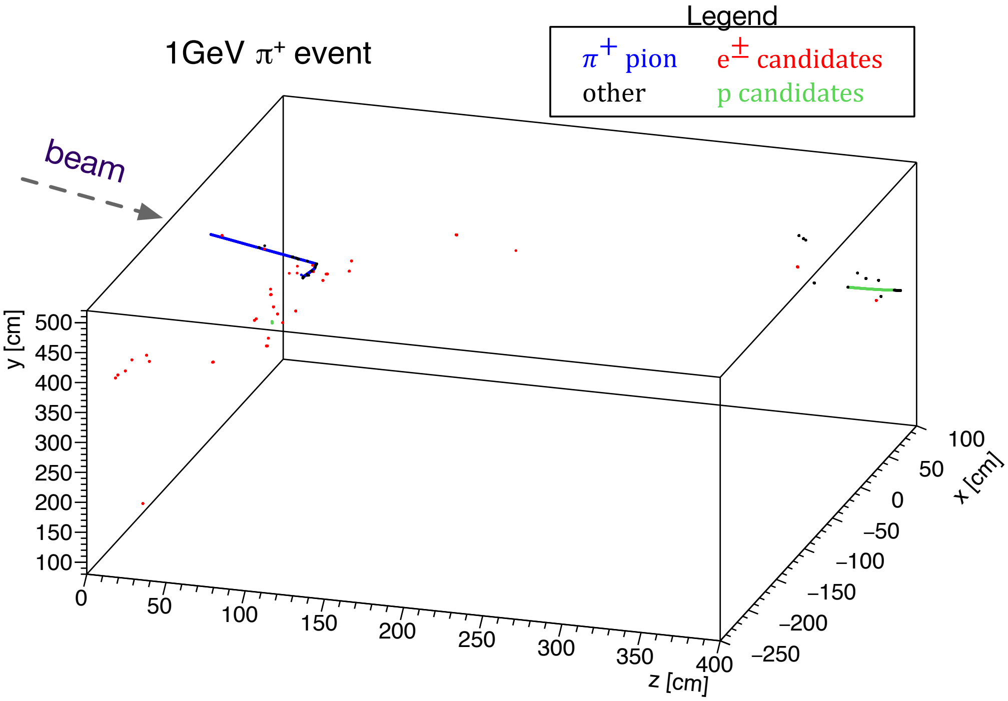

Figure 63: Neutron inelastic scatter resulting in a long proton track (green) meters away. Neutron capture and de-excitation gammas resulting in low energy deposits from Compton-scattered electrons are shown in red.

4.3. Previous experiments

Past LArTPC-based experiments have detected neutron interactions both at low and high energies.

4.3.1. ArgoNeuT

ArgoNeuT is a small (47 cm x 40 cm x 90 cm) detector designed to study neutrino and anti-neutrino cross sections in the energy range of 0.1-10 GeV. It was located 100 m underground in the Neutrinos at the Main Injector (NuMI) beamline at Fermilab and was in operation for a period of roughly six months, beginning in September 2009.

The ArgoNeuT data was also utilized to perform a detailed, low-energy (LE) analysis. The collaboration published their results in 2018 (Acciarri et al., 2018) demonstrating their ability to reconstruct LE gammas. The cluster summed energies and displacements from the neutrino vertex are shown in figure 64 below.

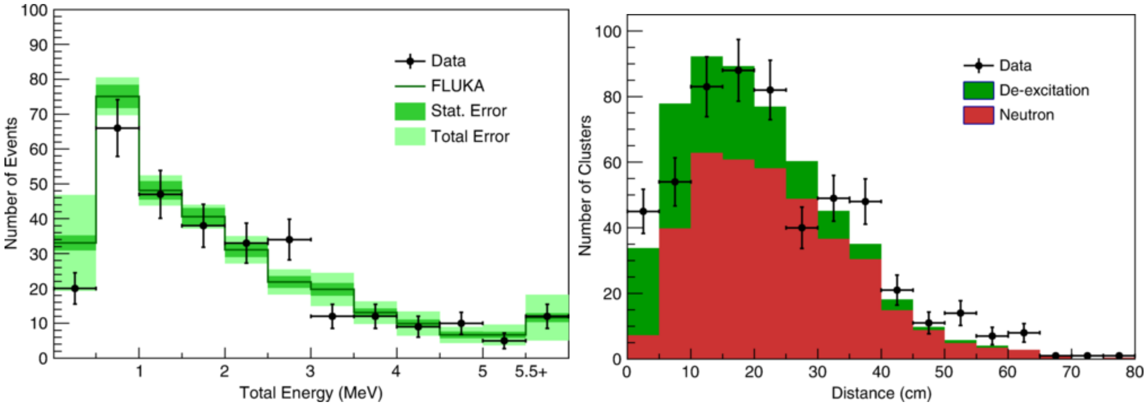

Figure 64: Left: Energy spectrum for reconstructed LE clusters. **Right:** Displacement for LE clusters. Figures from (Acciarri et al., 2018).

ArgoNeuT used FLUKA (Ferrari et al., 2006) to simulate the neutrino final state interactions, propagate neutrons in liquid argon, and to generate any de-excitation gammas from neutron inelastic collisions. The resulting charged particles and photon initial states served as inputs to the standard LArSoft simulation, which uses GEANT4 to generate the resulting energy deposits.

Gammas from nuclear de-excitation of the primary neutrino target and those from neutrons shared various characteristics such as reconstructed energy and thus ArgoNeuT does not distinguish them – rather, they fit their LE cluster candidates as distributions.

The source of these gammas was consistent with FLUKA simulations of nuclear de-excitation from neutron-argon interactions of the neutrino's target nucleus and by inelastic scattering of primary neutrons produced by neutrino-argon interactions.

4.3.2. MiniCAPTAIN

CAPTAIN is the Cryogenic Apparatus for Precision Tests of Argon Interactions with Neutrinos. MiniCAPTAIN is a detector designed to measure the neutron-Argon cross section in a monochromatic, neutron beam with kinetic energy between 100 and 900 MeV, i.e., the medium-to-high neutron energy regime. This was achieved by placing the detector within the Los Alamos Neutron Science CEnter (LANSCE) neutron beamline.

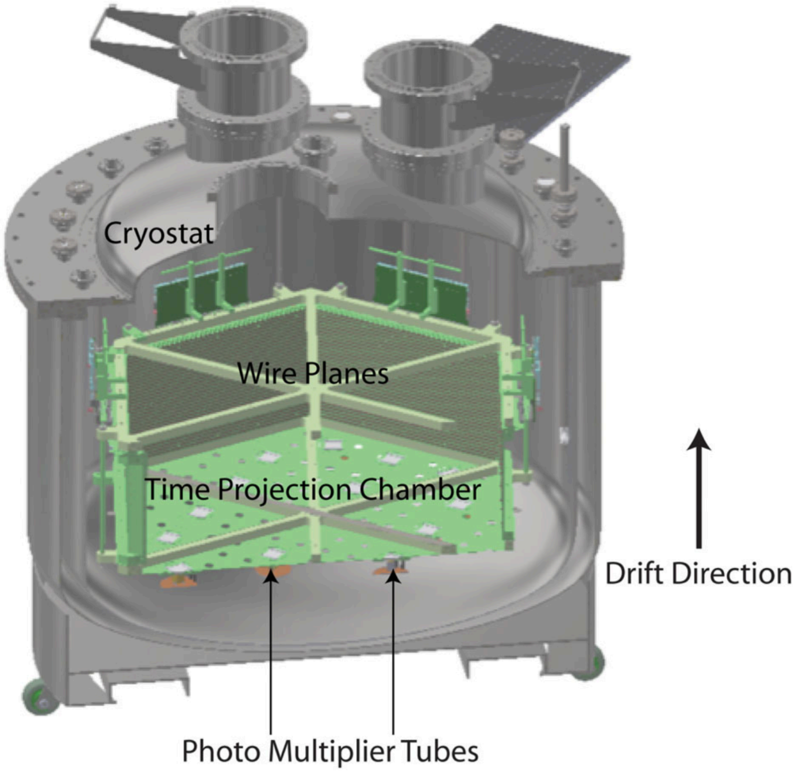

Figure 65: MiniCAPTAIN cryostat. Figure from (Bhandari et al., 2019).

The cryostat contains 400 kg, or 286 L, of active liquid Argon and was contained in a steel cryostat with a 32 cm vertical drift. It was also instrumented with 24 cryogenic PMTs: 16 mounted on the base and eight on the top to participate in the trigger decision.

Measurement The measurement was performed by looking for neutron inelastic collision candidate tracks. The neutron flux was controlled via the use of a shutter and constrained to roughly one neutron per spill to avoid pileup in the detector. Neutrons were identified via their inelastic collisions.

The interaction length, as a function of the cross section, is given by eqn. 4.3.

$$\lambda = \frac{1}{V\sigma_T}, \quad V = \frac{\rho_{LAr} N_A}{m_{Ar}}, \tag{4.3}$$

where ρ_{LAr} is the density of liquid argon (1.4 g/cm^3), N_A is Avogrado's number (6.022×10^{23} mol^{-1}), and m$_{Ar}$ is the molar mass of Argon (39.948 g/mol).

In a classical measurement of the cross section with a monochromatic neutron beam, the neutron extinction in a material, is defined as $1-T$ where T is the transmission. The beam extinction is a direct handle to the cross section.

$$dn_{\text{beam}}/ds = -V n_{\text{beam}} \sigma_T \tag{4.4}$$

$$n_{\text{beam}}(s) = n_0 e^{-V\sigma_T s} = n_0 e^{-s/\lambda} \tag{4.5}$$

The measurement was based on the beam extinction as a function of the proton candidate displacement in the beam direction.

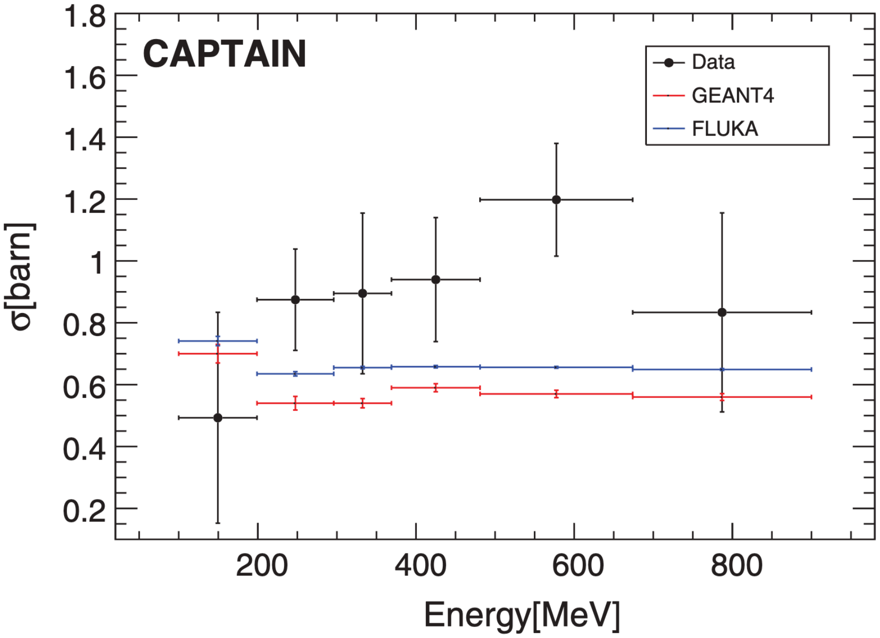

Figure 66: Neutron cross section measurement by the CAPTAIN collaboration between 100 and 800 MeV. Figure from (Bhandari et al., 2019).

CHAPTER 5 : SIMULATIONS

This chapter covers the ProtoDUNE-SP simulation as it pertains to the neutron cross section study and other relevant/guiding assumptions necessary to yield results. A brief introduction to LArSoft is provided here, but may be skipped in the interest of time, as it is very specific to the experiments that use this toolkit. Something that may be noted is the author's contribution to refactoring the simulation, which was a team effort, and that has yielded improved MC-Data agreement for various studies including the neutron analysis and has additional flexibility, particularly for choosing the physics list and allowing the ability to choose between different modules to perform detector simulations.

5.1. Introduction

Simulations and reconstruction for ProtoDUNE-SP rely on LArSoft which is a toolkit in the form of algorithms for LArTPC experiments (Knoepfel, 2020), primarily those based at Fermilab (ProtoDUNE-SP being the exception) and that adhere to a few criteria[1].

It serves as a base collection of code that is experiment-agnostic. The backbone of LArSoft is the *art* framework (Green et al., 2012) developed and maintained by the Scientific Computing Division at Fermilab to process events and interface with ROOT (Antcheva et al., 2011), an object-oriented, C++ framework for particle physics analysis. The input and output of LArSoft are art-ROOT formatted files.

The detector structure is stored in a geometry definition file (gdml) which is parsed by both GEANT4 and ROOT during the simulation. Within the gdml file there are sections for material definitions, the physical volumes they occupy, and declarations of the volumes that are sensitive to physics (LAr active volume, photodetectors, and scintillation counters).

---

[1] must have wire readout, and the active volume must be rectangular

5.1.1. Refactoring

LArSoft is not immune to the problems that afflict many toolkits written by physicists – it is constantly being improved and cleaned up[1]. Although GEANT4 can handle optical simulations, doing ray-tracing for all scintillation photons is not feasible without the use of GPUs and software such as Chroma (Land) or Opticks (Blyth, 2019). This was an issue since the inception of LArSoft, and the best way to handle scintillation light, at the time, was to use semi-analytic methods to produce optical hits in the photodetectors that are commonly incorporated in LArTPC detectors. To further reduce complications posed by the thousands of wires in most LArTPC designs, the optical photons are "propagated" in a separate geometry, and the physics for the scintillation process is defined in a GEANT4 parallel world.

This presented a departure from the use of one of the GEANT4 reference physics lists. At the time the decision to proceed with a parallel simulation of optical photons was made, the physics list was frozen at version of the QGSP_BERT physics list that is now a couple of decades old. The solution was not very elegant, or flexible – physics simulations were mixed with detector response (e.g., particle propagation and the optical hit determination were done in the same step, preventing changes to the optical model without re-running both).

The interface between *art* and GEANT4 was re-written by H. Wenzel (Fermilab) in 2016 for use with the g-2 experiment, and was first integrated with LArSoft, and more specifically, with the ProtoDUNE-SP simulations by the author (Rivera). This was done, initially, in an effort to correct artifacts in the neutron simulations that improperly treated neutron captures once thermalized. The refactoring has allowed for a return to the use of updated reference physics lists, maintained by the GEANT4 collaboration, and allowed the author to create and integrate custom physics lists, which can be extended during the GEANT4-stage configuration process. Another benefit of the refactorization is the modularity of various

---

[1] See (Knoepfel, 2020) for specific challenges for LArSoft.

services and service providers that can be selected as part of the simulations. A concrete example of this is drift simulation, which can run as a separate step following the simulation of charge deposits.

Once the migration to the refactored framework was set in motion, the WireCell team expressed interest in plugging in their drift and diffusion simulations with ProtoDUNE-SP, and a taskforce was assigned to fully integrate the refactored simulation with ProtoDUNE-SP. The author was responsible for profiling the code in terms of resource consumption (memory, disk, and time), in order to ensure that production samples are optimized to include as much precision as permissible by the cluster of machines designated for simulation job submission.

The migration to the refactored framework was completed in order to do the various Data and Monte Carlo comparisons included in the ProtoDUNE-SP performance paper.

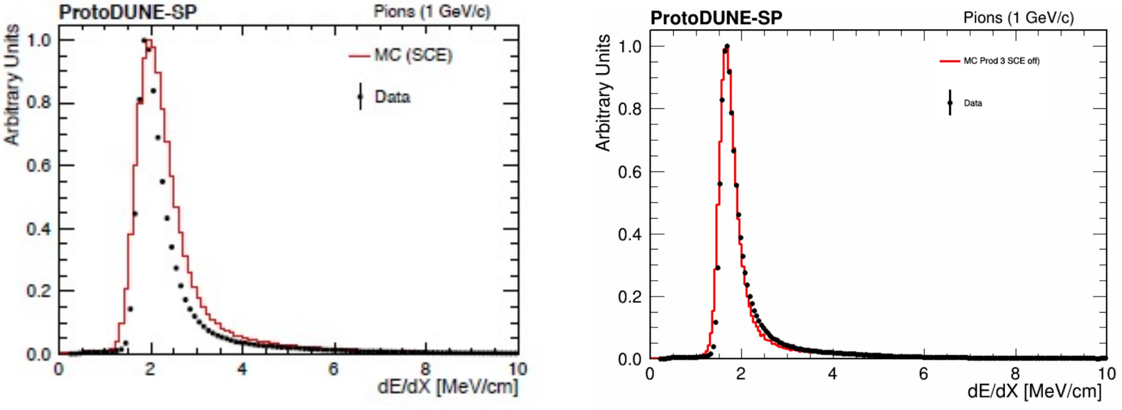

Figure 67: Pion dE/dx comparison between data and MC generated with the simulation prior to refactorization (**Left**), referred to as Legacy, and the refactored simulation (**Right**); published in (Abi et al., 2020a).

The large change in the width of the distributions in Figure 67 are due to the improved wire response[1] provided by the WireCell toolkit. The improved Data-MC agreement and the general flexibility of the refactored code also catalyzed the migration of both the DUNE

---

[1] The deconvolved pulse width has a more accurate intrinsic component plus a linear term that accounts for the diffusion along the drift distance.

and SBND simulations (currently in-progress).

5.1.2. Simulation flow

The overall flow for simulations in experiments that use LArSoft generally include:

- **Event generation** - all sources of initial state particles. Examples include the particle gun generator, radiological backgrounds, supernova neutrinos, and beam particle creation.
- **Particle propagation** - all initial state particles from the generation stage are handed off to GEANT4, which then simulates their passage through the materials in the detector geometry definition. Interactions that result in ionization in the active LAr volumes, or auxiliary subdetector volumes (PDS and CRT) result in energy deposits.
- **Detector simulation** - outputs of the particle propagation stage are convolved with the response of the corresponding detectors (sense wires, SiPMs, and scintillation counters) to generate waveforms similar to those that would be collected in data.
- **Reconstruction** - hit-finding and region-of-interest (ROI) finding is performed on the outputs of the detector simulation stage and reconstruction algorithms are used to organize the data into more useful objects such as tracks, clusters, and optical flashes.

Figure 68, below, depicts the standard simulation flow for ProtoDUNE-SP with some level of detail.

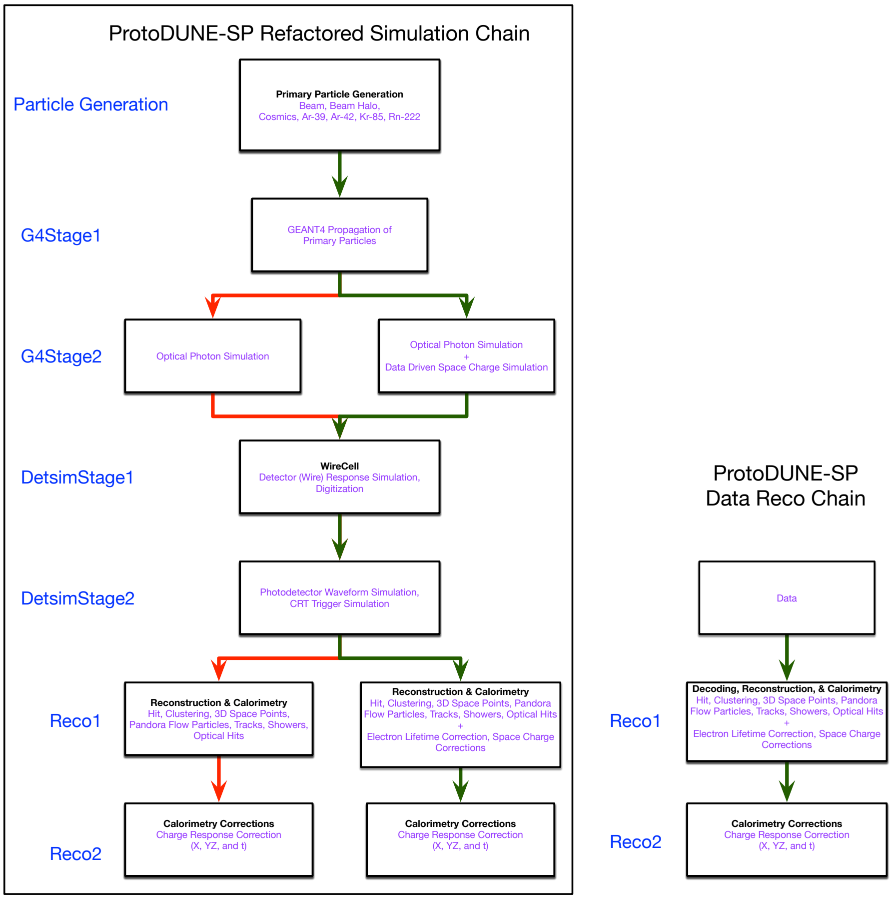

Figure 68: ProtoDUNE-SP simulation and reconstruction.

5.2. ProtoDUNE-SP simulations

ProtoDUNE-SP simulations in LArSoft can be performed by the user, however, the collaboration has a production team tasked with generating large data sets. The production data sets are the outputs of the reconstruction stage. The user is then able to analyze the data sets for their own purpose.

The production data sets were also intended to evaluate the ProtoDUNE-SP performance and generate the plots in (Abi et al., 2020a), and they included Beam + beam halo simulations, cosmic ray simulations, and some radiologicals (e.g. ^{39}Ar). The two former will be discussed in more detail below[1]. In future sections of this dissertation, the production

---

[1] The latter, radiologicals, are low energy (~ MeV) and are not a concern for this analysis because they

datasets will be referred to as **Full MC**.

Simulations by the user can include a subset of these generators or they can be different altogether.

5.2.1. Beam simulations

Beam simulations in ProtoDUNE include both the primary beam particles as well as some number of primary background particles which are associated with the beamline itself (Section 2.5.1). These are commonly referred to as the beam halo.

The beam generator relies on independent simulations of the beamline itself (Booth et al., 2019-06) performed using the G4beamline (Inc) simulation tool.Results from the beamline simulation are stored in persistent ntuple files for the collaboration. The LArSoft beam generator for ProtoDUNE-SP, samples events from these ntuples in order to produce primaries and the beam halo background.

5.2.2. Cosmic ray simulation

As a surface detector, ProtoDUNE-SP is intercepted with a large flux of cosmic rays (~10 kHz). Cosmic rays are simulated using the COsmic Ray Simulations In KAscade[1] (CORSIKA) (Alves et al., 2021), which is open software designed to simulate air showers from cosmic rays striking Earth's atmosphere. It was integrated with LArSoft as a primary particle generator by M. Bass et al. (Bass) (here) in 2015. The CORSIKA generator model simulates showers from high energy protons as well as light nuclei. The average number of cosmics rays that pile up with the 3 ms drift in ProtoDUNE-SP is 30 – the large majority of these are muons, which cross the detector from top to bottom.

The final state particles generated by CORSIKA include hadrons, gammas, muons, and positrons. There are many low energy particles that are produced is air showers, and many either don't have the penetrating power (gammas) or they are too computationally expensive

---

are very unlikely to be reconstructed as tracks

[1] The KASCADE experiment.

to simulate fully (neutrons), thus a 50 MeV was placed on the spectrum of generated showers when the CORSIKA input files for use with LArSoft were generated. The energy spectra for the primary CORSIKA particles observed in ProtoDUNE-SP simulations are shown in Figure 69.

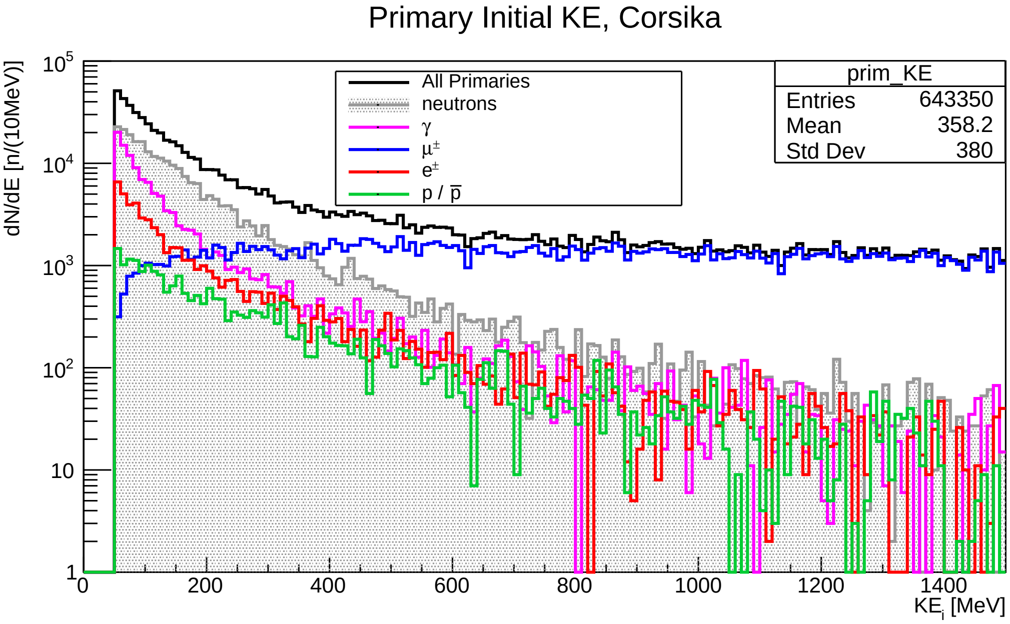

Figure 69: Corsika primary particle kinetic energy distributions.

Cosmic ray neutrons can enter the cryostat and fake neutrons from beam pions. A short study on the visible energy produced by cosmic ray neutrons can be found in Appendix D.

5.3. Reconstruction

5.3.1. Pandora

Pandora is a Software Development Kit (SDK) for pattern recognition in particle physics experiments that was originally envisioned for use in e^+e^- reconstruction, at the International Linear Collider(ILC). Pandora was later integrated with LArSoft and optimized for neutrino interactions with LAr, but has since been extended to include test-beam experiments. employed by ProtoDUNE-SP and other LArTPC experiments during reconstruction – see for example (Acciarri et al., 2017a) for its application in MicroBooNE to do neutrino interaction pattern recognition. The code and documentation for Pandora can be found on github in the PandoraPFA project.

The Pandora reconstruction procedure for ProtoDUNE-SP is summarized in Figure 70, below.

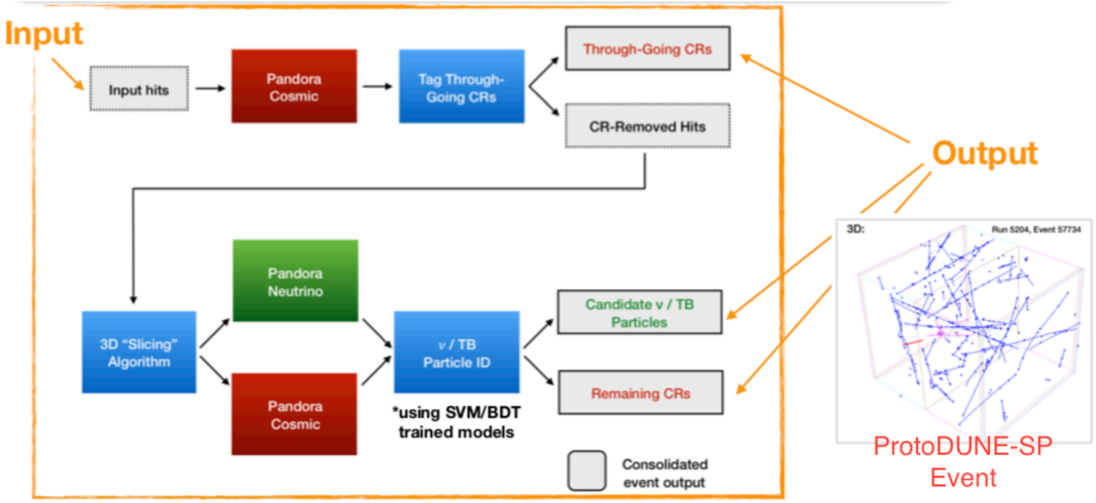

Figure 70: Generic Pandora reconstruction path for neutrino and test-beam (labeled TB) events in LArTPCs. Original figure from (Escudero et al.).

The Pandora-based reconstruction relies on hit clusters and is trained to fit track and shower hypotheses to collections of hit clusters, which are the leading topologies for medium-to-high energy interactions. The track and shower objects are associated to reconstructed particles, which are themselves arranged in hierarchies with the notion of parentage.

For surface LArTPC experiments such as ProtoDUNE-SP and MicroBooNE, there is a cosmic removal stage that precedes the core identification of the beam charged particle or neutrino vertex. Through-going particles are tagged as clear cosmics and their associated hits are removed from the remainder of the reconstruction procedure. The remaining 3D hit clusters are processed under parallel hypothesis of *remaining* cosmic rays and test-beam particles. A cosmic Boosted Decision Tree (BDT) score is calculated for the clusters The test-beam interaction pattern recognition then operates on the remaining 3D hit clusters with the end goal of sorting them into tracks and showers to produce a Particle Flow for test-beam candidates.

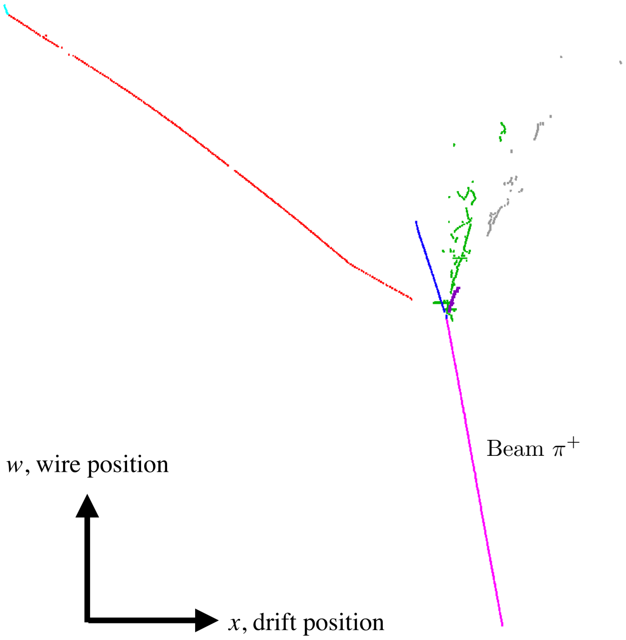

Figure 71: Pandora test-beam reconstructed event example on a beam pion. Hits associated with showers are shown in green and gray; the remainder correspond to tracks. Note the rotation of the coordinate system relative to ProtoDUNE-SP event displays. Original figure from (Abi et al., 2020a) (section 4.5.2).

Some reconstructed quantities are unique to showers and some to tracks e.g. shower opening angle, shower energy, and track momentum. The Pandora reconstruction can be configured to uniquely sort all reconstructed particles into the categories of tracks and showers or to carry out the calculations under both hypothesis for all particles. In situations when the track and shower distinction is not strong it is useful to carry out both hypothesis.

5.3.2. Post-Pandora

Convolutional Neural Network (CNN) scores can be calculated for reconstructed Pandora particles to aid in classifying particles as tracks, showers, or Michel electrons. These scores are calculated independently of Pandora and their aim is to provide supplementary information for the analyzer to rely on in order to classify the Pandora particle in question, regardless of what Pandora has determined. The three CNN scores available are the track score, the so-called Electromagnetic (EM) score, and a Michel score. The author relies on the track score (cnn_{trk}) and the EM score (cnn_{em}) to discriminate between gammas and $e^{\pm}$ and everything else. The CNNs were developed and trained by Aidan Reynolds. The full details of the performance and architecture can be found in his thesis (Reynolds, 2020).

5.4. The Space Charge Effect (SCE)

One of the complications for surface LArTPCs in the hundreds-of-tons scales is the accumulation of positive ions in the bulk of the detectors. The positive ions drift towards the negative HV cathode at a much slower rate than the ionization electrons, and given the 3.6 m drift distance there are significant variations near the detector boundaries as well as near the cathode. The balance is struck between the cosmic ray rate, the drift velocity, LAr purity, and recombination effects resulting in additional drift field non-uniformities and such that the charge deposition per unit length (dQ/dx) is position and time-dependent. An additional complication is introduced by the LAr purification and recirculation pump systems in the detector, which can cause some redistribution of the positive ions and impurities.

There have been efforts in ProtoDUNE-SP to model all of these effects, however, some of the more complicated effects, such as the fluid-flow dynamics, have yet to be verified. The verification process involves direct comparisons to data measurements of distortions and deviations from the expected dQ/dx profiles of cosmic rays that cross the detector. A parallel effort was developed to introduce the distortions, as determined from data, into the simulations as an alternative to the incomplete models and at the expense of lower resolution of these effects. The data-driven approach has been favored in order to more accurately simulate the net effects of the aforementioned factors, which are collectively referred to as the Space Charge Effect.

5.4.1. *Position correction*

The field distortions near the beam plug, which is close to to the HV cathode, are visible in event displays of raw data (see Figure 72).

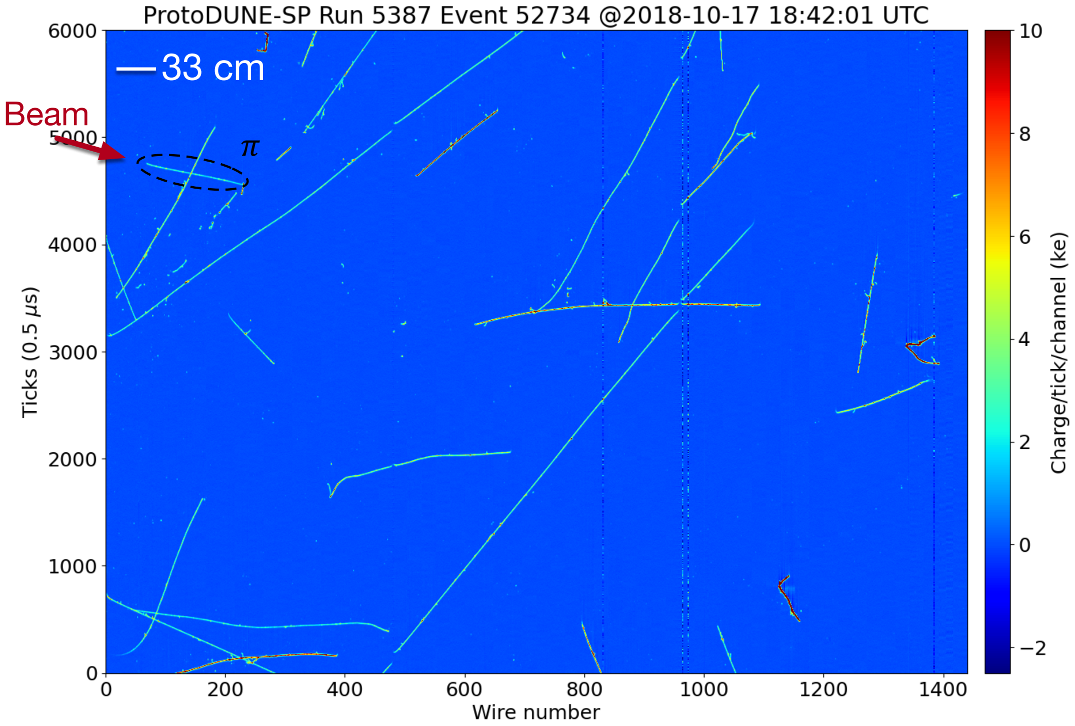

Figure 72: Example event. X-Z projection of the beam-side of the detector. The collection wires segment the z-direction. There are a total of 1440 wires that span a distance of ~7 m. The beam particle is labeled to highlight the effect of the Space Charge distortions to the field near the beam entry point. The effective track start for beam particles is in the order of 30 cm into the detector volume, and must be corrected.

A spatial correction is applied to account for SCE distortions using a data-driven field map, the form of the position correction is shown diagrammatically in Figure 73, below.

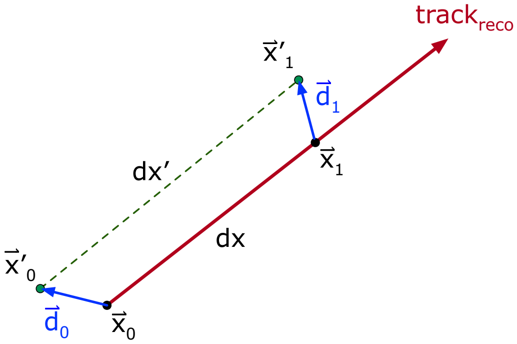

Figure 73: Spatial correction applied to a reconstructed track.

5.4.2. dQ/dx calibration approach

Cosmic rays (CR) enter the detector and pile up with the beam at an average rate of 30-40 per event, where an event is 3 ms long. The data calibrations are determined run-by-run, however the overall scale of the calibration is referenced to the global median across all runs of the same momentum.

The calibration follows a general approach standardized by the MicroBooNE collaboration (Adams et al., 2019) and reformulated for ProtoDUNE-SP. The overall procedure will be outlined here but the full details can be found in the ProtoDUNE-SP detector performance paper (Booth et al., 2019-06).

There are three sequential steps involved in calibrating the charge readout that apply to data as well as Monte Carlo that incorporates SCE simulation:

1. YZ dQ/dx calibration
2. X (time) dQ/dx calibration
3. dE/dx calibration with stopping muons

The goal of the calibration is to homogenize the detector charge response throughout the detector's active volume. Minimum Ionizing Particles (MIPs) crossing the detector serve as a source of reference charge signals with which we can equalize the response. The reconstructed CR tracks are first identified in each event of the run under consideration.

YZ All reconstructed charge depositions from the identified CR tracks in the active volume are divided into 5 cm × 5 cm cells in y and z and separated by plane (u,v,z), furthermore, the sub-volumes on either side of the cathode are treated independently. The dQ/dx values are mapped as a function of the y and z cell positions, from which the median values $(dQ/dx)_{\mathrm{YZ}}^{\mathrm{global}}$ are extracted for the run. The output of this calibration stage is a map with correction constants $C(y,z)$ given by equation 5.1.

$$C(y,z) = \frac{(dQ/dx)_{\mathrm{YZ}}^{\mathrm{global}}}{(dQ/dx)_{\mathrm{YZ}}^{\mathrm{local}}} \tag{5.1}$$

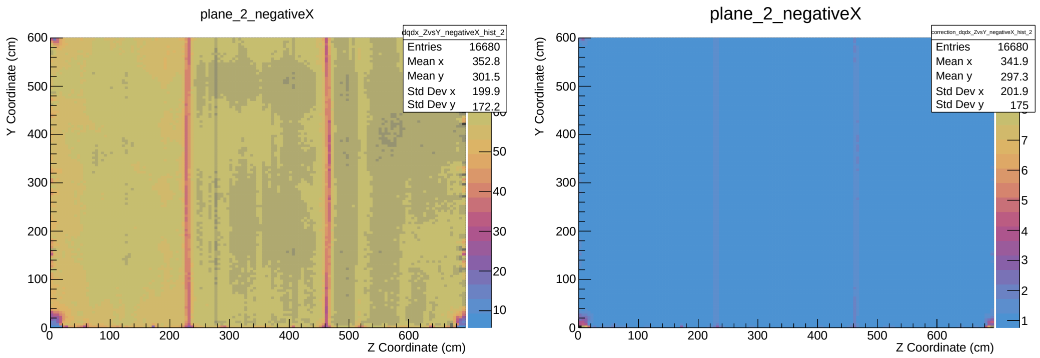

Figure 74: Left: Raw $(dQ/dx)_{\mathrm{YZ}}^{\mathrm{local}}$ for the collection plane in run 5809, for $x < 0$. **Right:** Correction factors $C(y,z)$ for the collection plane in run 5809, for $x < 0$.

X The C(y,z)-corrected dQ/dx values are then divided into 5 cm cells in the drift direction, x. Similarly, a set of corrections is calculated for the run to equalize the dQ/dx response in x as given by equation 5.2.

$$C(x) = \frac{(dQ/dx)_{\mathrm{X}}^{\mathrm{global}}}{(dQ/dx)_{\mathrm{X}}^{\mathrm{local}}} \tag{5.2}$$

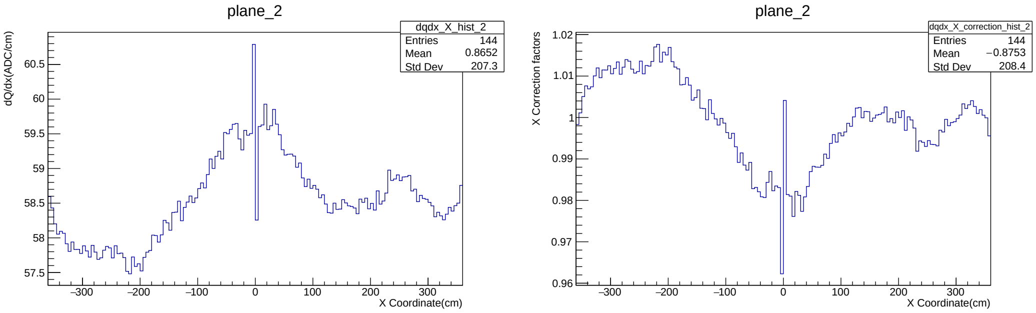

Figure 75: **Left:** Raw $(dQ/dx)^{\text{local}}_{\text{X}}$ for the collection plane in run 5809. **Right:** Correction factors $C(x)$ for the collection plane in run 5809.

The dQ/dx values are then equalized to the average dQ/dx value measured close to the APAs (x≈ ±360cm), where the effects of diffusion can be neglected.

$$N_Q = \frac{(dQ/dx)^{\text{anode}}}{(dQ/dx)^{\text{global}}} \tag{5.3}$$

Finally, the corrected dQ/dx value is given by equation 5.4.

$$(dQ/dx)_{\text{corrected}} = N_Q C(y,z) C(x) (dQ/dx)_{\text{reconstructed}} \tag{5.4}$$

dE/dx The energy scale correction, i.e. the conversion from dQ/dx to dE/dx, comes from stopping muons. The details of the selection for these two samples can be found in the ProtoDUNE-SP performance paper (Abi et al., 2020a) (Section 6.3).

The form of this correction is based on a model for the recombination that has been studied in tuned in the ArgoNeuT experiment (Acciarri et al., 2013), known as the Modified Box model. The final result for the calibration procedure is the calibrated dE/dx, which is given by Equation 5.5, below.

$$\left(\frac{dE}{dx}\right)_{\text{corrected}} = \left(\exp\left(\frac{(\frac{dQ}{dx})_{\text{corrected}}}{C_{\text{cal}}}\frac{\beta' W_{\text{ion}}}{\rho\mathscr{E}}\right) - \alpha\right)\left(\frac{\rho\mathscr{E}}{\beta'}\right), \tag{5.5}$$

where C_{cal} is the calibration constant used to convert ADC values to number of electrons, $W_{\mathrm{ion}} = 23.6 \times 10^{-6}$ MeV/electron (the work function of argon), $\mathscr{E}$ is the E field based on the measured space charge map, $\rho = 1.38$ g/cm^3 (liquid argon density at a pressure of 124.106 kPa), $\alpha = 0.93$, and $\beta' = 0.212$ (kV/cm)(g/cm^2)/MeV.

α and β' are the Modified Box model parameters, which were measured by the ArgoNeuT experiment at an electric field strength of 0.481 kV/cm.

The correction constants, i.e. the median values, calculated for each run as a whole are stored in a database and a reconstruction service applies them to the individual events within the run.

Simulations of ProtoDUNE-SP that include SCE, are also calibrated in the same way. In this case, a dataset containing the Full MC simulation is used to perform the stopping muon selection.

CHAPTER 6 : ANALYSIS

Primary hadrons in DUNE will produce neutrons with a spectrum of energies, and these neutrons will transport some of the energy away from their production point – until they interact or they exit the active volume. It is important to understand the neutron yield, the spatial distribution of neutron interactions from hadrons, as well as their energies. This will all be useful in quantifying the missing energy component due to neutrons and will help pin down the secondary hadronic uncertainty for neutrino interactions in DUNE.

This can be partially achieved by searching for neutrons from pion interactions in ProtoDUNE-SP. [1] However, because ProtoDUNE-SP is a surface detector and DUNE will be 30 km underground, there are some detector-specific uncertainties, such as those related to the large flux of cosmic rays piling up with every ProtoDUNE-SP event, that will not carry over to DUNE. Therefore, any leading systematic uncertainties must be considered and propagated to the results.

The goal of this analysis is to identify neutron inelastic scattering interactions, measure the cross section for this process, estimate the neutron energy, and fit for the number of neutrons from π^+ interactions in ProtoDUNE-SP through comparisons with Monte Carlo simulations. In the analysis, neutron candidates are exclusively identified by searching for reconstructed proton tracks that are *displaced* or *disjoint* from the primary pion interaction point as shown in Figure 85. The most likely production mechanism for these tracks is neutron inelastic scattering[2] at the above-30 MeV neutron kinetic energy range. The candidate neutron scatters are identified through the selection that will be outlined in Section 6.2.3. For each candidate, the distance (r) from the pion endpoint is measured as shown in Figure 85.

---

[1] Naturally, there will be other hadrons such as protons producing these secondary neutrons, but pions were chosen due to the large number of expected events collected by ProtoDUNE-SP and the larger number of pion-related analyses in progress at the time.

[2] This is supported by the simulations.

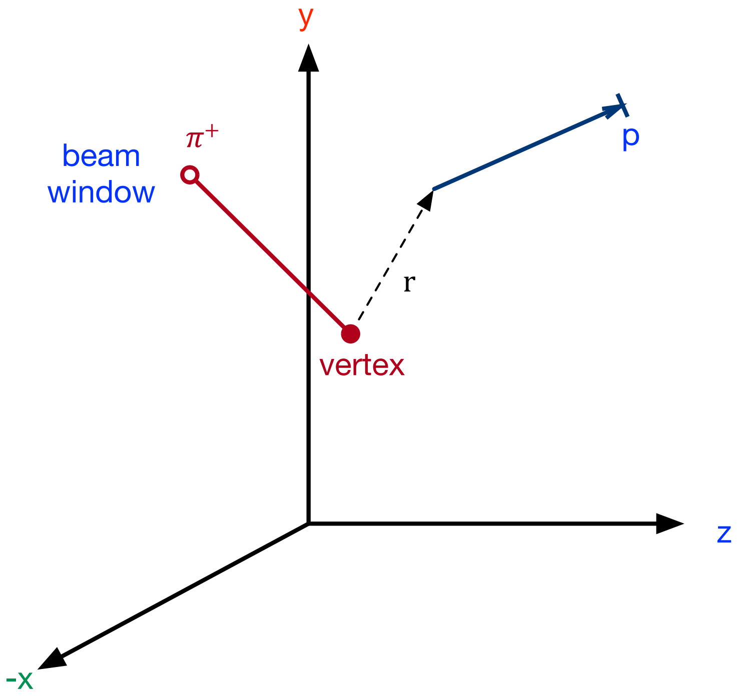

Figure 76: Schematic of proton candidate which is displaced from the primary beam vertex, with a 3D-distance r $= \sqrt{\Delta x^2 + \Delta y^2 + \Delta z^2}$.

The distribution of r in data is fit with a distribution of endpoint distances from an MC model including background, varying the neutron interaction length. The dominant systematic, which is the metric of distance, is determined using gamma rays from π^0-decays. This analysis is, in a way, tethered to the Bertini Cascade and the Barashenkov models used by GEANT4 when handling neutrons, but this is something that we must accept for now, as it is part of the challenge for studying neutrons in LArTPC experiments.

This chapter will proceed as follows: Signal and background definitions, data cleaning cuts and their efficiencies, followed by candidate-level cuts and efficiencies, systematic uncertainty estimation, and a discussion of the fitting method applied to extract the cross section results presented in CHAPTER 7.

6.1. Signal and background definitions

The following terminology will be used in defining signal and background:

- **primary** - an initial state particle in the simulation that gets handed directly to GEANT4 as an output of the generation stage in the simulation chain (Figure 68)
- **candidate** - particle track that passes selection cuts
- **ancestry/lineage** - the history of a particle as it relates to order of production.
  - e.g. a signal proton can have the lineage: $\pi^+ \to n \to p$. In this example the proton has a neutron mother and a pion grandmother. This is in-line with the notion of parentage in GEANT4.
- **ancestor** - a particle upstream in lineage
- **descendant** - a particle downstream in lineage
- **eve** - the "ultimate mother" for a lineage, i.e. the most upstream particle in the lineage

Signal For this analysis, any reconstructed track candidate with a lineage that contains, at least, one neutron ancestor where the neutron ancestor has undergone an inelastic process is a *true* neutron descendant. The source of neutrons for this analysis are pion interactions, therefore, in addition to being a true neutron descendant, the signal candidate must originate from the primary beam pion, i.e., the eve for the particle must be the beam pion.

The goal of the selection in this analysis is to identify neutrons via n-p inelastic scattering, therefore, the target final state particles are protons. The particle ID cut discussed in the next sections, is intended to select particles that are consistent with protons. The truth information from simulation (i.e., the MC-truth) indicates that bound states such as deuterons and tritons sometimes pass the selection criteria and also have a true neutron inelastic ancestor. The simulation suggests that this contribution is minor, in the order of 1.5%, nevertheless, because the production of these non-protons depends on the neutron inelastic cross section, these particles are combined into the category of signal when performing fits to data.

In summary, the signal is comprised of proton candidates that:

- have a true neutron inelastic ancestor **and** are descendants of the primary beam pion.

Backgrounds The backgrounds comprise the complementary set of proton candidates, i.e., particles that:

1. do not have a neutron ancestor that has undergone an inelastic process but are descendants of the primary pion
2. particles that pass the selection but are descendants of cosmic ray or beam halo primaries, some of which:
    - do have neutron inelastic ancestors
    - do not have neutron inelastic ancestors

According to the MC-truth, background 1. is the leading background, post-selection. This background does not depend on the neutron cross section and should therefore remain static when varying the neutron cross section. A large portion of these backgrounds, according to MC-truth information, consists of true protons produced by the primary pion interaction but with a misreconstructed starting position. This can fake a neutron candidate because the true proton will be reconstructed with a gap with respect to the pion vertex.

6.1.1. Beam runs

As mentioned in CHAPTER 2, ProtoDUNE-SP acquired data at seven beam momenta in the range of (0.3 GeV/c - 7 GeV/c). The neutron analysis presented here utilizes the 1 GeV data collected in late 2018, which was acquired over a total of 49 runs, with some runs being tens of minutes long and some lasting up to a day. The length of the run depended on the detector stability, the purpose of the run, and some were terminated to make a significant change in the detector configuration, e.g. to change the momentum setting[1]. Only 26 of the 49 1 GeV/c runs were taken while the drift field was at the nominal strength of 500 V/cm. These 26 runs were all deemed appropriate for the 1 GeV/c analyses in ProtoDUNE-SP and were analyzed by the author (after they were calibrated through a group effort of the author and other collaborators following the process outlined in Section 5.4.2).

Data cleaning Prior to reconstruction, data is prepared by a series of services that include ADC sticky code mitigation[2] and noise removal. This is followed by signal deconvolution and region of interest (ROI) finding for each channel, which then informs the hit-finding stage. Additional information about the ProtoDUNE-SP reconstruction can be found in chapter 4 of the ProtoDUNE-SP performance paper (Abi et al., 2020a).

The ProtoDUNE-SP detector suffered two occasional pathologies that are not simulated: missing data from Front End Mother Boards dropping out during a run as well as High Voltage (HV) instabilities.

The former is a result of insufficient tolerance in the design of the FEMBs for data cable connectors inside the cold, which resulted in events with missing data. The latter is not well understood, however, it resulted in scintillation light produced within the detector and persisting until the HV was reset – these were known as HV streamers. HV streamers were diagnosed by monitoring the current for the HV power supply – in the presence of a HV streamer the current draw dips below the nominal in a detectable way.

Filters are applied, at the event level, to remove periods of HV instability and missing Front End data. These same filters are applied when calibrating the runs as described in

---

[1] Beam settings, such as Magnet currents and Cherenkov threshold counter pressure, were all recorded in a database.

[2] The ADC design used in ProtoDUNE-SP had issues of Lowest significant bits getting stuck near the 64-bit boundaries.

section 5.4.

6.1.2. Cross section biasing

The custom physics list is based on QGSP_BERT_HP and makes the following changes:

- enables the Radioactive capture physics
- modifies the BertiniNeutronBuilder to accept and apply a constant cross section scale factor ($C_{\text{in-xs}}$) to the neutron inelastic cross section curve

MC simulations of beam pions entering the ProtoDUNE-SP cryostat were generated for 11 different neutron inelastic cross section scales, C_{in-xs}, as in Equation 6.1, below.

$$\sigma(KE)' = C_{\text{in-xs}} \times \sigma(KE)_{\text{nominal}}, \tag{6.1}$$

where $\sigma(KE)_{\text{nominal}}$ is the nominal neutron inelastic cross section from GEANT4, as shown in Figure 60.

6.2. Cuts

The cuts for this analysis are divided into data quality cuts, beam quality cuts, and neutron candidate cuts. Data quality cuts refer to the cuts described in the previous section 6.1.1, and they only apply to data, while beam and neutron candidate cuts apply to both data and MC equally. Additionally there is a Beam Instrumentation cut that only applies to data and Full MC simulations, because it includes a data-driven beamline instrumentation simulation.

Full MC simulations are generated by the DUNE production team at FNAL and are available to all collaborators. The event size is large (~200 MB/event), which limits the amount of Full MC that is available. At the time of this analysis, the 1 GeV/c Full MC and data are 1-to-1 in statistics.

Single Particle MC simulations were generated by the author to accumulate **sufficient** statistics for this analysis. It is not feasible at the moment, to generate the Full MC simulations with variations on the neutron cross section in order to perform a Full MC analysis – the author simulated only beam pions (π^+).

6.2.1. Beam cuts

The cuts discussed here are applied at the event level. Beam quality cuts are performed to select primary pion beam particles. The Beam Instrumentation (BI) cut has been tuned by the pion analyses

1. **Beam type cut** : The time-of-flight (t.o.f.) must be consistent with a pion or a muon
2. **BI quality cut** :
    - Require a single beam candidate – rejects events with pileup
    - Require that valid momentum and two valid position measurements from the downstream profilers exist for the candidate
3. **z-position cut** : restrict to events where the beam pion candidate interacts in the first APA (z<225 cm)
4. **Beam cut** :
    - track start (x, y, z) : tuned to accept events with a beam candidate near the beam window
    - track direction : tuned to select tracks consistent with the beam direction
5. **Beam χ^2 PID cut** : (χ^2_{proton}/n.d.o.f) $>$ 50.0, i.e., not consistent with a proton
6. **p candidate cut** : at least one reconstructed beam daughter in the event has χ^2_{proton}/n.d.o.f. $<$ 50.0

7. **p fiducial cut** : at least one reconstructed beam daughter is within the fiducial volume

The beam χ^2-PID cut, is based on templates of the dE/dx vs. residual range for various particles (see 10, for an example). The χ^2 statistic is calculated under a proton and a muon hypothesis. This cut was tuned to select beam pion candidates with high efficiency and reject protons or positrons. The cut was standardized for use with the ProtoDUNE-SP pion cross section analyses.

6.2.2. Beam event cut selection

The following tables present the effect of the each cut on the statistics for the three types of samples analyzed: Single Particle MC, Full MC, and Data.

Table 9: Single Particle MC cut summary for a sub-sample of events.

Cut	Pass (%)	Cumulative Passing (%)
Beam type cut	99.88	99.88
Beam cut	85.62	85.51
z-position cut	91.63	78.36
Beam χ^2 PID cut	97.57	76.45
p candidate cut	51.13	39.09
p fiducial cut	99.56	38.92

Table 10: Full MC Cut Summary

Cut	Pass (%)	Cumulative Passing (%)
Beam type cut	99.84	99.84
Beam cut	73.81	73.69
z-position cut	80.58	59.38
Beam χ^2 PID cut	95.43	56.67
p candidate cut	86.01	48.74
p fiducial cut	99.99	48.73

Table 11: Data Cut Summary

Cut	Pass (%)	Cumulative Passing (%)
Beam type cut	99.67	99.67
BI quality cut	85.83	85.55
z-position cut	79.59	68.09
Beam cut	59.05	40.21
Beam χ^2 PID cut	94.98	38.19
p candidate cut	87.68	33.49
p fiducial cut	100.00	33.49

6.2.3. Candidate cuts

The following cuts are applied to reconstructed tracks within the passing events from the previously-described, event selection.

Each candidates is required to pass the following cuts.

1. **Beam daughter cut** : Only Pandora Flow particles that are classified as daughters of the primary beam particle are considered
2. **Disjoint cut** : Candidate is required to be *disjoint* from the vertex by at least 5 cm
3. **Track score cut** : A cut is placed on the track CNN score calculated during reconstruction ($cnn_{trk} > 0.3$).
4. χ^2 **PID cut** : Candidate must pass the proton PID cut, χ^2_{proton}/n.d.o.f. < 50.0

The beam daughter and disjoint cuts offers the highest background rejection.

The author wrote an algorithm to determine the *disjointness* of both ends of all candidate tracks based on the wire hit information and the time in ADC ticks. The disjointness of a candidate track is determined by looking at both ends of the track and performing a check between the ends of the track and then ends of all other tracks as well as any hits not associated with any track.

For any track with track start t_i, and end t_n the distance in wire and time space can be defined using the approximate track length formula 3.5, utilized by the author for software triggering in DUNE. An example event is shown in Figure 77, below.

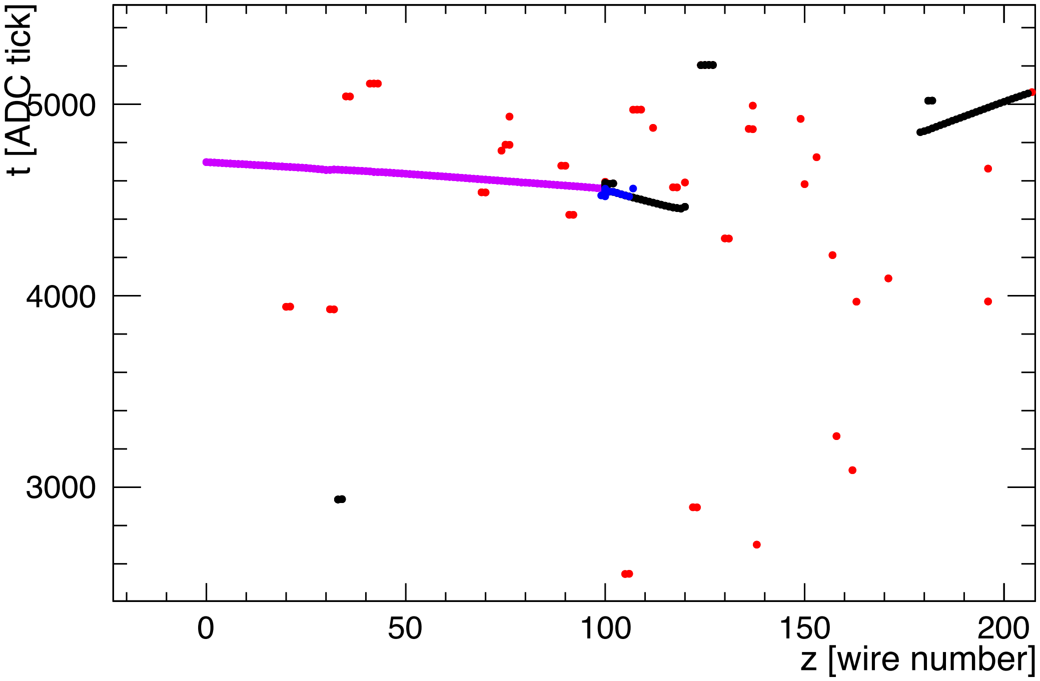

Figure 77: Simulated event with an incident pion (violet), low energy deposits (red), joined track hits (blue), and hits from tracks outside of the join radius (black).

The π^+ track in violet is clearly joined at its endpoint (z,t) = (104, 4720 ticks), however the track around wire 180 and tick 4800 is disjoint. Each track start/end is classified as either disjoint or not – true candidates must be at least start disjoint (t_i has no foreign hits in a 5 cm radius).

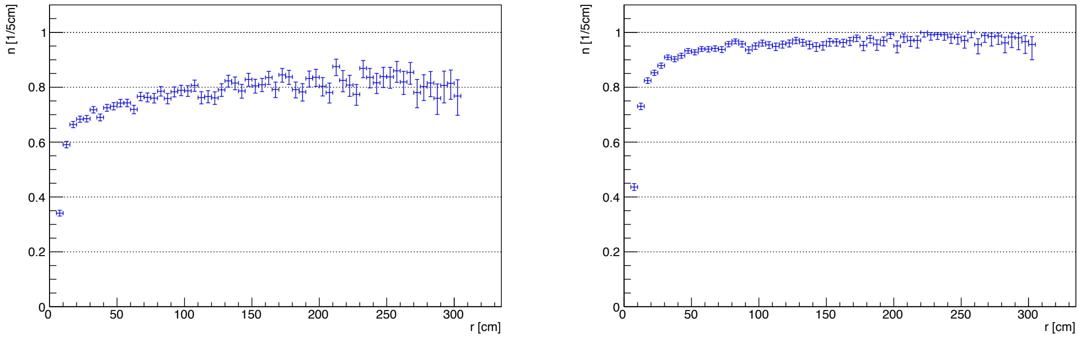

Figure 78: Efficiency (**left**) and purity (**right**) of candidate cuts for Single Particle MC as a function of r from Figure 63.

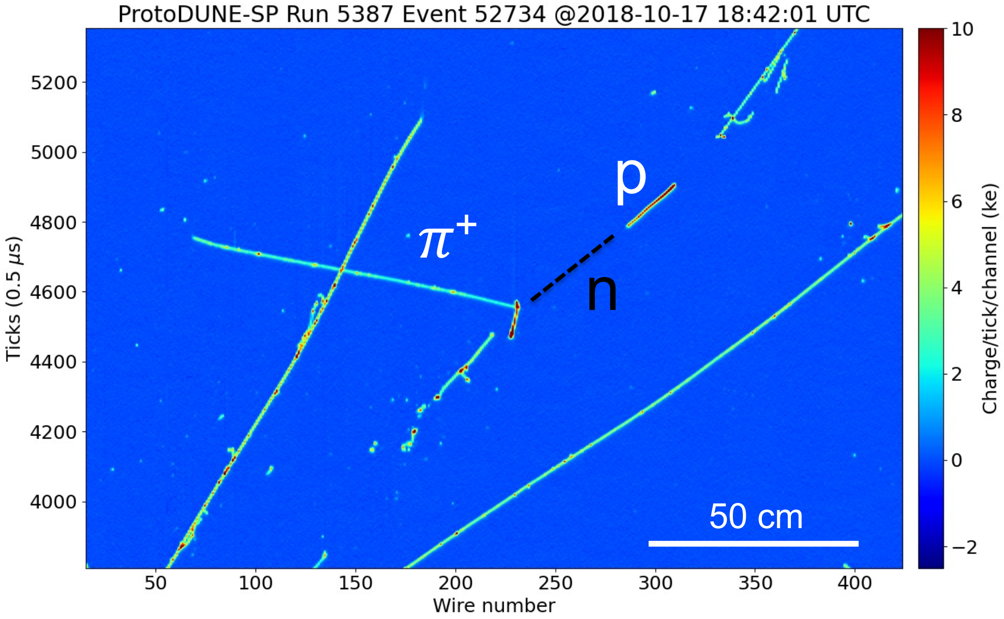

Figure 79: ProtoDUNE-SP neutron-proton candidate event. Event is labeled and zoomed-in to show details. The full beam-side event is shown in a previous figure, Figure 72.

6.3. Likelihood fitting

The measurements of the analysis (cross section, neutron number, and energy distribution) are made by varying the neutron inelastic cross section for these simulations and mapping the likelihood space for the r-distribution fits as a function of the variation, C_{in-xs} (Equation 6.1), in the simulation.

The likelihood can be calculated between a probability distribution functions (p.d.f.s) and data. The p.d.f.s can have a functional form or they can be in the form of a histogram as long as the error on the distribution is negligible – but more importantly the p.d.f.s must represent a normalized probability distribution.

For the measurements in this analysis, there are several complications such as the unknown nature of pattern recognition algorithms, including those employed by the Pandora-based reconstruction in LArSoft. Therefore, a good way of incorporating the unknowns is to generate simulations and carry them through the entire analysis in order to extract distributions equivalent to those obtained from running the same reconstruction algorithms on data. Naturally, the results from MC can be classified into signal and background.

The p.d.f.s for the neutron candidate interaction distances (signal and background) serve as inputs for the likelihood calculations. As with various fitting methods, the likelihood fit works by allowing certain parameters to vary. This can be as simple as an constant factor, or it could be a combination of various parameters that covary.

For a bin-by-bin likelihood fit between a data set and a p.d.f. the formula for the simplest fit that is searching for the normalization between data and a p.d.f. is given by :

$$\mathscr{L}(C) = \prod_{i=1}^{n_i} f(C; y_i) = \prod_{i=1}^{n_i} C \cdot y_i \tag{6.2}$$

$\mathscr{L}$ is the product of the probability distribution at each bin for a given value of C, therefore it is the joint probability density for observing the data for a given C. Naturally, the best fit value of C is the one that will maximize the joint probability density, and the p.d.f. normalization serves to constrain the possibilities.

The form of the fit for the neutron distributions is simply:

$$N_{\text{candidates}}(r) = n_{\text{sig}} \cdot f_{\text{sig}}(r) + n_{\text{bkg}} \cdot f_{\text{bkg}}(r), \tag{6.3}$$

where the $f_{sig}(r)$ and $f_{bkg}(r)$ are the p.d.f.s for signal and background, candidate radial distributions.

6.4. Systematics

In order for a study of neutrons in ProtoDUNE-SP to be informative for DUNE it needs to distinguish between detector-specific and physics-driven systematics. This is mainly because the lower flux of cosmic rays in DUNE (8000/day) is not expected to result in Space Charge Effects as significant as they are in surface detectors. The reduction in cosmic ray activity also means that the DUNE detector is expected to be “quieter” which calls for a reduction in hit thresholds. This is a challenge that a low energy neutron study would have to overcome, namely the low energy EM activity from cosmics which can outnumber those of neutrons.

The radial distance from the pion vertex to the neutron-proton candidate serves as a handle on the neutron mean interaction length, which is inversely proportional to the neutron cross section. A comprehensive systematic can be obtained from a calibration of known interaction length, in this case, gammas pose a golden opportunity to address the leading systematic for the neutron interaction length, i.e. the distance metric.

The radiation length, X_0, in LAr has been thoroughly measured and studied by various experiments and is well known to be 14 cm (BNL). A related quantity is the gamma conversion length, which approaches 9/7 X_0 (Rossi and Greisen, 1941-10), that is, 18 cm in LAr, in the high gamma energy limit.This can be confirmed in simulation, and is shown in Figure 80. Gammas are an ideal calibration source because their properties are far better understood than those of neutrons, which are the subject of this dissertation. They are similar to neutrons in that they both travel some distance before producing visible energy, and they do so indirectly.

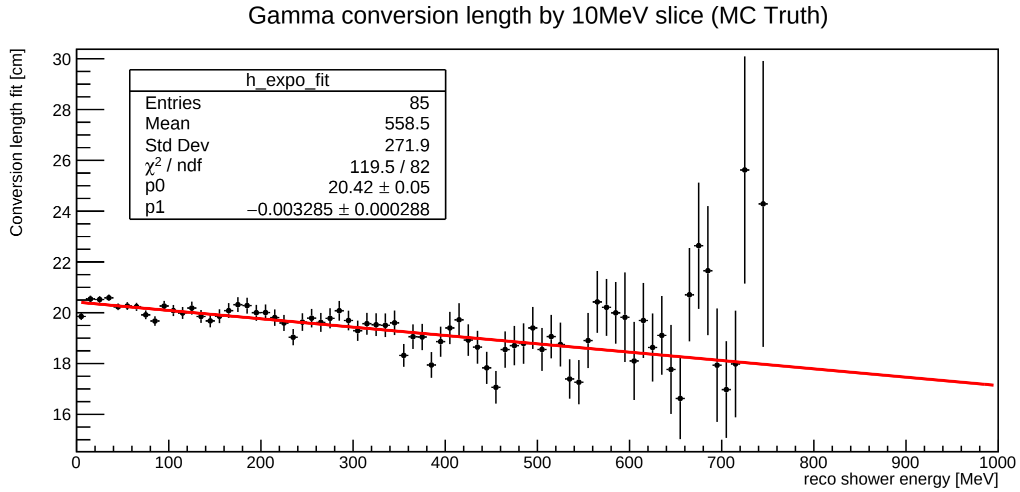

Figure 80: Gamma conversion length from fit to MC at increasing energy bins. The gamma interaction length approaches 18 cm, as predicted.

π^0s are copiously produced in charge-exchange interactions, in which, an incident π^+ interacts with a neutron to produce a proton and a π^0. These π^0s promptly decay electromagnetically (lifetime = 1e-18 s) into two gammas. The π^0-decay is almost immediate, therefore, the displacement from the π^+ vertex is negligible compared to the spatial resolution of the detector. The resulting gammas can subsequently undergo electromagnetic interactions, e.g., Compton scattering and pair-production (conversion), and depending on the energy, can produce showers and be tagged by the reconstruction.

Beam pions serve as the source of the π^0-decay gammas and neutrons for this analysis. The Pandora test-beam reconstruction applies similarly to both, and the selection for both candidates is analogous.

6.4.1. Gamma selection

Event-level cuts 1-5 in list 6.2.1 apply to this analysis as well, and are followed by candidate cuts 1-2 in list 6.2.3. An Electromagnetic CNN score cut is applied to the gamma candidates, namely, $cnn_{em} > 0.7$.

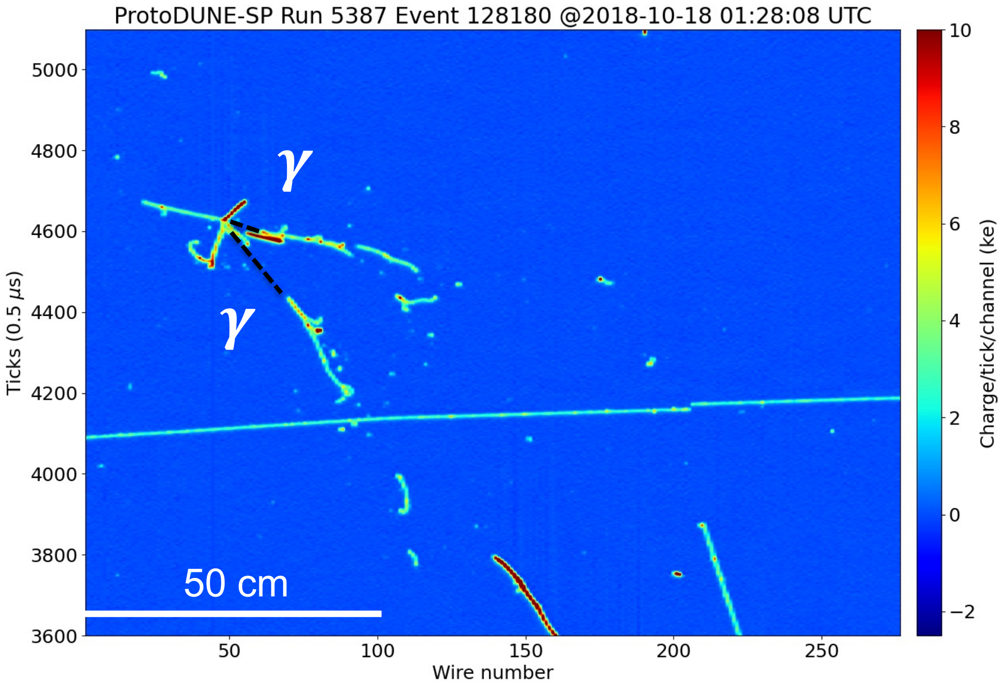

Figure 81: π^0-decay candidate event from 1GeV run 5387. Dashed lines outline the gap before the gamma showers.

6.4.2. Scale fit

The fit to the gamma data candidates has the form:

$$N^{\gamma}_{\text{candidates}}(r) = f\big((1+\alpha)r\big), \tag{6.4}$$

where f is the p.d.f. resulting from scaling all candidate, radial displacements by a factor $(1+\alpha)$.

Instead of creating a fixed set of scale factors (α_i), a χ^2 variable was constructed and the MINUIT (Lazzaro and Moneta, 2010) Migrad minimizer, available in ROOT, was used to scan the likelihood space. The fit for alpha involved the use of a, so-called, functor that generates the new distribution and re-calculates the likelihood when passed a value of α by the minimizer allowing it to converge with each successive approximation.

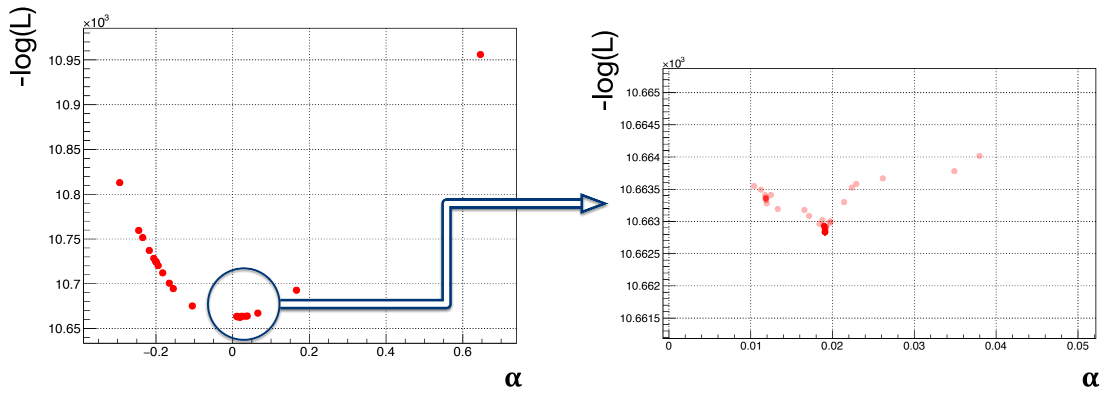

Figure 82: Likelihood space for fits of the gamma conversion length using π^0-decays.

The best-fit value for α is:

$$\boxed{\alpha = 0.019^{+0.002}_{-0.007}\ \text{(stat.)} \qquad (6.5)}$$

The scale factor, α, is conservatively taken to be ±2.1%.

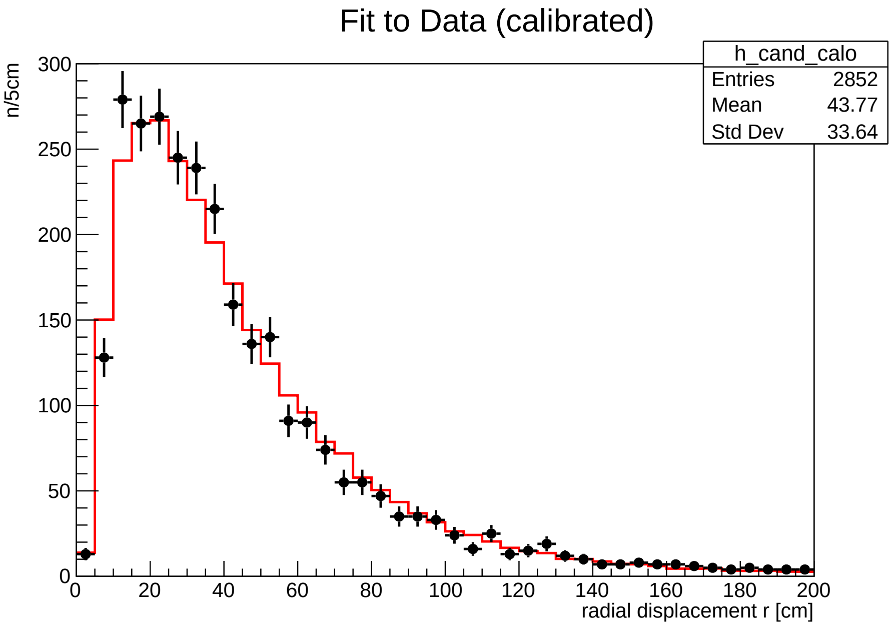

Figure 83: Best fit for the conversion length for π^0-decay gamma candidates.

6.4.3. Background systematic

Low statistics for the candidate selection in the Full MC production preclude a detailed study of the contributions from cosmics and beam halo to the backgrounds – these are shown in Figure 84, below. Relative to the leading background, the cosmics and beam halo contributions are deemed to be negligible.

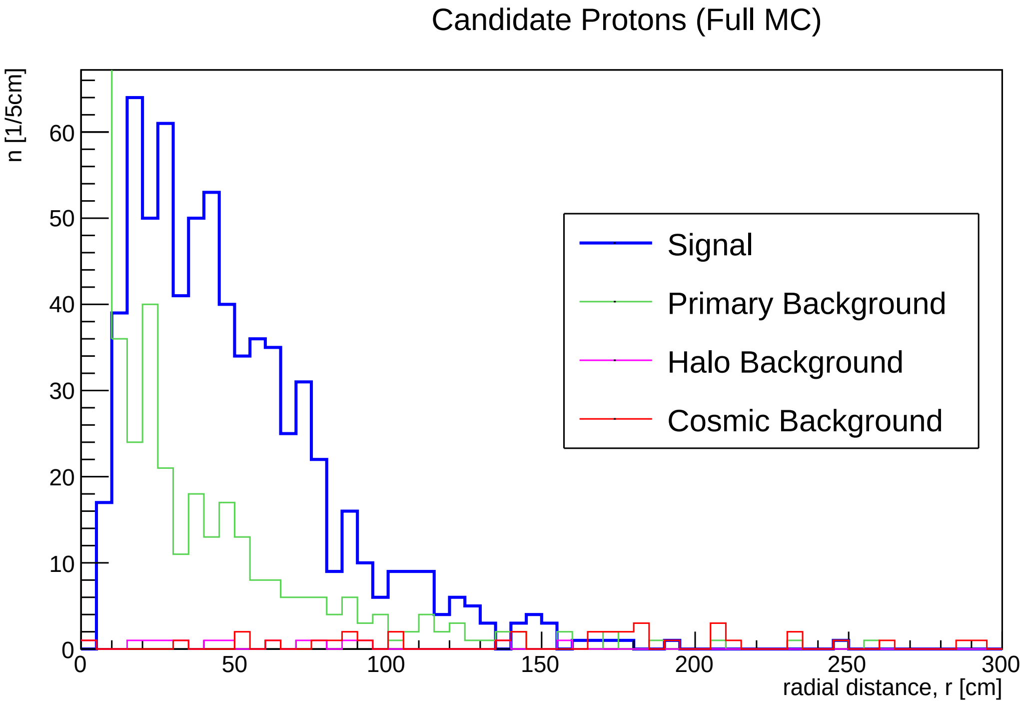

Figure 84: Proton candidate selection from full set of production Full MC simulations – including cosmics and beam halo backgrounds.

6.5. Fitting details

The neutron cross section measurement presented here is based on maximizing the likelihood space for the radial distributions of proton candidates.

The author wrote and utilized a custom physics list to vary the neutron inelastic cross section and repeated the simulation and selection procedures for each variation. The likelihood space was populated by simulating pion interactions, carrying these through the standard simulation flow described in section 5.1.2, applying neutron selection criteria, and using the candidate displacement distributions to generate p.d.f.s. The same neutron selection criteria were applied to data and the p.d.f.s generated from 11 different MC samples were used to fit the distribution from data.

A particle class, namely MCParticle, is the base object that contains the information for a GEANT4 track, e.g. creation process, final process before the particle is destroyed, as well as kinematic variables at each step in a particle's trajectory. Every particle has a track ID and a mother ID which allows for each particle to be backtracked to it's origin by first looking up it's mother, and proceeding in reverse order until a *primary* particle. Primary particles are those, which are produced by any generators and provided to the GEANT4 stage as initial state particles – in ProtoDUNE-SP the beam particles are primary, and so are any cosmics produced by CORSIKA.

The ancestry is determined, at the hit level, i.e., the full lineage for any particle that produces reconstructed hits is determined and associated to any higher-level objects constructed from these hits, such as hit clusters, tracks, and showers. The chain of processes leading to the charged particles that result in hits is also determined and associated.

6.5.1. Fitting software

The RooFit C++ library was used by the author to perform fits on the selected candidate distributions from simulations and data. RooFit is used in various high energy analyses; it is well documented ((Verkerke, 2010),(Roo)), and it also provides compact ways to store datasets, fitting models, and results [1].

---

[1] This is useful for storing reproducible results and for collaborating with peers.

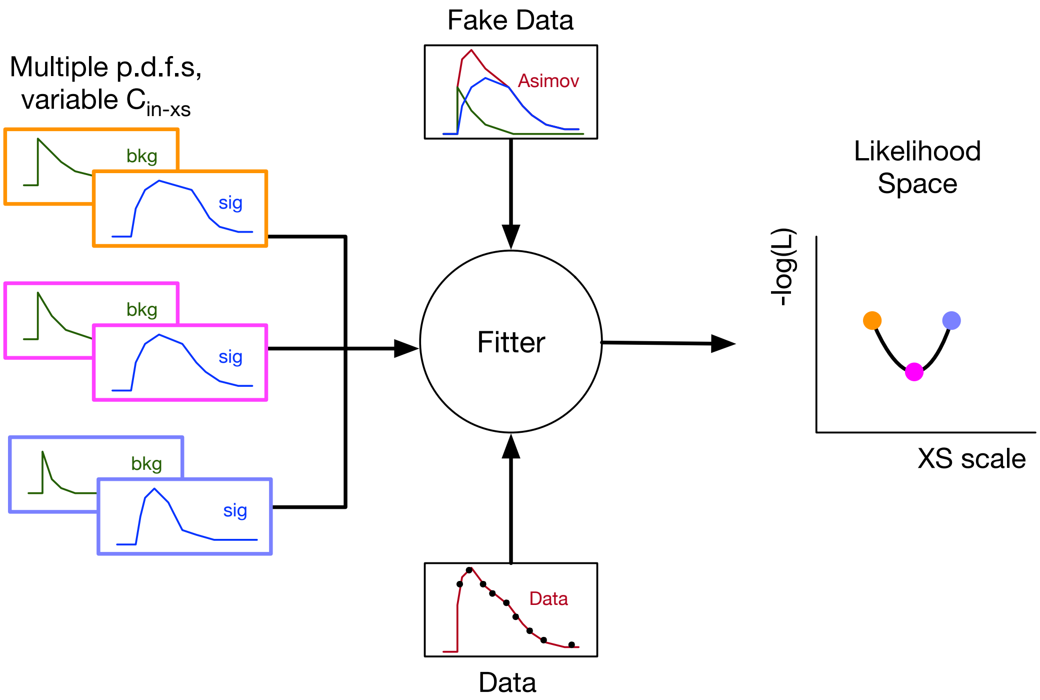

Figure 85: Schematic of fits for the neutron analysis. The inputs are signal and background p.d.f.s and either data or fake data sets.

A fake data set was produced for each value of $C_{\text{in-xs}}$, in order to confirm that the fitting algorithms returned the correct results when fitting the fake data of the same $C_{\text{in-xs}}$with p.d.f.s One such fit is shown in Figure 86. Roughly 1 M events were required to produce signal and background p.d.f.s whose statistical uncertainties were small. For this reason and because each dataset is roughly 500 GB, the author was restricted to a handful of datasets.

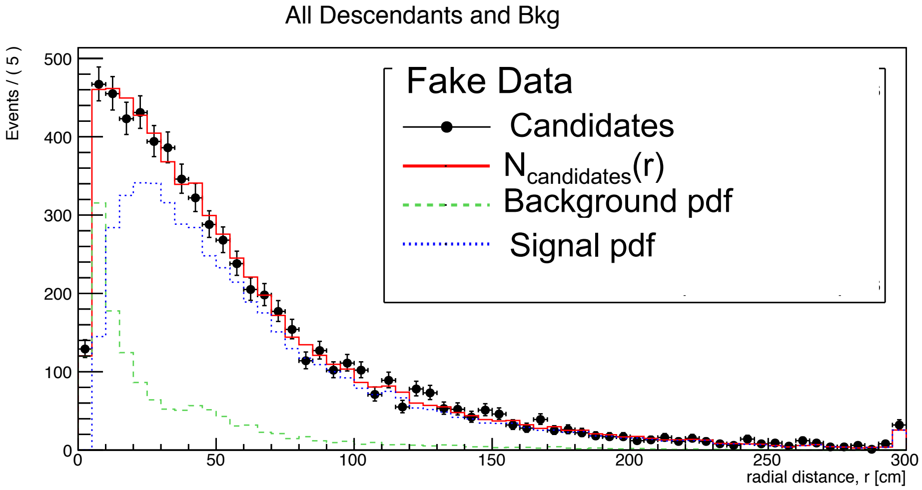

Figure 86: Fit to fake data with $C_{\text{in-xs}}$= 2.00.

CHAPTER 7 : RESULTS

In this chapter the final results are presented for the neutron cross section analysis based on the neutron candidates identified from the 1 GeV/c, ProtoDUNE-SP beam run. The results include: the most likely cross section scale factor (C_{in-xs}) from Equation 6.1, the number of signal (n_{sig}) and background candidates (n_{bkg}) that maximize the likelihood in Equation 6.3, and finally the cross section. The leading systematic extracted from the π^0-decay gammas is applied and used to calculate the systematic error on C_{in-xs} and the neutron inelastic cross section.

Additionally, as a sanity check, the reconstructed kinetic energy p.d.f. for proton candidates is generated from MC by summing the reconstructed KE pdfs for signal and background, *after* scaling by n_{sig} and n_{bkg}, respectively. Their sum is then compared to the reconstructed KE distribution from data candidates, and although we cannot directly measure the neutron kinetic energy, we can establish whether the reconstructed KE for the protons in data are in agreement with those from MC.

The cross section results can be reported alongside the results from MiniCAPTAIN (previously shown in Figure 66), under the assumption that the MC-Truth KE distribution for neutrons from 1 GeV/c pions that result in candidate protons, is accurate. This will be followed by a summary of the results and some final remarks about DUNE.

7.1. MC-Data comparisons

Figure 87 presents the likelihood space for the 11 fits of scaled MC to the full set of data candidates (1,384) passing the selection cuts.

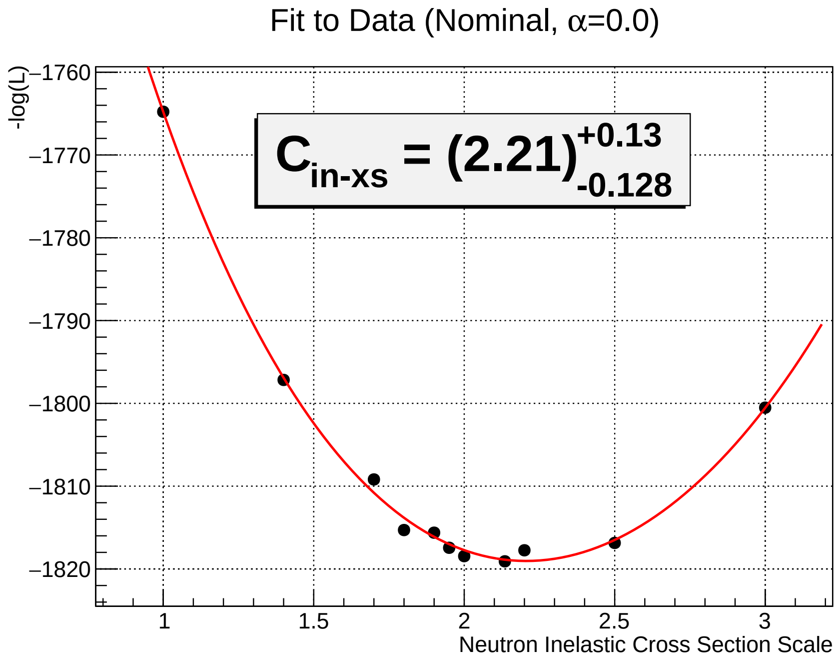

Figure 87: Negative likelihood space for fits to data with 11 data sets generated with cross section scales (C_{in-xs}) between 1.0 and 3.0.

A 4th-order polynomial, $f(\theta)$ (Equation 7.1), fit is performed on the likelihood space and used to extract the cross section that maximizes the likelihood space (i.e., minimizes the -log(L) space) as well as the 1σ uncertainty on the fit.

$$f(\theta) = p_0 + p_1\theta + p_2\theta^2 + p_3\theta^3 + p_4\theta^4 \tag{7.1}$$

The fit parameters from the fit in Figure 87 are: $p_0 =$ -1580.32, $p_1 =$ -286.272, $p_2 =$ 125.009, $p_3 =$ -25.8009, and $p_4 =$ 2.59429.

The best fit cross section is obtained by minimizing the functional form of the likelihood curve, $f(\theta)$.

$$0 = \frac{df(\theta)}{d\theta}\bigg|_{\theta_{\min}} = p_1 + 2p_2\theta + 3p_3\theta^2 + 4p_4\theta^3\bigg|_{\theta_{\min}} \tag{7.2}$$

$$\theta_{\min} = 2.2061 \tag{7.3}$$

A confidence interval is constructed using the classical relationship (Cowan, 1998) between the maximum likelihood estimate of a parameter (θ) and the change in this parameter by one standard deviation (σ_θ), expressed in Equation 7.4.

$$\mathrm{logL}(\theta \pm \sigma_\theta) = \mathrm{logL}_{\mathrm{max}} - \frac{1}{2} \tag{7.4}$$

However, since, the quantity for the fits presented in this dissertation is -log(L), the relationship is:

$$-\mathrm{logL}(\theta \pm \sigma_\theta) = -\mathrm{logL}_{\mathrm{max}} + \frac{1}{2}, \tag{7.5}$$

where $\theta = C_{in-xs}$.

In other words the 1σ statistical error on C_{in-xs} is attained where:

$$-\mathrm{log}L(\theta) = -1819.03 + 0.5 = -1818.53, \tag{7.6}$$

which occurs at $\Delta\theta_-$ = -0.128, $\Delta\theta_+$ = 0.130 about θ_{min}.

The $\Delta\theta$ form the 68.3% confidence interval for the best fit value of C_{in-xs} and is presented as the statistical uncertainty.

$$C_{in-xs} \quad \epsilon[2.078, 2.336] \tag{7.7}$$

7.1.1. Systematic evaluation

A sample of MC with C_{in-xs}=2.21 was generated following the minimization of the likelihood space for use in the remainder of the analysis. The maximum likelihood fit of signal and background distributions, for C_{in-xs} = 2.21, to the 1 GeV beam dataset, is shown in Figure 88. The uncertainty in the p.d.f.s due to the metric scaling factor (α) obtained in the fit to the gamma conversion distance (Figure 82), is depicted by the shaded regions overlaid over each r-bin.

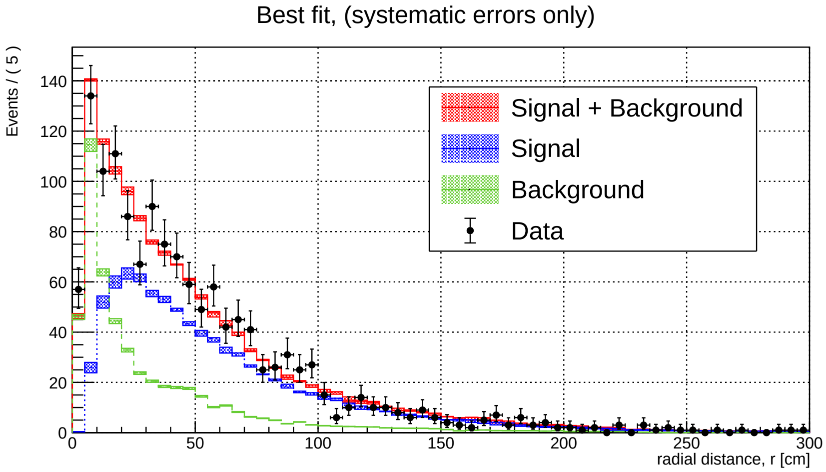

Figure 88: Fit to data with p.d.f.s with a 2.21 cross section scale. The systematic error is represented by the shaded regions.

The systematic uncertainties are obtained by applying the extreme value of α (± 0.021) as stated in Section 6.4.2 to the signal p.d.f. and quantifying the change in the best fit value of C_{in-xs} as a result of applying the scale factor.

The corresponding changes in the best fit value of C_{in-xs} are $\Delta\theta_{-}$ = -0.040, $\Delta\theta_{+}$ = 0.129. The $\Delta\theta_{\pm}$ form the 1σ confidence interval for the best fit value of C_{in-xs} as is presented as the systematic uncertainty.

7.1.2. Result

The 1σ, best-fit scale factor (C_{in-xs}) for the GEANT4 neutron inelastic cross section in liquid argon is:

$$\boxed{C_{in-xs} = 2.21^{+0.13}_{-0.13}\ (\text{stat.})^{+0.13}_{-0.04}\ (\text{syst.})}$$

in the kinetic energy range spanned by neutrons produced by 1 GeV π^{+}. This range is itself capped at the pion energy, by conservation of energy and momentum and limited from below by the minimum KE for a proton that can be reconstructed – in the case where a neutron transfers all of its kinetic energy to the proton. This lower limit is determined by the Pandora reconstruction – it is unlikely that a short track corresponding to a proton with KE below 30 MeV will be reconstructed as a Pandora particle and be associated with the beam as a daughter (as required in the selection described in Section 6.2.3). The proton momentum will be addressed in section 7.3, after discussing the best fit results.

7.2. Number of neutrons

The signal and background p.d.f.s prior to performing the fit to data are shown in Figure 89, below.

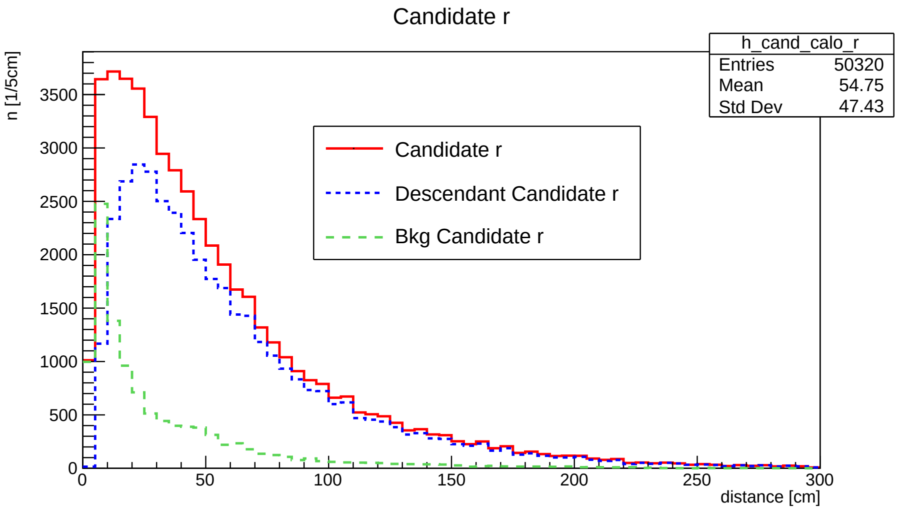

Figure 89: Signal and background p.d.f.s for Monte Carlo with $C_{in-xs} = 2.21$, prior to fitting.

Several values concerning the amount of signal and background in the MC and Data events are shown in Table 12.

Table 12: Signal and background ratios

Parameter	MC	Data
n_{events}	49,203	1,362
n_{sig}	39,406	870.4
n_{bkg}	10,914	505.0
$n_{\text{sig}}/n_{\text{events}}$	0.801	0.639
$n_{\text{bkg}}/n_{\text{events}}$	0.222	0.371
$n_{\text{sig}}/n_{\text{bkg}}$	3.611	1.723

It should be noted that both the number of signal candidates per event and the signal-to-background ratio are overestimated in MC compared to Data. This can be interpreted as a difference in the efficiency for the selection of neutron interactions between data and MC, or it could indicate a departure from the production model for neutrons in GEANT4 – namely, the Bertini Cascade model. Recall that the GEANT4 physics list treats the model for a process, such as neutron inelastic scattering, and the cross section curves independently, therefore this could also be indicative of a difference due to either one.

The two latter possibilities should be explored once the possible differences in efficiency for the selection in MC and data have been exhausted. The difference in efficiency could relate to the beam event cuts or to the candidate cuts. One possible difference between MC and data is residual beam μ^+ contamination. The contamination is due to the similarity in mass between muons and pions and consequently, the similar dE/dx. Beam muons cannot therefore be easily removed with standard particle-ID cuts. Muons have a higher penetrating power in the detector that all other particle – the z-position cut in Section 6.2.1 is intended to mitigate this background, however, this is one possible source of the relative increase in backgrounds per "good beam event" in data.

As a sanity check, an additional cut used in the pion cross section analyses, introduced by F. Stocker, based on a CNN Michel $e^{\pm}$ score for the beam vertex was explored by the author. The cut can be used to reject stopping μ^+, which decay and have a short positron track connected to the beam vertex. The author tested various Michel score cuts in order to determine whether this resulted in a significant change in accepted beam events. The Michel score cut is a -8% effect on the number of events passing the beam event level cuts. An 11% difference between the efficiency of the **proton candidate daughter cut** persists even after applying the Michel CNN score cut.

7.3. KE comparison

The reconstructed momentum provides another way to compare to data and simulation and check for consistency. The momentum is reconstructed in the neutron analysis for all candidates under a proton hypothesis using the dE/dx vs. residual-range information. This provides an estimate, based on the track length, for the momentum of the particle, which can then be used to calculate the KE for each candidate using Equation 7.8.

$$KE(p) = E - m_p = \sqrt{m_p^2 c^4 + p^2 c^2} - m_p c^2 = m_p c^2 \cdot \left[\sqrt{1 + \left(\frac{pc}{m_p c^2} \right)^2} - 1 \right] \tag{7.8}$$

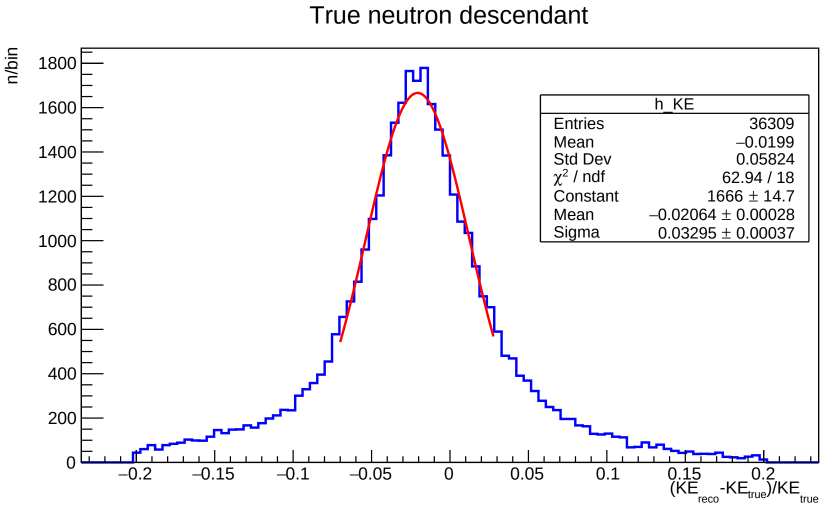

Figure 90: Comparison of the reconstructed proton candidate KE in MC.

There is a 2% negative bias in the reconstructed energy, although it should apply to data reconstruction as well. This is a small energy scale correction for the proton KE.

The momentum distributions for the fits to data below come from the simulation sample with a $C_{in-xs} = 2.21$ scale factor. The fit values for n_{sig} and n_{bkg} from Equation 6.3, shown in Table 12 , are used to weight the relative content of signal and background in the KE distributions.

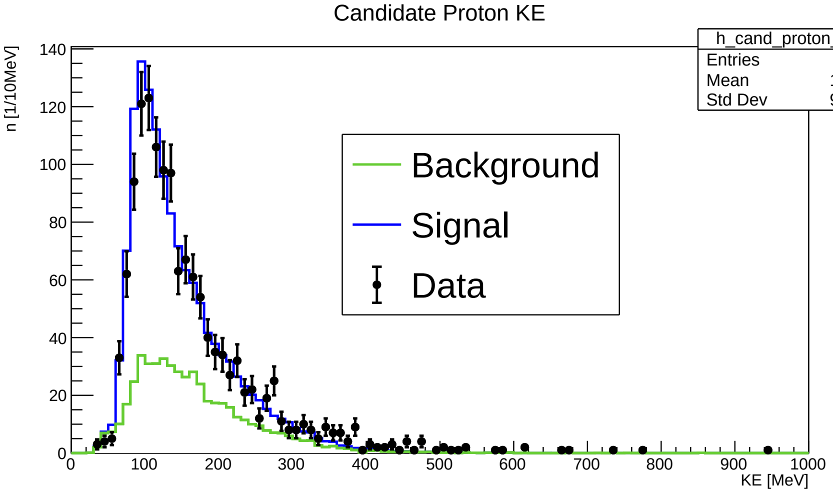

Figure 91: Comparison of the proton candidate KE to Data. Signal and background histograms are stacked.

The MC-Truth distribution of final kinetic energy (KE_f) for neutron ancestors of true signal particles (protons or otherwise) is shown in Figure 92.

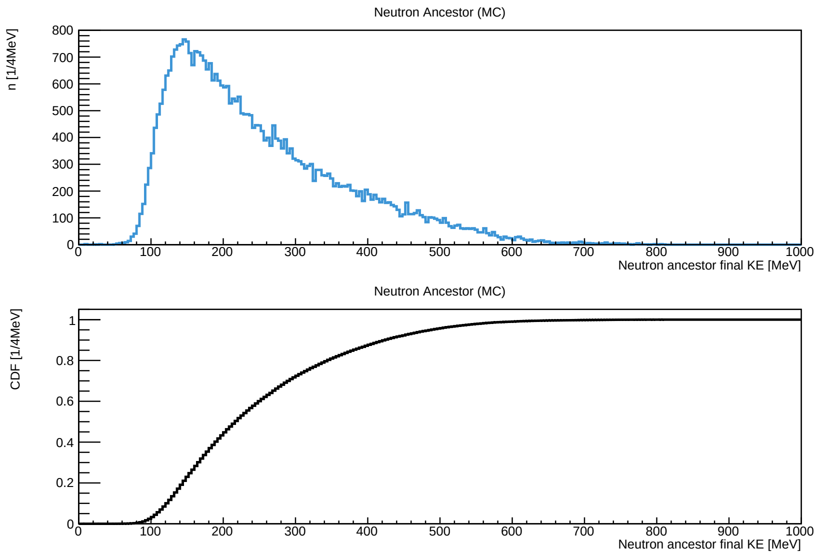

Figure 92: **Top**: True KE$_f$ distribution for neutron ancestor for signal candidate particles. **Bottom**: Cumulative distribution function for the neutron ancestor's KE prior to the interaction.

The neutron KE distribution is clearly skewed by the high energy tail; however it is peaked at roughly 146 MeV, and we can obtain the classical 68.3% confidence interval corresponding to the 1σ error band by looking for the low and high KE corresponding to 68.3% of the cumulative distribution function (c.d.f.) about the peak. From the bottom plot shown in Figure 92, this corresponds to the range of $[114, 314]$ MeV.

$$\boxed{KE_f \;\epsilon\; [114, 314] \text{ MeV} \qquad (7.9)}$$

7.4. Cross section

The nominal neutron inelastic cross section, σ_0, at 146 MeV is 561.463 millibarns (mb) – this is scaled by the best fit value for C_{in-xs} along with the asymmetric uncertainties, statistical and systematic summed in quadrature. The new central value of the cross section, $\sigma_{\text{inelastic}}$, becomes **1240.05 mb**.

$$\Delta C_{+} = \Sigma^{+}_{\text{stat}} \oplus \Sigma^{+}_{\text{syst}} = \sqrt{(+0.130)^2 + (+0.129)^2} = 0.184 \tag{7.10}$$

$$\Delta C_{-} = \Sigma^{-}_{\text{stat}} \oplus \Sigma^{-}_{\text{syst}} = \sqrt{(-0.128)^2 + (-0.040)^2} = 0.136 \tag{7.11}$$

where $\Sigma^{\pm}_{\text{syst}}$ and $\Sigma^{\pm}_{\text{stat}}$ are used instead of σ for clarity, to represent systematic and statistical errors.

It then follows that the best fit value for the inelastic cross section is: $\sigma_{\text{inelastic}}{}^{\Delta C_{+}\cdot\sigma_0}_{\Delta C_{-}\cdot\sigma_0}$.

The 1σ, neutron inelastic cross section in liquid argon from this measurement is:

$$\boxed{\begin{aligned}\sigma_{\text{inelastic}} =& \Big(C_{in-xs}\cdot\sigma_0\Big)^{\Delta C_{+}\cdot\sigma_0}_{\Delta C_{-}\cdot\sigma_0} \qquad (7.12)\\ =&1240^{+100}_{-80}\ \text{millibarns}\\ =&1.24^{+0.10}_{-0.08}\ \text{barns}\end{aligned}}$$

The 68% confidence interval in Equation 7.9 for the neutron final kinetic energy effectively represents the width of the neutron “beam” produced by 1 GeV/c π^{+} interactions in LAr. This allows for the comparison between the ProtoDUNE-SP results in Equation 7.12 and the MiniCAPTAIN measurements in Figure 66. The measurement presented here, spans an asymmetric range of 200 MeV peaked at 146 MeV, and overlaps with the low end of the energies in the MiniCAPTAIN measurement as shown below in Figure 93.

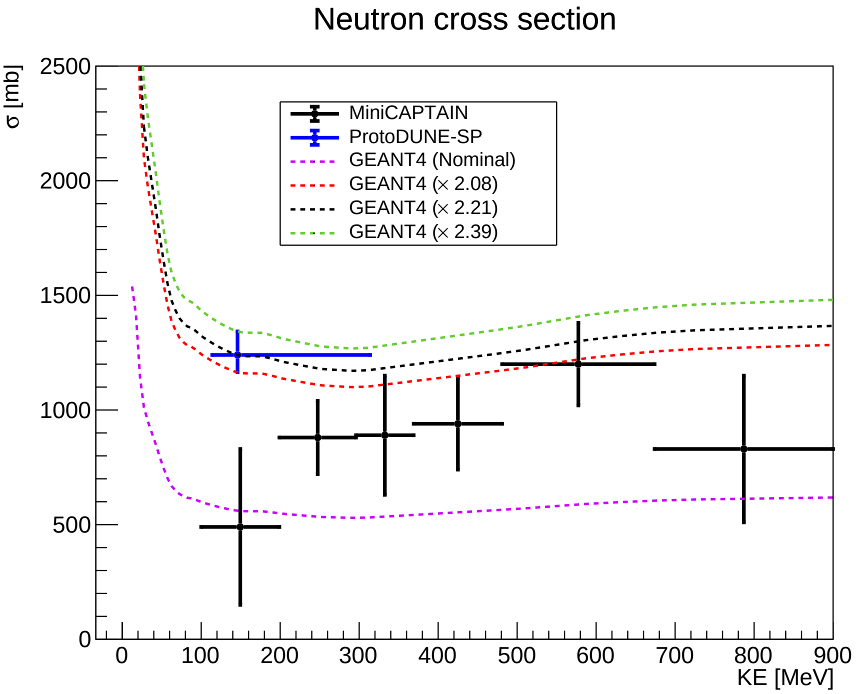

Figure 93: MiniCAPTAIN neutron cross section measurements with overlaid results from ProtoDUNE-SP. The dashed lines depict the 1σ bands based on this analysis, the best fit, and the GEANT4 nominal neutron inelastic cross sections. MiniCAPTAIN results reproduced using table I in (Bhandari et al., 2019).

Both the ProtoDUNE-SP and MiniCAPTAIN results call for a larger-than-nominal GEANT4 neutron inelastic cross section in LAr. The ProtoDUNE-SP measurement, taken at face-value to be the cross section at 146 MeV, is 2.2 sigma higher than the MiniCAPTAIN measurement in the 100-200 MeV bin and 1.98 sigma higher for the -1σ ProtoDUNE-SP value. A good level of agreement between the two experiments is attained above 200 MeV.

7.5. Summary

Not accounting for the hadronic uncertainty due to missing energy from neutrons, whether it be from neutrons escaping the active volume or from failing to associate neutron interactions (of all energies) with their source, will distort the neutrino energy spectra. For a precision neutrino oscillation experiment such as DUNE, this can result in a bias and a smearing in oscillation parameters such as the CP-violating phase, as shown in (Ankowski et al.,

2015) (Figure 1). Understanding the interaction length, energy, and number of neutrons is necessary to address a large portion of the hadronic energy uncertainty.

The analysis in this dissertation was carried out with the DUNE experiment in mind, in which there will be two distinct neutron components – the primary resulting from the neutrino interaction or from final state interactions within the nucleus, and the secondary component, which is due to the interaction of primary-component (charged) hadrons. Studying the neutron production in a charged test-beam experiment is ideal for pinning down uncertainties due to neutrons from the secondary component. The additional neutron activity observed by a neutrino LArTPC experiment, such as DUNE or SBND, will be due to the primary component.

Neutrons produce visible energy indirectly. They can be easily identified by looking for interactions, where they eject a proton, which then produces a track of visible energy. The neutron inelastic cross section was measured by searching for disjoint proton tracks up to 300 cm away from the reconstructed pion vertex and mapping their position distribution. The radial displacement from the vertex serves as a handle to the neutron cross section as an effective interaction length. The proton candidates in data were fit with signal and background p.d.f.s from reconstructed MC, where the neutron inelastic cross section curve was scaled by a constant factor using a custom physics list. A maximum likelihood approach was applied to identify the best fit value of the scale factor from 11 different fits to data.

A fit to the likelihood vs. cross section scale curve (Figure 87 yields a value of 2.21 for the most likely neutron cross section scale. The statistical and the leading systematic error were calculated and are included in the final result for the cross section scale and the cross section itself. The kinetic energy range for this measurement was extracted from simulation after verifying that the reconstructed kinetic energy for proton candidates in data agree with simulation. This allows us to supplement and compare the ProtoDUNE-SP measurement with previous results from MiniCAPTAIN.

Both the ProtoDUNE-SP and MiniCAPTAIN results suggest that the neutron cross section is higher than the nominal values in use by the simulation, as shown in Figure 93. This warrants further studies of the impact for DUNE physics.

7.6. Final remarks

DUNE will need to properly model and understand the hadronic energy resolution and, it would be beneficial to inform the energy reconstruction stage about any missing energy from neutrons. Ideally one could produce an estimator such as the number of neutron capture candidates, the number of protons (given correlations between neutrons and protons in final states), or some other metric indicative of the probable missing energy at an event-by-event basis. A useful result that could be directly applied is the interaction length, through the displacement r, of neutrons given a specific origin. For example, the reconstruction could look for proton candidates within some number of neutron interaction lengths and identify the most likely origin of the neutron candidate.

If the results are consistent across a much broader energy of neutrons then one could easily change the neutron inelastic cross section in simulation in order to propagate the results to physics analyses in DUNE. Additional tests and measurements (e.g. using higher energy beam in ProtoDUNE-SP) should be performed in order to test for overall higher-than-nominal neutron cross sections in LAr.

Additional studies are also needed to better understand the neutron yield. As previously mentioned this could be due to a difference in efficiency between data and MC or it could indicate that the production models for neutrons are different than in simulation.

APPENDIX A : THE TRIGGER LOGIC UNIT

The Trigger Logic Unit (TLU) is a custom firmware IP written by the author to classify High Level Triggers (HLTs) as Beam and Non-Beam related triggers. It is also responsible for driving the readout of the PDS subsystem in SBND.

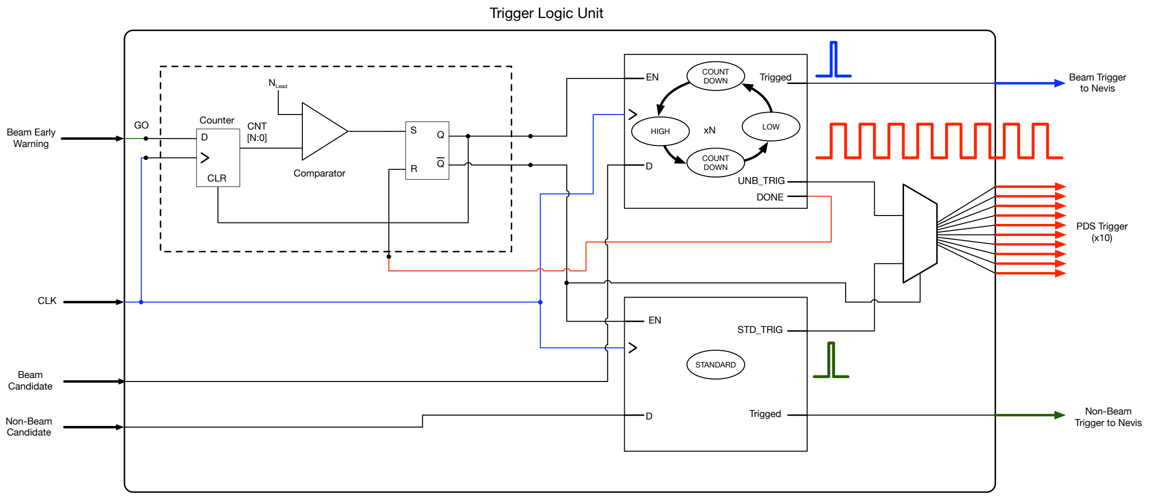

Figure 94: PDS Trigger Logic

All HLTs will be grouped into Beam and Non-Beam candidates through the use of input masks. Upon arrival of the beam early warning signal, the TLU begins counting until it reaches the number of 20 ns ticks configured as the lead time (N_{lead} in Figure 94) for the arrival of beam neutrinos to the detector. The PTB will open a “Beam Acceptance Gate” (BAG) upon reaching the lead time in order to look for beam triggers. Any PDS High Level Triggers in the Beam candidate category that is in coincidence with the BAG, will result in a Beam Trigger. A beam trigger can be configured in the TLU to result in a train pulse going to the CAEN PDS digitizers. Normally, a trigger pulse, whether of beam or non-beam origin result in a fixed 3μs window of PMT data. Thus, the purpose of the pulse train (shown in red in Figure 94) is to retrigger the digitizers and acquire N of these 3μs chunks of PDS data around beam triggers in order to be able to detect additional activity surrounding the beam neutrino candidate. This behavior is configurable, however, and depends on what digitization window is configured in the CAENs.

Three different versions of the Early Warning Signals from the BNB are available to the experiment, some are sent milliseconds in advance and some are closer in time, they also have different amounts of time jitter. An EWS will have to be chosen to minimize the jitter but also allow enough time to arm the trigger. A behavior that was envisioned by the collaboration was the ability change prescale[1] for the Cosmic Ray triggers during a window surrounding and including the 1.28 ms drift in order to have the PDS information for all cosmic rays that will effectively pile up and appear in the charge readout for a neutrino event – this time window will be referred to as the Cosmic Window. Cosmic triggers with no prescale will be put into coincidence with the Cosmic Window to allow the PDS electronics to capture flashes to do t_0 determination, and it will also aid in the CRT-PDS-TPC matching for cosmics entering the detector. Therefore, the lead time must be sufficient to accommodate for the Cosmic Window.

The lead time is configurable and will need to be determined, to first order, by measuring neutrino TOF and cable delays. A minimum bias study with varying lead times will also be useful for determining the best lead time configuration to use.

Except during the BAG, the PTB will only issue Non-Beam triggers. The difference in width of beam triggers and non-beam triggers (120 ns) was implemented to be able to easily tell which trigger. The readout system for the ARAPUCAs, known as the DAPHNE board will receive a single, concatenated stream of beam and non-beam triggers and will distinguish between the two by the width.

The logic performed by the TLU to determine when a trigger is consistent with a beam neutrino event was the responsibility of the Nevis Trigger Board. However, with time and with consistent progress with the PTB firmware this task was instead relegated to the PTB.

---

[1] A prescale is a simple “fire once for every N of these”-downscale for a particular trigger.

APPENDIX B : PTB-CRT INTERFACE

The CRT transfers trigger primitives in the form of 14 LVDS signals routed in pairs via long CAT5 cables between the CRT panels at their seven locations and the PTB rear panel. Galvanic isolation is established via the magnetics within the isolators. By design, the grounds must remain isolated and therefore the LVDS Signals must be referenced at the PTB before being converted to LVCMOS3.3V. This is achieved with a termination to the common-mode voltage (V_{cmm}) produced at the PTB. Various tests were performed at FNAL to ensure that the PTB receives signals produced in a two-ground scheme without introducing shorts between Detector and Building ground.

In lieu of a PTB at the ND building this test was performed in a room at FNAL containing the hardware (saturable inductor) that is used at ND to isolate the two grounds.

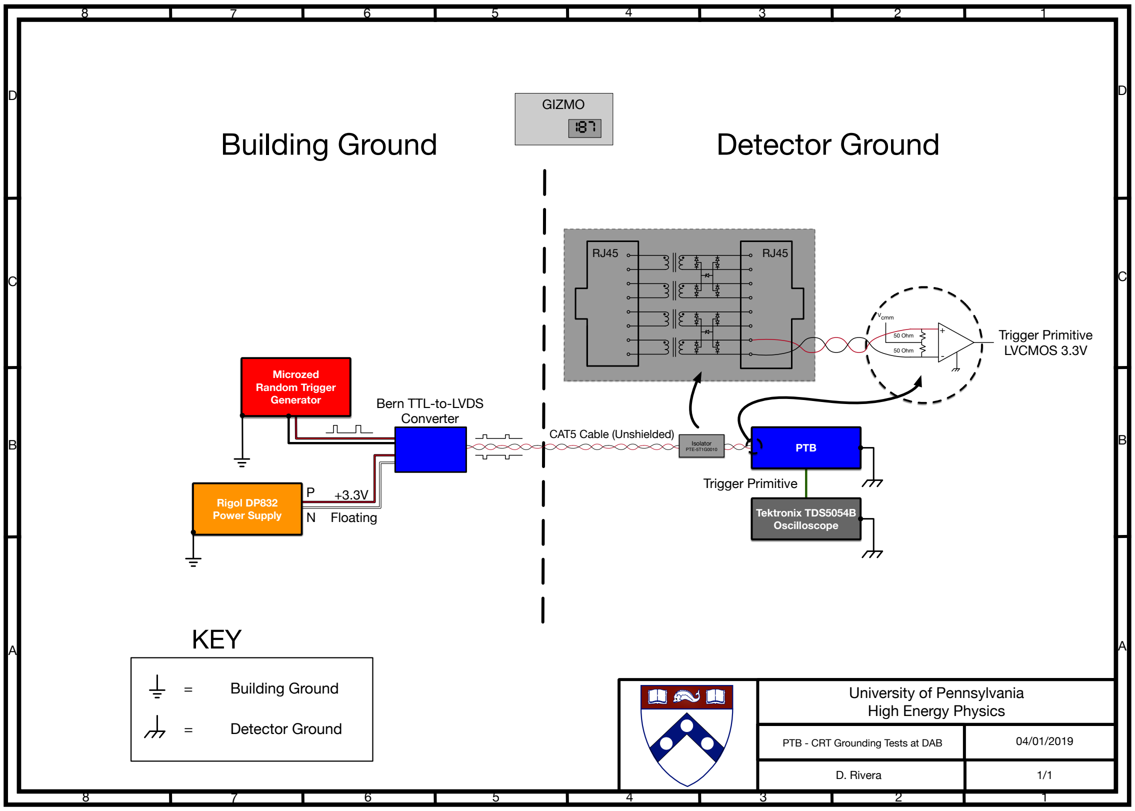

Figure 95: PTB-CRT grounding scheme circuit.

APPENDIX C : ADJACENT WIRE-HIT MULTIPLICITY RATES FROM AR-39

C.1. Accidental rate for two wires

For a LArTPC, accidental coincidences occur when background events for multiple wires pile up within a gated time window (Δt). There are multiple ways to go about looking for coincidences, e.g. we may decide to follow:

- (**Scheme 1:**) for each wire start a gate Δt everytime it is hit and look for overlaps between this window and any windows that also open in the neighbor wires
- (**Scheme 2:**) continuously look for coincidences in chunks of Δt

For simplicity, consider a two wire detector, and let wires A and B have equal and independent noise rates, r.

C.1.1. Scheme 1

In the first scheme, the accidental probability is the probability that A sees a noise hit in dt which initiates the gate and the probability that B also sees a hit some time within Δt *plus* the equivalent probability where B is hit first.

Let N_{acc} be the number of accidental events. As described, the accidental rate (Γ_{acc}) is then:

$$dN_{acc} = \Gamma_{acc} dt = (r_A dt) \cdot \overline{P_{B|0}} + (r_B dt) \cdot \overline{P_{A|0}} \tag{C.1}$$

where $\overline{P_{A|0}}$ denotes the probability that A is hit in a time window Δt i.e. the probability that n $\neq$ 0.

The probability that a process of rate r occurs in an infinitesimal time dt, depends on the amount of time that has elapsed without happening. Namely, the change in the probability that no event happens is:

$$d\overline{P_0} = P[n \geq 1, dt] \cdot P[n = 0, \Delta t] = rdt \cdot P_0 \tag{C.2}$$

Utilizing the fact that $P_0 + \overline{P_0} = 1$ and solving for the time-dependence of P_0:

$$\begin{aligned} \overline{dP_0} = -dP_0 &= rdt \cdot P_0 \\ \frac{dP_0(t)}{P_0(t)} &= -\, rdt \\ \int_0^t \frac{dP_0(t')}{P_0(t')} &= -\int_0^t rdt' \\ ln\Big(\frac{P_0(t)}{P_0(0)}\Big) &= -\, rt \\ P_0(t) &= P_0(0)e^{-rt} \end{aligned} \tag{C.3}$$

Note that $P_0(t = 0)$ is 1, by construction. Hence:

$$P_0(t) = e^{-rt} \tag{C.4}$$

Note that this represents the probability of not being hit in an interval of width t, and in order to obtain the probability that a decay does occur, $\overline{P_0}$, we can integrate over the collection time following eq. C.2. Thus we have that:

$$\begin{gathered} \overline{P_0}(\Delta t) = \int_0^{\Delta t} re^{-rt}dt = \frac{-r}{r}(e^{-r\Delta t} - 1) \\ \boxed{\overline{P_0}(\Delta t) = 1 - e^{-r\Delta t}} \end{gathered} \tag{C.5}$$

Substituting eq. C.4 into eq. C.1 we have:

$$\begin{aligned}\Gamma_{acc}dt &= (1-P_0(\Delta t))\cdot(r_A dt) + (1-P_0(\Delta t))\cdot(r_B dt)\\ &= (1-e^{-r_B\Delta t})\cdot(r_A dt) + (1-e^{-r_A\Delta t})\cdot(r_B dt)\\ &= (1-e^{-r\Delta t})\cdot(r dt) + (1-e^{-r\Delta t})\cdot(r dt)\\ &= 2(1-e^{-r\Delta t})\cdot(r dt)\end{aligned} \tag{C.6}$$

$$\Gamma_{acc}(t) = 2r(1-e^{-r\Delta t}) \tag{C.7}$$

Expanding the exponential in powers of $(r\Delta t)$:

$$e^{-r\Delta t} = \sum_{n=0}^{\infty}\frac{(-r\Delta t)^n}{n!} = 1-(r\Delta t)+\frac{(r\Delta t)^2}{2!}+... \tag{C.8}$$

In the limit that $r\Delta t$ is small compared to 1 we can neglect terms of $\mathcal{O}((r\Delta t)^2)$ and higher. Equation C.7 becomes:

$$\begin{aligned}\Gamma_{acc}(t) \approx& 2r(1-(1-(r\Delta t)))\\ \approx& 2r(r\Delta t)\end{aligned} \tag{C.9}$$

The rate for **scheme 1** is then:

$$\boxed{\Gamma_{acc} \approx 2r^2\Delta t} \tag{C.10}$$

C.1.2. Scheme 2

In scheme 2, we need to find the probability that, given a gate of width Δt that starts at an arbitrary point in time t_0, wires A and B both see noise hits.

$$dN_{acc} = \Gamma_{acc} dt = \overline{P_{A|0}} \cdot \overline{P_{B|0}} \cdot r_g dt \tag{C.11}$$

Where r_g is the rate at which we impose the windows i.e. $1/\Delta t$ and $\overline{P_{A,B|0}}$ are as derived before. Substituting for these in the expression we have:

$$\begin{aligned} dN_{acc} = \Gamma_{acc} dt &= (1 - e^{-r\Delta t})^2 \cdot \frac{dt}{\Delta t} \\ &\approx (r\Delta t)^2 \cdot \frac{dt}{\Delta t} = r(r\Delta t)dt \end{aligned} \tag{C.12}$$

The rate for **scheme 2** is then:

$$\boxed{\Gamma_{acc} \approx r^2 \Delta t} \tag{C.13}$$

The factor of 2 difference between the two rates arises from the fact that in the first scheme the time window is effectively twice as long since we are allowed to trigger the detector whenever either wire sees a hit and the wires have independent noise rates.

C.2. Fake rate for arbitrary n_{adj}, 1D case

In scheme 1, for higher number of wires n there are additional terms from the pileup combinations of the remaining $(n - 1)$ wires. Accidental rates in this scheme will always involve calculating the probability that the nth wire is hit in an infinitesimal slice of time dt.

In scheme 2, all that matters are the total number of distinct groupings that can be formed with an n-wire detector which is relevant for both.

C.2.1. Combinatorics

We can place a naive upper limit on the number of groups of wires that can form a group of interest. Namely, for an n_w-wire detector, the number of groups of adjacent wires n_{adj} follows:

$$n \leq \binom{n_w}{n_{adj}} \tag{C.14}$$

Clearly, for $n_w >> n_{adj}$, the number of groups is much smaller than this limit and for an adjacency of 1, n must equal n_w. Similarly, for $n_{adj} = n_w$, n must equal 1 since there is one unique group of all wires.

Claim: Given these boundary conditions, a possible solution is: $n = (n_w - n_{adj} + 1)$.

Proof: Let $\eta_n(k)$ denote the sets of k-tuples in an n-wire detector. Consider the following examples:

$$
\begin{aligned}
&\eta_2(2) = \Big(\{[1,2]\}\Big) \\
&\eta_3(2) = \Big(\{[1,2],[2,3]\},\{[1,3]\}\Big) \\
&\eta_4(2) = \Big(\{[1,2],[2,3],[3,4]\},\{[1,3],[2,4]\},\{[1,4]\}\Big) \\
&\eta_5(2) = \Big(\{[1,2],[2,3],[3,4],[4,5]\},\{[1,3],[2,4],[3,5]\},\{[1,4],[2,5]\},\{[1,5]\}\Big) \\
&\eta_3(3) = \Big(\{[1,2,3]\}\Big) \\
&\eta_4(3) = \Big(\{[1,2,3],[2,3,4]\},\{[1,2,4],[1,3,4]\}\Big) \\
&\eta_5(3) = \Big(\{[1,2,3],[2,3,4],[3,4,5]\},\{[1,2,4],[1,3,4],[2,3,5],[2,4,5]\},\{[1,2,5],[1,4,5]\}, \\
&\{[1,3,5]\}\Big)
\end{aligned}
\tag{C.15}
$$

If we apply an adjacency requirement, then only the groups in black are valid. Note that the total number of groups for a given $\eta_{n_w}(n_{adj})$ is equal to $\binom{n_w}{n_{adj}}$, and that only a fraction of these are retained as originally stipulated in eq. C.14.

Note, also, that the groups of adjacent n_{adj} wires have the following general structure:

$$
\eta_n(k) = \Big(\big\{\big[1,...,k\big],\big[2,...,(k+1)\big],...,\big[(n-(k-1),...,n\big]\big\},\{\text{gap terms}\}\Big) \tag{C.16}
$$

Where the terms in the "gap terms" are the remaining, non-contiguous groupings containing one or more gaps. Note also that there are exactly $n-(k-1)$ groups with k elements each in the list of contiguous groups that we're interested in; furthermore, this can be rewritten as $n-k+1$, matching the original claim.

$$
\boxed{n(n_w, n_{adj}) = n_w + 1 - n_{adj}} \tag{C.17}
$$

C.2.2. Three wires

Scheme 1

As an additional example, let X_1, X_2, and X_3 represent three adjacent wires. Following the previous example with 2 wires, the only choice for forming 3-wire accidental coincidences in scheme 1 is which wire is in coincidence with the two previously hit wires.

$$\begin{aligned}\Gamma_{acc}dt = &(1 - P_0(X_1, \Delta t))(1 - P_0(X_2, \Delta t)) \cdot (r_3 dt) \\ &+ (1 - P_0(X_1, \Delta t))(1 - P_0(X_3, \Delta t)) \cdot (r_2 dt) \\ &+ (1 - P_0(X_2, \Delta t))(1 - P_0(X_3, \Delta t)) \cdot (r_1 dt) \\ = &3(1 - e^{-r\Delta t})^2 \cdot r dt\end{aligned} \tag{C.18}$$

In the small $(r\Delta t)$ limit, applying the expansion in eq. C.8:

$$\Gamma_{acc} \approx 3r(r\Delta t)^2 \tag{C.19}$$

2-tuple accidental rate

The rate of 2-wire coincidences for a 3-wire detector is given by:

$$\Gamma_{acc}(n_c) = (\text{number of n}_c\text{-tuples}) \cdot \Gamma_{acc|n_w=n_c} \tag{C.20}$$

Substituting the two-wire rate in eq. C.7 for $\Gamma_{acc|n_w=2}$:

$$\Gamma_{acc}(n_c) = 2 \cdot 2r(1 - e^{-r\Delta t}) \approx 4r(r\Delta t) \tag{C.21}$$

In general, the accidental rate for n adjacent wires (n_{adj}) for an n_w-wire detector is:

$$\Gamma_{acc}(n_w, n_{adj}) = (n_w + 1 - n_{adj}) \cdot n_{adj} \cdot r(1 - e^{-r\Delta t})^{(n_{adj}-1)} \tag{C.22}$$

C.2.3. Scheme 2

In scheme 2 since we impose the gate, the rate is simply the number of distinct groupings of wires times the average rate, i.e.:

$$\Gamma_{acc}(n_w, n_{adj}) = (n_w + 1 - n_{adj}) \cdot r(1 - e^{-r\Delta t})^{(n_{adj}-1)} \tag{C.23}$$

C.2.4. Time-ordering constraint

Note, however, that for the second term in eq. C.18 if we place the additional constraint that all hits arrive in time order, i.e. that wire 2 is hit after wire 1 and before wire 3 or after wire 3 and before wire 1, then the number of valid combinations is $\binom{2}{1} = 2$, since, we are only deciding whether wire 1 or wire 3 are hit first. The rest is fixed by this choice.

The modified expression for Γ_{acc} in this scenario is given by:

$$\begin{aligned}
\Gamma_{acc}dt &= \overline{P_{X_1|0}}(t_0 < t_1 < t_0 + \Delta t) \cdot \overline{P_{X_2|0}}(t_1 < t_2 \leq t_0 + \Delta t) \cdot (r_3 dt) \\
&\quad + \overline{P_{X_3|0}}(t_0 < t_1 < t_0 + \Delta t) \cdot \overline{P_{X_2|0}}(t_1 < t_2 \leq t_0 + \Delta t) \cdot (r_1 dt) \\
&= \overline{P_{X_2|0}}(t_1 < t_2 \leq t_0 + \Delta t) \cdot \Big[\overline{P_{X_1|0}}(0 < t_1 < t_0 + \Delta t) \\
&\quad + \overline{P_{X_3|0}}(t_0 < t_1 < t_0 + \Delta t)\Big] \cdot (rdt)
\end{aligned} \tag{C.24}$$

But $\overline{P_{X_1|0}}$ and $\overline{P_{X_3|0}}$ are equivalent, thus C.24 becomes:

$$\Gamma_{acc}dt = rdt \cdot 2\overline{P_{X_{1,3}|0}}(0 < t_1 < \Delta t) \cdot \overline{P_{X_2|0}}(t_1 < t_2 \leq \Delta t) \tag{C.25}$$

where t_0 has been taken to be 0 for simplicity.

$$\begin{aligned} \Gamma_{acc} &= 2r \cdot (1 - e^{-rt_1}) \cdot (1 - e^{-r(\Delta t - t_1)}) \\ &\approx 2r(rt_1)(r(\Delta t - t_1)) < 2r(r\Delta t)^2 \end{aligned} \tag{C.26}$$

This lower rate for scheme 1 can only be achieved if the position and time resolution are sufficiently fine. Effects such as multiple scattering should be taken into account.

C.2.5. n wire coincidences in time order

The time order constraint is motivated by the topology of tracks, which for MIPs, are straight lines, and for particles with sufficient energy to ionize, are approximately straight lines. The factor of 2 in the previous example for scheme 1 is thus the number of types of straight lines that are acceptable (1-2-3 and 3-2-1). Without the time-ordered constraint the boundary conditions are periodic, i.e. 2-3-1 and 1-3-2 are permissible as well. Enforcing time-ordering, it follows from eq. C.26 that for $n_{adj} \leq n_w$ the rate is:

$$\Gamma_{acc}(n_{adj}, \Delta t) = 2(n_w + 1 - n_{adj}) \cdot r \prod_{n=1}^{n_{adj}-1} [1 - e^{-r(t_n - t_{n-1})}] \tag{C.27}$$

$$\lessapprox 2(n_w + 1 - n_{adj}) \cdot r(r\Delta t)^{n_{adj}-1} \tag{C.28}$$

Again, this rate is bounded from above.

In a LArTPC, when LAr is ionized, the ion and electrons drift in opposite directions following the E-field lines. The ions drift towards the Cathode while electrons are collected at the Anode Plane Assemblies (APAs) where the wires of interest reside.

In a real Liquid Argon TPC, ^{39}Ar events produced randomly in space can fake tracks by arriving at the wires with some delay. The detector can be divided into an m-by-n grid, where m is the number of wires and n represents the number of time slices between the cathode and the APAs. For now, let the definition of adjacency encompass only hits that are next to each other in four directions, namely, for a cell (m_i, n_0), the adjacent cells are: (m_{i+1}, n_0), (m_{i+1}, n_1), (m_{i-1}, n_1), and (m_i, n_1). Note that (m_{i-1}, n_0) takes precedence over (m_i, n_0) and is therefore only counted once. The 4 classes of adjacencies in this Toy Model are as depicted in figure 96.

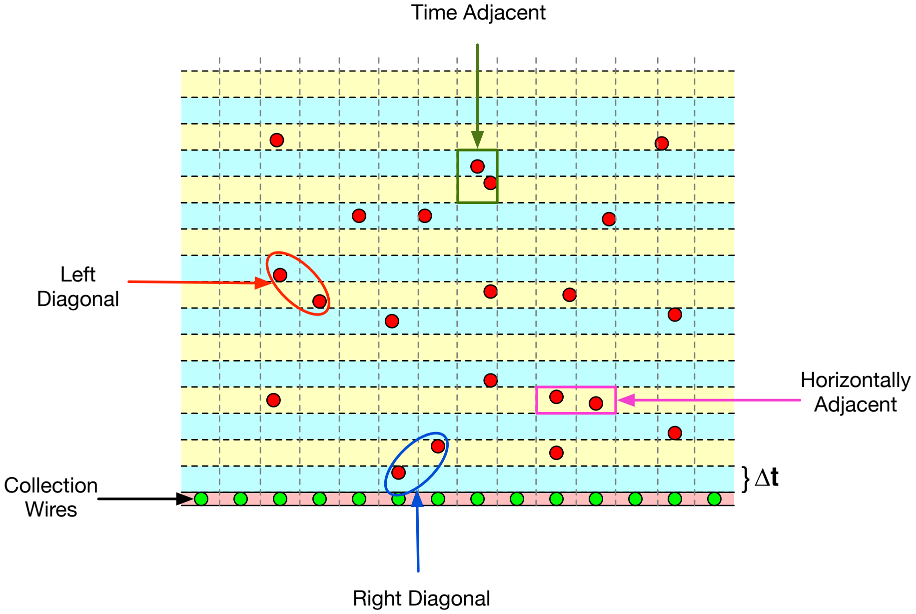

Figure 96: The four classes of adjacencies: horizontal, time adjacent, and left and right-diagonal adjacencies.

C.3.1. General expression

The combinatorics for the 2D case are identical to the ones in the 1D case except that there are now 3 additional directions, and since the time axis is ongoing, the maximum adjacency in the time direction is n_w.

Given sufficiently long time windows, the prefactor for the rate is:

$$n(n_w, n_{adj}) = \begin{cases} (n_w + 1 - n_{adj}) = n_w & , n_{adj} = 1 \\ [3(n_w + 1 - n_{adj}) + n_w] & , 1 < n_{adj} \leq n_w \\ n_w & , n_{adj} > n_w \end{cases} \tag{C.29}$$

Note that for $n_{adj} = 1$, we recover the total noise rate of the detector namely we have that:

$$\Gamma_{acc}(n_w, 1) = n_w \cdot r \tag{C.30}$$

Substituting for the second prefactor in eq. C.29 we have:

$$\Gamma_{acc}(n_{adj}, \{t_1, t_2 ... t_n\}) = [3(n_w + 1 - n_{adj}) + n_w] \cdot r \prod_{n=1}^{n_{adj}-1} [1 - e^{-r(t_n - t_{n-1})}] \tag{C.31}$$

$$\leq [3(n_w + 1 - n_{adj}) + n_w] \cdot r (r\Delta t)^{n_{adj}-1} \tag{C.32}$$

C.4. Toy MC simulations

The general approach consists of dividing up the detector into time slices that are populated randomly and compared to previous time slices in order to look for hits occurring across adjacent channels and adjacent time slices.

The simulation presented here is based on the activity and dimensions of a DUNE 10kt Single Phase Module. The main parameters and assumptions are shown in Table 13, below.

Table 13: Parameters for study.

Parameter	Value
LAr Volume	10kt
^{39}Ar content	1 Becquerel/kg
Dimensions (L×W×H)	58m× 12m× 14.5m
Active Drift Volume per wire plane	3.6m
Wire pitch	5mm
Drift velocity	1mm/μs
Number of active[2]collection wires	96,000
Average ^{39}Ar rate/wire	104.167 Hz

It is likely that we will want to set the coincidence gate to be something in the order of, at least, ten microseconds. **Note:** The shaping time of the Front End Electronics are up to[3] 3μs which means that a delta function of charge will produce signals that take roughly twice that long to return to the baseline.

The charge distribution for ^{39}Ar was not taken into account here; the purpose of this short study is to set an upper limit on the pileup rate as a function of wire hit multiplicities. The simulation selects a time slice at the far end of the drift volume which is then populated as it drifts. Randomly filling the active volume first and then cycling through each time slice without additional drifting yielded the same results which is consistent with expectations.

---

[3] Configurable to 0.5, 1.0, 2.0, and 3.0 μs

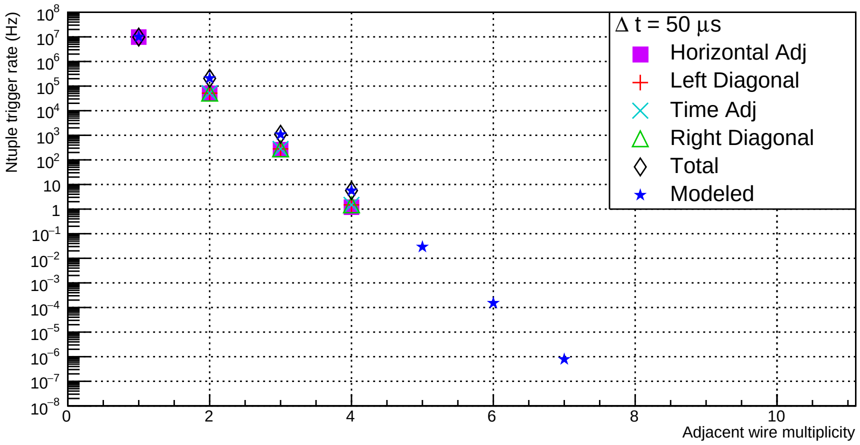

Figure 97: Total simulated rates by component vs. modeled rate from eq. C.29

C.5. SuperNova Burst Condition

Suppose that we now require n_B of any given adjacent wire multiplicity, then if we want to calculate the rate of an n_B-Burst then we take the rate from the previous sections (for now consider the 1D case) and define a new time interval, T.

$$\tilde{r} \equiv (n_w + 1 - k)r(1 - \exp\{-r\Delta t\})^{n_{adj}-1} \tag{C.33}$$

$$P(n_B; \tilde{r}T) = \frac{(\tilde{r}T)^{n_B-1}\exp^{-\tilde{r}T}}{(n_B-1)!} \tag{C.34}$$

The probability of seeing n_B hits needs to account include, also, the probability of seeing $n_B + 1$, $n_B + 2$, ... and so on. Thus, we need to instead, use the probability of seeing at least n_B hits. Thus the rate at which these bursts occur is given by:

$$\tilde{\Gamma} = \tilde{r} \cdot (1 - C.D.F.[P(n_B - 1; \tilde{r}T)]) \tag{C.35}$$

where $C.D.F.[P(n_B - 1; \tilde{r}T)]$ is the probability seeing less than n_B hits.

APPENDIX D : COSMIC RAY NEUTRONS

The results from a sample of 19600, individual cosmic ray primaries generated by CORSIKA and propagated by GEANT4 within LArSoft. The main goal behind this study is to determine the origin and spatial distribution of cosmic neutrons.

The provenance, or ancestry, of a particle is defined as the chain of interactions leading up to the particle of interest – the descendant. Ionization depositions events (IDEs) refer to ionization charge generated by particles in the GEANT4 simulation.

Figure 98 below, is a X-Z view (looking down from above the cryostat) of the IDEs produced by neutron descendants. Figure 98 is a Y-Z view from the side (looking toward the drift volume from the beam side).

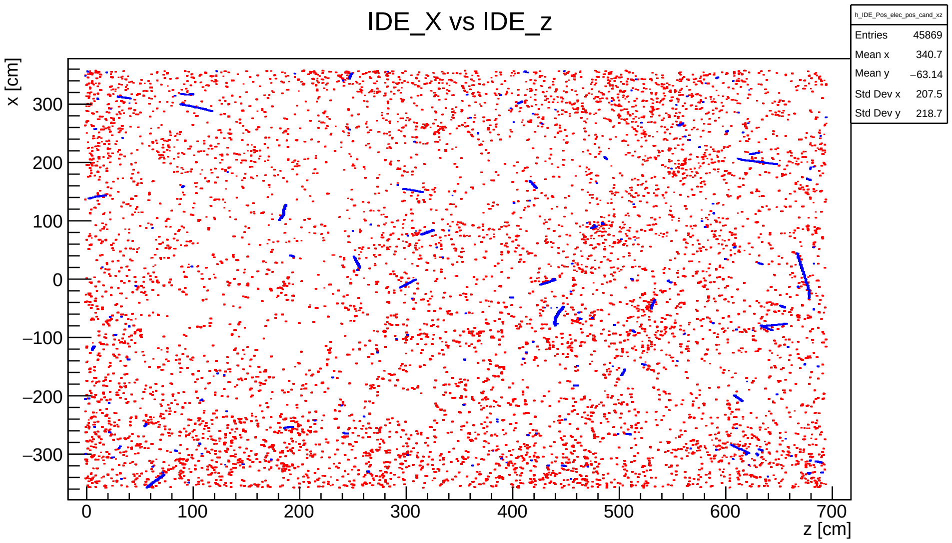

Figure 98: Ionization Deposition Event locations for protons and electrons with neutron ancestors. 19600 single, cosmic ray events.

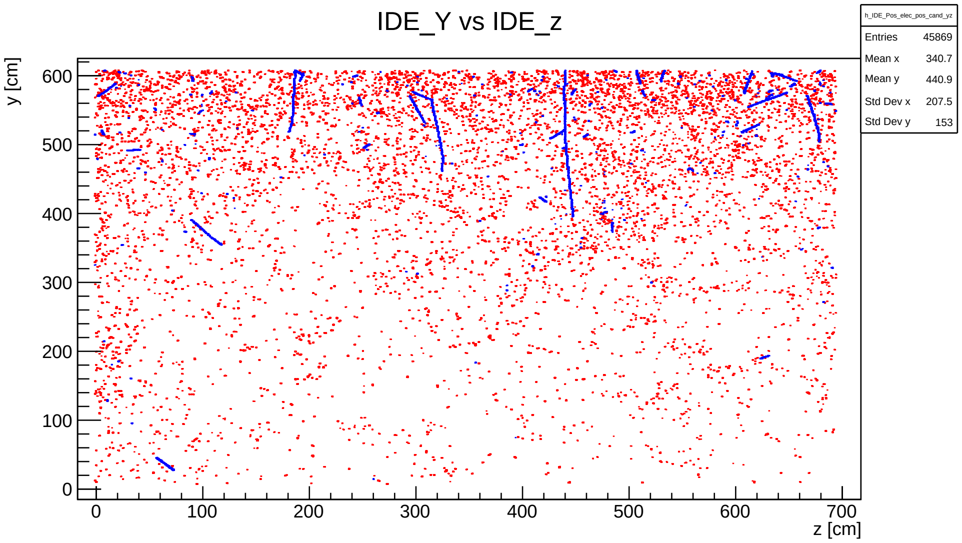

Figure 99: Ionization Deposition Event locations for protons and electrons with neutron ancestors. 19600 single, cosmic ray events.

This figure depicts the energy depositions backtracked to neutrons via two different interactions chains. The ionization depositions (in blue) belong to protons which have neutron mothers and have been inelastically scattered from an ^{40}Ar atom. Depositions in red belong to electrons that have a gamma mother, where the gamma itself, has a neutron mother. These are indicative of neutron capture events, or they can be the result of neutron momentum transfers with Argon atoms that lead to de-excitation gammas.

Table 14: Electron Candidate Hit Summary

Provenance	Percent
$\mathrm{n} \rightarrow \gamma \rightarrow \mathrm{e}^-$	96.77%
$\mathrm{n} \rightarrow \mathrm{n} \rightarrow \gamma \rightarrow \mathrm{e}^-$	2.95%
$\pi^\pm \rightarrow \mathrm{n} \rightarrow \gamma \rightarrow \mathrm{e}^-$	0.15%
$\mu^\pm \rightarrow \mathrm{n} \rightarrow \gamma \rightarrow \mathrm{e}^-$	0.09%
$\mathrm{p} \rightarrow \mathrm{n} \rightarrow \gamma \rightarrow \mathrm{e}^-$	0.04%

For electron candidate IDEs with gamma mothers of neutron provenance (45869), the majority are from primary neutrons (44389). Of the remaining IDEs (1480), 1352 have neutron provenance, 17 have proton provenance, 41 have μ^- provenance, 53 have π^- provenance, 17 have π^+ provenance.

For proton candidate IDEs with neutron mother (6054), there are roughly equal amounts of candidate IDEs from primary (2805) and secondary (3128) neutrons. The rest are from primary protons and pions.

Table 15: Proton Candidate Hit Summary

Provenance	Percent
n → n → p	51.67%
n → p	46.33%
p → n → p	1.72%
$\pi^\pm$ → n → p	0.28%

Out of the 61,584 neutrons in the simulation, 17,194 were captured 6492 exited the entire geometry without interacting and 37,898 inelastically scattered as their final process. Note that this includes neutrons that escape the fiducial volume which can capture on the cryostat steel or the concrete walls for example. The number of captures within the fiducial volume are 867. A subset of the electrons with neutron provenance are a result of these 867 captures.

580 candidate IDEs were produced in an ArgoNeut-sized cut near the beam window across all 19600 single cosmic ray events. The majority of these IDEs were from electron candidates (567/580).

APPENDIX E : GLOSSARY

E.1. Acronyms

ADC	Analog to Digital Converter
ALEPH	Apparatus for LEP PHysics
ANL	Argonne National Laboratory
APA	Anode Plane Assembly
ARAPUCA	Bird Trap (in Portuguese). Device used for trapping scintillation light
ARM	Advanced RISC Machine
ASIC	Application Specific Integrated Circuit
ATLAS	A Toroidal LHC ApparatuS
AV	Active Volume
AXI	Advanced eXtensible Interface
BAG	Beam Acceptance Gate
BDT	Boosted Decision Tree
BERT	BERTini cascade
BI	Beam Instrumentation
BNB	Booster Neutrino Beam
BNL	Brookhaven National Laboratory
CAEN	Costruzioni Apparecchiature Elettroniche Nucleari
CAPTAIN	Cryogenic Apparatus for Precistion Test of Argon Interactions with Neutrinos
CC	Charged Current
CDF	Collider Detector at Fermilab
CDR	Conceptual Design Report
CERN	European Organization for Nuclear Research
CHIPS	CHiral Invatiant Phase Space
CMC	Constant Mass Composition
CMOS	Complementary Metal-Oxide Semiconductor
CNN	Convolutional Neural Network
CORSIKA	COsmic Ray SImulations for KAscade
CP	Charge Parity
CPA	Cathode Plane Assembly
CPU	Core Processing Unit
CR	Cosmic Ray
CRT	Cosmic Ray Tagger
CTB	Central Trigger Board
DAB	D-Zero Assembly Building
DAQ	Data AcQuisition
DELPHI	DEtector with Lepton Photon and Hadron Identification

DMA	Direct Memory Access
DOE	Department of Energy
DP	Dual-Phase
DUNE	Deep Underground Neutrino Experiment
ECL	Emitter-Coupled Logic
EM	Electromagnetic
ENC	Equivalent Noise Charge
ES	Elastic Scattering
EW	Electroweak
EWS	Early Warning Signal
FC	Field Cage
FD	Far Detector
FE	Front End
FEMB	Front End Mother Board
FIFO	First In First Out
FLUKA	A Multi-Particle Transport Code.
FNAL	Fermi National Accelerator Laboratory
FPGA	Field Programmable Gate Array
FSM	Finite State Machine
FW	Firmware
GEANT4	Toolkit used to do particle propagation and simulate physics.
GLoBES	General Long-Baseline Experiment Simulator
GPU	Graphics Processing Unit
HEP	High Energy Physics
HI	HIgh
HLT	Hight Level Trigger
HP	High Precision
HV	High Voltage
I/O	Input and Outputs
IBD	Inverse Beta Decay
ICARUS	Imaging Cosmic And Rare Underground Signals
ID	IDentification
IH	Inverted Hierarchy
IP	Intellectual Property
JETP	Journal of Experimental and Theoretical Physics
JINST	Journal of INSTrumentation
JSON	JavaScript Object Notation
KE	Kinetic Energy
LANL	Los Alamos National Laboratory
LANSCE	Los Alamos Neutron Science CEnter
LAr	Liquid Argon
LArSoft	Liquid Argon Software.
LBNL	Lawrence Berkeley National Laboratory

LE	Low Energy
LED	Light Emitting Diode
LEP	Large Electron Positron
LHC	Large Hadron Collider
LLT	Low Level Trigger
LN$_2$	Liquid Nitrogen
LO	LOw
LSND	Liquid Scintillator Neutrino Detector
LVDS	Low Voltage Differential Signal
MB	Mother Board
MC	Monte Carlo
MCC	Monte Carlo Challenge
MED	MEDium
MH	Mass Hierarchy
MI	Main Injector
MIP	Minimum Ionizing Particle
MPV	Most Probable Value
MSW	Mikheyev Smirnov Wolfenstein
MTC/A	Master Trigger Card/Analog
MW	MegaWatts
NC	Neutral Current
ND	Near Detector
NH	Normal Hierarchy
NIM	Nuclear Instrumentation Module
NIST	National Institute of Standards and Technology
NP04	Neutrino Platform 04
NuMI	Neutrinos at the Main Injector
OPAL	Omni-Purpose Apparatus at LEP
OS	Operating System
PB	PetaBytes
PCB	Printed Circuit Board
PDF	Probability Distribution Function
PDG	Particle Data Group
PDS	Photon Detection System
PDSP	ProtoDUNE Single-Phase
Penn	University of Pennsylvania
PID	Particle ID
PL	Programmable Logic
PMNS	Pontecorvo Maki Nakagawa Sakata
PMT	PhotoMultiplier Tube
POT	Protons On Target
PS	Processing System
PSL	Physical Sciences Laboratory
PTB	Penn Trigger Board

QCD	Quantum ChromoDynamics
QED	Quantum Electrodynamics
QGSP	Quark Gluon String
RAM	Random Access Memory
RC	Resistor-Capacitor
RC	Run Control
RISC	Reduced Instruction Set Computing
RMS	Root Mean Square
ROI	Region of Interest
ROOT	An object-oriented C++ framework for particle physics analysis.
SBN	Short Baseline Neutrino
SBND	Short Baseline Near Detector
SCE	Space Charge Effect
SiPM	Silicon PhotoMultiplier
SLD	SLAC Large Detector
SM	Standard Model
SN	SuperNova
SNO	Sudbury Neutrino Observatory
SNP	Solar Neutrino Problem
SoC	System-on-a-Chip
SP	Single Phase
SPS	Synchroton Proton Source
SSM	Standard Solar Model
SU	Special Unitary
SURF	Sanford Underground Research Facility
TADC	TPC ADC
TB	Trigger Board
TCP	Transmission Control Protocol
TDR	Technical Design Report
TOF	Time-Of-Flight
TOT	Time Over Threshold
TPB	tetraphenyl-butadeine
TPC	Time Projection Chamber
TTL	Transistor-Transitor Logic
VEV	Vacuum Expectation Value
VHDL	VLSI Hardware Description Language
VLSI	Very Large Scale Integration
VUV	Vacuum Ultraviolet
WADC	Wire ADC
XS	Cross Section
ZYNQ	Family of SoCs designed by the Xilinx technology company.

BIBLIOGRAPHY

Liquid Argon Properties (Tables and Calculators). URL `https://lar.bnl.gov/properties/index.html#scint`. LAr Properties. x, 32, 34, 139

https://pdg.lbl.gov/2019/reviews/rpp2018-rev-passage-particles-matter.pdf. URL `https://pdg.lbl.gov/2019/reviews/rpp2018-rev-passage-particles-matter.pdf`. Passage of Particles Through Matter. xii, 30, 31

ROOT: RooFit Tutorials. URL `https://root.cern/doc/master/group__tutorial__roofit.html`. 144

Large Hadron Collider. URL `http://en.wikipedia.org/wiki/Large%20Hadron%20Collider`. 48

Abe, K. et al. Constraint on the matter–antimatter symmetry-violating phase in neutrino oscillations. *Nature*, 580(7803):339–344, 2020. ISSN 0028-0836. doi: 10.1038/s41586-020-2177-0. xx

Abi, B. et al. The Single-Phase ProtoDUNE Technical Design Report. *arXiv.org*, physics.ins-det, 06 2017. URL `arXiv.org`. 165 pages, fix references, author list and minor numbers. xiii, 28, 41, 52, 65, 95

Abi, B. et al. First results on ProtoDUNE-SP liquid argon time projection chamber performance from a beam test at the CERN Neutrino Platform. *Journal of Instrumentation*, 15(12):P12004 – 101, 12 2020a. doi: 10.1088/1748-0221/15/12/p12004. xi, xii, xiii, xvii, 28, 31, 38, 39, 48, 50, 51, 114, 116, 120, 125, 131

Abi, B. et al. Deep Underground Neutrino Experiment (DUNE), Far Detector Technical Design Report, Volume IV: Far Detector Single-phase Technology. *arXiv*, 2020b. x, xii, 33, 37, 39, 40, 75

Abi, B. et al. Deep Underground Neutrino Experiment (DUNE), Far Detector Technical Design Report, Volume II: DUNE Physics. *arXiv*, 2020c. 75

Abud, A.A. et al. Deep Underground Neutrino Experiment (DUNE) Near Detector Conceptual Design Report. *arXiv*, 2021. 35

Acciarri, R. et al. A study of electron recombination using highly ionizing particles in the ArgoNeuT Liquid Argon TPC. *Journal of Instrumentation*, 8(08):P08005–P08005, 2013. doi: 10.1088/1748-0221/8/08/p08005. 125

Acciarri, R. et al. A Proposal for a Three Detector Short-Baseline Neutrino Oscillation Program in the Fermilab Booster Neutrino Beam. *arXiv*, 2015a. 73

Acciarri, R. et al. Long-Baseline Neutrino Facility (LBNF) and Deep Underground Neutrino

Experiment (DUNE) Conceptual Design Report Volume 2: The Physics Program for DUNE at LBNF. *arXiv.org*, physics.ins-det, 12 2015b. URL `arXiv.org`. xii, 35, 36, 37

Acciarri, R. et al. The Pandora multi-algorithm approach to automated pattern recognition of cosmic-ray muon and neutrino events in the MicroBooNE detector. *arXiv*, hep-ex, 08 2017a. URL `arXiv.org`. Preprint to be submitted to The European Physical Journal C. 118

Acciarri, R. et al. Design and construction of the MicroBooNE detector. *Journal of Instrumentation*, 12(02):P02017–P02017, 2017b. doi: 10.1088/1748-0221/12/02/p02017. 28

Acciarri, R. et al. Demonstration of MeV-Scale Physics in Liquid Argon Time Projection Chambers Using ArgoNeuT. *arXiv.org*, hep-ex(1):483, 10 2018. doi: 10.1103/physrevd.99.012002. URL `arXiv.org`. xvi, 107, 108

Acciarri, R. et al. The Liquid Argon In A Testbeam (LArIAT) experiment. *Journal of Instrumentation*, 15(04):P04026–P04026, 2020. doi: 10.1088/1748-0221/15/04/p04026. 28

Acero, M.A. et al. An Improved Measurement of Neutrino Oscillation Parameters by the NOvA Experiment. *arXiv*, 2021. xx

Adams, C. et al. Calibration of the charge and energy loss per unit length of the MicroBooNE liquid argon time projection chamber using muons and protons. *arXiv.org*, physics.ins-det (0):P03022, 07 2019. doi: 10.1088/1748-0221/15/03/p03022. URL `arXiv.org`. Accepted version. 123

Adams, D.L. et al. Photon detector system timing performance in the DUNE 35-ton prototype liquid argon time projection chamber. *Journal of Instrumentation*, 13(06), 2018-06. doi: 10.1088/1748-0221/13/06/p06022. xiii, 28, 55

Adamson, P. et al. Search for flavor-changing non-standard neutrino interactions by MINOS. *Physical Review D*, 88(7):072011, 2013. ISSN 1550-7998. doi: 10.1103/physrevd.88.072011. xx

Adamson, P. et al. First measurement of muon-neutrino disappearance in NOvA. *arXiv*, 2016. doi: 10.1103/physrevd.93.051104. 95

Agostinelli, S. et al. Geant4—a simulation toolkit. *Nuclear Instruments and Methods in Physics Research Section A: Accelerators, Spectrometers, Detectors and Associated Equipment*, 506(3):250–303, 2003. ISSN 0168-9002. doi: 10.1016/s0168-9002(03)01368-8. 97

Aguilar-Arevalo, A.A. et al. Observation of a Significant Excess of Electron-Like Events in the MiniBooNE Short-Baseline Neutrino Experiment. 05 2018. URL `https://arxiv.org/abs/1805.12028`. xi, xx, 26

Ahmad, Q.R. et al. Measurement of the Rate of e + d → p + p + e- Interactions Produced by B8 Solar Neutrinos at the Sudbury Neutrino Observatory. *Physical Review Letters*, 87(7):071301, 2001. ISSN 0031-9007. doi: 10.1103/physrevlett.87.071301. 15

Alves, A.A. et al. CORSIKA 8. *EPJ Web of Conferences*, 251:03038, 2021. doi: 10.1051/epjconf/202125103038. 117

Anderson, C. et al. Analysis of a large sample of neutrino-induced muons with the ArgoNeuT detector. *Journal of Instrumentation*, 7(10):P10020, 2012. ISSN 1748-0221. doi: 10.1088/1748-0221/7/10/p10020. 28

Ankowski, A.M. et al. Missing energy and the measurement of the CP-violating phase in neutrino oscillations. *Physical Review D*, 92(9):091301, 2015. ISSN 1550-7998. doi: 10.1103/physrevd.92.091301. URL `http://dx.doi.org/10.1103/physrevd.92.091301`. xi, xxii, 157

Antcheva, I. et al. ROOT — A C++ framework for petabyte data storage, statistical analysis and visualization. *Computer Physics Communications*, 182(6):1384–1385, 2011. ISSN 0010-4655. doi: 10.1016/j.cpc.2011.02.008. 112

Bahcall, J.N. et al. Standard Neutrino Spectrum from B-8 Decay. *arXiv.org*, nucl-th(1): 411 – 422, 01 1996. doi: 10.1103/physrevc.54.411. URL `arXiv.org`. Revised version, to appear in Phys. Rev. C. xv, 87, 89

Barashenkov, V.S., Gudima, K.K. and Toneev, V.D. Cross Sections for Fast Particles and Atomic Nuclei. *Fortschritte der Physik*, 17(10):683–725, 1969. ISSN 1521-3979. doi: 10.1002/prop.19690171002. xvi, 103

Bass, M. Interfacing CORSIKA air shower simulations with LArSoft. URL `https://indico.fnal.gov/event/10893/contributions/5770/attachments/4097/5393/MBass_LArSoftCoordMtg_CorsikaGen.pdf`. CORSIKA. 117

Bass, M. The Short Baseline Neutrino Oscillation Program at Fermilab. *arXiv.org*, physics.ins-det, 02 2017. URL `arXiv.org`. Conference proceedings for ICHEP 2016. xiii, 43

Bettini, A. et al. The ICARUS liquid argon TPC: a complete imaging device for particle physics. *Nuclear Instruments and Methods in Physics Research Section A: Accelerators, Spectrometers, Detectors and Associated Equipment*, 315(1-3):223–228, 1992. ISSN 0168-9002. doi: 10.1016/0168-9002(92)90707-b. 27

Bhandari, B. et al. First Measurement of the Total Neutron Cross Section on Argon Between 100 and 800 MeV. *arXiv.org*, hep-ex(4):042502, 03 2019. doi: 10.1103/physrevlett.123.042502. URL `arXiv.org`. 5 pages, 1 table, 3 figures, submitted to Physical Review Letters. xvi, xix, 109, 111, 157

Biery, K. et al. artdaq: DAQ software development made simple. *Journal of Physics:*

Conference Series, 898(3):032013, 2017. ISSN 1742-6596. doi: 10.1088/1742-6596/898/3/032013. 64

Blum, J. Overview · pothosware/PothosCore Wiki. URL `https://github.com/pothosware/PothosCore/wiki/Overview`. 63

Blyth, S. Opticks : GPU Optical Photon Simulation for Particle Physics using NVIDIA® OptiXTM. *EPJ Web of Conferences*, 214:02027, 2019. doi: 10.1051/epjconf/201921402027. 113

Booth, A.C. et al. Particle production, transport, and identification in the regime of 1 - 7 GeV /c. *Physical Review Accelerators and Beams*, 22(6):061003, 2019-06. doi: 10.1103/physrevaccelbeams.22.061003. 49, 117, 123

Carena, M. et al. Neutrinos in Large Extra Dimensions and Short-Baseline e Appearance. *arXiv.org*, hep-ph(9):549, 08 2017. doi: 10.1103/physrevd.96.095014. URL `arXiv.org`. 15 pages, 11 figures. 25

Cavanna, F., Ereditato, A. and Fleming, B.T. Advances in liquid argon detectors. *Nuclear Inst. and Methods in Physics Research*, 907:1 – 8, 2018-11. doi: 10.1016/j.nima.2018.07.010. xi, 28

Chadwick, J. The existence of a neutron. *Proceedings of the Royal Society of London. Series A, Containing Papers of a Mathematical and Physical Character*, 136(830):692–708, 1932. ISSN 0950-1207. doi: 10.1098/rspa.1932.0112. 1

Cleveland, B.T. et al. Measurement of the Solar Electron Neutrino Flux with the Homestake Chlorine Detector. *The Astrophysical Journal*, 496(1):505 – 526, 1998-03. doi: 10.1086/305343. 13, 14

Collaboration, T.A. et al. Precision Electroweak Measurements on the Z Resonance. *arXiv.org*, pages arXiv:hep – ex–0509008, 2005-09. URL `arXiv.org`. 302 pages, v2: minor corrections and updates of references. Accepted for publication by Physics Reports, v3: further small corrections and journal version; Phys.Rept.427:257-454,2006; doi:10.1016/j.physrep.2005.12.006. xi, 24

Cowan, C.L.J. et al. Detection of the Free Neutrino: A Confirmation. *Science*, 124(3):103 – 104, 1956-07. doi: 10.1126/science.124.3212.103. 1, 16

Cowan, G. The method of maximum likelihood. In *Statistical Data Analysis*, pages 70–94. Oxford University Press Inc., New York, 1998. ISBN 0-19-850156-0. 149

Danby, G. et al. Observation of High-Energy Neutrino Reactions and Existence of 2 Kinds of Neutrinos. *Physical Review Letters*, 9(1):36 – +, 1962. doi: 10.1103/physrevlett.9.36. 17

Escudero, L. et al. Pandora pattern recognition for LArTPCs. URL `https://indico.fnal.gov/event/18523/contributions/47922/`

`attachments/29818/36721/PandoraPatternRecognition_LorenaEscudero_CalibrationReconstructionWorkshopLArtPCs_December2018.pdf`. pandora presentation. xvii, 119

Ferrari, A. et al. FLUKA: A Multi-Particle Transport Code. 2006. doi: 10.2172/877507. 108

Formaggio, J.A. and Zeller, G.P. From eV to EeV: Neutrino cross sections across energy scales. *Reviews of Modern Physics*, 84(3):1307–1341, 2012. ISSN 0034-6861. doi: 10.1103/revmodphys.84.1307. URL `http://dx.doi.org/10.1103/revmodphys.84.1307`. xv, 96

Friedland, A. and Li, S.W. Understanding the energy resolution of liquid argon neutrino detectors. *arXiv.org*, hep-ph(3):89, 11 2018. doi: 10.1103/physrevd.99.036009. URL `arXiv.org`. 22 pages, 20 figures; clarifications, references, and new figures added; results unchanged; updated to match the published version. xv, 93, 94

Giunti, C. and Kim, C.W. The Higgs mechanism. In *Fundamentals of Neutrino Physics and Astrophysics*, pages 83–88. Oxford University Press Inc., New York. ISBN 978-0-19-850871-7. 10

Giunti, C. and Kim, C.W.. *Fundamentals of neutrino physics and astrophysics*. Oxford ; New York : Oxford University Press. Oxford ; New York : Oxford University Press, 2007. ISBN 0198508719. doi: 10.1093/acprof:oso/9780198508717.001.0001. 22

Goldhaber, M., Grodzins, L. and Sunyar, A.W. Helicity of Neutrinos. *Physical Review*, 109 (3):1015 – 1017, 1958. doi: 10.1103/physrev.109.1015. 8

Green, C. et al. The art framework. *Journal of Physics: Conference Series*, 396(2):022020, 2012. ISSN 1742-6596. doi: 10.1088/1742-6596/396/2/022020. 112

Group, P.D. Atomic and nuclear properties of liquid argon (Ar). URL `https://pdg.lbl.gov/2021/AtomicNuclearProperties/HTML/liquid_argon.html`. LAr Atomic and Nuclear Properties. 32

Inc, M. Final Technical Report on STTR Project DE-FG02-06ER86281 Particle Tracking in Matter-Dominated Beam Lines (G4beamline). doi: 10.2172/1013856. 117

Kajita, T. et al. Establishing atmospheric neutrino oscillations with Super-Kamiokande. *Nuclear Physics B*, 908:14–29, 2016. ISSN 0550-3213. doi: 10.1016/j.nuclphysb.2016.04.017. 15

Klein, J.R. Solar neutrinos, 2019. Private communication. 88

Knoepfel, K. LArSoft and Future Framework Directions at Fermilab. *EPJ Web of Conferences*, 245:05008, 2020. doi: 10.1051/epjconf/202024505008. 112, 113

Kuźniak, M. and Szelc, A.M. Wavelength Shifters for Applications in Liquid Argon Detectors. *Instruments*, 5(1):4, 2020. doi: 10.3390/instruments5010004. 34, 35

Land, B. Simulating optical physics with Chroma | ben.land. URL `https://ben.land/post/2020/12/07/optical-physics-chroma/`. Chroma intro. 113

Lazzaro, A. and Moneta, L. MINUIT package parallelization and applications using the RooFit package. *Journal of Physics: Conference Series*, 219(4):042044, 2010. ISSN 1742-6596. doi: 10.1088/1742-6596/219/4/042044. 141

Machado, P.A., Palamara, O. and Schmitz, D.W. The Short-Baseline Neutrino Program at Fermilab. *Annual Review of Nuclear and Particle Science*, 69(1):363–387, 2019. ISSN 0163-8998. doi: 10.1146/annurev-nucl-101917-020949. 43

Marx, J.N. and Nygren, D.R. The Time Projection Chamber. *Physics Today*, 31(10):46–53, 1978. ISSN 0031-9228. doi: 10.1063/1.2994775. 27

Mocioiu, I. and Shrock, R. Neutrino Oscillations with Two Δm2 Scales. *arXiv.org*, hep-ph (11):050 – 050, 06 2001. doi: 10.1088/1126-6708/2001/11/050. URL `arXiv.org`. 24 pages, revtex, 5 postscript figures, some refs. added. 25

Motta, H.D. et al. ARAPUCA light trap for large liquid argon time projection chambers. *Proceedings of The 19th International Workshop on Neutrinos from Accelerators NUFACT2017 — PoS(NuFact2017)*, page 153, 2018. doi: 10.22323/1.295.0153. 35

Nunokawa, H., Parke, S. and Valle, J.W.F. CP Violation and Neutrino Oscillations. *arXiv.org*, hep-ph(2):338 – 402, 10 2007. doi: 10.1016/j.ppnp.2007.10.001. URL `arXiv.org`. 78 pages, 46 figures, minor misprint corrections, a few new references and an acknowledgement to a funding agency. Review to be published in Prog. Part. Nucl. Phys. 23

Pontecorvo, B. Mesonium and Antimesonium. *Soviet Journal of Experimental and Theoretical Physics*, 6:429, 1958. 14

Pontecorvo, B. Neutrino experiments and the question of leptonic-charge conservation. *Journal of Experimental and Theoretic Physics*, 26:984, 1968. 17

Reynolds, A. *Evaluating the low-energy response of the ProtoDUNE-SP detector using Michel electrons*. PhD thesis, 2020. Thesis. 121

Rivera, D. Migrating to the refactored larg4 - LArG4 - Fermilab Redmine. URL `https://cdcvs.fnal.gov/redmine/projects/larg4/wiki/Migrating_to_the_refactored_larg4`. PDSP migration. 113

Rossi, B. and Greisen, K. Cosmic-Ray Theory. *Reviews of Modern Physics*, 13(4):240 – 309, 1941-10. doi: 10.1103/revmodphys.13.240. 139

Rossi, B. et al. The DarkSide Program. *EPJ Web of Conferences*, 121:06010, 2016. doi: 10.1051/epjconf/201612106010. 28

Rubbia, C. The Liquid-Argon Time Projection Chamber: A New Concept For Neutrino Detector, 5 1977. 27

Sternheimer, R.M. General expression for the density effect for the ionization loss of charged particles. *Physical Review B*, 24(11):6288–6291, 1981. ISSN 1098-0121. doi: 10.1103/physrevb.24.6288. 32

Sutton, C. Ghosts in the machine – CERN Courier, 07 2016. URL `https://cerncourier.com/a/ghosts-in-the-machine/`. The 1956 experiment that proved neutrinos exist. xi, 12

Totani, D. and Cavanna, F. First calorimetric energy reconstruction of beam events with ARAPUCA light detector in protoDUNE-SP. *Journal of Instrumentation*, 15(03): C03033–C03033, 2020. doi: 10.1088/1748-0221/15/03/c03033. 35

Verkerke, W. RooFit. *EPJ Web of Conferences*, 4:02005, 2010. doi: 10.1051/epjconf/20100402005. 144

White, D.H. and Collaboration, L. Neutrino oscillation results from LSND. *Nuclear Physics B - Proceedings Supplements*, 77(1-3):207–211, 1999. ISSN 0920-5632. doi: 10.1016/s0920-5632(99)00419-3. xx

Wright, D.H., Kelsey, M.H. and Grp, G.H.W. The Geant4 Bertini Cascade. *Nuclear Instruments & Methods in Physics Research Section a-Accelerators Spectrometers Detectors and Associated Equipment*, 804:175 – 188, 2015. doi: 10.1016/j.nima.2015.09.058. 100

Zyla, P.A. Number of Light Neutrino Types from Collider Experiments. *pdg.ihep.su*. 23